Cardiff University
School of Engineering

Investigation of Surface Discharges in Insulation Gases Through Synchronisation of Improved Electrical and Fast Enhanced-Imaging Techniques

---

Thesis submitted to Cardiff University
for the degree of Doctor of Philosophy

Michail Michelarakis

Cardiff, Wales, U.K.
March 2022

Summary

This thesis investigates the generation of discharge activity in the regions where gaseous and solid dielectrics meet with energised conductors, frequently referred to as triple points/junctions. Such conditions are frequently met in practical complex assemblies of equipment and apparatus used in medium- and high-voltage applications, and the common discharge phenomena to appear are known as surface discharges.

An optimised test configuration which replicates strongly non-uniform field conditions on the surface of solid dielectric samples was developed. As gaseous insulation, atmospheric gases are considered namely, technical air (21/79 % O_2/N_2), nitrogen (N_2) and carbon dioxide (CO_2), and the eco-friendly mixture of trifluoroiodomethane (CF_3I) with carbon dioxide (30/70 % CF_3I/CO_2). The examined solid dielectric materials include polytetrafluoroethylene (PTFE), epoxy resin and silicone rubber, all of which are frequently found in electric power industry applications of different types.

The experimental investigation included the electrical detection of surface discharge activity in various gaseous compound/solid dielectric type combinations with the use of optimally developed current sensing circuits. Furthermore, a new enhanced-performance high-speed camera system was developed synchronised with the electrical detection system for the study of the propagation patterns and morphology of the discharges.

From both electrical and optical detection methods, it could be concluded that the 30/70 % CF_3I/CO_2 mixture performed the best with N_2 being the least effective. Technical air was found to withstand flashover better compared to CO_2 however, the latter showed better performance in suppressing the inception of partial discharge activity and the extension of surface streamers.

A list of more detailed conclusions and discussion points are presented at the end of each chapter and which are further developed in the last chapter of this thesis. Suggestions that can potentially be implemented in future works, experimental and theoretical, are also listed.

Acknowledgements

This PhD research project was carried out in the Advanced High Voltage Engineering Research Center (AHIVE), School of Engineering, Cardiff University, Cardiff, Wales, U.K. between January 2017 and February 2021. The present Thesis report was submitted to Cardiff University for the degree of Doctor of Philosophy.

First of all, I would like to express my sincere gratitude to my Cardiff University supervisors, Prof. A. (Manu) Haddad, Dr. Phillip Lugg-Widger and Dr. David Clark for their advice, guidance and continuous support throughout the implementation of this research project. Without your contributions this research project would not have been possible.

I would like also to thank my external supervisor, Prof. A. Beroual from École Centrale de Lyon, University of Lyon for his guidance and support through his extensive knowledge and experience on the topic.

My sincere thanks also goes to Dr. Houssem Eddine Nechmi, Dr. Mohammed El Amine Slama, Dr. Daniel Carr, Mrs. Kate Osbaldeston, Dr. Athanasios Mermigkas, Mrs. Sofia Mavidou, Mr. Christopher Stone and Mr. Meirion Hills for their support and advice. I am also grateful to all of the members of the AHIVE Research Group, with whom I have had the pleasure to work during this and other projects. I greatly appreciate the support, motivation and guidance received from Professor Emeritus Ronald T. Waters. It was a privilege and pleasure for me to share time and discussions with you.

My gratitude also goes to my fellow PhD student Jonathan Colin James. His support inside and outside our working environment made this PhD work an even more

pleasant journey. Our extensive scientific and friendly level discussions were a continuous source of motivation.

I gratefully acknowledge the funding received towards my PhD from Cardiff University. Also, a big thank you to all the members of the academic and administrative staff at the School of Engineering at Cardiff University. Many thanks to all the members of the Mechanical workshop, Mr. Andrew Rankmore and Mr. Malcolm Seaborne, for all their support and advice received.

Lastly, a special thanks to my family for their continuous encouragement and all my friends in Greece, Sweden and Wales for being next to me continuously and unconditionally.

List of Publications

Conferences

M. Michelarakis, P. Widger, A. Haddad and A. Beroual, "Creeping Discharge Development Over Insulator Surfaces in Natural Gases: Design and Implementation of Test Procedure," *2018 IEEE International Conference on High Voltage Engineering and Application (ICHVE)*, 2018, pp. 1-4, doi: 10.1109/ICHVE.2018.8642172.

M. Michelarakis, P. Widger, A. Beroual and A. Haddad, "Development of Surface Discharge Over PTFE Insulator Surfaces in Nitrogen and Air ," *12th Universities High Voltage Network Colloquium (UHVnet)*, 2019.

Journals

M. Michelarakis, P. Widger, A. Beroual, and A. (Manu) Haddad,"Electrical Detection of Creeping Discharges over Insulator Surfaces in Atmospheric Gases under AC Voltage Application," *Energies*, vol. 12, no. 15, p. 2970, Aug. 2019, doi: 10.3390/en12152970.

M. Michelarakis, D. Clark, P. Widger, A. Beroual, R. T. Waters and M. A. Haddad, "Triple Point Surface Discharge Photography in Atmospheric Gases Using Intensified High-Speed Camera System," in *IEEE Transactions on Dielectrics and Electrical Insulation*, vol. 29, no. 1, pp. 153-161, Feb. 2022, doi: 10.1109/TDEI.2022.3148481.

Further contributions

M. Michelarakis, G. Gulics, E. Bailey, S. Lane, R. Montano and A. M. Haddad, “Retrofit of outdoor medium voltage circuit breaker with eco-friendly gas to replace SF_6,” *CIRED 2021 - The 26th International Conference and Exhibition on Electricity Distribution*, 2021, pp. 504-508, doi: 10.1049/icp.2021.1515.

H. E. Nechmi, M. Michelarakis, A. (Manu) Haddad, and G. Wilson, “Clarifications on the Behavior of Alternative Gases to SF_6 in Divergent Electric Field Distributions under AC Voltage,” *Energies*, vol. 14, no. 4, p. 1065, Feb. 2021, doi: 10.3390/en14041065.

Contents

List of Figures

List of Tables

List of Abbreviations

Abbreviation	Expansion
2D	Two-Dimensional
3D	Three-Dimensional
AC	Alternating Current
Al_2O_3	Aluminium Oxide
BSO	Bismuth Silicon Oxide (crystal)
CaF_2	Calcium Fluoride
CAS	Chemical Abstracts Service
CC	Connecting Cable
CCD	Charge-coupled device
CD	Coupling Device
CF_3I	Trifluoroiodomethane
CMOS	Complementary metal-oxide-semiconductor
CO_2	Carbon Dioxide
DC	Direct Current
DSO	Digital Storage Oscilloscope
EC	Electric Currents (COMSOL Multiphysics® module)
EPDM	Ethylene Propylene Diene Monomer
ER	Epoxy resin
ES	Electrostatics (COMSOL Multiphysics® module)
FFKM	Perfluoroelastomer
FKM	Fluorocarbon-based fluoroelastomer
FOV	Flashover Voltage
fps	Frames per second
g^3	Green Gas for Grid - g cubed
GCB	Gas Circuit Breaker
GDT	Gas Discharge Tube
GE	General Electric
Ge	Germanium
GIL	Gas Insulated Line
GIS	Gas Insulated Switchgear

Continued on next page

Continued from previous page

Abbreviation	**Expansion**
GWP	Global Warming Potential
H_2O	Water molecule
HFCT	High Frequency Current Transformer
HFOs	Hydrofluoroolefins
HV	High-Voltage
IIR	Isobutylene-Isoprene Rubber
IPCC	Intergovernmental Panel on Climate Change
IR	Infrared
kBr	Potassium Bromide
$LC_{50\,\%}$	Lethal Concentration $(50\,\%)$
MgF_2	Magnesium Fluoride
MI	Measuring Instrument
MV	Medium-Voltage
N_2	Nitrogen
NBR	Nitrile-Butadiene Rubber
NIST	National Institute of Standards and Technology
ODP	Ozone Depletion Potential
OH radicals	Hydroxyl radicals
PC	Polycarbonate
PCB	Printed Circuit Board
PD	Partial Discharge
PE	Polyethylene
PET	Polyethylene Terephthalate
PFCs	Perfluorocarbons
PI	Polyimide
PMMA	Poly(methyl meth-acrylate)
PRPD	Phase-Resolved Partial Discharge
PTFE	Polytetrafluoroethylene
PVC	Polyvinyl Chloride
PVDF	Polyvinylidene Fluoride
RC filter	Resistor-Capacitor filter
SF_6	Sulphur Hexafluoride
Si	Silicon
S-parameters	Scattering Parameters
SR	Silicone Rubber
TFE	Tetrafluoroethylene
TTL	Transistor-Transistor Logic
UNFCCC	United Nations Framework Convention on Climate Change
UV	Ultraviolet

Continued on next page

Continued from previous page

Abbreviation	**Expansion**
UVFS	UV Fused Silica
VCM	Vinyl Chloride Monomer
VFTO	Very Fast Transient Overvoltage
VIS	Visible light of spectrum
VNA	Vector Network Analyzer
ZnSe	Zinc Selenide

List of Mathematical Symbols

Symbol	Definition
$(E/N)_{\text{lim}}$	Critical reduced electric field
A	Weight of a compound
a_{d}	Interfacial/space charge polarisability
a_{e}	Electronic polarisability
a_{i}	Ionic polarisability
a_{o}	Orientation polarisability
a_{total}	Total polarisability
α_{r}	Radiative efficiency of carbon dioxide
α_{x}	Radiative efficiency of a compound
C	Capacitance
$C\,[f]$	Rate change in function f
D	Effective diameter
d	Distance
$\boldsymbol{D}$	Electric displacement field
E	Electric field magnitude
e	Elementary charge
E_{max}	Maximum electric field
E_{mean}	Mean electric field
f	Electron distribution in the six-dimensional phase space
F_{a}	Apparent elastic limit
f_{AC}	AC frequency
$\hbar$	Planck's constant
h_0	Humidity at reference atmospheric conditions
I	Current
I_{avg}	Average discharge current
J_{c}	Conduction current density
J_{e}	External current density
K	Empirical constant for calculation of circular window thickness
k	Number of test attempts

Continued on next page

Continued from previous page

Symbol	**Definition**
L	Inductance
m	Mass
m_{e}	Electron rest mass
M_{gas}	Molecular weight of a gas compound
n	Amount of substance
N	Gas density
$n_{\mathrm{e,\,0}}$	Number of primary electrons
n_{e}	Number of electrons
n_{pd}	Pulse repetition rate
N_{pd}	Pulse repetition frequency
P	Gas pressure
p	Gas pressure
$\boldsymbol{P}$	Polarisation
P_{pd}	Discharge power
P_{s}	Allowable operational pressure
P_{t}	Test pressure
p_0	Pressure at reference atmospheric conditions
Q	Increase in potential energy after a collision
q	Apparent charge
Q_{j}	Distributed current source
Q_{max}	Maximum integral energy gained during a collision
R	Ideal gas constant
r	Radius
$r\,(t)$	Time-dependent decay in abundance of the instantaneous release of carbon dioxide
R_{a}	Arithmetic average of the absolute values of the profile height deviations from the mean line
R_{c}	Resistance of components
$\rho_{\mathrm{Gas\ Den.}}$	Gas density
s_{bd}	Standard deviation for disruptive discharge tests
SF	Safety Factor
T	Temperature
T_{AC}	AC period
t_{i}	Time of occurrence
T_{ref}	Reference time interval
$T_{\mathrm{Wind.}}$	Thickness of circular window
t_0	Temperature at reference atmospheric conditions
τ_{ocean}	Ocean uptake
τ_{soil}	Soil uptake

Continued on next page

Continued from previous page

Symbol	Definition
τ_{strat}	Stratospheric lifetime of a substance
τ_{total}	Total lifetime of a substance
$\tau_{\mathrm{total}}^{\mathrm{atm}}$	Total atmospheric lifetime of a substance
TH	Time horizon of observation
U	Voltage level
u	Speed
U_{bd}	Breakdown voltage
u_{d}	Drift velocity
u_{i}	Instantaneous applied voltage level
V	Volume
V_{e}	Electric potential
$x\left(t\right)$	Time-dependent decay in abundance of the instantaneous release of the substance
x_{i}	Weight fraction of a compound in a mixture
Z	Impedance
Z_0	Characteristic impedance
α	Townsend's first ionisation coefficient
$\bar{\alpha}$	Effective ionisation coefficient
γ	Secondary ionisation coefficient
$\delta\left(\phi\right)$	Average energy loss per collision
$\varDelta EN$	Electronegativity difference
ε	Permittivity of a material
ε_0	Permittivity of free space
$\varepsilon_{\mathrm{air}}$	Permittivity of air
ε_{r}	Relative permittivity
η	Electron attachment coefficient
$\eta_{\mathrm{E.F}}$	Field efficiency factor
λ	Free path of a particle between collisions
$\bar{\lambda}$	Mean free path
μ	Electrical mobility of a particle
ρ_{c}	Free charge or space charge
σ	Collision cross section
τ_{r}	RC filter rise time
ϕ	Work function
ϕ_{i}	Phase of occurrence
χ_{e}	Electric susceptibility
ω	Angular frequency

Chapter 1

Introduction

1.1 Background

Gaseous insulation is an important part in electrical engineering application concepts especially at elevated operating voltage levels such as those utilised in medium-voltage distribution and high-voltage transmission systems. Over the years, air at atmospheric conditions has been the subject of several studies, under various experimental and theoretical concepts. Synthetic gaseous substances, with superior electric properties compared to atmospheric air, started to attract attention as early as the late 19th century [1]. It was until the 1950's when SF_6 was chosen as the best option for enclosed pressurised electrical applications with the delivery of the first commercial circuit breakers. To this day, various gaseous insulating substances, such as atmospheric and synthetic fluorinated, have been researched, proposed and more recently adopted, all of them with different properties effectively resulting in a long list of practical considerations.

Solid insulators and insulating compartments have also been very important and necessary parts in the assemblies of distribution and transmission power system apparatus where atmospheric air or enclosed pressurised synthetic gases are used. In most of the occasions, the role of such compartments is to provide mechanical support to the conducting electrodes, energised and/or earthed, while, at the same time, their impact on the rated insulating performance of the device assembly is maintained at operational level. Different types of materials that are met in outdoor, indoor and enclosed electrical applications include ceramics, resins, glass, polymers, rubbers, paper etc., in some of the cases blended with fillers of various types and sizes [2].

Gas electronics and gas discharge physics cover terms and processes which are considered quite complex to fully describe in their entire spectrum of cases. This happens for two reasons: first the phenomena associated with gas discharge physics require speciality equipment and experimental arrangements to be generated, and second, these kinds of processes have a strong probabilistic behaviour which makes the experimental outputs very demanding to interpret appropriately. The challenge is further enhanced when solid dielectrics are part of the experimental arrangement and the object under observation [3] as the induced electric discharge phenomena depend on both gaseous and solid insulation.

There are a wide range of case studies that can be reduced into small scale and fully controlled laboratory experiments and which can represent typical defects in gas insulated switchgear (GIS) and gas insulated lines (GIL) equipment [4–7]. The case, which is investigated throughout the present thesis report, is related to the well-known triple junctions [8, 9]. Under this term, are defined points or small regions where the gaseous insulation, solid dielectrics and charged metals meet. The most direct effect of triple junctions is the appearance of elevated electric field stresses in these regions, and which can be the source of discharge development and potentially failure of the insulation or its degradation in the long term. They are part of the practical design considerations and they need to be treated by adopting geometrical and resistive (linear and non-linear) field grading techniques in the quest of delivering reliable device assemblies.

Fast rising and extinguishing partial discharge phenomena, such as surface discharges, are challenging in their recording. Sensing circuits of sufficiently wide frequency response are required and which need to perform such a task accurately without exposing delicate recording equipment at risk. Capturing of surface discharge images is also a challenging task since many parameters, such as optical performance and operation process of the equipment, need to be balanced so that the maximum quality in the outputs is achieved. The synchronous implementation of those two can provide a new way of observing such phenomena and even expand that study approach in future works.

In this thesis, the development of surface discharges over solid insulator surfaces as a result of the presence of triple junctions is investigated. Different gaseous insulating media are examined in combination with solid insulator materials of different types. An important aspect of the experimental approaches that will be presented in the next chapters is the detail in the preparation of the employed configurations so that the maximum possible accuracy in the recording and capturing of the transient phenomena is achieved. Surface discharges are described as a sub-category of partial discharges [10–12] and thus their detection techniques are very similar in terms of technical specification and sensitivity requirements. Various imaging and photography techniques have been developed [13–18] for the detection and depiction of surface discharges. Photographic techniques can generate images where the light emitted from the discharge event is captured while a method such as the electro-optical Pockels effect can provide a visualisation of the residual surface charge distribution. Although there are differences between these methods, with regards to the implementation principle and practical advantages, all of them can provide very useful outputs. The outlook of this work will provide a synopsis on how the investigated gaseous media perform at test conditions such as failure of insulation (flashover) and pre-failure (PD). It will also provide an overview of how the different solid dielectric material types affect that performance. The range of outputs that will be presented in the next chapters will potentially constitute a useful insight when conditions, similar or close to the ones investigated in this thesis, are of interest in practical designs.

The experimental methods and preparatory stages, including validation procedures that are presented in this thesis can potentially serve as a useful reference for future investigations where accurate measurements and reliable image captures are required for such or similar case studies.

1.2 Research aims and objectives

A large number of studies have been published examining the pre-breakdown and breakdown phenomena in, primarily, gaseous insulation alone. Similar studies in solid/gas interfaces are fewer with many of them focusing on the final propagation length of these discharges. The aim of this thesis is to investigate the phenomenon of electric discharges that develop on the surface of solid dielectric samples of different materials and thicknesses immersed in different gaseous compounds at applied voltage levels lower than the corresponding flashover. Of major focus will be the study of atmospheric gases (technical air, N_2, CO_2) and the strongly attaching mixture of 30/70 % CF_3I/CO_2, all of them at a pressure level close to the atmospheric. The generated phenomena will be examined under the application of AC voltage waveform in a point-plane electrode configuration so that a a strongly non-uniform electric field is achievable.

At first, the study of the surface discharges will be performed by means of accurate electrical detection methods, where smaller and larger datasets are examined. Following that, the electrical detection methods will be combined with a newly developed UV-intensified high-speed camera system so that the propagation patterns and morphology of the discharges are further examined. The outputs of this work will hopefully contribute to the further understanding on the generation of the surface discharge phenomenon in the duration of the full AC-cycle at conditions where the defect is present although the failure levels of the insulation are not yet reached.

To achieve the above, the following steps are taken:

- Survey the researched gaseous insulation compounds and identify their key physical properties and environmental impact. Describe the fundamental physics concepts of gaseous and solid dielectrics and their interface. Survey on the electric strength of the gaseous compounds of technical air (21/79 % O_2/N_2), nitrogen (N_2), carbon dioxide (CO_2) and the 30/70 % CF_3I/CO_2 mixture with major focus on strongly non-uniform electric field conditions.

- Develop test set-ups for the experimental investigation of discharges on the surface of solid dielectric samples. This objective includes:
  - Design optimised electrode configuration for producing strongly non-uniform electric field conditions.
  - Implement circuits capable of accurately sensing the fast-rising discharge pulses.
  - Design and manufacture a pressure chamber able to incorporate the above.
  - Establish the protocols that will be adopted for AC voltage tests.
- Characterise surface discharge activity using accurate electrical detection combined with recordings of enhanced sampling rate. List key characteristics of the different gaseous compounds tested, along with differences between them, by examining the discharge patterns and the recorded high-resolution discharge pulses.
- Characterise surface discharge activity by examining longer duration recordings where data from several AC-cycles are incorporated. Produce illustration for the obtained recordings through a post-processing algorithm which isolates the discharge activity signals that exceed a specified threshold from the time-resolved recordings. List key characteristics and differences between the different test cases.
- Develop a high-speed camera system for the image capturing of the light emitted from the surface discharge activity. Of major focus are:
  - The optical response of the camera system: it needs to provide enhanced performance in the ultraviolet (UV) spectral and low end of the visible

    (VIS) range.

  - The system needs to operate synchronised with the signal recording system so that an event-based capturing and recording of the discharge activity is achieved.

- With the newly developed UV-intensified high-speed camera system, operated synchronously with the electric detection system, capture the surface discharge activity and the corresponding transient current signals. The main tasks under this objective are:

  - Capture the development of surface discharge activity in the duration of a full AC-cycle: list the differences in the captured patterns between different gaseous media and solid dielectric materials.
  - Perform event-based capturing and recording of the surface discharge activity: each discharge needs to be captured in a single frame accompanied with the corresponding time-resolved high-resolution discharge pulse. For each captured discharge it will be examined how its morphology reflects to the corresponding recorded transient pulse.
  - Identify how factors such as applied voltage magnitude, current pulse magnitude, phase of occurrence of the discharge, gaseous medium and solid dielectric material type affect the propagation and morphology of the generated discharge activity.

The AC waveform is of high practical interest since it is the operational waveshape in distribution and transmission power systems. At the power frequency of 50 Hz, the AC wave varies its magnitude slowly relative to the speed the charged particles drift in the presence of an externally applied electric field and it incorporates two half-cycles of different polarities. Pressure levels close to the atmospheric are also of practical interest especially in medium-voltage applications switchgear and for the cases where strongly attaching gases and mixtures are used. The comparative study between strongly attaching gases and atmospheric gases at such pressure levels is of practical interest as it contributes to the overall assessment on the suitability of each of the gaseous insulation compounds despite the known better performance of mixtures where fluorinated compounds are added. A charged needle-grounded plane electrode configuration is used to replicate protrusion defects on charged conductors. The presence of solid dielectrics of different types can provide observations on the impact such materials have in the development and propagation of generated discharge phenomena in the proximity of elevated electric field stress points.

1.3 Contributions of the research

The main contributions of this work are listed here and which summarise some of the key achievements presented in this thesis relevant to the objectives listed in Section 1.2. More extensive analysis can be found in the next chapters.

- An extensive literature review and summary of the researched options on gaseous insulation compounds including atmospheric gases, sulphur hexafluoride (SF_6) gas and the environmentally friendly SF_6 replacement candidates that have been proposed and researched over the recent years. Their key physical properties, such as their molecular weight and structure, were summarised and how these reflect to their environmental impact. The fundamental physics of gaseous and solid/gas interfaces are described with main focus on addressing the terminology that is widely used to describe them. The electric performance of gases and solid/gas interfaces is also summarised primarily from published literature where the test conditions were relatable to the ones adopted in this thesis.
- An optimised electrode configuration was designed and implemented through which the generation of strongly non-uniform electric field conditions were achievable on the surface of solid dielectric samples. Also, with that design,

it was possible to incorporate a sufficient connection for the high-frequency response electrical detection circuits. As the experimental studies for the characterisation of the electrically detected surface discharges and combined electrical detection with high-speed photography were performed at different stages, it was important to maintain the same test conditions, an aspect which is achievable with the implemented electrode configuration.

- Accurate electrical detection of the surface discharge activity was performed using the HFCT and shunt resistor techniques. Both circuits were validated for their efficiency by measuring the corresponding scattering parameters (S-parameters) and the entire sensing and recording configurations by injecting charge pulses of specific magnitude prior of running each test campaign. It was found that both of them were sufficiently sensitive (at least 10 pC) and could perform in a wide frequency range.
- Characterisation of surface discharges using the electrical detection method demonstrated the differences between the different gaseous media and combinations with solid dielectrics. This part of the work was performed in two stages. At first, the discharge activity was recorded in a high-resolution and sampling configuration of the recording devices. The differences between the different gaseous compounds were identified with most noticeable the absence of negative polarity discharges during the negative half-cycle for N_2 and the lower PD magnitudes recorded for CO_2 and 30/70 % CF_3I/CO_2. At the same time, the enhanced resolution current pulses demonstrated the differences between the different gaseous compounds with, again, CO_2 and 30/70 % CF_3I/CO_2 showing faster positive polarity pulses while N_2 the slowest developing. Recordings of back-discharges are also reported. Different solid dielectric materials and thicknesses showed very similar patters in their corresponding recordings. Through the use of large data sets, the differences between cases is presented with greater confidence.

- A new UV-intensified high-speed camera system was developed for the recording of the light emitted from the generated surface discharge activity. The system was operated synchronously with the electrical detection system (sensing circuit and recording devices), and two different trigger techniques were implemented. For the first, the development and propagation of the discharges in the duration of a full AC-cycle was achievable. For the second, discharge events were captured in separate frames while the corresponding discharge pulses were also recorded.
- From both synchronisation techniques described before, it was identified the dependence of the current pulse magnitude and applied voltage level the instant the discharge appears. It could be said that, for the positive half-cycle, the closer to the peak value of the voltage wave the discharge appears the longer its propagation will be. On the other hand, the higher the current magnitude is, the more spread the discharge channels will be. A capture of a back-discharge was also achieved which is rare considering that such discharges extend at very short distances from their point of origin.

1.4 Thesis contents

The contents of the thesis, as these are presented in separate chapters, include:

Chapter 2: An extensive literature review on the physical properties of the researched gaseous insulation compounds. This includes gases that are widely in use such as air, atmospheric and/or technical, and sulphur hexafluoride (SF_6) along with the synthetic proposed replacement candidates of the latter. The qualities that make SF_6 a very good insulating medium are recalled, and which appear to be the required characteristics for the proposed replacement compound(s). A summary of the fundamental physics related to gaseous and solid dielectrics is also presented in this chapter. An overview of the electric performance of the gaseous compounds investigated in this thesis are also examined. Towards the end of the chapter, the different techniques for capturing images of surface discharge activity are described.

Chapter 3: In this chapter the equipment and basic components of the experimental set-ups are extensively described. The processes regarding the application of the test voltages are followed throughout the test procedures presented in this thesis. The frequency response of the employed current sensing circuits is also validated. In that way, the capability of the electrical detection system to sufficiently detect fast transient discharge phenomena is demonstrated.

Chapter 4: In this chapter are summarised the outputs of the experimental process using the electrical detection of surface discharge activity. Current sensing was performed using the developed circuit based on the high frequency current transformer (HFCT) technique. All the relevant technical specifications are presented and discussed.

Chapter 5: This chapter is a continuation of Chapter 4. Electrical detection is again used, this time, for the generation of surface discharge activity pattern plots. Two different approaches are employed for the analysis of the acquired data: current peaks and charge magnitudes density patterns. A comparative study based on these generated illustrations is performed.

Chapter 6: In this chapter is extensively described the newly developed UV-intensified high-speed camera system. This enhanced performance photographic system is synchronised with the developed high-accuracy electrical detection system resulting in a very efficient overall electro-optical detection system. The reported captures accompanied with the corresponding signal recordings are extensively described and useful outcomes related to the generated discharge patterns and their morphology are presented.

Chapter 7: The conclusion of the research that has been carried out and presented in this thesis. Suggestions and further considerations related to the topic are also listed and which can potentially be subject to further studies that can be conducted in the future.

Appendix A: The content of this Appendix chapter is supplementary to the main chapters of this thesis.

Appendix B: In this Appendix chapter are extensively described the finite element method (FEM) models as these were implemented using COMSOL Multiphysics®.

Chapter 2

Literature review on gaseous and solid dielectrics

2.1 Introduction

This chapter examines the published literature with regards to the gaseous insulation and solid/gas interfaces. At first, the physical properties of the researched gaseous dielectrics, naturally-occurring and synthetic, are summarised with emphasis given on the characteristics that reflect on the environmental impact of each compound. The purpose of the latter is to support the overall discussion on the reasons why a well-performing compound such as sulphur hexafluoride (SF_6) needs to be replaced and what are the requirements a replacement candidate needs to fulfil.

In an optimally designed insulating system, gaseous insulation co-exists with solid dielectrics. The role of gaseous insulation, is to provide adequate and continuous insulating performance against elevated electric field magnitudes and suppress discharge phenomena. Solid dielectrics usually have specific roles within the assemblies: (a) to provide mechanical support to conductors and other compartments and/or (b) act as dielectric barriers between sections of highly divergent electric fields. The next area of this chapter is dedicated to the fundamental physics related to gaseous and solid dielectrics and their interface and primarily attempts to clarify the terms of electronegativity and relative permittivity which are frequently used to compare the electric performance of the dielectrics. Supplementary material can be found in the Appendix A.

Another aspect of this chapter is the overview of the electric strength of gases and the discharge phenomena at solid/gas interfaces. For the first, atmospheric gases and the strongly attaching mixture of 30/70 % CF_3I/CO_2 in strongly non-uniform electric field conditions under alternating (AC) voltage application and of major interest. Published works on breakdown strength and insulating performance against partial discharges are explored. For the second, a number of studies dealing with the topic of surface discharges are referred. Impact of the solid dielectric material type and performance against flashover are of major focus.

In the final section, an overview of the imaging techniques for capturing surface discharge activity is presented. The practical advantages and limitations of each method are presented. An important part of the experimental work presented in this thesis is related to the capturing of light emitted from discharges developing on the surface of solid dielectrics and the further study of their morphology.

2.2 Overview of gaseous insulating media and their physical properties

2.2.1 Atmospheric air

Atmospheric air is available in nature and is a key parameter for the design and dimensioning of outdoor insulation systems and apparatus. Factors such as temperature, pressure and humidity have a direct impact on the density of atmospheric air, and therefore, should be highly considered during the evaluation, testing and design stages of equipment. Atmospheric pollution and contamination affect the performance of equipment, and speciality tests need to be carried out for the assessment of components and assemblies [19]. Examples of high voltage outdoor applications are insulators used in transmission lines (pin, suspension and strain) and bushings (transformers, switchgear and circuit breakers). Areas of highly contaminated atmosphere such as industrial parks, shorelines and areas of high precipitation, require further considerations in the selection of the appropriate equipment in order to mitigate the local environmental conditions.

The normal atmospheric conditions as these are described in the relevant standards [20] are listed in Table 2.1 below:

Table 2.1: Standard reference atmospheric conditions [20].

Temperature	$t_0 = 20\,°\mathrm{C}$
Absolute pressure	$p_0 = 1013\,\mathrm{hPa}\,(1013\,\mathrm{mbar})$
Absolute humidity	$h_0 = 11\,\mathrm{g/m^3}$

During high voltage testing, any deviation from the values of Table 2.1 should be corrected by adopting the correction factors recommended in [20] to compensate potential increases in air density and/or humidity. Nitrogen (N_2), oxygen (O_2), argon (Ar) and carbon dioxide (CO_2) are dominant in the composition of the atmosphere with $78.08\,\%$, $20.95\,\%$, $0.93\,\%$ and $0.04\,\%$ mole percent respectively.

2.2.2 Technical air

Technical air, frequently referred to as dry air, synthetic air or clean air, has a composition close to atmospheric air with 21±0.5 % oxygen balanced with nitrogen [21]. Various grades are available depending on the application for instance, medical and pharmaceutical applications require $100\,\%$ oil- and dust-free mixtures although, even for industrial applications the purity exceeds $98\,\%$.

Regarding its composition, the main advantages of technical air (21/79 % O_2/N_2) over atmospheric are that humidity excessive consternation and contaminants are filtered, and it does not contain any quantities of CO_2.

2.2.3 Nitrogen (N_2)

The molecule of nitrogen (N_2) is formed by the triple covalent bond of two nitrogen (N) atoms. The difficulty in breaking this tight bond makes N_2 extremely inert in standard conditions. When it breaks at high temperatures it can lead to the formation of very small amounts of nitrogen oxides (NO & NO_2) [22]. N_2 at standard conditions is also colourless, odourless, tasteless, non-flammable and non-toxic and its co-existence with molecular oxygen (O_2) is essential for life on the planet.

The atomic number of N is 7 and its atomic weight is 14.01 u⁽¹⁾ while the molecular weight of N_2 is 28.02 g/mol. The two N atoms which constitute the N_2 molecule have no electronegativity difference despite, in atomic level, N has a relatively high electronegativity of 3.04 (Pauling scale). The bond pairs of electrons are equally distributed between the two atoms resulting in an overall non-polar molecule. Each nitrogen atom has 5 electrons in its outermost shell and, after the bonding of two of them, 6 electrons in total will be shared through a triple covalent bond making the total number of outer shell electrons 8 for both atoms.

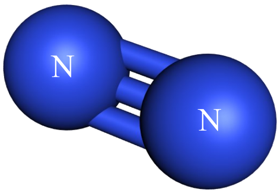

Figure 2.1: Molecular structure of nitrogen (N_2).

Nitrogen in its gaseous form, along with CO_2, is frequently utilised as a buffer gas when mixed with smaller quantities of synthetic fluorinated insulating gases. The mixing of SF_6 with N_2 can be achieved with some compromise in reduction of environmental impact and dielectric performance of the mixture compared to the use of pure SF_6.

---

(1) Unified atomic mass unit.

2.2.4 Carbon dioxide (CO_2)

Carbon dioxide (CO_2) is considered the reference greenhouse gas. It naturally exists in the atmosphere in significantly smaller quantities compared to nitrogen (N_2) and oxygen (O_2), and its role is to trap infrared radiation maintaining that way earth's average temperature at sustainable levels. The electronegativity of carbon is 2.55 (Pauling scale) while, for oxygen, it is 3.44 with a resulting electronegativity difference in each C-O bond of ~ 0.89. This difference appears toward the oxygen atom, as it is the one with the highest electronegativity, resulting to a bond dipole. At the molecular level, the two atomic bonds are placed at opposite directions, shifted by 180°, resulting in an overall zero dipole moment ultimately producing a non-polar carbon dioxide (CO_2) molecule. Carbon (C) has an atomic number of 6 with 4 outer shell electrons while oxygen has an atomic number of 8 with 6 electrons in its outer shell. When two oxygen atoms (O) bond with one carbon atom (C) two double covalent bonds will be created and form the carbon dioxide molecule (CO_2), as shown in Figure 2.2.

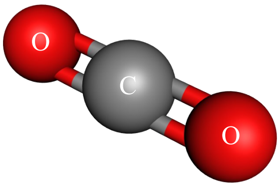

Figure 2.2: Molecular structure of carbon dioxide (CO_2).

Carbon dioxide (CO_2) has been researched as a buffer gas mixed with SF_6 [23–25] at various ratios, but, also it has been extensively investigated in its pure form. Because of their low ozone depletion potential (ODP), both gases are considered good alternatives to SF_6. Their dielectric performance will be described and summarised in a later section.

As mentioned, carbon dioxide has an important role in maintaining life on the planet however, further emissions in the atmosphere are gradually affecting the average global temperatures. The main sources of emission are industrial activity such as combustion of fossil fuels and coal, and activities related to the treatment of petroleum, natural gas and cement. Industrial pollutants also include sulphur oxides, nitrogen oxides, particulate matter and heavy metals(2).

2.2.5 Sulphur hexafluoride (SF_6)

The sulphur hexafluoride (SF_6) molecule consists of six fluorine atoms (F) bonded to one sulphur atom (S). The electronegativity of the fluorine atom is 3.98 and for sulphur is 2.58, both in Pauling scale, with their atomic numbers being 9 and 16 respectively.

The atomic bonds in the SF_6 molecule are considered covalent as non-metallic atoms are bonded together. The electronegativity difference for each S-F bond is ~ 1.4, which is not large enough to be considered as ionic. SF_6 has an octahedral structure with the bonds shifted by 90° to each other resulting in a symmetric arrangement of the six fluorine atoms surrounding the single sulphur atom (Figure 2.3). As a result of this atomic structure, the overall dipole moment of SF_6 is zero and its molecule is non-polar.

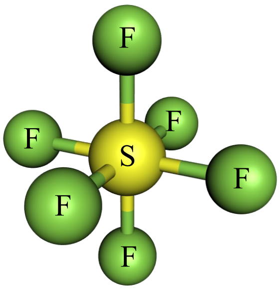

Figure 2.3: Molecular structure of sulphur hexafluoride (SF_6).

The molecular weight of SF_6 is 146.06 g/mol while its density can be calculated following the ideal gas law described by Equation (2.1)

$$\rho_{\text{Gas Den.}} = \frac{P \cdot M}{R \cdot T} \qquad [\text{g/L}] \qquad (2.1)$$

---

(2)Source: “Industrial pollutant releases to air in Europe ”, European Environment Agency, Published online: Published: 12/04/2022, Accessed: 01/08/2022 where P is the pressure in bar, M the molecular weight of the compound in $\mathrm{g/mol}$, T the temperature in K (Kelvin) and $R = 8.314 \times 10^{-2}\,\mathrm{L \cdot bar \cdot K^{-1} \cdot mol^{-1}}$ is the ideal gas constant.

A great advantage of SF_6 is its low boiling point, approximately $-63\,^{\circ}\mathrm{C}$ at 1 bar (Figure 2.4), which is a result of its relatively low molecular weight, compared to other synthetic insulating gases, and its symmetrical octahedral structure which, in turn, results in weak intermolecular forces. Such a characteristic makes the use of this gaseous compound suitable for applications at very low operational temperatures before liquefaction occurs. For operational pressures up to 5 bar the corresponding temperature on the saturation curve is around $-30\,^{\circ}\mathrm{C}$ which is considerably below $0\,^{\circ}\mathrm{C}$. If the liquefaction point is required to be even lower, a common practice is to mix SF_6 with N_2 with variations in the dielectric performance of the mixture [26]. Apart from the dielectric performance, mixing SF_6 with one of the carrier/buffer gases is adopted by many manufacturers in an attempt to minimise the partial content of SF_6 in their applications and the overall environmental impact footprint.

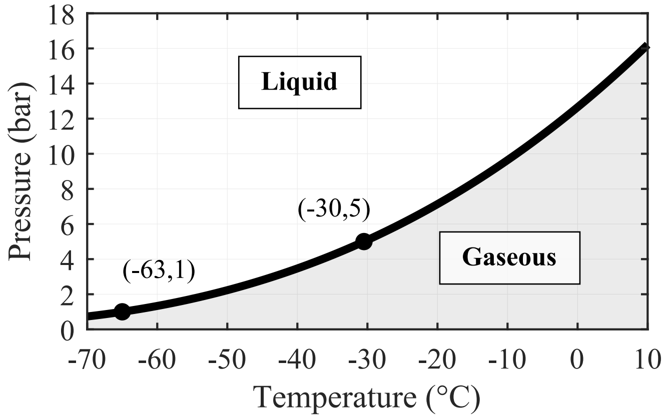

Figure 2.4: Saturation vapour pressure curve of SF_6.

In addition to the above, SF_6 has very good thermal performance characteristics. The constant pressure molar heat capacity, frequently referred to as specific heat, describes the amount of thermal energy required to raise the temperature of one mole of the compound by one degree of temperature. The heat capacity of SF_6 at 1 bar pressure and $25\,^{\circ}\mathrm{C}$ is found to be $96.88\,\mathrm{J}/\left(\mathrm{mol}\cdot\mathrm{K}\right)$, more than three times greater compared to that of technical air. In addition, the thermal conductivity of the gas peaks around $2000-2500\,\mathrm{K}$ which is considered relatively close to the generated arc temperature. Such a characteristic implies the high arc-quenching capability of the compound. In its pure clean gaseous form, SF_6 is non-reactive, non-toxic, non-flammable, non-explosive and as it is not oxygen, it does not support life.

2.2.6 Trifluoroiodomethane (CF_3I)

Trifluoroiodomethane, or trifluoromethyl iodide, consists of three fluorine and one iodine atoms bonded to one carbon atom, and is described by the chemical formula of CF_3I (Figure 2.5). Iodine (I) has an atomic number of 53 and forms a single covalent bond with the carbon atom (C), same as the three fluorine atoms (F). The ionisation energy and electron affinity of iodine (I) are $1008\,\mathrm{kJ}\cdot\mathrm{mol}^{-1}$ and $295\,\mathrm{kJ}\cdot\mathrm{mol}^{-1}$ respectively, resulting in an electronegativity of 2.66 [22] which is very close to the corresponding value for carbon (C). On the other hand, the electronegativity difference $(\mathit{\Delta} EN)$ between carbon (C) and fluorine (F) is relatively high at ~ 1.43. As the carbon atom is surrounded by four atoms in a tetrahedral arrangement, with one of them being different than the others, then the dipoles do not cancel each other symmetrically. As a result, the formed molecule has an overall dipole moment greater than zero, determined to $1.048\,\mathrm{D}$(3) [27]. The bond strength between C and I has a dissociative energy of around $253\,\mathrm{kJ/mol}$ which is not as strong as the C and F meaning that it is more likely to break when the required energy levels are met, resulting in the appearance of relevant by-products such as C_2F_5I, C_3F_7I, C_3F_7IO, CF_4, etc [28–30].

Duan et al. [31] developed a vapour pressure equation based on data measured within the temperature range of $-30\,^{\circ}\mathrm{C}$ to $120\,^{\circ}\mathrm{C}$, a plot of which is shown in Figure 2.6. The high boiling point close to atmospheric pressure and the required operational pressures close to 5 bar absolute in high-voltage gas insulated circuit breakers,

---

(3) Debye (D) unit.

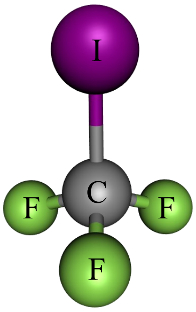

Figure 2.5: Molecular structure of CF_3I.

make the use of CF_3I in its pure form very difficult [32]. Mixing CF_3I with CO_2 or N_2 is a common practice to prevent liquefaction under low ambient temperatures.

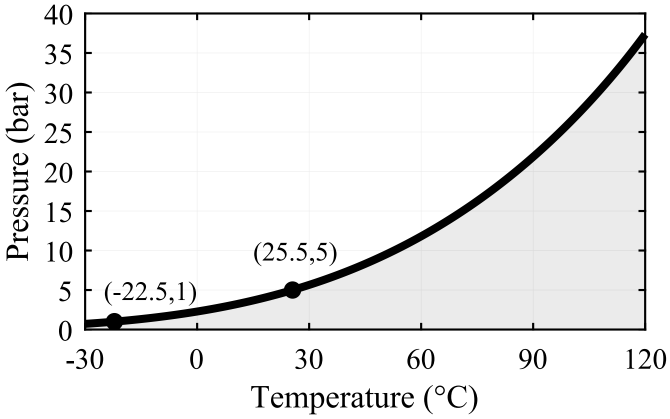

Figure 2.6: Saturation vapour pressure curve of CF_3I.

Heat capacity of CF_3I at 1 bar and 25 °C is 70.89 J/ (mol · K), still higher than air and, as reported by the authors in [33], the decomposition of CF_3I starts at 300 °C, peaks at 400 °C and completes at 600 °C.

2.2.7 Fluoronitriles

The most common insulating gas of the fluoronitriles family is the commercially known 3M^{TM} Novec^{TM} 4710 Insulating Gas with the chemical formula $(CF_3)CFCN$ [34]. Its molecule consists of four carbon atoms, seven fluorine atoms and one nitrogen atom (Figure 2.7), frequently referred to as C_4F_7N or C_3F_7CN or just C4, and is considered a polar molecule [35]. In its pure form, it is odourless, colourless, non-flammable and non-toxic.

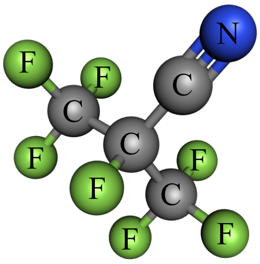

Figure 2.7: Molecular structure of C_4F_7N.

The combination of its relatively high molecular weight 195 g/mol, the "chain" structure of the molecule and the lack of symmetries result in a relatively high boiling point of around −5 °C at 1 bar absolute making the practical use of this insulating gas medium unsuitable in its pure form. Figure 2.8 shows the corresponding saturation vapour pressure diagram [34]. At 5 bar absolute, which is a common operational pressure level for SF_6, the boiling point is found to be at 43 °C, making the mixture of C_4F_7N with a buffer gas the only viable option in order to prevent liquefaction.

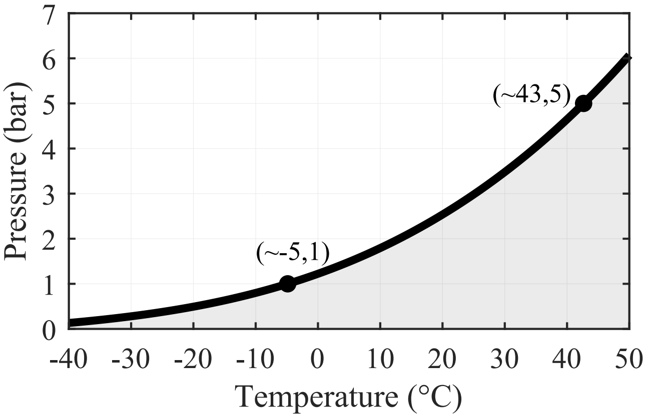

Figure 2.8: Saturation vapour pressure curve of C_4F_7N.

The dissociation process of the molecule initiates at around 650 °C with the fluoronitrile being fully decomposed at around 880 °C, as reported by the authors in [36].

2.2.8 Fluoroketones

Fluoroketones have a similar molecular structure as fluoronitriles (chain) where, instead of a nitrogen atom, an oxygen atom is double bonded to one of the carbon atoms. Their generic chemical formula is $C_nF_{2n}O$ and depending on the number of carbon atoms in the molecule, they are referred to as C5-F-ketone (C5-FK) and C6-F-ketone (C6-FK) (Figure 2.9) [37, 38].

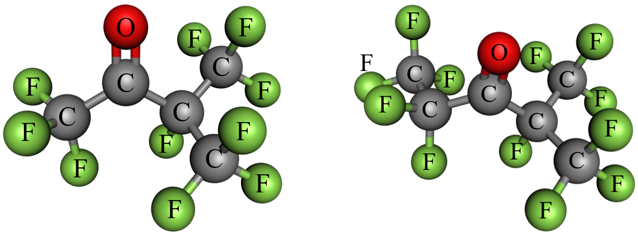

(a) C5-FK **(b)** C6-FK

Figure 2.9: Molecular structures of fluoroketones [37].

One of the first fluoroketone molecules developed was the C6-FK which is mainly used as a fire-extinguishing fluid. In its pure form this compound has a considerably high boiling point, around 50 °C at 1 bar absolute, while, even at small partial pressures, the liquefaction point is outside the range of practical interest for high voltage insulation applications and for operational ambient temperatures [38]. These limitations introduce significant application and design restrictions both in extreme and standard environmental conditions.

An improved alternative to C6-FK is the C5-FK ($CF_3C(O)CF(CF_3)_2$), one of the commercial versions of which is 3M^{TM} Novec^{TM} 5110 Insulating Gas manufactured by 3M^{TM} Company. The molecular weight of C5-FK is 266 g/mol, 50.04 g/mol lower than that of C6-FK (316.04 g/mol) resulting in a lower boiling point, $\sim$ 26 °C at 1 bar pressure. Such a characteristic still prevents the use of this compound in its pure form but instead it must be mixed with a buffer gas at relatively low concentrations. Figure 2.10 summarises the saturation vapour pressure curves for the two fluoroketone compounds described.

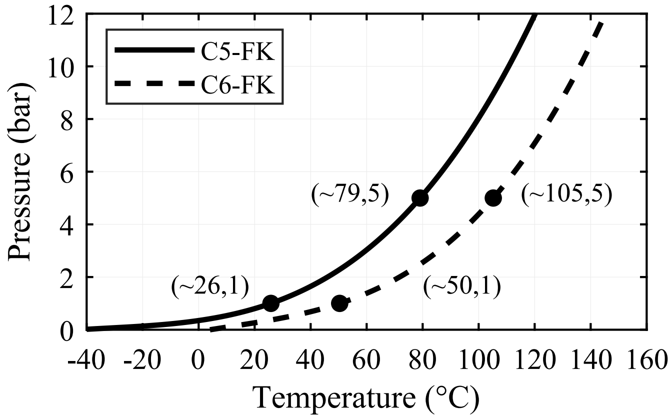

Figure 2.10: Saturation vapour pressure curves of fluoroketones [39, 40].

2.2.9 Fluoroorixanes

As described in the relevant patent [41] for the use of fluorinated oxiranes as dielectric fluids in electrical devices, they have a chemical structure where the sum of carbon atoms is 3 to 15, in which combinations of hydrogen together with fluorine atoms and one of the fluoroalkyl groups are bonded, preferably fluorine atoms or a perfluoroalkyl group. When 4 or more carbon atoms are present, it is preferable that no hydrogen atoms are present.

Fluorooxiranes have the same generic chemical formula as fluoroketones [35, 38], $C_2F_{2n}O$, with the difference that the oxygen atom is single bonded to two different carbon atoms. The illustration of the molecular structure of C_4F_8O fluooroxirane is shown in Figure 2.11. According to [38], that bond results in a very resistant molecule when exposed to UV radiation and thus to a compound of high global warming potential (GWP).

The boiling point of C_4F_8O at atmospheric pressure levels is also considered relatively high compared to other fluorinated compounds, identified in the vapour pressure curve of Figure 12 [42, 43] at approximately $-0.74\,°C$.

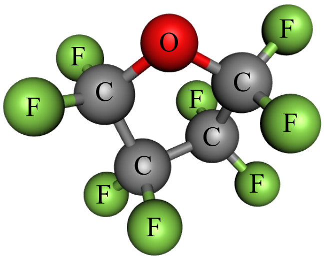

Figure 2.11: Molecular structure of C_4F_8O fluorooxirane.

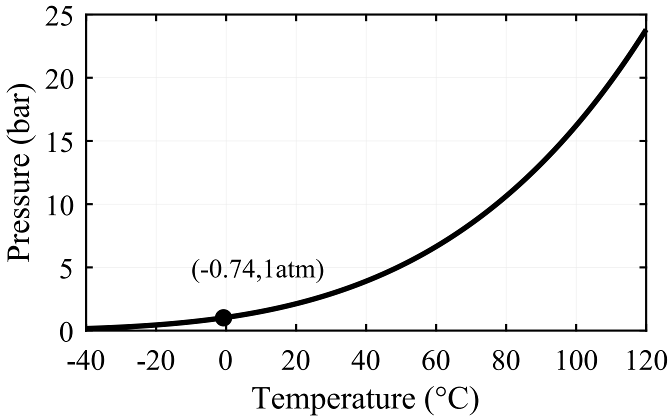

Figure 2.12: Saturation vapour pressure curve of C_4F_8O [42, 43].

2.2.10 Perfluorocarbons (PFCs)

Perfluorocarbons (PFCs) are halogen compounds as they are combined exclusively from fluorine (F) and carbon (C) atoms. Known PFCs for electrical insulation applications are CF_4, C_2F_6, C_3F_8 and c-C_4F_8 [35], the molecules of which are shown in Figure 2.13.

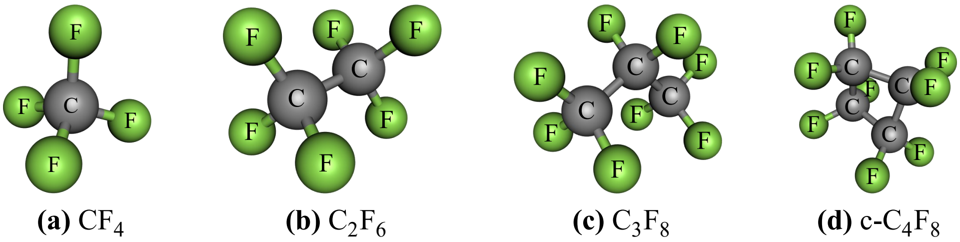

(a) CF_4 **(b)** C_2F_6 **(c)** C_3F_8 **(d)** c-C_4F_8

Figure 2.13: Molecular structure of perfluorocarbons (PFCs).

The more carbon atoms are present (1, 2, 3 or 4), accompanied with more fluorine atoms, the higher the molecular weight will be, resulting in that way in higher boiling point of the compound. Perfluorocarbon compounds are mainly used as refrigerants and quite extensively for plasma etching in the silicon semiconductor manufacturing industry. The vapour pressure curves of the PFCs described above are presented in Figure 2.14 [44–46]. The corresponding boiling points are identified at, −128 °C, −78 °C, −36.6 °C and −6 °C, in the same order as presented in the graph.

Despite their thermodynamic properties and good dielectric performance, their high global warming potential (GWP) and atmospheric lifetime are preventing factors for these compounds to be considered as SF_6 replacements. The values of GWP and lifetimes as these were reported in the Scientific Assessment of Ozone Depletion in 2018 from the World Meteorological Organization (WMO) [47] are summarised in Table 2.2.

2.2.11 Hydrofluoroolefins (HFOs)

Hydrofluoroolefins gases, frequently referred to as HFOs, are compounds composed of hydrogen, fluorine and carbon atoms, and are described by the generic chemical

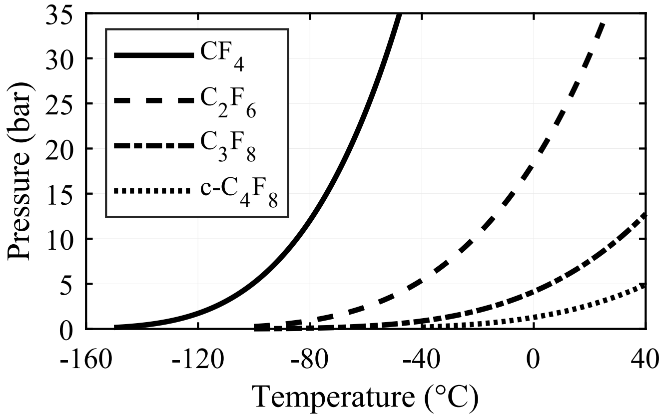

Figure 2.14: Saturation vapour pressure of curves PFCs [44–46].

Table 2.2: GWP and atmospheric lifetime of the PFCs [47].

Compound	**GWP (100 years)**	**Atmospheric lifetime (years)**
CF_4	6630	> 50000
C_2F_6	11100	> 10000
C_3F_8	8900	2600
c-C_4F_8	9540	3200

formula $C_n(H,F)_{2n}$ [35]. There are two main molecules in the HFOs family, HFO-1234ze(1,3,3,3-tetrafluoroprop-1-ene) and HFO-1234yf(2,3,3,3-tetrafluoropropene) [48], both with the same chemical formula and molecular weight, $C_3H_2F_4$ and 114.04 g/mol respectively. HFO-1234ze is distinguished in two different geometric isomers, HFO-1234ze(E) and HFO1234ze(Z), corresponding to the trans- and cis- geometric isomerism respectively. The molecular structures of these compounds are shown below in Figure 2.15.

The difference in the isometric geometry of the two HFO-1234ze isomers results in a significant difference in the volumetric capacity of the two molecules and considerable difference in the corresponding boiling points [49]. The liquefaction points at 1.013 bar (atmospheric pressure levels) for the three compounds described previously are $-29.4\,°C$, $-11.3\,°C$ and $-9.8\,°C$, in the same order as those are presented in Figure 2.15. The corresponding vapour pressure curves are summarised in Figure 16.

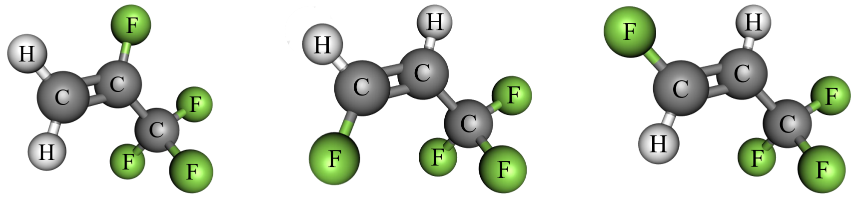

(a) HFO-1234yf **(b)** HFO-1234ze(E) **(c)** HFO-1234ze(Z)

Figure 2.15: Molecular structures of the three basic hydrofluoroolefins (HFOs) [48].

HFO-1234yf and HFO-1234ze(Z) have been classified as extremely flammable (H220 - GHS Classification) by the European Chemicals Agency (ECHA).

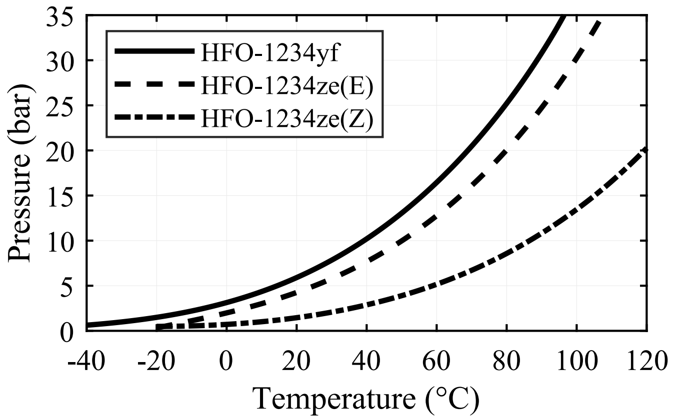

Figure 2.16: Saturation vapour pressure curves of hydrofluoroolefins [50, 51].

HFO compounds are used as refrigerants mainly for industrial heat pumps which in turn are used to replace conventional combustion systems in an overall effort to minimise fuel usage and CO_2 emissions [52]. They are proposed for the replacement of refrigerant fluids, such as R-134a, with considerably higher global warming potential (GWP) and relatively recently they were proposed for use in high voltage applications [53, 54].

2.2.12 Summary of physical properties

Table 2.3 summarises the molecular weight and boiling point values for the compounds described in the previous sections. Figure 2.17 illustrates the variation in the boiling point over the increase in the molecular weight for all the compounds considered.

Table 2.3: Summary of the physical properties for the described compounds.

Compound	**Molecular weight (g/mol)**	**Boiling point at 1.013 bar (^{o}C)**
Technical air	29	-194
N_2	28.01	-195.79
CO_2	44.01	-78.48 (Sublimation point)
SF_6	146.06	-63.8
CF_3I	195.91	-22.5
C_4F_7N	195	-4.72
$C_5F_{10}O$	266	+26.89
$C_6F_{12}O$	316.01	+49.2
c-C_4F_8O	216.03	-0.74
CF_4	88	-128
C_2F_6	138.01	-78
C_3F_8	188.02	-36.6
c-C_4F_8	200.03	-6
HFO-1234yf	114.04	-29.4
HFO-1234ze(E)	114.04	-11.3
HFO-1234ze(Z)	114.04	+9.8

It can be clearly seen that, there is an increase trend in the boiling point as the molecular weight increases, with some exceptions which deviate from this pattern mostly because of their molecular geometry. HFOs have their carbon atoms placed in a chain arrangement, a characteristic which leads to relatively stronger intermolecular forces and a higher boiling point compared to molecules with higher molecular weight but different structure. Carbon dioxide (CO_2) has a considerably higher boiling point compared to carbon tetrafluoride (CF_4) despite its lower molecular weight because of the tetrahedral structure of CF_4 which results in weaker intermolecular forces.

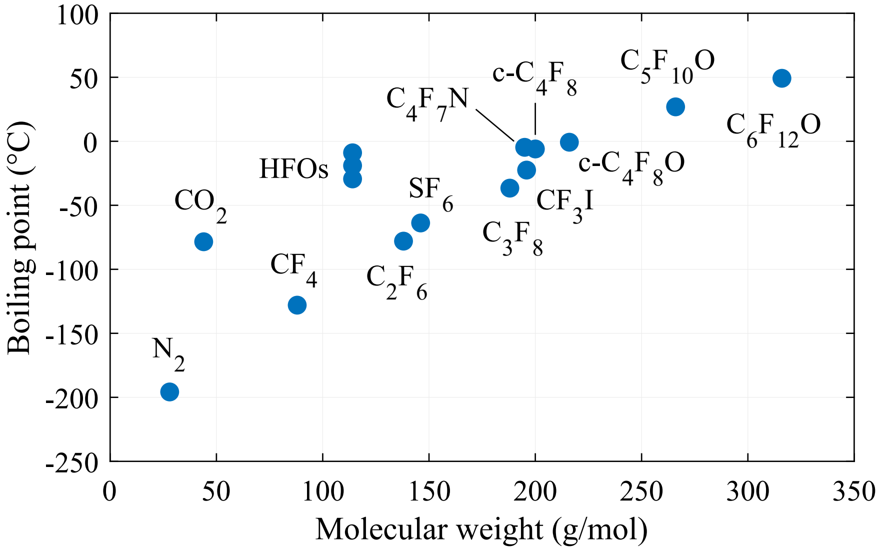

Figure 2.17: Boiling point over molecular weight for the compounds described.

2.2.13 Environmental impact of synthetic insulating gases

Over the years, the extensive use of fluorinated compounds has been beneficial in many industrial and scientific sectors because of their unique performance in a wide range of applications. However, their environmental impact has introduced many concerns regarding their future use, and efforts are focused in the search for alternative options. The Kyoto protocol, overseen by the United Nations Framework Convention on Climate Change (UNFCCC), has listed a number of greenhouse gases in its Annex A, three of which are fluorinated, including SF_6. Regulation (EU) No 517/2014 and the Paris Agreement of 2015 are aiming for the reduction of greenhouse gases via regulation.

The main parameters used to describe the overall environmental impact of a compound are: (a) atmospheric lifetime measured in years, (b) ozone depletion potential (ODP) and (c) global warming potential (GWP). The definitions of these parameters are extensively described in the relative report of the Intergovernmental Panel on Climate Change (IPCC) [55] from which are retrieved and presented below.

2.2.13.1 Global warming potential

Global warming potential (GWP) is a parameter that quantifies the relative contribution of a compound to climate warming. More specifically, as defined from the Intergovernmental Panel on Climate Change (IPCC) [55], GWP describes the approximation of the integral over time of unit mass of a greenhouse gas relative to the same unit mass of carbon dioxide (CO_2). Equation (2.2) summarises this relation

$$\mathrm{GWP}\left(x\right) = \frac{\int_0^{TH} \alpha_{\mathrm{x}} \left[x\left(t\right)\right] dt}{\int_0^{TH} \alpha_{\mathrm{r}} \left[r\left(t\right)\right] dt} \tag{2.2}$$

where TH is the time horizon of the observation, α_{x} is the radiative efficiency in $\mathrm{Wm}^{-2}\mathrm{kg}^{-1}$ after a unit increase of the compound in the atmosphere and $x\left(t\right)$ is the time-dependent decay in abundance of the instantaneous release of the substance. The denominator variables describe accordingly the reference gas which is carbon dioxide (CO_2).

The capacity of a gas to absorb infrared (IR) radiation, both solar and black body from earth's surface, the spectral location of the absorbing wavelengths and the atmospheric lifetime, all affect the corresponding global warming potential levels [56]. For the case of fluorinated gases, where very strong carbon-fluorine (C-F) bonds are present, there are two major issues. First, the bond is unreactive to the oxidising environment of the troposphere (OH radicals) which leads to relatively long atmospheric lifetimes and second, the infrared absorbance of these bonds is within the range of $8 - 12\,\mu$m of the IR light spectrum, a part which is not absorbed by naturally occurring gases. Figure 2.18 shows the IR absorbance spectrum for the main natural IR absorbing gases and, as examples, the two PFCs with the longest atmospheric lifetimes are included. The relevant data was retrieved from the National Institute of Standards and Technology (NIST) database [57]. The presented data agrees with the observation that the higher the number of carbon-fluorine bonds, the higher the radiative forcing of the compound will be.

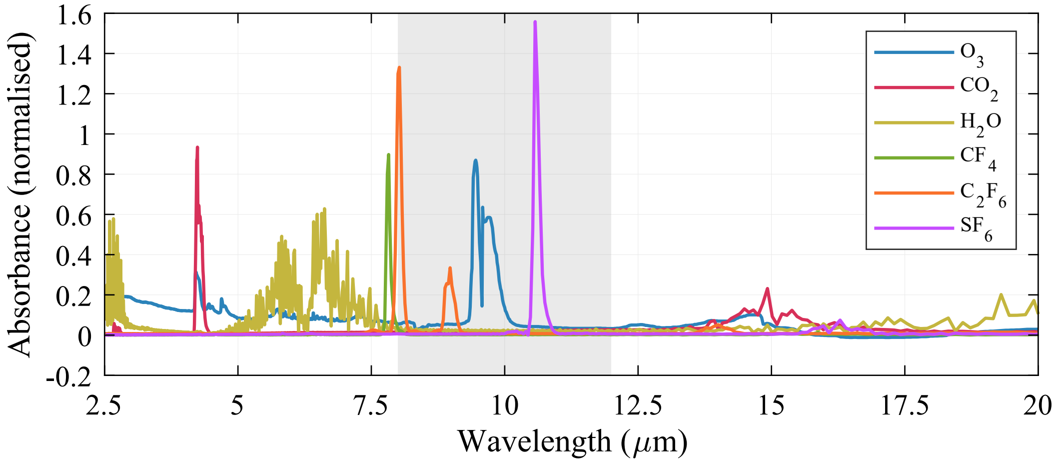

Figure 2.18: Infrared absorbance spectrum of ozone (O_3), carbon dioxide (CO_2), water vapour (H_2O) and the two perfluorocarbons (PFCs) with the longest atmospheric lifetime, i.e., CF_4 and C_2F_6 [57]. SF_6 is also included.

According to [58], for the case of a mixture, the GWP is calculated as the sum of the products of the weight fractions of each compound x_i multiplied with their corresponding GWPs.

$$\sum_{1}^{n}((x_1 \times \mathrm{GWP}_1) + (x_2 \times \mathrm{GWP}_2) + \ldots + (x_\mathrm{n} \times \mathrm{GWP}_\mathrm{n})) \tag{2.3}$$

As an example, the calculation of the GWP of $20\,\%$ $3\mathrm{M}^{\mathrm{TM}}$ $\mathrm{Novec}^{\mathrm{TM}}$ 4710 mixed with $80\,\%$ CO_2 will be described. The two compounds have a molecular weight of $195\,\mathrm{g/mol}$ and $44.01\,\mathrm{g/mol}$ respectively. The apparent molecular weight of the mixture is found to be $74.21\,\mathrm{g/mol}$. When a given volume V needs to be filled with the mixture up to a pressure P at a temperature T then, based on Dalton's law, CO_2 will have a partial pressure of $0.8 \times P$. The ratio between the required grams of CO_2 and the total weight of the mixture will be expressed as:

$$\frac{A_{\mathrm{CO_2-g}}}{A_{\mathrm{Mixture-g}}} = \frac{\frac{0.8P \cdot V \cdot A_{\mathrm{CO_2-Molecular\ Weight}}}{RT}}{\frac{P \cdot V \cdot A_{\mathrm{Mixture-Molecular\ Weight}}}{RT}} = 0.8\frac{A_{\mathrm{CO_2-Molecular\ Weight}}}{A_{\mathrm{Mixture-Molecular\ Weight}}} = 0.4745 \tag{2.4}$$

The weight fraction for 20 % 3M™ Novec™ 4710 will be

$$\frac{A_{\mathrm{C_4F_7N-g}}}{A_{\mathrm{Mixture-g}}} = 1 - \frac{A_{\mathrm{CO_{2-g}}}}{A_{\mathrm{Mixture-g}}} = 0.5256 \tag{2.5}$$

The global warming potential (GWP) of the mixture will be

$$\mathrm{GWP_{Mixture}} = (0.4745 \times 1) + (0.5256 \times 2100) = 1104.13\,\mathrm{years} \tag{2.6}$$

The change of GWP over the volumetric percentage content of the buffer gas for the cases of C_4F_7N/CO_2 and C_4F_7N/N_2 is shown in Figure 2.19.

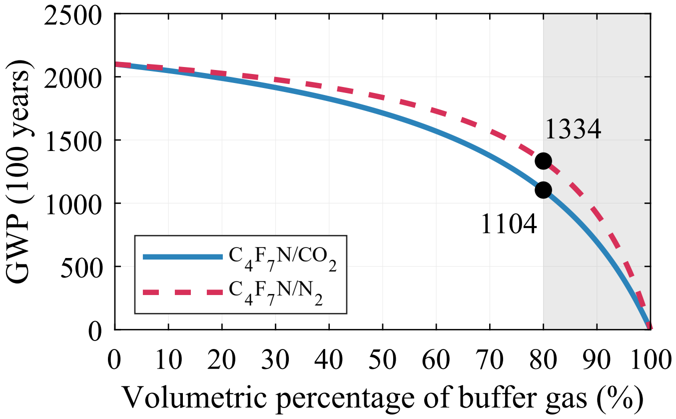

Figure 2.19: GWP over buffer gas volumetric content. The shaded area represents the cases where C_4F_7N content ranges between $0-20\,\%$.

2.2.13.2 Atmospheric lifetime

Global atmospheric lifetime, measured in years (yr), is the amount of time for an atmospheric pollutant or greenhouse gas to return to its natural levels within the atmosphere. It is defined as the burden measured in tera-grams (Tg) divided by the mean global sink (Tg/yr) when the burden remains unchanged.

Source strength and sink strength are essential quantities when accuracy of the atmospheric lifetime specification is required. For the case of synthetic greenhouse gases, atmospheric source of excessive concentrations are emissions from human activity and thus the corresponding source strengths can be accurately specified [55]. The sink strength for the same type of gas can be specified through atmospheric observations in a relatively large timespan combined with laboratory experiments and model outputs.

In addition to the above, the definition of atmospheric lifetime may vary depending on the level of the troposphere the emission of the pollutant or greenhouse gas is performed. Most of the greenhouse gases with lifetimes greater than 2 years, longer than the troposphere layers mixing time, are not affected by the location of the emission sources [55].

Carbon dioxide, which is considered as the reference greenhouse gas, is removed from the atmosphere primarily by natural chemical processes while greenhouse gases with at least one hydrogen atom in their molecule are removed in the troposphere when reacting with hydroxyl radicals (OH). Gases that do not react with OH are removed in the stratosphere, or above that, when exposed to UV solar radiation [55]. Also, gases with long atmospheric lifetime will circulate between the troposphere and stratosphere several times before they decompose.

In the Appendix A of the Scientific Assessment of Ozone Depletion: 2018 (WMO) [47], the total atmospheric lifetime ($\tau_{\text{total}}^{\text{atm}}$) is described as the combination of tropospheric $\left(\tau_{\text{trop}}\right)$, stratospheric ($\tau_{\text{strat}}$) and mesospheric ($\tau_{\text{meso}}$) losses, with the latter being considered negligible except for very long-lived compounds. The total lifetime (τ_{total}) of a compound combines the atmospheric lifetime with the lifetimes due to ocean (τ_{ocean}) and soil (τ_{soil}) uptake. These descriptions are summarised by Equation (2.7) below [47].

$$\frac{1}{\tau_{\text{total}}} = \frac{1}{\tau_{\text{total}}^{\text{atm}}} + \frac{1}{\tau_{\text{ocean}}} + \frac{1}{\tau_{\text{soil}}} \tag{2.7a}$$

$$\frac{1}{\tau_{\text{total}}^{\text{atm}}} = \frac{1}{\tau_{\text{trop}}} + \frac{1}{\tau_{\text{strat}}} + \frac{1}{\tau_{\text{meso}}} \tag{2.7b}$$

2.2.13.3 Ozone depletion potential

Ozone depletion potential (ODP) describes the relative strength of a chemical compound to destroy ozone. It is defined as the ration of the change in global ozone for a given mass emission of a substance to the change in global ozone when CFX-11 ($CFCl_3$) of the same mass is emitted [47].

Stratospheric ozone, chemical symbol O_3, ($10 - 15\,\mathrm{km}$ from earth's surface) is responsible for blocking/absorbing all the UV-C ($100 - 280\,\mathrm{nm}$) and most of the UV-B ($280 - 315\,\mathrm{nm}$) solar radiation which is biologically harmful for all forms of life on earth. Emissions of halogen gases containing chlorine (Cl) and bromine (Br) accumulate in the lower troposphere and are gradually transmitted to the stratosphere. Their chemical reaction with UV solar radiation converts them to reactive halogen gases which cause chemical depletion of the stratospheric ozone. If a gas has a long lifetime, it will need more time to convert meanwhile it will circulate between the stratosphere and the troposphere several times. Halogens which contain fluorine (F) and iodine (I) are not classified as ozone depleting substances although many of them are still classified as greenhouse gases because of their high global warming potential (GWP).

2.2.13.4 Summary of environmental characteristics

As described in this section, the environmental impact of a gas and its suitability to replace SF_6 from an environmental perspective depends on weighting the three factors described before. Knowledge on the chemical characteristics of each compound and its behaviour in the atmosphere will help to shortlist the available options. Table 2.4 summarises the environmental impact characteristics for the compounds described in Section 2.2. More recent research indicates an atmospheric lifetime of 850 years for SF_6 [59].

Table 2.4: Summary of the environmental characteristics of the presented dielectric gases.

Compound	**ODP**	**Lifetime (years)**	**GWP (100 years)**	**Ref.**
CO_2	0	-	1	[47]
SF_6	0	3200*	23500	[47]
CF_3I	<0.09	<5 days	<5	[47,60]
C_4F_7N	0	30	2100	[34]
$C_5F_{10}O$	0	14-15 days	<1	[39]
$C_6F_{12}O$	0	7 days	<1	[40]
c-C_4F_8O	0	-	8700	[61,62]
CF_4	0	50000	6630	[47]
C_2F_6	0	10000	11100	[47]
C_3F_8	0	2600	8900	[47]
c-C_4F_8	0	3200	9540	[47]
HFO-1234yf	0	12 days	<1	[47]
HFO-1234ze(E)	0	19 days	<1	[47]
HFO-1234ze(Z)	0	10 days	<1	[47]

2.2.14 Requirements for the ideal SF_6 replacement compound

As described previously in Section 2.2, the dielectric performance, chemical stability and physical properties of SF_6, make this gaseous compound an excellent solution for use in medium- and high-voltage equipment. However, its environmental impact, and the fact that human activity is the only source of atmospheric emissions, counterbalance the benefits of its use. Next, the necessary requirements that a replacement candidate needs to fulfil are briefly summarised in order to be considered as a potential substitute to SF_6, the industry proposals towards that direction and a summary of the basic characteristics of the replacement candidates that have been researched so far.

The ideal SF_6 replacement gas should be able to provide performance characteristics similar to those of SF_6 with the lowest possible environmental impact. More specifically, a new insulating medium should be able to meet the requirements listed in Table 2.5. The "Relations" column represents the correlation between the different items on the same table.

Table 2.5: Characteristics which need to be fulfilled by potential SF_6 replacement candidate compounds.

No.	Characteristic	Details	Relations
1	Non-flammable	Safer handling and operation when exposed to high temperature plasmas	
2	Non-explosive	Safer handling and operation when exposed to high temperature plasmas	
3	Non-toxic	Zero toxicity in its pure form leads to safer use	
4	Material compatibility	Non-corrosive to materials (metals, polymers, resins, adhesives, lubricants etc.) used in relevant equipment	
5	Chemically inert	Maintains its purity when in contact with the build materials of the relevant equipment over long periods of time	4
6	Low concentration and toxicity of arcing by-products	Low amounts of decomposition products will help maintain the gas content percentage higher for longer time periods. Low toxicity levels will contribute to safer gas handling at any stage of its serviceable life cycle	5
7	Low boiling point	Maintains its gaseous form at low serviceable temperatures	
8	Serviceable when pressurised	Does not liquefy at elevated pressure levels	7
9	Thermally stable	High dissociation temperature	
10	High heat capacity	Contributes to the cooling of the gas filled equipment	
11	High thermal conductivity	Absorbs and dissipates heat easier during and right after an arcing event	9
12	Non ODP	Stratospheric ozone depletion potential (ODP) near zero	

13	No atmospheric lifetime	Be able to decompose in the troposphere	
14	Low GWP	Not be able to absorb IR radiation that is not absorbed by naturally occurring substances	12, 13
15	High dielectric strength	Similar to SF_6 and higher than air for the same pressure levels	
16	Fast arc-quenching	Rapid recombination after dissociation and high thermal conductivity	11
17	Footprint same to SF_6	Same dimensional footprint will allow retrofit of the equipment currently in service with minimum adjustments	4, 5, 7, 8, 15

In Table 2.6, all the information presented for the gases discussed so far, is summarised. The dielectric strength of each compound relative to that of SF_6 is also included.

2.3 Fundamental physics of gaseous and solid dielectrics

Describing the physical phenomena behind gaseous discharges and kinetics of particles can be a very challenging task. The physical mechanisms of gaseous discharges alone are already quite complex, and the presence of solid insulators enhances that complexity. Most of the occurring physical events consist of several superimposed smaller scale phenomena with most of them undergoing a probabilistic behaviour, making even the simulation approach computationally demanding and subject to compromises and approximations. In the following subsections, an attempt is made to describe in a comprehensive way the fundamental physics and processes of related to gas and solid dielectrics, requiring a sufficient knowledge of the fundamental concepts.

Table 2.6: Basic characteristics of insulating gaseous media in their pure form [34, 35, 38, 39, 47, 60–64]. Background colour: *white* – atmospheric gases, *purple* – iodine containing trifluoroiodomethane, *blue* – fluoronitrile, *strong red* – fluoroneketones, *light red* – fluorooxirane, *green* – perfluorocarbons (PFCs), *gray* – hydrofluoroolefins (HFOs), *orange* – sulphur hexafluoride

Compound	**Molecular weight (g/mol)**	**Boiling point (^{o}C) at 1 bar**	**ODP**	**Atmospheric lifetime (years)**	**GWP (100 years)**	**Relative di-electric strength**
SF_6	146.06	$-63.9\,^{\circ}$C	0	3200	23500	1
Air	28.85	$< -183\,^{\circ}$C	0	0	0	$0.37 - 0.40$
CO_2	44.01	$-78.48\,^{\circ}$C	0	0	1	$0.32 - 0.37$
N_2	28.01	$-195.79\,^{\circ}$C	0	0	0	$0.34 - 0.43$
CF_3I	195.91	$-22.5\,^{\circ}$C	< 0.09	0.014	< 5	1.23
C_4F_7N	195	$-4.72\,^{\circ}$C	0	30	2100	$2.0 - 2.2$
$C_5F_{10}O$	266	$+26.89\,^{\circ}$C	0	0.04	< 1	2.0
$C_6F_{12}O$	316.01	$+49.02\,^{\circ}$C	0	< 0.02	< 1	2.5
c-C_4F_8O	216.03	$-0.74\,^{\circ}$C	0	-	8700	1.6
CF_4	88	$-128\,^{\circ}$C	0	50000	6630	0.39
C_2F_6	138.01	$-78\,^{\circ}$C	0	10000	11100	0.79
C_3F_8	188.02	$-36.6\,^{\circ}$C	0	2600	8900	0.97
c-C_4F_8	200.03	$-6\,^{\circ}$C	0	3200	9540	1.25
HFO-1234yf	114.04	$-26.4\,^{\circ}$C	0	0.035	< 1	0.8
HFO-1234ze(E)	114.04	$-11.3\,^{\circ}$C	0	0.05	< 1	0.95
HFO-1234ze(Z)	114.04	$+9.8\,^{\circ}$C	0	0.03	< 1	0.8

2.3.1 Electronegativity in atoms and molecules

Before describing electronegativity, it is important to refer to the terms of ionisation energy and electron affinity of an atom. For the convenience of the discussion, whenever necessary the cases of fluorine (F) and sulphur (S) atoms, as these are shown in Figure 2.20, will be referred, with atomic numbers 9 and 16 and electron structures $1s^2 2s^2 2p^5$ and $1s^2 2s^2 2p^6 3s^2 3p^4$ respectively.

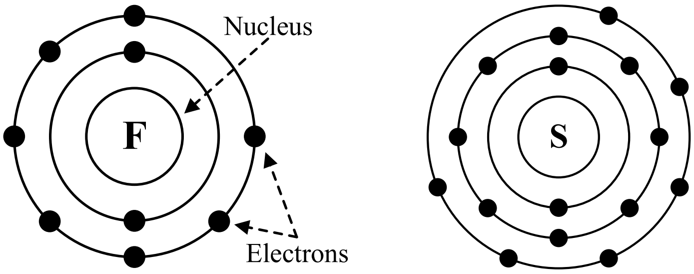

(a) Fluorine (F) **(b)** sulphur (S)

Figure 2.20: Fluorine (F) and sulphur (S) atoms.

Ionisation energy represents the amount of energy that a gaseous atom needs to absorb to be able to lose one electron. Having a non-charged atom (ground state), the first ionisation energy corresponds to the energy required to remove the most loosely held electron from the outermost shell of the atom.

$$X\,(g) \rightarrow X^{+}\,(g) + e^{-} \qquad \varDelta E > 0 \tag{2.8}$$

Further ionisation energies (second, third, etc.) will increase since the atom will become more positively charged as its number of electrons will be decreasing. Factors affecting the ionisation energy include atomic radius, the number of electron shells, electron shielding and number of paired electrons within an orbital. The periodic table incorporates the pattern on increasing ionisation energy with increasing element group and decreasing element period. According to [65], for the case of sulphur, the first ionisation energy is $10.36001 \pm 0.00013\,\mathrm{eV}$ or $999.615\,\mathrm{kJ/mol}$, the second

$2251.82\,\mathrm{kJ/mol}$, and so on. For fluorine, on the other hand, the first ionisation energy is identified at $1681.09\,\mathrm{kJ/mol}$. The atomic radius of sulphur is about two times larger than that of fluorine [66] while, at the same time, the outermost electrons will be more loosely held in sulphur because of the electron shielding.

Electron affinity describes the opposite process compared to ionisation energy i.e., the enthalpy change when an electron is attached to an atom [22], and it quantifies the tendency of a neutral atom to attract an electron.

$$X\left(g\right)+e^{-}\rightarrow X^{-}\left(g\right)\qquad \mathit{\Delta} H<0 \tag{2.9}$$

Electronegativity will describe the ability of an atom to lose and gain electrons, or as it is frequently mentioned [22] to compete for them, and it is strongly related to the ionisation and electron affinity. Elements with both values high will be practically resistant in loosing electrons and, at the same time, will have a high tendency to gain them. Such elements are classified as highly electronegative. The opposite occurs when both these values are low. Table 2.12 summarises all the definitions described previously of the atoms considered so far for the synthetic insulating gases described.

Table 2.7: Ionisation energy, electron affinity and electronegativity of the elements (atoms) discussed so far and are part of the molecular structures of the synthetic insulating gases. [Kr] corresponds to the electron configuration of Krypton which is $1s^22s^22p^63s^23p^63d^{10}4s^24p^6$.

Atom	**Atomic number**	**Electron configuration**	**First ionisation energy (kJ/mol)**	**First electron affinity (kJ/mol)**	**Electronegativity**
Sulphur (S)	16	$1s^22s^22p^63s^23p^4$	1000	-200	2.58
Fluorine (F)	9	$1s^22s^22p^5$	1681	-328	3.98
Nitrogen (N)	7	$1s^22s^22p^3$	1042	+7	3.04
Carbon (C)	6	$1s^22s^22p^4$	1086	-122	2.55
Oxygen (O)	8	$1s^22s^22p^4$	1314	-141	3.44
Iodine (I)	53	$[Kr]4d^{10}5s^25p^5$	1008	-295	2.66
Hydrogen (H)	1	$1s^1$	1312	-73	2.20

In a molecular structure, at least two atoms will be bonded together to form a molecule. Electrons placed at the outermost shell have an important role during the bonding. In [66], Pauling quantified the ionic character of a bond in relationship to the absolute electronegativity difference $\varDelta EN$ of the two atoms. According to his description, bonds between atoms with electronegativity difference of 1.7 have $50\,\%$ ionic character and $50\,\%$ covalent. For differences less than 1.7, the covalent character is greater than the ionic and vice versa for values greater than 1.7. When the bond is considered ionic, the electron is not equally shared between the atoms and it is displaced towards the atom with the highest electronegativity value. All the above are described mathematically by Equation (2.10) while Figure 2.21 illustrates that behaviour.

$$\text{Ionic character } [\%] = 100 \times \left(1 - e^{-0.25\varDelta EN^2}\right) \tag{2.10}$$

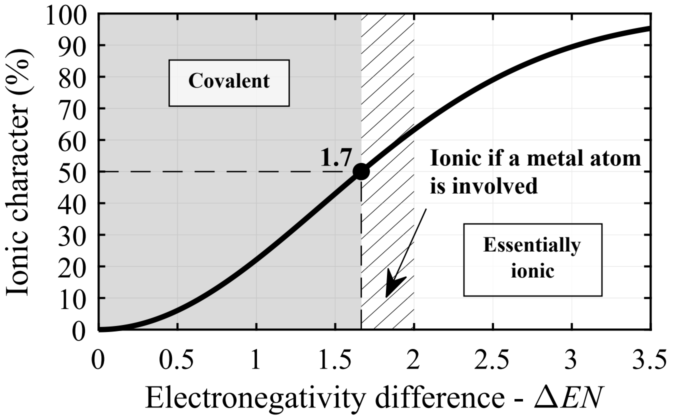

Figure 2.21: Ionic character of a bond as a function of the absolute electronegativity difference [22, 66].

2.3.2 Polarisation of solid dielectrics

The definitions for non-polar and polar solids are retrieved from [67] and they describe the polarisation of solid dielectrics in the absence of an electric or magnetic field. Non-polar solids are described as solids for which the centres of gravity of positive and negative charges coincide and their overall dipole moment is zero. On the other hand, as polar solids are described solids that are composed of polar molecules for which the centres of gravity for charges of both polarities do not coincide and thus molecular polarisation exhibits.

Examples of non-polar and polar polymers, composed of monomers covalently bonded into a chain, are polyvinyl chloride (PVC) and polytetrafluoroethylene (PTFE) respectively. PVC is produced by polymerisation of vinyl chloride (VCM) and PTFE by polymerisation of tetrafluoroethylene (TFE), the structures of which are shown in Figure 2.22. As was described in Chapter 2, the C-F bond does not have a zero-dipole moment. However, the structure of the TFE monomer molecule results in a zero overall dipole moment.

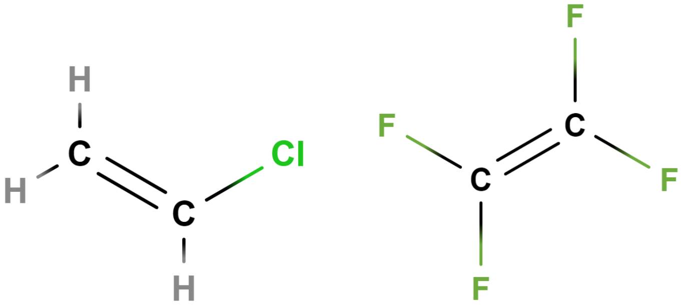

(a) Vinyl chloride **(b)** Tetrafluoroethylene

Figure 2.22: Molecular structures of vinyl chloride (VCM) and tetrafluoroethylene (TFE) monomers.

Making a list of the practical advantages and disadvantages of non-polar substances over polar, and vice versa, in a wide range of applications based only on the molecular polarisation would not be enough. It would require an exhaustive analysis on the atomic composition of the molecules and how these reflect in to actual applications. For the purposes of this thesis, focus will be maintained on the electronic balance and polarisability of the materials. As PTFE was mentioned above and is widely considered in electrical applications, it is worth highlighting its very good chemical resistance, low dielectric constant, low dissipation factor and high volume and surface resistance values. Hydrophobicity, or increased water repelling capability, is a characteristic of fluorocarbons [68]. However, the extent up to which these terms should be used has been questioned [69, 70]. In general terms, intermolecular forces affect the solubility of the solute into the solvent, and it is widely regarded that non-polar molecules do not dissolve inside polar ones, such as H_2O (water).

There are four major mechanisms of polarisation, descriptions of which can be found in almost all the textbooks related to electrodynamics:

(i). Electronic, a_e
(ii). Ionic, a_i
(iii). Orientation, a_o
(iv). Interfacial/space charge, a_d

At this stage, the given descriptions correspond to materials with very low number of charge carriers (low conductivity). Electronic polarisation refers to the displacement of the outermost electrons of the atom or molecule with respect to the positively charged atomic cores/nucleus in the presence of an electric field. Ionic polarisation is mostly related to compounds of ionic bonds. The most described is sodium chloride (NaCl) but it also appears in most of ceramics, such as aluminium oxide (Al_2O_3). With the influence of electric field, the position of positive and negative ions will change and align with its direction. Because of the crystal lattice structure of these compounds, the permanent dipoles do not contribute to the overall polarisability [71]. Molecules with asymmetrical bonding and which do not have a crystal lattice structure exhibit a permanent dipole. A well-known example is H_2O (water). Under the influence of an electric field, the molecules will experience a torque with reference to their centre of mass. This torque will rotate the molecule and align it with the electric field direction. Finally, interfacial polarisation appears at the interfaces between different materials as an accumulation of charge. Accumulated charges of a specific polarity will leave a remainder of opposite polarity and those two together will constitute dipole moments. That separation between different polarity charges takes place under an applied electric field. The generated space charge also affects the electric field distribution.

The total polarisability of a material will be the result of the separate components described above [71],

$$a_{\text{total}} = a_{\text{e}} + a_{\text{i}} + a_{\text{o}} + a_{\text{d}} \tag{2.11}$$

Depending on the type of the material's molecule and structure, different types of polarisation will exhibit. For instance, non-polar materials will experience only electronic polarisation in the form of a non-permanent displacement of their valence electrons. On the other hand, polar materials will experience a displacement of their valence electrons and a displacement in the position of their ions i.e., both electronic and ionic polarisation. If the polar material has an asymmetrical bonding and not a crystal lattice structure, frequently referred as dipolar, then it will also exhibit orientational polarisation. No material has a perfect crystal structure and none of them is a perfect insulator, meaning that a small number of charge carriers will always exist. Because of these two factors, space charge polarisation shall also be considered.

2.3.3 Electron interaction in solid/gas interfaces

The presence of a dielectric within an electrode geometry introduces a larger number of factors under consideration when attempting to describe the electronics of discharges. Two terms should be clarified before proceeding, photoionisation and photoemission.

Photoionisation occurs when a high energy photon interacts with an atom or molecule forcing it to lose one electron and thus ionise it. This mechanism is possible when the ionisation energy of the absorbing atom/molecule is less than that of the photon. The process is symbolically expressed as:

$$M + \hbar v \rightarrow M^{+} + e^{-} \tag{2.12}$$

where $\hbar$ is Planck's constant and v the frequency of the photon. Prior to the release of the photon, an electron of lower energy will excite an atom, or molecule, to a higher energy state. When it returns to its ground level, the atom will radiate a quantum of energy of a photon [72].

With the presence of a solid material, when a photon which does not have enough energy to ionise the gas molecule is generated, it is likely to reach the surface of the material at some point. If the material is of low work function, that is lower than that of the striking photon, then it is likely that an electron will be released. This mechanism is usually referred to as secondary electron emission by photon impact. Photons are not the only ones responsible for emission of secondary electrons, but it may be also achieved by the impact of ions and metastable atoms, and this is a known mechanism of producing secondary electrons from the surface of the metal cathode. Work function ϕ values in eV for some of the most common metals are summarised in Table 2.8

Table 2.8: Electron work function of common transition metals [73–75].

Metal	**Chemical symbol**	**Work function ϕ (eV)**
Aluminium	Al	4.28
Copper	Cu	4.65
Tungsten	W	4.55
Iron	Fe	4.5
Silver	Ag	4.26
Titanium	Ti	4.33
Gold	Au	5.47
Zinc	Zn	3.63
Nickel	Ni	5.15

As described in [3], when a photon strikes the surface of a metal with sufficient energy $(> \phi\,(\mathrm{eV}))$ to cause the emission of an electron then another electron in the conduction band will take its place so that the metal will maintain its neutrality. This will not be the same for the case of a dielectric. A photon needs to have enough energy to move an electron from the valence to the conduction band and then overcome the work function. Once an electron is released and since the availability of free electrons within a dielectric, for instance a polymer, is low, after the detachment of the electron the emitting surface will remain positively charged. In [76] and [77], which are also referred in [3], low energy threshold values are listed ($\sim 4\,\text{eV}$) for some very common polymers in the electrical engineering applications such as polyethylene (PE), nylon 6 and polytetrafluorethylene (PTFE). It could be summarised that because of the photoemission capability of the dielectric surface, it partially behaves as an electron source.

Following again the simulation results and findings in [3], it was shown that within a uniform electric field distribution when the electric field magnitude is well above the breakdown threshold, then the collisional ionisation is dominant over photoionisation and photoemission. As the electric field decreases, approaching the breakdown threshold which is assumed $3\,\text{MV/m}$ for nitrogen at atmospheric pressure ($760\,\text{Torr}$), the electrons added to the simulated space from photoemission increases relative to the number of electrons originating from collisional ionisation. Combined with the data of [78], it is shown that for lower electric fields, the electrons striking the dielectric surface do not have enough energy to liberate an electron through the secondary electron emission mechanism which leads them to be trapped. These weakly trapped electrons will later be released through photoemission.

In Figure 2.23, the photoemission quantum yield for Teflon$^{\text{TM}}$ is shown. The term quantum yield describes the number of photons emitted relative to the number of photons absorbed [79]. For instance, the ionisation energy of molecular nitrogen is around $15.58\,\text{eV}$, well above the minimum recorded value in the graph of Figure 2.23. However, the quantum yield is relatively low for photon energy values close to $\sim 6\,\text{eV}$.

Reference [82], describes the modification of the ionisation and attachment coefficients from the presence of a dielectric compared to the case without it. According to the authors, three mechanisms are responsible for this: (a) the emission of electrons released because of the electron bombardment of the dielectric surface, (b) the trap of electrons on the surface and (c) the further electrostatic attraction of positive ions, all three described in the paragraphs before. Figure 2.24 shows the corresponding ionisation and attachment coefficients with and without the presence of a dielectric surface in

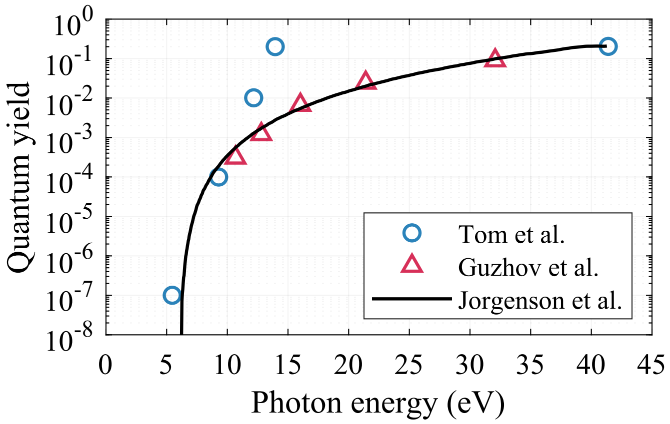

Figure 2.23: Photoemission quantum yield over photon energy for Teflon$^{\mathrm{TM}}$. Graph was replotted from [3]. Data points were collected from [80] and [81].

air. For electric fields higher than the corresponding at the intersection points, the ionisation process will predominate attachment and conditions will support the inception of discharge activity.

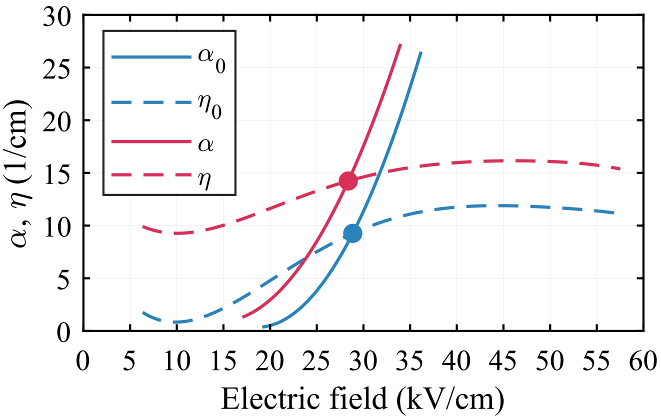

Figure 2.24: Ionisation (α and α_0) and attachment (η and η_0) coefficients for air alone (blue lines) and air with the presence of a PVC surface (red lines). Curves were extracted and replotted from [82].

2.4 Electric strength of gases and solid/gas interfaces

This section reviews part of the published bibliography related to the electric strength of the insulating gases. Atmospheric gases i.e., technical air (21/79 % O_2/N_2), nitrogen (N_2) and carbon dioxide (CO_2), and the strongly attaching mixture of 30/70 % CF_3I/CO_2 are of mayor focus as these compounds are further investigated in the experimental part of this thesis.

2.4.1 Breakdown voltage characteristics under non-uniform electric field conditions

CIGRE Working Group D1.51 published its outcomes in the corresponding technical brochure [4]. Part of the presented results include a direct comparison between natural-origin gases and SF_6 and SF_6/N_2 gas mixtures under different voltage wave stresses and electric field conditions, using the same electrode configurations.

Figure 2.25 shows the gas pressure dependence of the positive polarity basic lightning impulse 50 % breakdown voltage ($U_{\mathrm{bd50\%}}$) and 50 % partial discharge initiation voltage $\left(U_{\mathrm{pdp50\%}}\right)$ in dry air, N_2, CO_2 and SF_6 under non-uniform electric field conditions. The results were first reported by the authors in [83] and were later included in [4].

As shown in Figure 2.25a and commented by the authors in [83], the positive 50 % breakdown voltage of SF_6, CO_2 and N_2 saturate with the increase of gas pressure. At the same time, the $U_{\mathrm{bd50\%}}$ of the atmospheric gases is 30 % to 70 % of that of SF_6. Dry air showed a higher withstand to breakdown compared to the rest of the atmospheric gases. It could be added that, for the atmospheric pressure level $(0.1\,\mathrm{MPa})$, $U_{\mathrm{BD-DryAir}} > U_{\mathrm{BD-CO_2}} > U_{\mathrm{BD-N_2}}$, which is of particular interest as it will be shown later in the experimental part of this thesis.

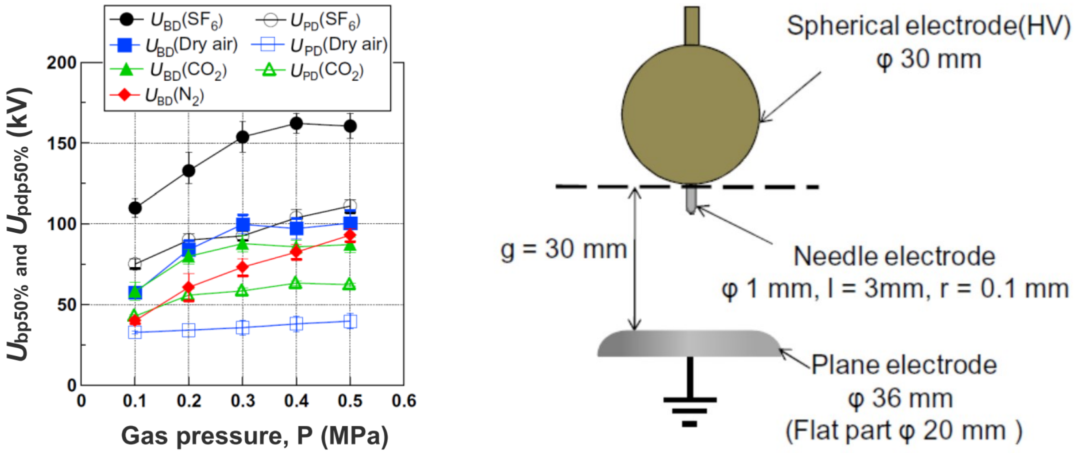

(a) Test results **(b)** Electrode configuration

Figure 2.25: Gas pressure dependence of the 50 % positive breakdown and PDIV under non-uniform electric field [4, 83].

In [84] the authors investigated the breakdown voltage of CO_2, N_2, SF_6 and mixtures of them under different voltage waveforms. In part of the presented experiments, strongly non-uniform electric field conditions were tested. A needle-plane electrode configuration was used with a tip radius of $10 \pm 0.5\,\mu$m. Figure 2.26 summarises the obtained results.

As it is commented by the authors in [84], the breakdown voltage increases with the increase of the gas pressure and the increase of the gap distance. The breakdown voltage levels of CO_2 are higher than N_2, same as was shown before in Figure 2.25a for lightning impulse. The breakdown voltages of SF_6 are more than three times higher than the two atmospheric gases.

In the experimental outputs of the published work [85], the authors presented a comparison of the 50 % breakdown voltage of 30/70 % CF_3I/CO_2 and SF_6 in a needle-plane electrode configuration at different gap distances in the pressure range between $0.1 - 0.3$ MPa. The reported results are shown in Figure 2.27.

As described by the authors [85], the breakdown voltage of 30/70 % CF_3I/CO_2 and SF_6 increase with the increase of the pressure for all the different gap distances. However, the slope of the curves that describe SF_6 is larger. In all cases pure SF_6 is

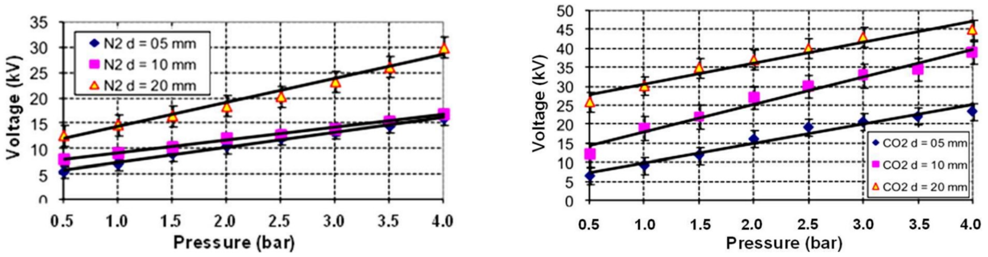

(a) N_2 **(b)** CO_2

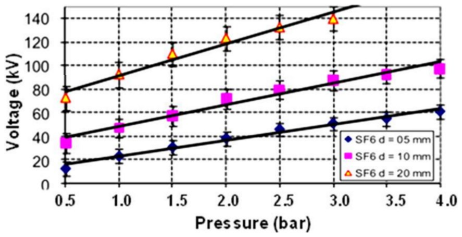

(c) SF_6

Figure 2.26: AC breakdown voltage of gases in a point-plane electrode arrangement [84]. The presented voltage values are AC peaks.

superior to the strongly attaching mixture of 30/70 % CF_3I/CO_2 mixture.

In the recently published technical brochure of the CIGRE Working Group (WG) D1.67 [86], an extensive summary of the state-of-the-art know-how of non-SF_6 fluorinated compounds was summarised together with a large amount of results from newly conducted test campaigns. One of the study cases presented was the 30/70 % CF_3I/CO_2 mixture.

The experimental results reported in Section 8.8 of [86] demonstrate the better electric performance of SF_6 when compared to 30/70 % CF_3I/CO_2 for all the investigated test cases summarised in Figure 8-32 (a), Figure 8-32 (b), Figure 8-33 (a) and Figure 8-33 (b) found in the technical brochure. Various different electrode configuration were used. Two of them were needle-plane, one suitable for medium-voltage conditions and another for high-voltage. For strongly non-uniform electric field conditions, only lightning impulse tests were carried out. The breakdown voltage of 30/70 % CF_3I/CO_2 was $60 - 75$ % relative to SF_6. AC tests were performed for the sphere-plane electrode configuration with a large observed scatter in the recordings. In overall, tests that in-

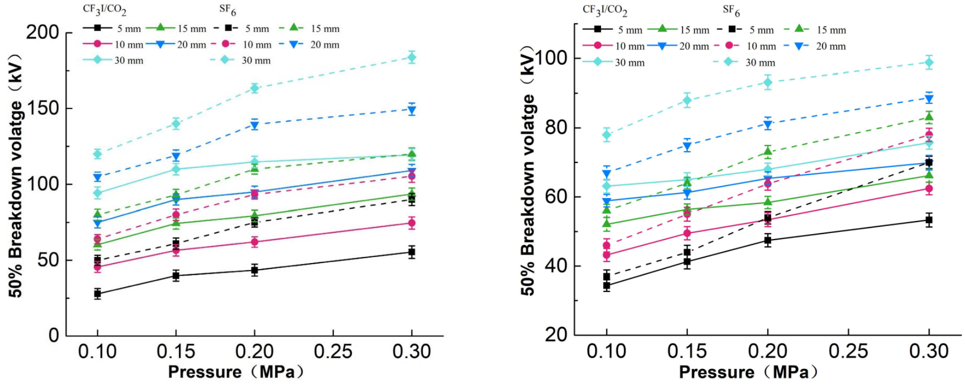

(a) Negative polarity LI **(b)** Positive polarity LI

Figure 2.27: Comparison of 50 % breakdown voltage of 30/70 % CF_3I/CO_2 and SF_6 gas in a needle-plane electrode configuration [85].

volved the CF_3I/CO_2 mixture were reportedly found to be problematic because of the decomposition of CF_3I compound during the experiments.

In [87] the authors presented breakdown voltage measurements of CF_3I/CO_2 mixtures under AC voltage application. One of the investigated electrode configurations was the needle-plane and the corresponding results are shown in Figure 2.28.

According to the authors, the breakdown withstand of CF_3I/CO_2 mixture at $0.15 - 0.20$ MPa can exceed the one of SF_6 at 0.1 MPa. The presence of CF_3I also improves the insulation characteristics of pure CO_2. It can be observed that the breakdown voltage of 30/70 % CF_3I/CO_2 at 0.1 MPa, which is of interest for the work shown in this thesis, is more than two times higher than that of pure CO_2.

2.4.2 Partial discharges

2.4.2.1 Practical classification of partial discharges

There are many different versions of gas discharge classifications available in the bibliography which are mainly performed based on application and observation principle. Some examples are, self-sustaining and non-self-sustaining discharges, steady discharge and unsteady discharge, cold and hot cathode discharges, etc. The discharge

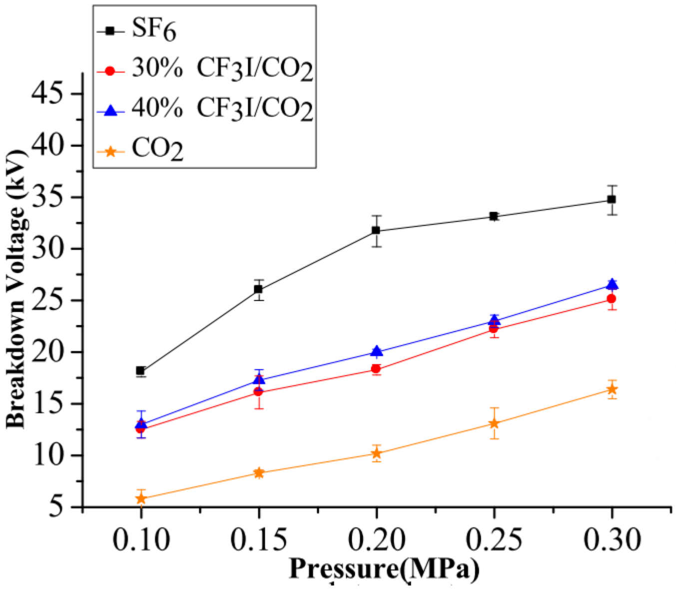

Figure 2.28: Breakdown voltage of CF_3I CO_2, SF_6 and CO_2 in a needle-plane (5 mm) electrode configuration under AC voltage application [87].

classification described in [10], and reproduced in Figure 2.29, is found to be more convenient as it can be easily correlated to practical applications where gases are utilised as insulating media. It could be commented that electron attachment also results to an electrically charged atom.

Internal discharges are frequently met in the bibliography as partial discharges in cavities or voids in solid insulation and describe a known situation in practical insulation systems. Cavities in solid insulation compartments are usually introduced during the manufacturing process such as cable insulation. The dielectric strength of the cavity and the relative permittivity of its content are lower compared to the surrounding dielectric. The magnitude of the generated electric field is also much higher, resulting in the gradual degradation of the solid insulation and, eventually, its failure at voltage levels lower than the expected.

Surface discharges refer to discharges occurring on the surface of a dielectric and are also the main research objective of this investigation. As it will be seen in the next chapter, the detection approach of this kind of discharges shows many similarities with

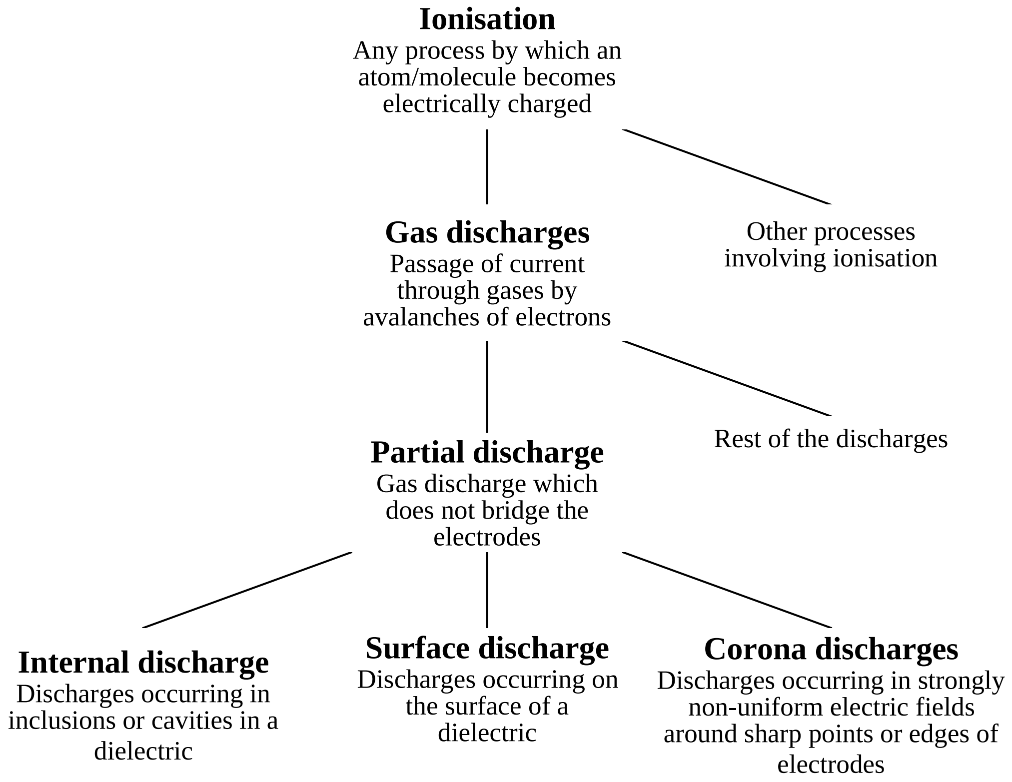

Figure 2.29: Classification of gas discharges [10].

that of partial discharges. However, the inclusion of a dielectric increases the level of complexity in terms of undergoing background physics. Further information on the theory covering solid/gas interfaces will be presented within the next sections of this chapter.

Corona discharges are very common to appear at sharp points where the electric field levels are considerably enhanced. Depending on the conditions, they can become luminous accompanied by a high pitch sound. They usually appear at voltage levels much earlier than the corresponding of breakdown withstand. Corona noise and disturbances induced from power lines to communication systems has been a known issue of this type of discharges.

2.4.2.2 Partial discharge measurement circuits

The basic partial discharge measurement circuit was retrieved from the relevant standards [88] and is shown in Figure 2.30. In this circuit, U is the high-voltage supply, Z is a filter on the input voltage side of the circuit, C_a is the test object, C_k is the coupling capacitor, Z_mi is the input impedance of the measuring system, CD is the coupling device and CC the connecting cable to the measuring system MI.

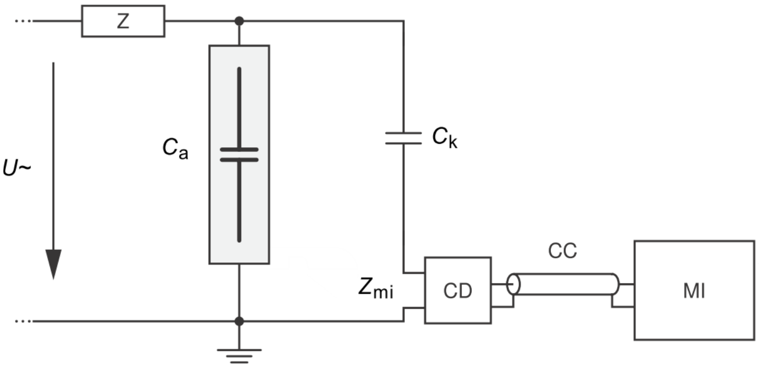

Figure 2.30: Basic partial discharge measurement circuit [88].

The filter Z_mi between the test object and the voltage source attenuates disturbances that may be generated by the source, practically improving the sensitivity of the measuring system. Such an arrangement is usually implemented by commercial partial discharge measuring and analysis systems. An alternative to the measuring system of Figure 2.30 is shown in Figure 2.31. For this case, the coupling device is connected to the earth terminal of the test object and the coupling capacitor is connected right after the voltage and filter arrangement.

As stated in [88], the circuit of Figure 2.31 provides a better sensitivity compared to the circuit of Figure 2.30, when the test circuit consists of low capacitance components. If the stray capacitances to earth are much larger than the capacitance of the test object, then the coupling capacitor C_k can be removed. In this work, the test objects were connected to the test circuits based on the proposed circuit of Figure 2.31.

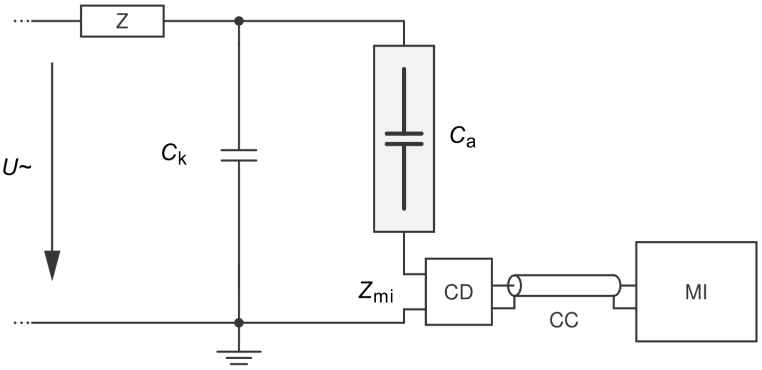

Figure 2.31: Alternative to the circuit of Figure 2.30 [88].

2.4.2.3 Characteristics of individual partial discharge pulses

In most of the occasions, individual partial discharge pulses appear to have a double exponential waveshape, with a steep rising part and a slower decaying part. Because of their very short duration, it could be said that individual pulses are transient phenomena which, on occasions, are very dense in the frequency of their appearance. If the bandwidth range of the utilised devices allows, these transient pulses shall appear on both the current detection system and superimposed to the applied voltage waveform. For the next sections, the term partial discharge will refer to pulses detected on the current signal, unless otherwise described. The most significant information that can be derived by an accurately measured current partial discharge pulse are the below:

- *Pulse peak*: the absolute maximum of the partial discharge pulse.
- *Rise time*: the time difference between the $10\,\%$ and $90\,\%$ of the peak value during the rising slope of the pulse.
- *Decay time*: the time difference between the $90\,\%$ and $10\,\%$ of the peak value during the decay slope of the pulse.
- *Pulse width*: the time difference between the $50\,\%$ of the peak value on the rising slope and $50\,\%$ of the peak value on the decaying slope.
- *Pulse duration*: time difference between the $10\,\%$ of the peak value during the

rising slope and 10 % of the peak value during the decaying slope.

- *Apparent charge*: for the case where the partial discharge is a current pulse expressed over time, then the integral of the current signal over that time interval will return the apparent charge of that individual pulse:

$$q = \int_{t_1}^{t_2} i\left(t\right) \mathrm{d}t \tag{2.13}$$

According to the standard BS EN 60270 [88], the apparent charge does not equal the amount of charge locally involved at the site of the discharge. The description provided in [89] based on the $a - b - c$ model of Gemant and Philippoff states that as the capacitance of the test object increases then the apparent charge becomes a smaller fraction of the true charge.

Figure 2.32 shows an example of a partial discharge pulse that is generated at a triple junction point between a charged needle, PTFE disc insulator of 4 mm thickness and technical air. Such cases will be extensively described in the outputs of the experimental part of this work.

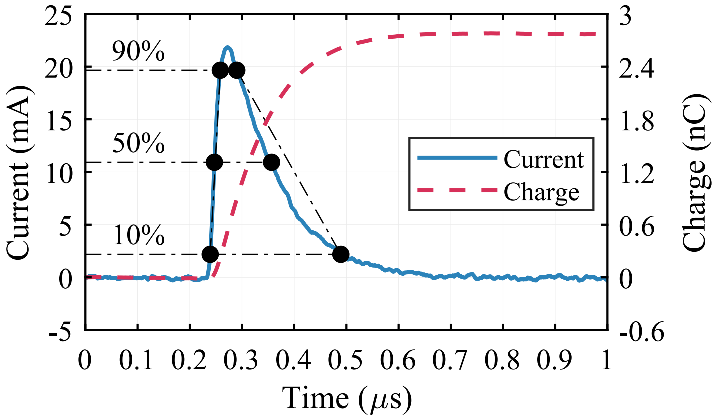

Figure 2.32: Example of a current pulse, associated with a surface discharge event, and the analysis of it.

For this specific pulse, a rise time 10 − 90 % is measured as 19.37 ns, the decay time 90 − 10 %, as 199.37 ns, the pulse width 50 − 50 %, as 109.51 ns, and the pulse duration

$10 - 10\,\%$, as $250.28\,\mathrm{ns}$. The apparent charge is calculated using Equation (2.13) and it is clearly observable its dependence on the characteristics of the pulse.

From Figure 2.32, it can be clearly seen that this pulse duration is well below $1\,\mu\mathrm{s}$. Such a characteristic, together with the very fast rise time $(19.37\,\mathrm{ns})$, indicates the bandwidth requirements that both the current sensing and recording devices shall fulfil. An expression that relates the minimum rise time and the $-3\,\mathrm{dB}$ bandwidth of the analogue-to-digital converter systems, is given in Equation (2.14) and is derived by combining the time- and frequency-dependent approaches of the ideal RC low-pass filter circuit.

$$\tau_{\mathrm{r}} = \frac{0.35}{f_{3\mathrm{dB}}} \tag{2.14}$$

Equation (2.14) is frequently referred to as a rule of thumb and it is used to estimate the measuring capability of oscilloscopes and/or digitisers with regards to the rise time of the obtained signals and can be found in many manuals and user guides provided by the manufacturers of such equipment [90]. For the case of a partial discharge pulse, with rise time similar to the one shown in Figure 2.32, the current sensing and recording equipment need to have an upper cut-off frequency of at least $18.07\,\mathrm{MHz}$, according to Equation (2.14). It is obvious that the shorter the rise time is, the higher the upper cut-off limit of the equipment needs to be.

2.4.2.4 Phase-resolved partial discharge (PRPD) patterns and their interpretation

A phase-resolved partial discharge (PRPD) pattern plot is the representation of the partial discharge activity relative to the 360° of one AC-cycle. As defined in [88], a PD pattern is the display of the apparent charge q versus the phase angle ϕ_{i} of the PD pulses recorded during a specified time interval Δt. Figure 2.33 shows an example of a PRPD pattern.

An extensive summary of the options related to the PD analysis can be found in [91] and which can be performed primarily with data included in the $q - \phi$ PD pattern

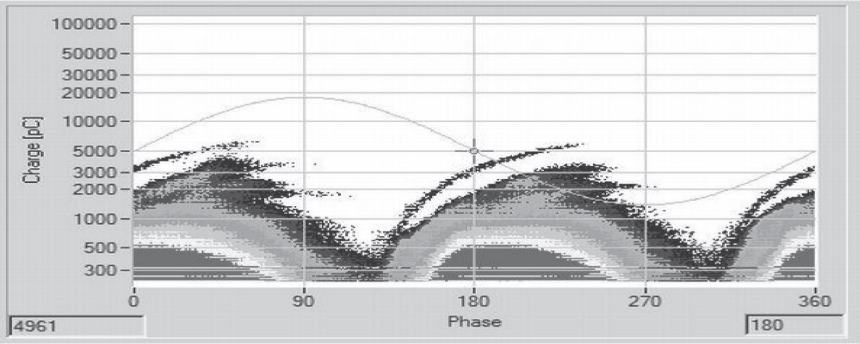

Figure 2.33: Example for a phase-resolved PD pattern [88]. PD pulses occurring during the negative half-cycle of the test voltage have been inverted which appear thus like positive pulses.

plots. It could be said that three are the major, although not limited to these, analytical procedures:

- Analysis of integrated discharge quantities derived from the PD recurrence such as pulse repetition rate, average discharge current, discharge power, quadratic rate etc. The definition of these terms can be found in [88, 89, 91] and the Appendix A.5.
- Phase-resolved PD analysis of the discharge patterns in relation to the AC-cycle: The AC-cycle is divided in small segments and for each phase window the integrated quantities described before are calculated. The distribution of the calculated quantities is then expressed as a function of ϕ. Further calculations on the distribution of these newly generated patterns are found to provide information on the type of defect [92].
- PD pattern recognition based on neural network [93–95] which according to [91] is an alternative to statistical analysis. They excel to problems involving pattern classification, association and generalisation. Limitations of this technique are mainly associated with the known problem of network training.

2.4.2.5 Partial discharges in technical air, N_2, CO_2 and CF_3I/CO_2 mixtures

In [5] the authors presented partial discharge inception voltage (PDIV) measurements for three different types of defects, i.e., protrusion, floating electrode and free metallic particle, under the AC and DC voltage application. The obtained results were also referred in the CIGRE technical brochure in [4]. Figure 2.34 shows the obtained results for the case where AC voltage waveform was applied to the test objects.

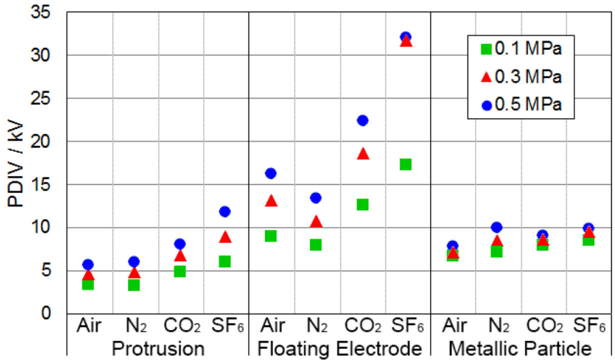

Figure 2.34: PDIV under AC voltage with different gas types and gas pressures [5].

Focusing on the first batch of results shown in Figure 2.34, for the case of the protrusion defect, which is close to the experimental arrangement that is used in this thesis, at 0.1 MPa the PDIV values of dry air, N_2 and CO_2 are quite close. However, it is still visible that $\mathrm{PDIV}_{\mathrm{CO}_2} > \mathrm{PDIV}_{\mathrm{Tech.\ Air}} > \mathrm{PDIV}_{\mathrm{N}_2}$. For the same pressure level SF_6 is superior to the atmospheric gases again for the case of the protrusion.

In [96] the authors investigated the synergy between CF_3I and CO_2 with regards to the PDIV in a needle-plane electrode configuration at power frequency voltage application. Figure 2.35 summarises part of the reported results where the variation in the PDIV over the CF_3I percentage content for different gap distances is shown [96].

In Figure 2.35 it is obvious that with the increase of the CF_3I the PDIV increases for all the gap distances that were investigated. In the attached graphs, it can be observed that the ratio of the PDIVs between 30 % and 0 % CF_3I content (pure CO_2) is around

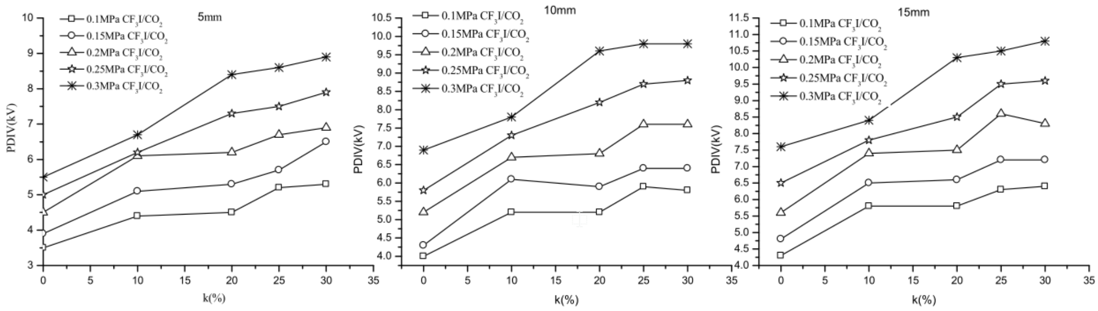

Figure 2.35: Changes in PDIV of CF_3I/CO_2 with the mixture ratio at different gas pressures under AC voltage application [96].

$1.45-1.5$. The authors compared the CF_3I/CO_2 results with the SF_6/CO_2 mixture under the same test conditions. It was found that the PDIVs for CF_3I/CO_2 were approximately $1-1.2$ times that of the SF_6/CO_2 mixture.

2.4.3 Discharge phenomena at solid/gas interfaces

In this section are summarised published works related to discharge phenomena on the solid/gas interfaces. In most of these works, the test objects include solid dielectrics of cylindrical shape. As it will be seen in a later section, experimental studies that included configurations with disc-shaped solid dielectrics are fewer and those available are met in studies where imaging techniques are of major focus although.

In [97], a large set of results were reported by the authors comparing the propagation of positive streamers within an electrode gap (Rogowski profile) with and without the presence of a dielectric surface and under negative dc voltage energisation. The differences in the relative permittivity between the different versions of silicone rubber are not big. However, very useful observations were made regarding the streamer propagation field, velocity and charge distribution during the streamer development. It was shown that the presence of the dielectric surface increases the magnitude of the ionisation intensity which, in turn, is described to be affected by the field enhancement due to the relative permittivity and the deposited charge on the surface. In addition to these two factors, the importance of photoionisation is highlighted when the role of dielectric surfaces in the discharge mechanism is examined.

In another very interesting research work [98], where there is a common observation with [97], it was discussed that the velocity of the generated streamers is higher when propagating along an insulator surface rather than in the gap without it. In both studies, such a behaviour was justified by the higher ionisation efficiency at the head of the generated streamers due to the photoionisation of the surface. A very interesting observation is made regarding the streamer propagation and formation. It was observed that, it consists of two different components: one which depends on the solid dielectric material, along the surface of which the streamer propagates, and one propagating with a velocity very close to that of air alone. Such a case in not observed for ceramic samples. It would be interesting to know the exact microscopic composition of the ceramic and examine how this composition and polarisability of the contained substances are correlated, and might have an influence on such an output.

In [99], the corona propagation and charge deposition on cylindrical PTFE surfaces is presented. In addition to [98], current measurements are also performed along with optical detection. Some of the reported observations showed that the decay time of the presented current pulses is essentially smaller with the presence of the dielectric compared to the cases without it. Also, at around 20 ns, the peak current progresses with small incremental distances from the high electric field magnitude area in the proximity of the charged electrode. After this progression, the fast reduction in current occurs due to the attachment of electrons to the PTFE surface. The deposited charge was measured using an electrostatic probe, and an increased deposited positive charge was observed near the streamer ends and close to the charged rod when discharge activity was intense.

The surface charge decay on insulators in air and SF_6 was examined from simulation and experimental perspectives in [100] and [101] respectively. Both approaches highlighted the dependence of surface charge decay by three mechanisms: (a) electric conduction through the volume of the insulator, (b) electric conduction along the surface of the insulator and (c) charge neutralisation by the gas ions. No clear distinction between the three mechanisms is made indicating their importance. In the simulation approach in [100], the polarisation of the material is considered stabilised and the space charge effects in the volume of the insulator are neglected contributing that way, as stated by the authors, to the simplicity of the model. Surface current density is considered proportional to the electric field component and inverse proportional to the surface resistivity. As proposed and validated mathematically, the contribution of gas ions to the described process should be considered in the form of a current source rather than a constant impact on the electrical conductivity of the insulating gas. The simulation results are compared with experimental outputs on three different dielectric materials frequently met in electrical engineering applications.

An experimental set-up very similar to [98] was presented in [102]. In this study, six different materials of different relative permittivities were examined, including PTFE and ceramic (CERG), with the lowest and highest ε_r values respectively. Also, in [102], reported results suggest the existence of two different discharge components of significantly different propagation velocities in the generated streamers. As described by the authors, the faster component depends on the dielectric material properties while the slower is similar for all different cases and thus is dependent on the surrounding insulating gas. Other observations suggest that materials of higher relative permittivity will accumulate more charge on their surface and streamers will require higher electric fields to propagate on such surfaces. However, the same does not occur with ceramic surfaces, where lower required electric fields were observed.

The authors in [8] investigated the triple interface between N_2 and SF_6 gases, with PTFE and epoxy resin solid dielectrics and a cylindrical conductor. They performed PDIV and FOV tests in the pressure range of $0.1 - 0.45$ MPa under AC voltage application. They found that with the lower permittivity PTFE both partial discharge inception and flashover levels were higher compared to epoxy resin, for all pressure levels, which was attributed to the difference in the permittivities of the two materials. Although, because of the type of their electrode configuration, the values of PDIV and

FOV were close. SF_6 gas performed better than N_2 in suppressing the inception of PD activity.

In another study in [103], the impact of oxygen content was investigated in the O_2/N_2 gas mixtures. In the experimental part of the work it was investigated the PDIV and FOV performance of triple junctions on the surface of PTFE (Teflon®) using "knife" shaped electrodes. Despite that, for the majority of the conducted tests, the pressure levels tested were higher than atmospheric, it was shown overall the $20/80\,\%$ O_2/N_2 mixture performed better when AC applied waveform was used. It could be commented that a ratio close to that of the composition of air performs better than pure N_2.

In [104], the authors investigated the effect of surface discharges on different polymer material types. Disc-shaped samples of 2 mm thickness were placed between a rod-plane electrode configuration with the first having a curved edge of 1 mm radius. The tests were performed at atmospheric air conditions and under AC voltage application. The recorded PDIVs were found to be inversely proportional to the relative permittivity of the materials, i.e., the higher the ε_r is the lower the resulted PDIV. With short partial discharge acquisition measurements it was found that lower permittivity materials showed stronger resistance against partial discharge with only the material properties and the environmental conditions affecting the PD behaviour. With longer duration PD measurements (2 hours) it was shown that factors such as the material surface conductivity and oxidation state have an impact on the generated phenomena.

In the study of [105], the authors investigated the flashover levels on cylindrical solid insulators made of epoxy resin with aluminium oxide (Al_2O_3) fillers placed between two parallel plate electrodes and under particle-contaminated and non-contaminated conditions. The gases that were tested were dry air, N_2 and CO_2 as various pressure levels while for part of the tests AC voltage waveform was applied. The reported results are shown in Figure 2.36.

As described by the authors [105], for the case of no particle contamination (Fig-

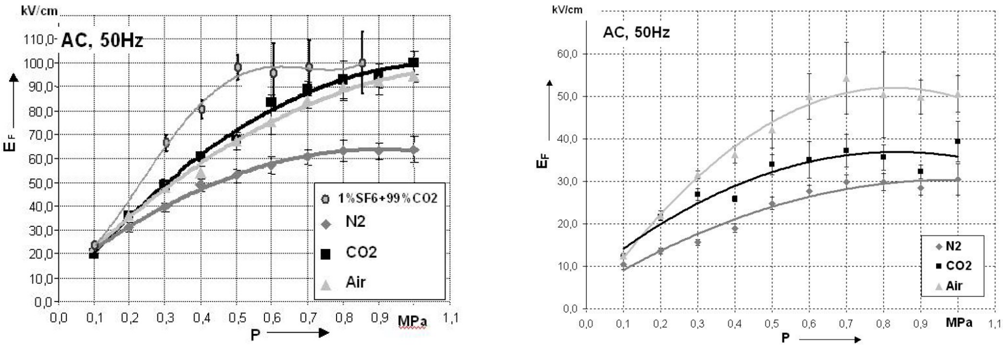

(a) No particle contamination **(b)** With particle contamination

Figure 2.36: Flashover field strength vs. pressure for compressed air, N_2 and CO_2 [105].

ure 2.36a) CO_2 and compressed air show a fairly similar performance with nitrogen exhibiting the lower strength over the the whole pressure range. With the addition of a metal particle (Figure 2.36b), CO_2 demonstrates the highest reduction in its electric field strength. For pressure levels higher than 0.6 MPa, the curves of compressed air and CO_2 seem to saturate which is attributed to the corona stabilisation phenomenon during the AC voltage application.

Reported works on surface flashover that investigate CF_3I or mixtures of it are rare compared, for instance, to those with SF_6. In [106] were investigated the flashover characteristics of pure CF_3I under the application of a nanosecond square pulse voltage waveform. Figure 2.37 shows part of the reported results.

As described in [106], SF_6 showed the highest flashover levels followed by CF_3I, with air being the lowest. Another observation, among others, was that the flashover levels of SF_6 and air hardly change with the occurrence of previous flashover events. With CF_3I, once the first flashover occurs then the subsequent flashover levels become lower. It was shown that flashover voltage level of CF_3I in the early test attempts is $1 - 1.2$ times higher than that of SF_6 but when the number was increased the flashover level of CF_3I dropped to 0.6 times than that of SF_6. It could be commented that this work highlights the better performance of the CF_3I compounds compared to SF_6 and

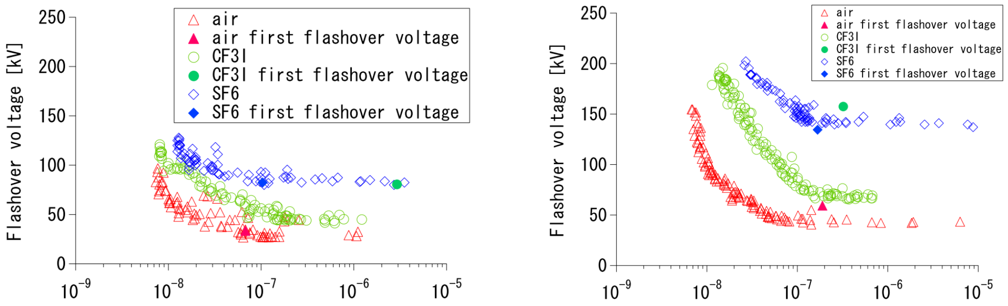

(a) 10 mm gap **(b)** 20 mm gap

Figure 2.37: Flashover on PTFE insulators under nanosecond square pulse voltage of positive polarity at 0.1 MPa [106].

air, however, the ageing factor after being exposed to arcing events has a significant impact in that performance.

2.5 Image capturing techniques of surface discharges

In this section are summarised published works about capturing images of surface discharge patterns in experimental configurations relatively similar to the one investigated in this thesis. The most known methods in the published literature are:

- Dust figure technique,
- electro-optical Pockels technique,
- photographic techniques.

The first method i.e., Dust figure technique, was first proposed by Lichtenberg in 1977. The experimental configuration that is utilised to this day includes an earthed plane electrode on top of which a solid dielectric is placed with an energised electrode, usually sharp-edged, pointing towards its adjacent surface. A voltage is applied to the energised electrode, sufficient enough to cause a discharge phenomenon to appear on the surface of the solid dielectric. Shortly after the applied voltage has extinguished, charged dust particles which consist of a mixture of positively charged red-coloured lead oxide powder and negatively charged yellow-white sulphur powder are sprayed on the surface of the dielectric. The interaction between the charged dust particles and the residual charges, caused by the surface discharge phenomenon, will interact between them and a coloured dust figure will be formed on the surface [107].

In [16] the authors presented a series of tests where a nanosecond pulse voltage was applied and the dielectric was made of glass coated with a silicon film for increased surface resistivity. The duration of the applied voltage pulse and its magnitude were the varying parameters while the diameter of the captured corona streamers, the charge density and the average velocity of the streamers were observed. Shorter duration pulses and higher in magnitude resulted in faster developing streamers. It was also observed that the charge quantity of the streamer increases slower compared to the streamer extension when the duration of the voltage pulse increases. It was explained that when the streamer reaches its final length, the charging currents that correspond to the discharge propagation are still flowing. The extension of the discharge will remain approximately the same but the charge distribution will vary considerably. Another important observation was made after the applied voltage had fall to zero and back-discharges appeared. In their tests this happened for voltage pulses of longer duration. Similar observations were summarised from the same research group in [17].

The operating principle of Pockels technique is the electro-optical effect. Under the variation of the electric field some transparent materials show the effect of optical anisotropy which involves the Pockels and the Kerr effects. Under the Pockels effect the material changes its optical refractive index linearly to the generated electric field while with Kerr effect the change in the refractive index is square. The method is suitable for thin transparent insulating materials [107].

In [14] the authors used the electro-optical Pockels effect technique to measure the dynamic surface charge distributions on a dielectric surface after applying a single AC-cycle of a sinusoidal voltage wave of 10 Hz frequency. They examined the cases where the voltage starts from either the positive or negative half-cycle at different distances of the needle electrode from a bismuth silicon oxide (BSO) crystal. The AC-cycle was divided in segments of 3 ms each. As it was described, when the needle electrode is placed at 0 mm distance from the BSO crystal and when the AC voltage starts from the positive half-cycle, positive discharges appear during the rising slope and negative polarity back-discharges during the falling slope. During the negative half-cycle, negative discharges and positive back-discharges appear in the rising and falling slopes as well. When the distance is larger than 1 mm, space discharges are described to appear (spark and corona discharges) but also back-discharges are still observable. The authors observed a transition region 0 mm $<$ distance between needle and BSO ≤ 0.6 mm at which space discharges and surface discharges coexist.

In [18] the authors employed a configuration and experimental approach similar to the one presented in [14]. This time surface discharges on the polymers polyimide (PI), polyerthylene terephthalate (PET) and polyvinylidene fluoride (PVDF) were investigated, with the relative permittivity of PVDF being almost double the values of PI and PET. The applied voltage was AC of 20 Hz frequency. It was concluded that negative charge distribution is smaller than positive due to the polarity effect. The different materials showed also different charge distribution patterns especially with the generated positive streamers. In PI and PET streamers were found to grow gradually in a snake-like pattern while for PVDF they developed instantaneously in a spoke-like pattern. It was also discussed the influence of the different band gaps of the materials.

The operating principle of the photographic technique is quite straightforward, i.e., the light that reaches the sensor of the camera is captured on the corresponding frame that is generated as an output. Advanced scientific CMOS or CCD sensor cameras are capable to record at very high frame rates, up to several hundreds of thousands frames per second (fps). In experiments that require the capturing of discharges, only the light emitted from such activity is captured. This method does not offer the advantage of obtaining dynamically the charge density of the discharge. However, it is more practical in its use as it can be applicable in a wider range of cases without limitations in the type of the object that needs to be observed.

In [108] the authors investigated the morphology and stopping length of creeping discharges over solid insulator samples in different gases and gas mixtures under AC voltage application. The electrode configuration that was used is very similar to the one that is presented in the experimental part of this thesis. The generated creeping discharges were recorded using a CCD camera connected to a video card. It was shown that materials of higher relative permittivity produce creeping discharges with more dense branches. The propagation length of discharges along the observed surfaces was longer for weaker attaching gaseous compounds, i.e., $L_\mathrm{f}\,(\mathrm{N_2}) > L_\mathrm{f}\,(\mathrm{CO_2}) > L_\mathrm{f}\,(\mathrm{SF_6})$. Also, the same length decreases with the increase of the thickness of the solid insulator sample while the density of the branches decrease. The same authors performed a similar test campaign this time under DC voltage application [109]. The propagation length of the discharges was influenced in the same way as happened with AC applied voltage. However, under DC the extension of the discharges was not always radial.

2.6 Discussion and conclusions

In this chapter, an overview of the gaseous insulating media was presented. The listed compounds can be distinguished in two different main categories: atmospheric and synthetic. The first refers to substances which naturally occur in the composition of the atmosphere, although, the term shall not be confused with those referred as natural gas or gases. The second category refers to compounds that are artificially made and includes cases such as the well-known sulphur hexafluoride (SF_6), which is widely in use, and its replacement candidates, in which the carbon-fluorine (C-F) bond is dominant in their molecular composition.

It is found to be necessary that the physical characteristics and molecular structure of each compound are well understood, and which can help understand the reasons why some of the substances are superior over the others when it comes to practical use and environmental impact. A useful observation is that, among the summarised gaseous compounds, those of higher molecular weight and a polar overall dipole moment show a higher boiling point, a characteristic which makes them, in most of the cases, unsuitable for use in their pure form when they are compressed. On the other hand, the presented synthetic molecules that exhibit a geometrical symmetry and a zero overall dipole moment, such as SF_6 and CF_4, show considerably lower boiling points, and at the same time, a very high GWP. At this stage, it could be questioned whether a molecule can sufficiently meet these two necessities: having a boiling point sufficiently low so, when compressed, it can meet the practical requirements of an electrical insulation system and, at the same time, the same molecule is sensitive to atmospheric conditions (OH radicals and UV radiation) so that it is decomposed when exposed to them.

Furthermore, the fundamental physics related to gaseous and solid dielectrics are described. Reasonably, the basic terminology needs to be well understood as it is frequently referred in the available bibliography, and it is necessary when an analysis of relevant phenomena is attempted. In many of the cases, when it comes to the description of gaseous insulating compounds, the term “electronegative” is frequently referred as a parameter of comparison while for solid dielectrics, their electrical properties are summarised by indicating the value of relative permittivity. The physical meanings of these two terms are clarified. In the same section, it was showed that under certain conditions solid dielectrics have a double role, acting as an electron sink and/or source. This characteristic seems reasonable to be considered when relevant experiments are performed.

Under strongly non-uniform electric field conditions, the withstand to breakdown of the 30/70 % CF_3I/CO_2 mixture is superior to the atmospheric gases of technical air, N_2 and CO_2 which is reasonable considering the high content of the strongly attaching CF_3I compound. A similar trend is observed in the electric performance against partial discharge activity in needle-plane electrode configurations under AC voltage application. At atmospheric pressure level $(0.1\,\mathrm{MPa})$ the PDIVs of the atmospheric gases follow the trend $\mathrm{PDIV}_{\mathrm{CO}_2} > \mathrm{PDIV}_{\mathrm{Tech.\ Air}} > \mathrm{PDIV}_{\mathrm{N}_2}$. The presence of a dielectric as part of the test object supports the propagation of streamer discharges along the surface of the solid dielectric primarily because of its contribution to the photoionisation process. Solids of higher relative permittivity seem to be more keen to accumulate charge on their surface which affects electric field and ultimately the propagation of the streamers. PDIV measurements also showed that the PD inception is inversely proportional to the relative permittivity of the material.

Imaging techniques that have been reported in the bibliography for capturing of surface discharge activity show advantages over each other with all of them capable of providing interesting insights on the generated patterns of such phenomena. In this thesis the photographic method is adopted and a newly developed UV-intensified high-speed camera system is used. With that system, the light emitted from the discharge events is captured following triggering methods that also allow event-based capturing. The main advantage of the used photographic method over the other summarised methods is the flexibility that is offered in the configuration of the test object so that the capturing of images is made possible.

Chapter 3

Laboratory experimental set-up

3.1 Introduction

This chapter describes the laboratory experimental set-ups and the different pieces of equipment used during the test programmes developed in this research work. Information only on the used hardware will be presented here. Regardless of the scope of each experiment, every component is described separately in the different subsections. The aim of this chapter is to give an overview of the design techniques and choices made during these preparatory stages of the test programme, as many of the critical components used in these experiments are custom designed, manufactured and rated according to the relevant regulations and standards. Additional information on the hardware components used during testing is also provided in the relevant subsequent chapters where the complete test procedures, together with the outputs are presented.

3.2 Pressure vessel

Experimental set-ups utilised for compressed gaseous media applications, require the use of pressure chambers able to withstand pressure levels, much above the maximum operational pressure, with minimum or even no leakage rates over the experimental time scales. The required withstand level is described by the relevant standards [110], and is given by Equation (3.1)

$$P_{\mathrm{t}} = 1.43 \times P_{\mathrm{s}} \tag{3.1}$$

where P_{t} is the test pressure measured at the highest point of the vessel (applies mostly for hydrostatic tests) and P_{s} is the maximum allowable operational pressure of the vessel, effectively giving a safety margin of $43\,\%$.

For the purposes of this research investigation, a cylindrical stainless steel pressure vessel was manufactured with a maximum operating pressure limit of $10\,\text{bar}$ absolute. The effective volume height is of $500\,\text{mm}$ and the inner diameter is of $480\,\text{mm}$, resulting in a total volume of approximately $90.5\,\text{L}$. The entire assembly was designed using SOLIDWORKS®, and the final design is shown in Figure 3.1.

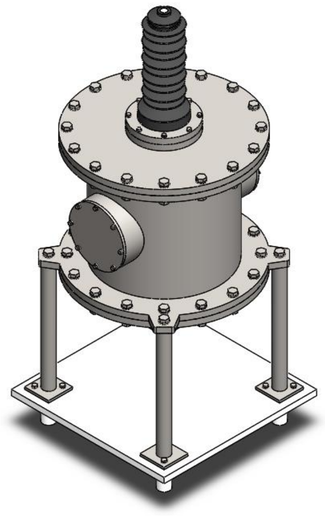

Figure 3.1: Pressure vessel assembly as designed in SOLIDWORKS®.

The main cylindrical pressure vessel body incorporates two side apertures of $200\,\text{mm}$ inner diameter each. In normal test procedures, these apertures are covered by circular blanking plates of $10\,\text{mm}$ thickness to prevent ambient light entering the main volume which is filled with the insulating gaseous medium. Also, four detachable legs made of 50.8 mm diameter round bars are used to support the main body. The flanged top and bottom of the vessel are of 684 mm outer diameter, matching the corresponding dimensions of a full-scale gas insulated line (GIL) elbow structure. In this way, it is possible to attach the vessel to a full-scale 400 kV gas insulated busbar and bushing assembly (Figure 3.2). This allows to perform tests at applied voltage levels much higher than the rating of the bushing shown in Figure 3.1.

Figure 3.2: Pressure vessel attached to the high-voltage 400 kV bushing. Picture taken at the Advanced High Voltage Engineering Research Centre (AHIVE), Cardiff University.

As it can be seen on Figure 3.1, on the top plate is attached the bushing through which the voltage is applied to the test object(s) installed inside the main volume. On the bottom plate, shown in Figure 3.2, the required feedthroughs are mounted. All the internal surfaces are dull polished ($R_\mathrm{a} \approx 1\ \mu$m average roughness) while the outer surfaces are sand blasted to remove any dirt or small sharp particles attached on the surface during the welding process. The welding points inside the volume are smoothed and cleaned to prevent the formation small gaps which can potentially trap dirt or solid residuals from tests over time.

Side apertures and top and bottom flanged areas incorporate appropriate grooves to house the necessary toroidal o-rings that provide a gas tight sealing of the volume. The necessary information for the right choice of the o-rings, and the appropriate design of the corresponding grooves, was retrieved from the relevant standards [111] and Research Report 485 of the Health and Safety Executive [112].

An example of a groove design is shown in Figure 3.3. In this example, the case of a toroidal o-ring with a cross-section diameter of 3 mm is described. The height of the groove was chosen to be $85\,\%$ of the o-ring diameter i.e., $2.55\,\mathrm{mm}$, as implied by [111, 112]. The reason for this choice is that high compression of the o-ring will result to a large deformation of the shape of the elastomer which can potentially become permanent affecting its sealing performance over a long time period. Another condition that is also harmful for the sealing system is the fast decompression of the volume which needs to be taken into account even if all the necessary precautions are in place to prevent such an event to taking place. When compressed, the o-ring shall be able to fill $90\,\%$ of the groove. In such a case it is ensured that, under any circumstances, the sealing system will not move outside the groove and the vertical and horizontal forces on the elastomer will be well balanced. All the edges are rounded to prevent sharp points that might damage the elastomer. It is worth noting that cracks usually initiate from the centre of the elastomer and move towards the outside surface. In such scenarios, the damage might not be easily detectable by visual inspection. However, the sealing performance is greatly affected. This is an important consideration especially for cases where the vessel volume is filled with environmentally harmful and/or chemically hazardous compounds.

The choice of appropriate materials for the sealing system was conducted based on the chemical compatibility databases provided by the relevant elastomer manufacturers. The most common materials are nitrile-butadiene rubber (NBR), ethylene propylene

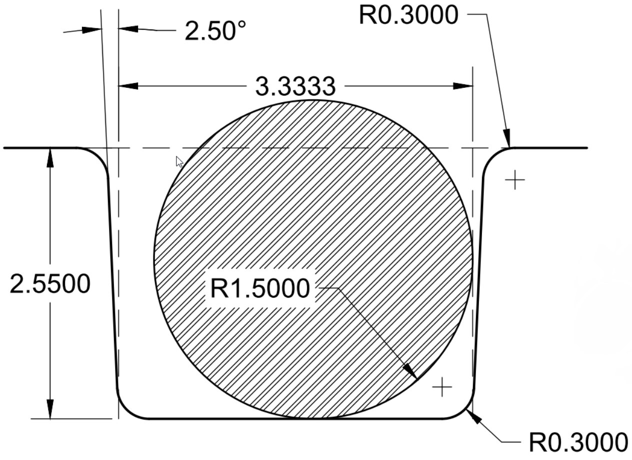

Figure 3.3: Seal groove designed based on the dimensions of the chosen toroidal o-ring. Here, the elastomer o-ring is assumed to have a cross-section diameter of 3 mm.

diene monomer (EPDM), fluorocarbon-based fluoroelastomer (FKM), perfluoroelastomer (FFKM), isobutylene-isoprene rubber (IIR) and many others with varying characteristics and applicability. It is important to mention that the compatibility of each elastomer with each gaseous compound, especially the synthetic fluorinated insulating gases, shall be carefully assessed as the complexity of the involved molecules requires attention. Especially for industrial applications where service lifetime is of high importance and the environmental impact is of a large scale, extensive studies and evaluations need to be delivered to assess performance.

3.3 Bushing

The main role of a bushing is to carry a live/charged conductor through an earthed barrier, for instance a metal enclosure or a wall [113]. Depending on the rating of each bushing, it should be able to provide electrical insulation for the rated voltage and for service overvoltage as these are specified in [114].

As can be seen from Figure 3.1, the bushing is mounted concentrically to the main cylindrical volume on the centre of the top plate. It is made of silicon rubber with a copper central conductor. Figure 3.4 shows a picture of the actual bushing used in this work.

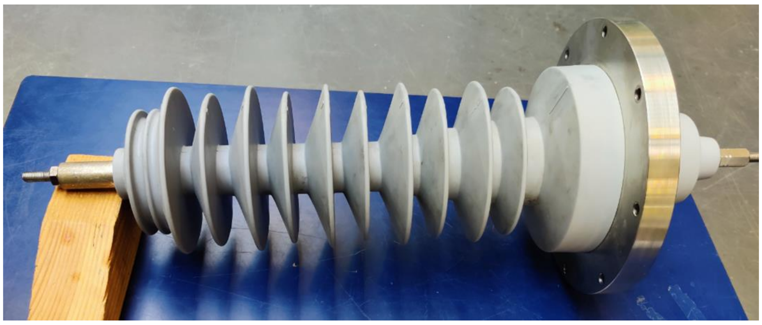

Figure 3.4: 38 kV rms bushing.

Through the central conductor the applied voltage is safely transferred to the test object preventing the occurrence of flashover events close to the earthed enclosure. At the bottom end of the conductor, an M10 threaded hole is made to steadily mount different electrode and/or test arrangements. The rated values of the bushing are summarised in Table 3.1.

Table 3.1: 38 kV rms bushing ratings.

AC operational	38 kV rms
AC dry at power frequency	70 kV rms for 1 minute
Partial discharge	$<$ 10 pC at 24.5 kV
Basic lightning impulse	170 kV peak

3.4 Fittings

The pressure vessel assembly described in the previous sections is equipped with a number of fittings, with their main role to safely provide all the required connections to a wide range of experimental set-ups. All installed parts are rated for use at pressure levels above 10 bar absolute and are further pressure tested as part of the entire assembly and according to the relevant regulations as these were described previously in Section 3.2. The list of available fittings is:

- One electrically isolated single electrode made of stainless steel and rated to carry continuously current of 15 A. This is useful when breakdown/flashover test arrangements are studied.
- One coaxial, SMA type, isolated shield feedthrough, having a $50\,\Omega$ characteristic impedance and rated up to 18 GHz frequency response for experimental set-ups that require high frequency measurements.
- One ultraviolet (UV) rated $(200 - 2500\,\mathrm{nm})$ optical feedthrough for $200\,\mu\mathrm{m}$ diameter core optical fibre cables, suitable for ultraviolet-visible-near infrared (UV-VIS-NIR) light transmission.
- One octa-pin electrically isolated feedthrough, rated at 350 VDC, 5 A and $\sim$ 15 bar absolute for connecting equipment that requires low voltage power supply.
- One T-type thermocouple for continuous monitoring of temperature levels inside the vessel volume
- One analogue, bourdon tube pressure gauge, rated from -1 to 20 bar gauge, for continuous and uninterrupted monitoring of the pressure levels inside the vessel volume.
- One high pressure rated stainless steel ball-valve with an ISO 7241-1 Series B plug attached for gas injection and recovery.
- One high pressure rated stainless steel ball-valve with a DN8 plug for gas injection and recovery.
- One proportional relief valve preset at 11 bar absolute.

All the feedthroughs are made of stainless steel of grades either 304, 304L, 316 or 316L, similar materials as that of the pressure vessel enclosure. Lock-thread adhesive was used for the connection joints during installation of the feedthroughs to minimise the risk of gas leakages.

3.5 Viewports

Optical viewports are frequently used in many applications and in experimental arrangements where sub-atmospheric and atmospheric pressure levels are considered. For such cases, there are many options available in the market which fall within the vacuum rated range of products. It is rather challenging finding appropriately rated viewports for high pressure applications, which are suitable for mounting speciality optical elements. For this reason, two custom-designed side viewports were manufactured and assembled and each viewport was pressure tested for operational pressures up to 10 bar absolute in order to meet the ratings of the entire vessel assembly.

Figure 3.5 shows the basic parts of the side viewport design. The first, and largest, part is the main plate of 25 mm thickness and 250 mm diameter on which the groove is made for the housing of the toroidal o-ring, following the principle shown in Figure 3.3. An FKM (Viton®) o-ring is placed inside the groove for sealing purposes. An optical element with an overall diameter of 100 mm and an effective diameter of 80 mm is placed in contact with the o-ring. A PTFE gasket is placed on top of the outer surface of the optical element to prevent direct contact with the metal circular cover. All the parts are tightened together gradually using a wrench of adjustable torque. It is important that all the holding bolts are tightened at the same level so that the FKM o-ring seals uniformly against the contact surface and avoid any excessive stress at any point of the optical element surface that can potentially damage the glass material.

The overall pressure withstand level of the assembly of Figure 3.5 is defined by the withstand level of the optical element. These levels can be calculated in advance, with a safety margin maintained to ensure that the final result will meet the requirements of its initial purpose. The equation through which the thickness of a circular window can be calculated is Equation (3.2) [115]

$$T_{\mathrm{wind.}} = D \cdot \sqrt{\frac{SF \cdot K \cdot P}{4 \cdot F_{\mathrm{a}}}} \tag{3.2}$$

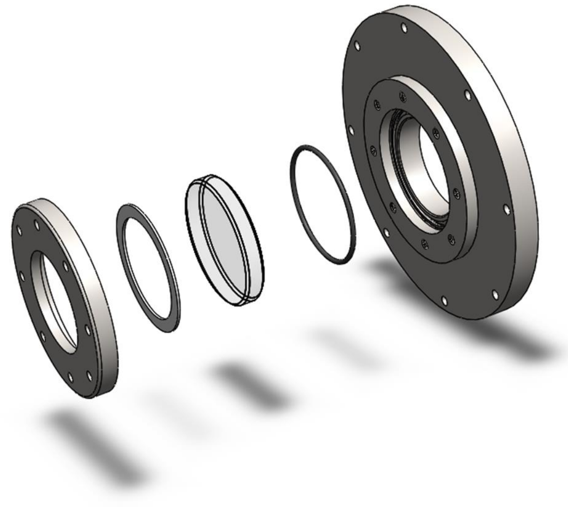

Figure 3.5: Exposure view of side viewport as this was designed in SOLIDWORKS®.

where K is an empirical constant which depends on the method of support of the window i.e., for clamped $K = 0.75$ and for unclamped $K = 1.125$ (see Figure 3.6), F_{a} is the apparent elastic limit or rupture modulus of the window material in MPa, P in MPa is the pressure that the window is subjected to and SF is the safety factor which expresses the number of times less than the apparent elastic limit the maximum stress shall be. According to feedback from manufacturers of optical elements, the value that covers 99 % of the applications is $SF = 4$.

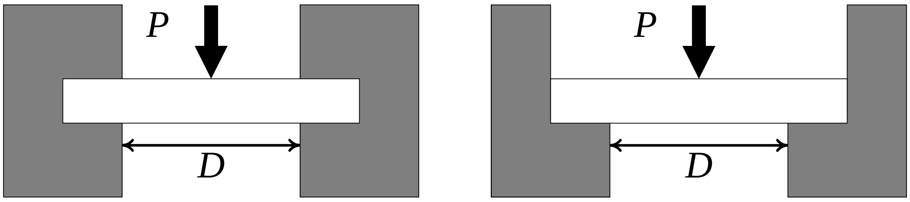

(a) Clamped **(b)** Unclamped

Figure 3.6: Clamped and unclamped circular glass window mounting [115].

Optical glass materials that will be discussed later are calcium fluoride (CaF_2) and acrylic (PMMA). The rupture modulus for these two is 36.54 MPa for CaF_2 and 60 −

70 MPa for PMMA. Considering a minimum safety factor of $SF = 4$ and an effective diameter of $D = 80$ mm, the calculated window thicknesses for the applied pressure range is shown in Figure 3.7. The subjected pressure, as this is shown in Figure 3.6, corresponds to the pressure differential between the high- and low-pressure sides.

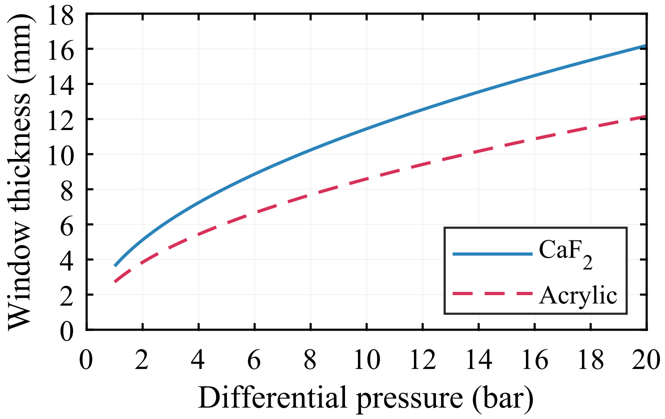

Figure 3.7: Window thickness over subjected differential pressure (Equation (3.2)).

For a pressure system rated up to 10 bar absolute a calcium fluoride window of approximately 12 mm thickness will be required while, for acrylic, a 9 mm thick window will also be sufficient. For the purposes of the utilised system, windows of 15 mm thickness and effective diameter of 80 mm each, made from both materials, were used.

3.6 Properties of optical materials

The choice of the appropriate optical element, depending on the requirements of each test procedure, is of significant importance. There is a wide range of choices available in the market with varying efficiencies and which are able to meet the necessary criteria of each experimental set-up. When the main purpose is to perform optical or photography studies, it is reasonable that the most important criterion for selecting the correct substance is the transmission efficiency within the light emission spectrum of interest.

For studies involving infrared (IR) light emission, such as recording with thermal IR cameras, substances such as silicon (Si), germanium (Ge), zinc selenide (ZnSe), potassium bromide (kBr) etc. are preferred. When studies involve ultraviolet (UV) light, then substances like sapphire, calcium fluoride (CaF_2), magnesium fluoride (MgF_2) and UV fused silica (UVFS) are more common. The transmission efficiency rates for some of the basic optical element materials are shown in Figure 3.8.

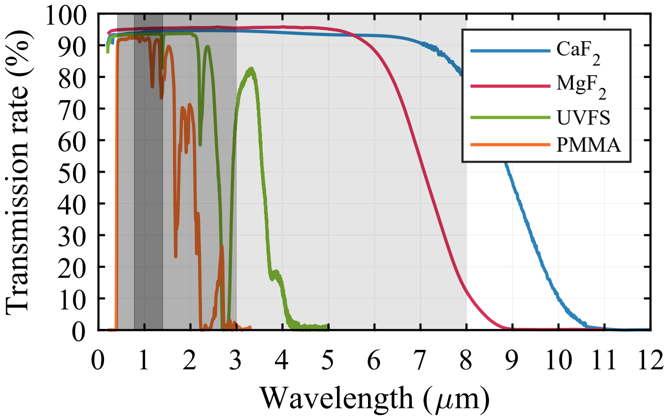

Figure 3.8: Transmission rate over wavelength for basic optical element materials. The shaded areas represent the visible (VIS), near-infrared (NIR), short-wave-infrared (SWIR) and mid-wave-infrared (MWIR) spectra of light in the same order they appear on the plot from left to right [116].

From Figure 3.8, it can be easily seen that calcium fluoride (CaF_2) has a very wide range of transmission starting from around 180 nm up to 8 μm, effectively covering middle-ultraviolet, near-ultraviolet, visible, near-infrared, short-wave-infrared and mid-wave-infrared spectra. It is, thus, suitable for studies that involve UV light and for applications where recording with thermal cameras is required. Acrylic seems to be a very good and affordable choice when transmission of visible (VIS) light is required, such as recording of breakdown and/or flashover arcs which are very luminous. The transmission rate of PMMA in the $400 - 700$ nm spectrum is $\sim 92\,\%$ whereas, for substances like CaF_2, the effective range transmission rate can reach values up to $95\,\%$. Another option could be the use of polycarbonate (PC), which is even better than acrylic from a mechanical performance perspective since its elastic limit is on average around 115 MPa. However, its transmission rate is around $80\,\%$. It is also known the ability of polycarbonate (PC) to block light transmission below 400 nm which effectively corresponds to the entire UV spectrum. The transmission rates and ranges of window materials and substances need to be well specified and taken into consideration during the design of the test arrangement. It is recommended to prevent ambient UV light from entering the volume where the gaseous insulation is tested, especially when gaseous compounds very sensitive to UV radiation are used such as CF_3I.

3.7 Gas injection and extraction system

As described in Section 3.4, gas injection inside the pressure vessel volume is performed through one of the available fittings (ISO 7241-1 Series B or DN8) installed on the vessel. Atmospheric gases namely, technical air (21/79 % O_2/N_2), nitrogen (N_2) and carbon dioxide (CO_2), are supplied compressed from Brin's Oxygen Company Ltd (BOC Ltd) in 50 L cylinders (Figure 3.9). In the outlet of each gas cylinder, a two-stage regulator is installed for the control of the gas flow. Prior to the gas injection, the pressure vessel volume is vacuumed down to < 1 mbar using a vacuum pump. Once the required vacuum levels are reached, the vacuuming process continues for 30 additional minutes in order to minimise the presence of humidity residuals. Before the start of the vacuuming and the gas filling processes, the pressure vessel is opened and cleaned extensively with isopropyl alcohol. A time gap of 1 hour between the cleaning process and vacuuming is maintained to ensure that the alcohol has been fully vaporised.

The same preparatory work, as described in the previous paragraph, is followed also for the case when CF_3I/CO_2 gas mixtures are about to be injected. However, the gas circulation process needs to be performed in a closed loop to ensure that no gas leakage will take place. Figure 3.10 shows a basic diagram of the gas circulation process followed when the gas mixture is prepared within the volume of the pressure vessel. For example, when a test requires the investigation of 30/70 % CF_3I/CO_2 gas mixture at 1 bar, CF_3I will be injected first up to 0.3 bar and then it will be balanced with 0.7 bar of CO_2. A minimum settle time is required for the mixture compounds to

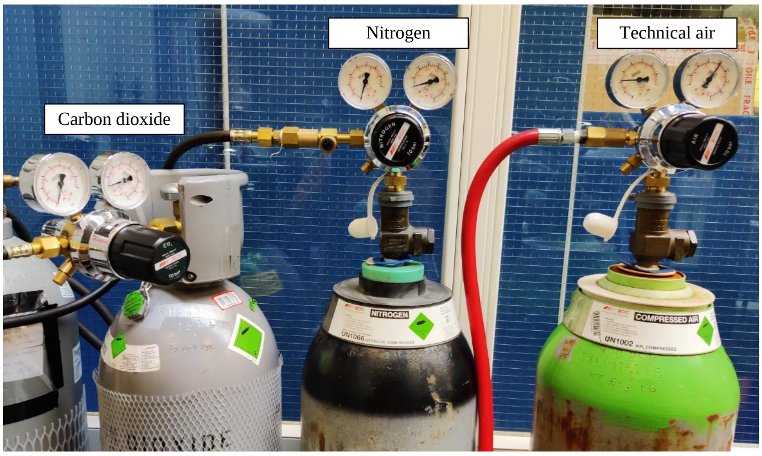

Figure 3.9: Gas cylinders containing atmospheric gases.

diffuse.

At the end of the series of tests, a certified gas recovery system is connected to the vessel together with a gas cylinder where the used CF_3I/CO_2 mixture is stored (Figure 3.11). The condition of the used gas mixture is analysed after each test series and appropriate labelling rules and markings are followed for the storage cylinder.

3.8 Generation of test voltages

In laboratory-based fully controlled high-voltage experiments there are three basic voltage waveforms, and their variations, that can be applied to a test object:

1. DC voltage
    (a) Positive polarity
    (b) Negative polarity
2. AC voltage
    (a) Power frequency $(50/60\,\mathrm{Hz})$
    (b) Variable frequency and waveshape
3. Impulse voltage
    (a) Lightning impulse $(1.2/50\,\mu\mathrm{s})$
        i. Positive polarity

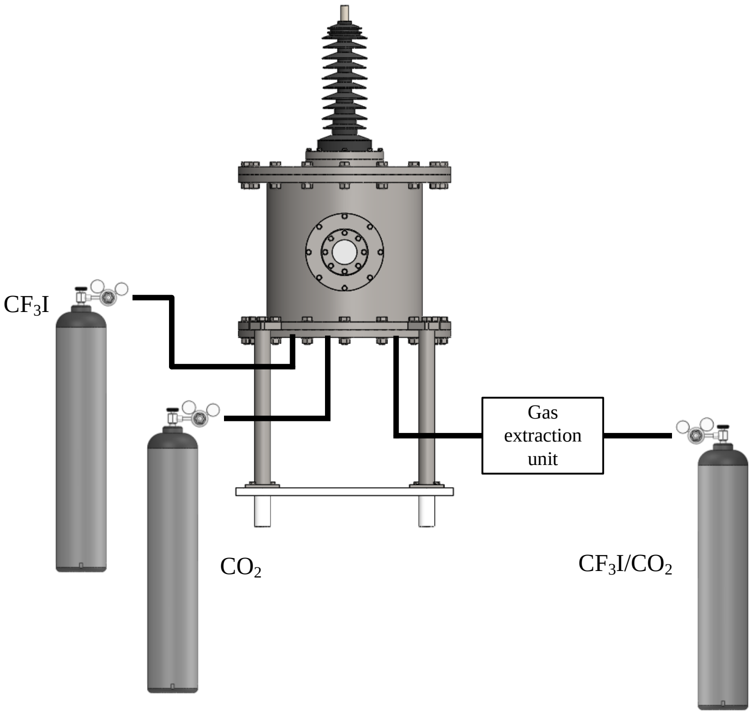

Figure 3.10: Basic diagram representing gas circulation.

    ii. Negative polarity
  (b) Switching impulse $(250/2500\,\mu\text{s})$
    i. Positive polarity
    ii. Negative polarity

In the above list, the generation of very fast voltage transients in an attempt to replicate very fast transient overvoltage (VFTO) conditions could be added. In practical situations, this kind of overvoltage frequently appears in gas insulated switchgear (GIS) during disconnector switch operation and is characterised by short duration and of a dominant frequency component of around $100\,\text{MHz}$ [117].

For each kind of waveform, there is a number of shape and magnitude specifications that need to be met and which are described in detail in the relevant standard [20]. For tests with direct voltage (DC), the ripple factor of the voltage applied to the test object should not exceed $3\,\%$. For short duration tests $(\leq 60\,\text{s})$, the measured values of the test voltage shall be within $1\,\%$ of the required level while, for longer test durations

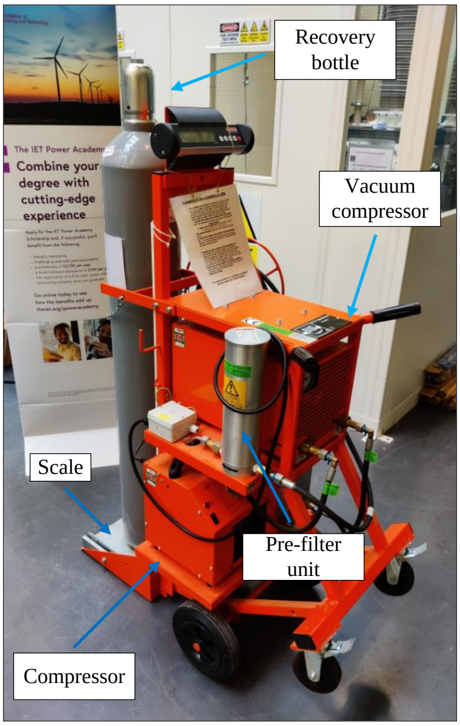

Figure 3.11: DILO mini-series service cart.

$(> 60\,\mathrm{s})$, the voltage should be maintained within $\pm 3\,\%$ throughout the test.

For tests with power frequency $(50\,\mathrm{Hz})$ alternating voltage (AC), the frequency of the sinusoid waveform needs to be maintained in the range of $45 - 65$ Hz. The difference between positive and negative peak values shall not exceed $2\,\%$ and the ratio of peak to rms shall equal $\sqrt{2} \pm 5\,\%$. The same tolerances, relevant to the duration of the test as for the case of DC, apply also here. Tests with lightning impulse $(1.2/50\,\mu\mathrm{s})$ waveforms also require basic tolerances to be satisfied [20] for both polarities and with regards to the quality of the generated waveform, such as:

- Test voltage: $\pm 3\,\%$
- Front time: $\pm 30\,\%$
- Time to half-value: $\pm 20\,\%$

For switching impulse $(250/2500\,\mu\mathrm{s})$ waveforms, the corresponding tolerances are:

- Test voltage: ±3 %
- Front time: ±20 %
- Time to half-value: ±60 %

Figure 3.12 shows an example of recorded AC waveform. For this case, the required test voltage was 32 kV rms. The recorded rms voltage was $\sim$ 31.73 kV, $\sim$ 0.85 % lower than required value. The period of the signal was measured at $\sim$ 19.95 ms indicating a sinusoidal waveform of $\sim$ 50.13 Hz frequency. The positive peak value was measured at 45.02 kV, meaning that the ratio between rms and peak value is $\sqrt{2} \pm 0.33\,\%$. The negative peak value was measured at $\sim$ 44.87 kV indicating a percentage difference between the absolute values of the positive and negative peaks also at 0.33 %. According to the requirements listed on the relevant standards [20], and the recorded values extracted from Figure 3.12, the AC applied waveform meets all the required qualities.

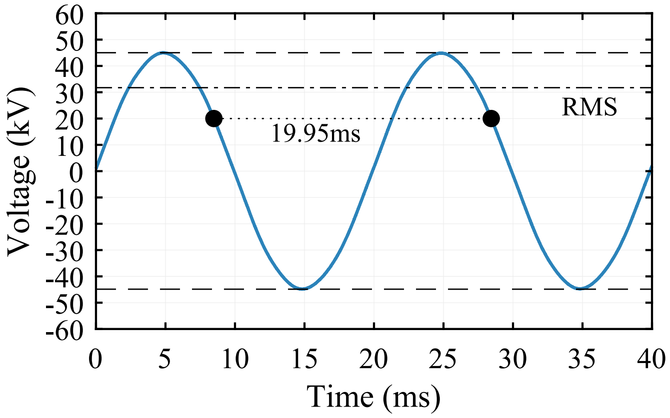

Figure 3.12: Example of generated AC waveform.

Generation of power frequency alternating (AC) high-voltage was performed with the use of a 50 kV/3.75 kVA transformer. The low voltage supply to the primary of the transformer is controlled through a variable autotransformer with a percentage scale of 0 – 100 %. Between the autotransformer and the primary of the test transformer, an LC low-pass filter arrangement is connected to maintain the sufficient quality of the supplied 50 Hz sinusoid waveform. The experimental arrangement is isolated from the low-voltage (LV) supply side with the use of an isolation transformer connected between the autotransformer and the LC filter input.

The applied voltage is scaled down to safe measurable levels with the use of an RCR voltage divider of ratio $3750 : 1$ and rated at 50 kV AC rms. Sensing of the generated current signals will be explored extensively in Section 3.9.3.1 of the same chapter. Recording of the relevant voltage and current signals is performed using digital storage oscilloscopes (DSO). Later, the use of DSOs and how they are incorporated more actively in the experimental and measuring set-up will be described in detail. Each of the components of the experimental set-up that were described before are shown in Figure 3.13 in the sequence of their actual connection.

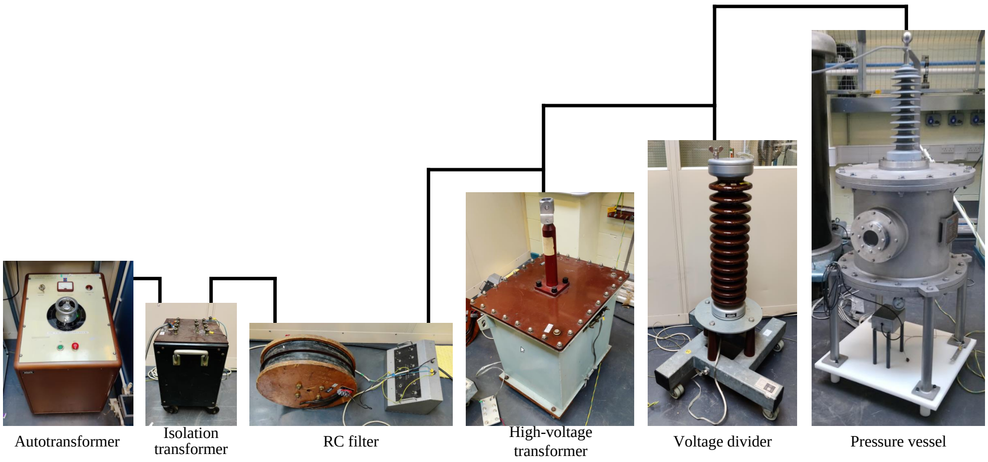

Figure 3.13: Components of the AC experimental set-up.

Figure 3.14 shows the full experimental set-up assembled right before testing. The entire set-up is placed inside a test cage equipped with a three-level interlock system to prevent access of personnel when the equipment is energised.

3.9 Experimental techniques

For the case of alternating (AC) voltages, the quality requirements for the sinusoidal generated waveform at power frequency ($50/60$ Hz) were detailed given in Section 3.8.

Figure 3.14: Experimental set-up ready for testing.

The different test procedures are clearly described in the relevant standards [20]. However, depending on the subject of each study, their variations or totally different procedures may be implemented. Often, alternating voltage refers to sinusoid waveforms of $50/60\,\mathrm{Hz}$ frequency. However, if the definition is expanded then it could refer to a voltage waveform that reverses its polarity within the duration of one full period cycle resulting into two mirror half-cycles. With that in mind, alternating voltages and their impact on different cases under test can be examined by different means, such as:

- Different frequency/period
- Different waveshape (sinusoid, square, triangular, sawtooth etc.)
- Duration of the voltage application, usually expressed in multiples of the period
- Different rms or amplitude levels, and more

From a practical standpoint, sinusoidal alternating voltages at power frequency $(50/60\,\mathrm{Hz})$ have the main benefit that are of high practical interest since they are used in actual applications in transmission and distribution power systems. From a physics perspective, the voltage magnitude during a sinusoid of $50/60$ Hz frequency varies relatively slowly which gives the opportunity to the observer to draw more distinct conclusions regarding the movement of charges during the time duration of a full AC-cycle. For cases where solid insulators are part of the experimental investigation, then the background physics get even more complex compared to the cases where only gaseous insulation is under study. The test procedures, as these are described in the standards, were used as the main process of implementing the experiments of the presented research work. Two basic test procedures were followed [20].

(i). *Withstand voltage tests*: where no disruptive discharges are allowed
(ii). *Disruptive-discharge voltage tests*: including breakdown and flashover tests

3.9.1 Withstand voltage tests

Withstand voltage tests are usually of short duration, maximum 60 s, and are performed in order to specify if the test object/arrangement under test is able to withstand the required test voltage level. When testing specific devices, as part of an overall dielectric performance assessment, it is highly recommended that also the corresponding active standards are carefully examined before proceeding with the test procedure.

The voltage applied to the test object needs to be increased gradually starting from a sufficiently low value in order to prevent any impact of switching transients during energisation. The increase rate is suggested to be 2 % of the required test voltage level per second when the applied voltage has exceeded 75 % of this level. Instructions on how the voltage shall be applied from 0 to 75 % are not clear. When the required test voltage levels are reached, then it shall be maintained at this level for the required duration and then gradually be decreased to 0 V and not suddenly interrupted as this may generate switching transients which can damage the test object or distort the results. Figure 3.15 shows an example of an AC voltage test where the required test voltage level was 25 kV rms. For this specific case, the applied voltage increase rate was maintained at 2 % per second from 0 to 25 kV, effectively producing a ramp of 50 s duration.

The test voltage was maintained for 10 s as, in this case, this duration was sufficient for the desired recording/observation. As the entire recording was performed using a data acquisition card, the closure time was not recorded in order to keep the exported recording file within a manageable size. Such tests are frequently referred to as AC ramp tests mainly because of the ramp increase that appears from $0 - 50$ s. It is very important to monitor the applied voltage during the entire test duration to ensure that the quality (see Figure 3.12) of the generated AC sinusoidal waveform is well maintained.

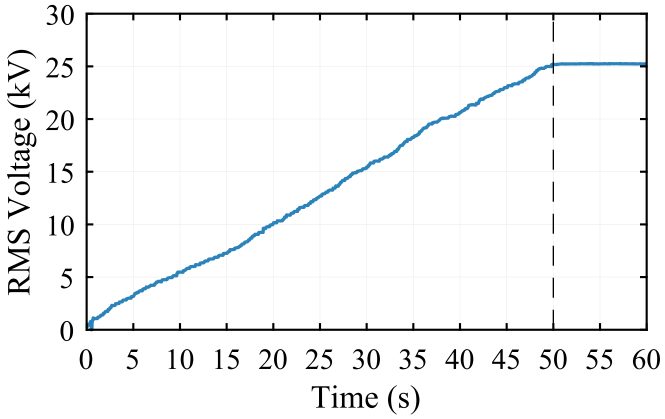

Figure 3.15: Example of AC withstand ramp test.

The procedure described in the previous paragraph for the voltage application was adopted in the experimental investigation of this research work. The time duration that the required test voltage was maintained varied depending on the time needed to perform the acquisition of the necessary data. The time between consecutive tests was maintained at 2 min unless otherwise specified.

3.9.2 Disruptive discharge tests

The main process for the disruptive discharge tests is the same as the withstand tests although there is no specific test voltage that needs to be reached. The applied voltage is again increased gradually, this time until a disruptive discharge, gas gap breakdown or flashover, occurs. Figure 3.16 shows an example of a disruptive discharge. As it can be seen, when the insulation withstand is no longer sufficient the voltage falls to zero while at the same time the current magnitude increases.

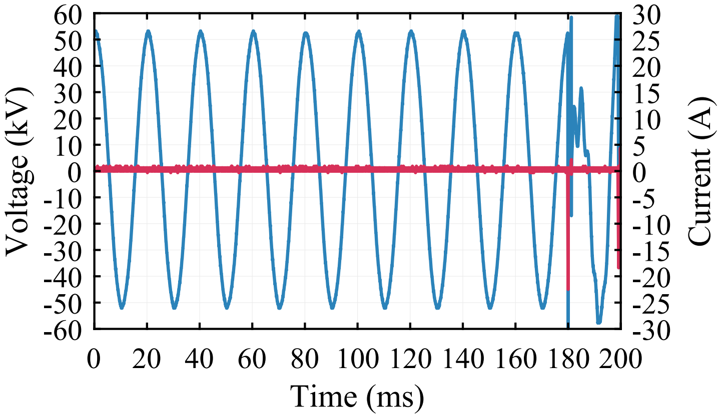

Figure 3.16: Example of disruptive discharge recording.

The rms value of the voltage waveform, as this was measured right before the time instant where the disruptive discharge appears, is recorded as the disruptive discharge voltage level for this particular test run. For the case of Figure 3.16, the disruptive discharge is specified to be 36.87 kV rms. Several test attempts need to be performed to ensure that there is a statistical convergence in the measured disruptive discharge voltage levels. The number of the test attempts may vary depending on the impact this kind of discharges may have on the condition of the test object after it was exposed to such elevated stress conditions. It is common that the average of all the recorded values is calculated together with the corresponding standard deviation, as shown in Equations (3.3) and (3.4):

$$U_{\mathrm{bd}} = \left(\sum_{i=1}^{k} U_{\mathrm{i}} \right) / k \tag{3.3}$$

$$s_{\mathrm{bd}} = \sqrt{\frac{1}{k-1} \sum_{i=1}^{k} |U_{\mathrm{i}} - U_{\mathrm{bd}}|^2} \tag{3.4}$$

where U_{bd} is the calculated average value of the recorded disruptive discharge voltages, U_{i} the disruptive discharge voltage values recorded in each test attempt, k the total number of test attempts, and s_{bd} the calculated standard deviation assuming a normal distribution.

3.9.3 Partial discharges

As was described in a Section 2.4.2.1, the term of partial discharges (PD) covers discharges that do not bridge electrically an energised conductor with another at ground potential. The definition given in [88] describes partial discharges as localised electrical discharges that do not bridge the insulation between conductors and which can or cannot occur near a conductor. The main reason of partial discharge occurrence is the high electric field stress that appears locally within the insulation. Some areas where elevated electric field magnitudes may appear are the triple junctions, the interfaces where metal conductor and solid and gaseous insulation meet. Partial discharges usually appear as pulses of short duration of $< 1\,\mu$s, or even less, and their appearance can be an indicator of the insulation efficiency within the compartments of a device and/or the design quality of the device itself.

The detection of partial discharges is a rather challenging process and differs based on the conditions where this detection is performed. In laboratory-based, fully controlled experiments, study of partial discharge phenomena can be more focused and case-oriented compared to actual power devices located in substations. However, very advanced equipment and industrial type devices are available for on-site measurements and continuous monitoring. It is vital, and required, for every device currently in operation in transmission and distribution networks to be assessed for partial discharge and provide easy connections for continuous monitoring systems.

3.9.3.1 Laboratory-based measuring circuits

The two measuring circuits described previously in Section 2.4.2.2 are considered basic not in terms of complexity, but because they are implemented with most of the commercial measuring systems and, also, they are used as a reference for implementing their variations. Next, two different methods of sensing current pulses in the MHz range are compared, which is considered to be of practical interest for the detection of partial discharge in gaseous insulation experiments. These methods were adopted for the implementation of partial discharge detection in the experimental part of this research work.

3.9.3.1.1 High frequency current transformer (HFCT)

The operating principle of current transformers is based on Faraday's law of induction. Its primary conductor consists of only one turn while its secondary from multiple turns terminated with a sensing resistor [118]. The current that flows though the primary conductor induces a magnetic field in the core which, in turn, will induce a current to the secondary winding. The operating concept is the same from small PCB surface-mounted current transformers up to large scale devices that are used in substations to drive the protection systems. For the latter, the input current and power ratings are reasonably high, and the range of available device options is much wider in lower power applications.

Wide bandwidth devices are also available and which are suitable for the detection of partial discharges, with cut-off frequencies up to several MHz or even to the GHz range. The volt to ampere sensitivity (V/A ratio of the output) varies from 0.01 up to values greater than 1. The current rating also differs between different versions, and there is a common trend that devices of high V/A ratio and bandwidth have a low current rating and vice versa. One of the main disadvantages of current transformers is their inability to sense direct currents (DC) or currents of very low frequency component. On the other hand, their main advantage is the electrical isolation they offer since they are not in direct contact with any of the energised components.

For the purposes of the presented research project, for part of the experiments a high frequency current transformer (HFCT) manufactured by Magnelab Inc. was used [9]. The rating characteristics of the employed device are summarised in Table 3.2.

In order to avoid any possible attenuation or distortion of the generated pulses,

Table 3.2: Magnelab HFCT rating values.

Model name	CT-F5.0
Output V/A in 1 MΩ termination	5.0
Output V/A in 50 Ω termination	2.5
Max rms current (AC)	2 A
Max peak current	200 A
Droop	$3\,(\%/us)$
Minimum rise time	0.875 ns
Max $I \cdot t$ in 50 Ω termination	$0.0002\,\mathrm{A} \cdot \mathrm{s}$
Low cut-off frequency $(-3\,\mathrm{dB})$	4800 Hz
Upper cut-off frequency $(-3\,\mathrm{dB})$	400 MHz

it was considered important to find a safe passage for the generated current to exit the stainless-steel pressure vessel and pass through the current transformer aperture undistorted. For this purpose, the coaxial SMA feedthrough installed on the pressure vessel was used. The high frequency current transformer (HFCT) was placed inside an EMI/RFI shielded aluminium enclosure, with two SMA connectors mounted on the top and bottom of a C101 alloy copper rod. The diameter of the rod was calculated based on the 50 Ω coaxial characteristic impedance principle using Equation (3.5)

$$Z_0 = \frac{138}{\sqrt{\varepsilon_{\text{air}}}} \log\left(\frac{d_1}{d_2}\right) \qquad [\Omega] \tag{3.5}$$

where Z_0 is the characteristic impedance, d_1 the diameter of the HFCT aperture $(50.8\,\mathrm{mm})$, d_2 the diameter of the copper conductor rod and ε_{air} the relative permittivity of atmospheric air. The HFCT was held steady, with the copper rod centred in its aperture by two 3D printed plastic parts, made of polylactic acid (PLA). An illustration of the described enclosure configuration is shown in Figure 3.17. Similar implementations have been presented in published work related to the characterization of such HFCT sensors [119, 120].

The scattering parameters (S-parameters) of the configuration were needed to be measured to ensure the transmission efficiency of the set-up. For such an evaluation,

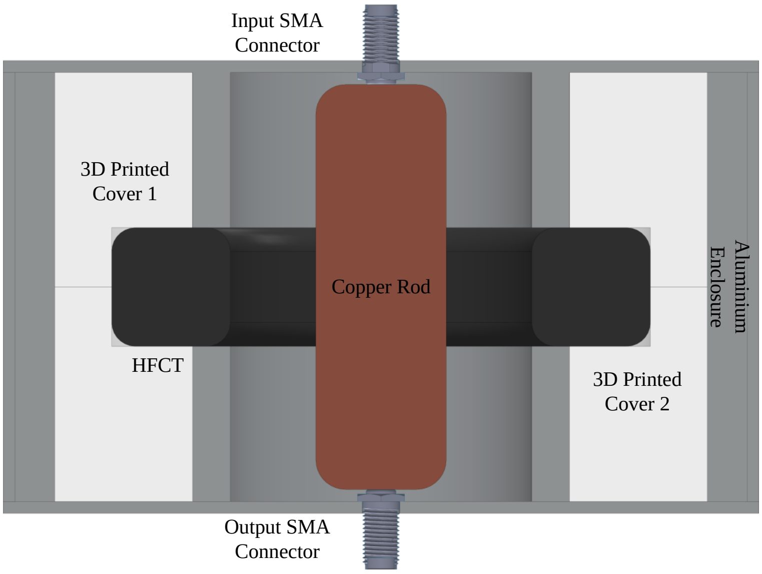

Figure 3.17: Illustration of the HFCT enclosure configuration [9].

a Rohde & Schwarz R&S® ZVL Vector Network Analyzer, 9 kHz – 6 GHz, was used. Prior to the measurement, the VNA device was calibrated using the relevant calibration kit, consisting of a 50 Ω load termination, provided by the manufacturer. For the measurement of the S-parameters, the coaxial cables and the vessel feedthrough, which were used in the set-up, were also included in the circuit under measurement. Figure 3.18 shows the set-up the day the measurement was performed.

Figure 3.19 shows the measured S-parameters. The frequency range up to 400 MHz corresponds to the rated upper cut-off frequency of the HFCT, as this was described in Table 3.2.

In case of an efficient circuit, the S_{12} and S_{21} parameters are required to be as close to 0 dB as possible indicating that the signal leaving Port 1 is properly transmitted to Port 2 of the VNA, with minimum attenuation. When S_{12} and S_{21} are close to 0 dB, then S_{11} and S_{22} are of high absolute values ($S_{11}\&S_{22} < 0$), effectively indicating that no proportion of the signal leaving one of the ports will be reflected back to it.

The upper cut-off frequency, at -3 dB attenuation, was identified at 359.46 MHz, a value quite close to the upper cut-off limit of the HFCT. The above measurements constitute a good indicator that the entire HFCT configuration will have a capability of

Figure 3.18: Measuring of the S-parameters for the entire current sensing circuit.

sensing current pulses of rise times down to $\sim 1\,\text{ns}$, according to Equation (2.14).

3.9.3.1.2 Shunt resistor

The use of a shunt resistor for current sensing is possibly the simplest approach both with regards to the operating principle and the convenience of installation. Such an implementation is based on Ohm's law and practically measures the voltage drop across the resistor which is proportional to the value of the current flowing through it. A wide range of resistor types are available in the market. However, none of them is an "ideal resistor" meaning that it will not be a purely resistive load. This is an important factor when considering the frequency response of the current sensing circuit for which the resistor is part of.

A non-ideal resistor has a general circuit equivalent similar to the one of Figure 3.20 where L is the lead inductance, C is the parasitic capacitance, which is the combination of the lead and leakage capacitances, and R_c is the actual resistance of the component.

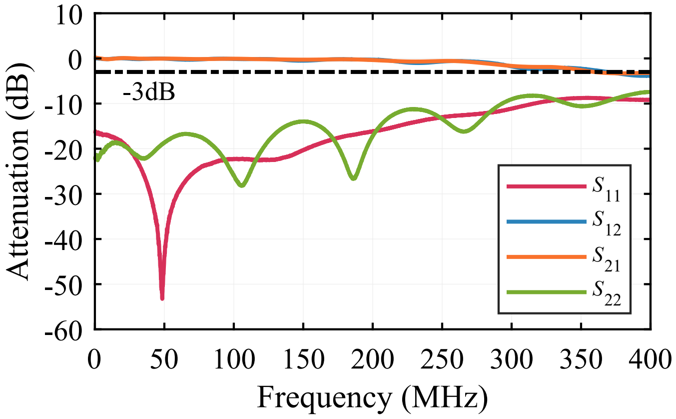

Figure 3.19: S-parameters as measured for the full circuit of Figure 3.18. The range of the frequency values shown correspond to the rated frequency response range of the HFCT.

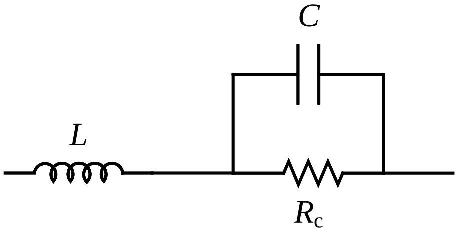

Figure 3.20: Non-ideal resistor equivalent circuit.

The impedance of the circuit in Figure 3.20 is expressed by Equation (3.6)

$$Z = \frac{j\omega L + R_c\left(1 - \omega^2 LC\right)}{j\omega R_c C + 1} \tag{3.6}$$

where ω is the angular frequency $(2\pi f_{\mathrm{AC}})$.

Some characteristic values for C and L for TO-style power film resistors are 7.3 nH and 0.6 pF. With that in mind, Equation (3.6) can be easily plotted over frequency or, even better, to be simulated using a SPICE software package as it is demonstrated in Figure 3.21.

Even the case described above is not fully representative of practical circuits. For example, in the case of a simple TO-style resistor, it will need a printed circuit board (PCB) to be mounted on and soldered or even connected with copper wires, all of

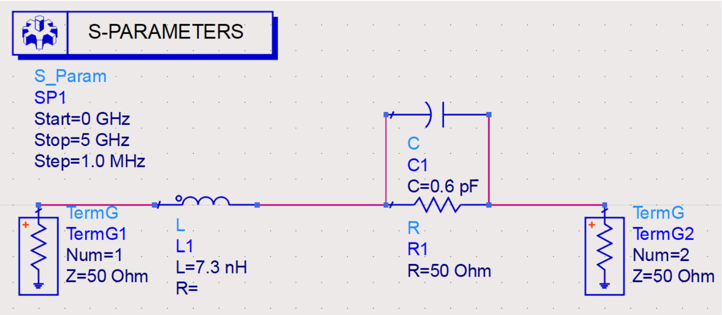

(a) Simulated circuit

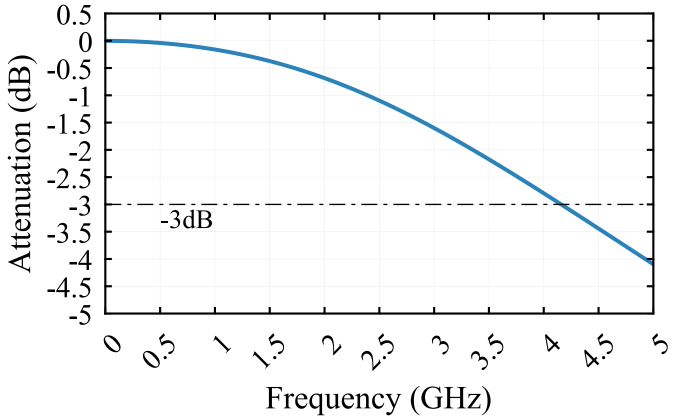

(b) S_{12} parameter

Figure 3.21: Simulation of the non-ideal resistor (Figure 3.20) using Keysight® ADS.

which will distort the measurements when the VNA will be used to measure the S-parameters. In this research work, the most efficient way to implement a resistor as a shunt component to the ground was found to be with the use of a coaxial $50\,\Omega$ load termination, as shown in Figure 4.25.

The induced current will flow through the central pin of the tee adaptor and through the $50\,\Omega$ resistor of the load termination. The second SMA jack connector will return the voltage across the load termination resistor. The higher the load termination bandwidth rating is, the wider the frequency response range of the overall current sensing system will be. Figure 3.23 shows the measured S-parameters of such an arrangement using the same approach as for the case of Figure 3.19.

The curves of Figure 3.23 are directly exported from the VNA device. The hor-

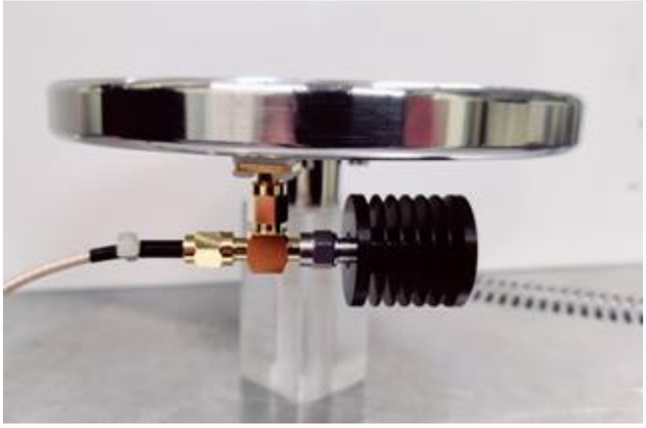

Figure 3.22: 50 Ω load termination connected as a shunt resistor.

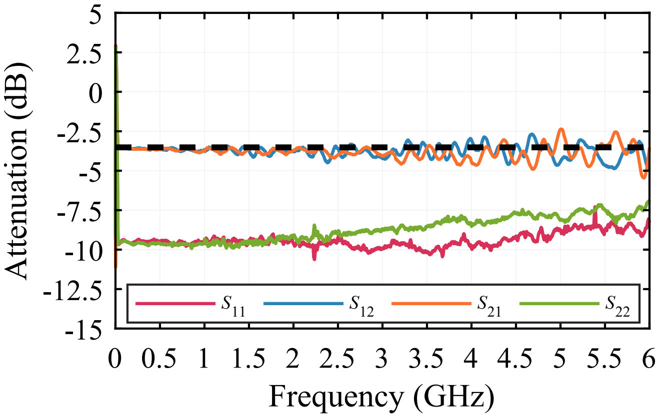

Figure 3.23: Frequency response of a coaxial 50 Ω load termination connected as a shunt resistor (ex. Figure 3.22).

izontal dashed line represents the -3.52 dB level. Considering the 50 Ω termination of the VNA device inputs and the connected sensing resistor, then the overall circuit corresponds to a 50 Ω matched tee implementation. It can be clearly seen that the frequency response is maintained at optimal levels for the range of $0 - 6$ GHz. It is very important that the load termination is of relatively high-power rating, since such components are vulnerable to permanent damage in case a disruptive discharge occurs. As the generated voltage signal will be directly connected to the measuring DSO device, it is required that a coaxial overvoltage protection component (coaxial gas discharge tubes (GDTs) are recommended), also of relatively high bandwidth, is used between the shunt resistor configuration and the DSO.

3.9.3.1.3 Comparison of the two methods

A short comparison summary of the two methods is presented in this section. Table 3.3 summarises the main differences between the two approaches.

Table 3.3: Basic differences between HFCT and shunt resistor current sensing techniques.

Function	**HFCT**	**Shunt resistor**
Electrical isolation	Yes	No
Able to detect DC currents	No	Yes
Output directly compatible with ADC devices	Yes (overvoltage protection is required)	Yes (overvoltage protection is required)
Frequency response	Up to hundreds of MHz	Up to GHz level
Amplification of sensed current	A typical maximum of $5\,\mathrm{V/A}$ ratio	$V/I = 50\,\Omega$
Operating principle	Faraday's law (inductive)	Ohm's law (resistive)

It could be added that, for the case of HFCTs, which usually are of high winding ratios, the parasitic capacitance is increased compared to shunt resistors, which reduces the measurement bandwidth and common mode noise rejection [118]. As was shown before, the installation and use of and HFCT is not always easy as it may require the use of a special configuration (Figure 3.17) to ensure that there is no distortion in the measured signal. HFCTs with a bandwidth in the GHz level are also available in the market, but they can be very costly.

Load terminations that are used as shunt resistors can present a hazard for the recording equipment in case a breakdown/flashover occurs in the test circuit. The voltage output signal is proportional to the current flowing through the resistor and, thus, in case of a disruptive discharge, the output voltage levels may exceed significantly the rated levels of the coaxial input of a DSO. In such cases, coaxial gas discharge tubes (GDTs) of low capacitance are recommended to be used, in line connected with the input of the DSO. High power rated and wide bandwidth, up to several GHz, load terminations can be very bulky and expensive.

3.10 Discussion and conclusions

This chapter describes in detail the equipment used during the experimental part of this research investigation. The information provided aims to highlight that the technical specifications of the employed equipment at every stage of the test process were carefully examined, well considered and addressed.

The pressure chamber is custom designed and built with main focus on the gas tightness performance in order to ensure a safe use and handling under pressurised conditions. The optical components are extensively described since they are of high importance when performing optical detection and photography experiments. The custom designed and built optical viewport is able to withstand differential pressure levels up to the rated operating pressure chamber where it is installed while the chosen optical element is able to transmit emitted light in a wide range of the light spectrum.

The necessary validations regarding the quality of the applied voltage waveforms are also performed. Prior to this, an extensive description of the necessary characteristics is provided based on the information retrieved from the relevant standards. It is shown that the alternating voltage waveshape meets all the necessary quality requirements under the specified tolerance levels. The procedures followed during the disruptive and partial discharge tests were also described.

In the next chapters, for the purposes of the partial discharge tests, two different current sensing methods will be reported, the HFCT and the shunt resistor. Both of them are extensively described in this chapter and all the necessary configurations and validation measurements are reported. The corresponding frequency response ranges are presented after being identified using a VNA device. It is shown that the HFCT is capable of sensing partial discharge transient pulses of approximately as low as of 1 ns while the shunt resistor technique can exceed that level. A comparison of these two methods is included which may be considered as a useful summary of the advantages and disadvantages of each practical approach.

Chapter 4

Characterisation of surface discharges using electrical detection methods

4.1 Introduction

The detection of discharge phenomena such as surface discharges introduces the same challenges, as these are known for partial discharges, with regards to the requirements in frequency response of the sensing circuit and the recording devices. Discharges on their own are source of many physical phenomena which have been the basis for the development of several detection methods using different approaches. These methods, as listed by Kreuger in [10] for the case of partial discharges, are shown in Figure 4.1.

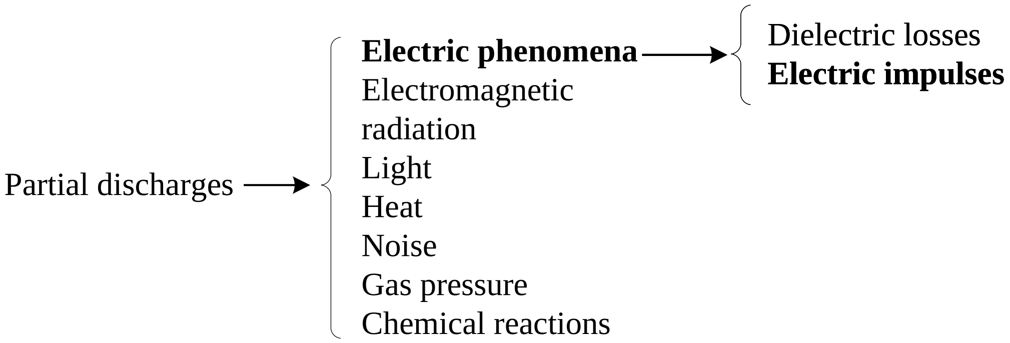

Figure 4.1: Classification of phenomena induced from partial discharge activity [10].

This chapter is dedicated in developing accurate measurement techniques for the electrical detection of surface discharges, in a laboratory-based and fully controlled experiment. The experimental procedures that were followed will be fully described with reference to the previous chapters of this thesis, together with additional information whenever necessary.

The tests were undertaken using a needle-plane electrode configuration for the generation of discharge activity on the surface of disc-shaped solid dielectric samples. Four different gaseous insulating media were investigated, technical air (21/79 % O_2/N_2), N_2, CO_2 and the strongly attaching mixture of 30/70 % CF_3I/CO_2. Prior to the main part of the test campaign, a series of tests were perform to identify the corresponding flashover levels.

The results presented in this chapter aim to, primarily, demonstrate the differences between the different utilised gaseous media and, potentially, the differences between different solid dielectric materials. For the latter it was found that larger, in duration, datasets would allow more confidence in the observations. For the used electrode arrangement and test conditions, technical air showed better withstand against flashover compared to the rest of the atmospheric gases, while, the mixture of 30/70 % CF_3I/CO_2 was superior to all of them. The high resolution current recordings of the surface discharge activity demonstrated the differences between the different gaseous media that were tested. Both the discharge patterns in the duration of a full AC-cycle and the transient PD pulses exhibit unique characteristics for each gas medium.

4.2 Experimental arrangement

For description purposes, the experimental set-up will be divided into different sections depending on practical role within the implemented experiment. These main sections are:

(i). Voltage generation,
(ii). Test object,

(iii). Sensing circuit, and

(iv). Recording devices

An illustration of the full experimental set-up is shown in Figure 4.2.

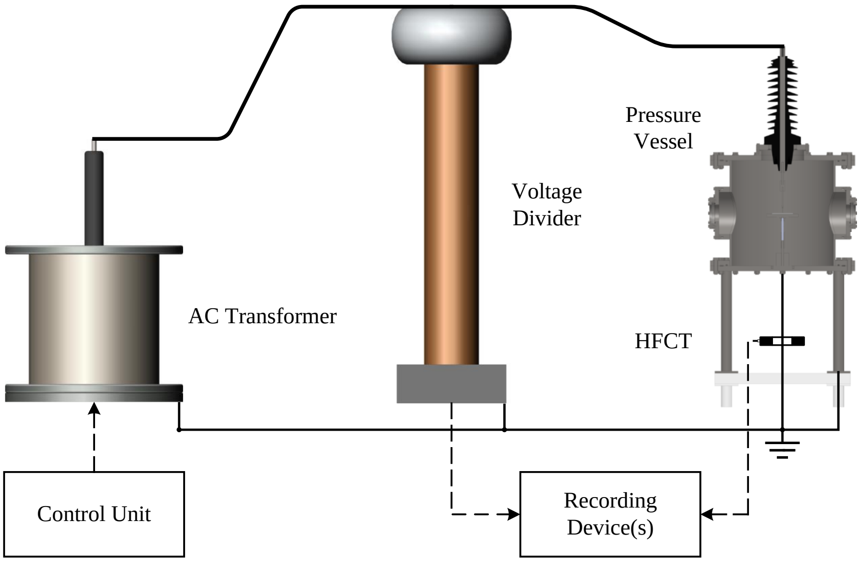

Figure 4.2: Full experimental set-up [9].

4.2.1 Voltage generation

A 50 Hz alternating (AC) voltage was adopted for the experiments. The voltage generation set-up was extensively described in Section 3.8 and was illustrated in Figure 3.13. The voltage waveform quality was validated according to the relevant standards [20] (see Figure 3.12) through a series of preliminary tests and was continuously monitored during the tests. A 50 kV/3.75 kVA transformer was used for the generation of the AC sinusoidal waveform while the voltage control was performed with a variable autotransformer.

4.2.2 Test object

The test object comprises a needle-plane electrode arrangement with a disc-shaped insulator sample placed between the two electrodes with an illustration shown in Figure 4.3 [9].

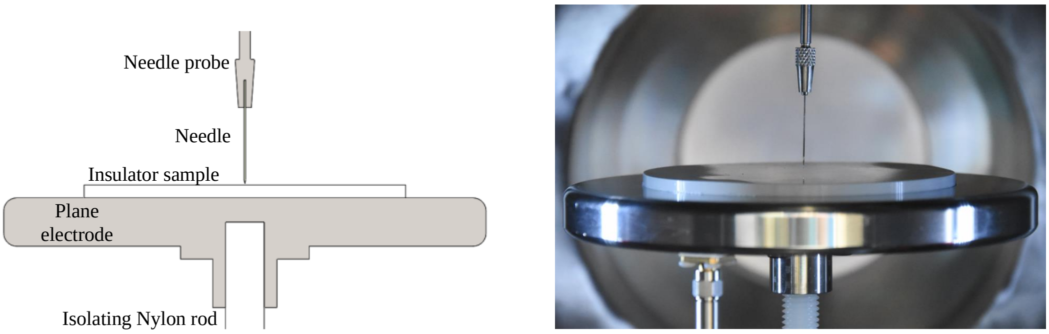

(a) 2D illustration **(b)** Actual picture

Figure 4.3: Needle-plane electrode configuration with a disc-shaped insulator sample: (a) two-dimensional illustration of the configuration with the relevant notations (b) actual picture of the practical test configuration as set up inside the pressure vessel [9].

Some of the reasons which make the test configuration in Figure 4.3 of practical interest are:

(i). The needle-plane is the most severe divergent electric field configuration.

(ii). The solid dielectric acts as a dielectric barrier when placed between the electrodes of different potential levels.

(iii). The coupling between the metal electrodes, energised and earthed, is small which can potentially allow the accurate measurement of discharge activity with minimum distortion.

(iv). Sharp points on the surfaces of energised conductors and/or their interfaces with solid dielectrics is a known situation. Usually, they appear as a result of insufficiently optimised design of electrical apparatus and/or, in occasions, as defects during assembling.

(v). Similar electric field stress conditions are met in GIS spacers/insulators as well as many other configurations in HV equipment.

(vi). In addition to the reasons described above, the configuration shown in Figure 4.3 offers the flexibility to be used for studying the morphology of the surface discharge phenomena with the newly developed high-speed photography system that will be presented later. The maximum possible effective area on the surface of the solid dielectric is visually accessible and through this the streamer channels that extend further from the sharp point are detectable.

The needle is made of tungsten with a high-precision tip diameter of $20 \pm 0.5\,\mu$m, 0.51 mm shaft diameter and a length of 32 mm. It is attached to a stainless-steel needle holder/probe and is placed perpendicularly and in close proximity, 0.5 mm, to the insulator sample disc centre. The plane electrode incorporates a dull polished stainless-steel planar surface of 150 mm diameter and 15 mm thickness, and it is electrically separated from the rest of the mounting system with a nylon threaded rod. The entire configuration is placed vertically and centred inside a cylindrical 90 L dull polished stainless-steel pressure vessel of inner diameter of 480 mm. The disc-shaped insulator sample has a diameter of 100 mm, and different thicknesses were investigated in this chapter.

When a voltage is applied to the needle electrode, a strongly non-uniformly distributed electric field is generated, which when combined with the presence of the dielectric disc, triple junction conditions are replicated.

4.2.3 Measurement technique

Signals that are required to be recoded need a relevant sensing circuit or device. In this experiment, the signals of interest are the applied voltage and generated current associated with surface discharge activity. For the voltage waveform, an RCR voltage divider of ratio $3750 : 1$ and 40 pF, rated at 50 kV AC rms, is used to scale down the generated voltage to safe measurable levels.

The current sensing circuit varies depending on the purpose of the experiment. For breakdown/flashover tests, the current transducer needs to scale down the generated current so that its output signal will not damage the recording devices. The current signals related to discharge events, which are not a result of breakdown or flashover events, are sensed with either a high frequency current transformer (HFCT) or a low inductance shunt resistor. The techniques developed and adopted in this work were described in Section 3.9.3.1, and the necessary calibration and quality checks were presented.

For the batch of results presented in this chapter, the HFCT current sensing technique was used. The configuration shown in Figure 3.17 of Chapter 3 was utilised and which is shown in Figure 4.4, this time the actual device.

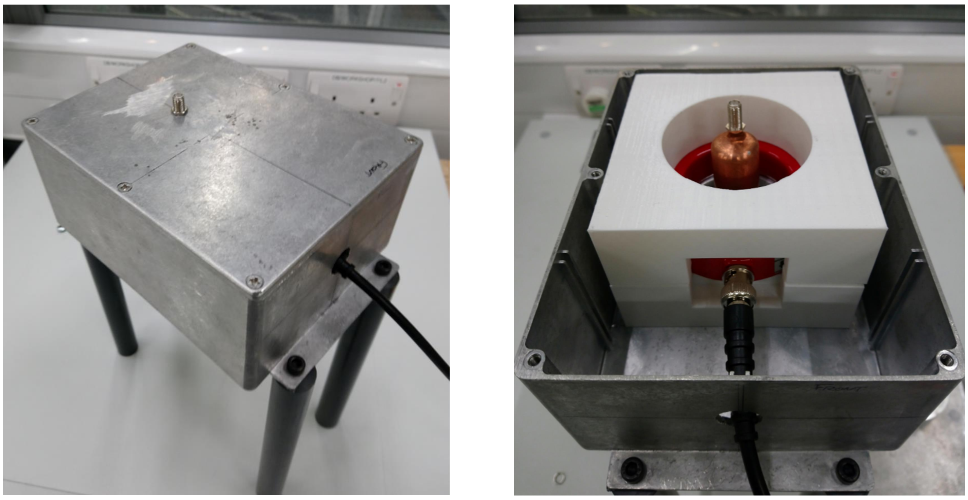

(a) HFCT box closed **(b)** HFCT box opened

Figure 4.4: High frequency current transformer (HFCT) installed inside an EMI/RFI rated box.

The HFCT has a sensitivity ratio of $5\,\mathrm{V/A}$ and a bandwidth of $4.8\,\mathrm{kHz}$ up to $400\,\mathrm{MHz}$. The bandwidth of the full configuration has an upper cut-off frequency $-3\,\mathrm{dB}$ of $359.46\,\mathrm{MHz}$. On the top SMA connector, shown in Figure 4.4, one end of an RG-405 coaxial cable is connected while the other end is connected on the low-pressure side of an SMA feedthrough mounted on the pressure vessel. On the high-pressure side of the pressure vessel, a second coaxial cable of the same type connects the feedthrough to the plane electrode. An SMA 4-hole surface mount connector is attached on the bottom of the plane electrode, as shown in Figure 4.5.

A $2\,\mathrm{mm}$ thick piece of PTFE is installed between the enclosure of the connector and the plane electrode so that only the central pin of the SMA is electrically (metal-to-

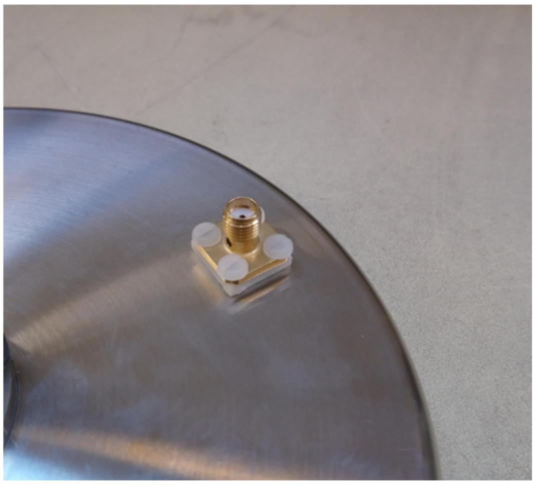

Figure 4.5: SMA connector attached at the bottom of the plane electrode.

metal) connected to the plane. Four Nylon M2.5 bolts are used to hold the connector in place for the same reason as the PTFE piece was used. Figure 4.3b shows the connection between the coaxial cable and the plane electrode.

A coaxial termination needs to be connected at the bottom SMA connector of the HFCT box configuration (see Figure 3.17), preferably at same characteristic impedance as the coaxial cable, i.e., $50\,\Omega$. This can be a so-called load termination (or dummy load) or an attenuator and will help to prevent signal reflections, due to impedance mismatches, which cause signal distortion. Figure 4.6 shows the described connection.

4.2.4 Test data recording devices

The recording of the voltage waveform and the associated currents was performed in two different stages. Single trigger recordings were performed using a Teledyne LeCroy HDO6104 oscilloscope of 1 GHz bandwidth, $2.5\,\mathrm{GS/s}$ maximum sample rate and 12-bit resolution. The buffer size of this device is $50\,\mathrm{MS}$ for each channel meaning that for a sample rate of $1.25\,\mathrm{GS/s}$ the maximum time duration of the recorded signal will be $40\,\mathrm{ms}$, practically two full $50\,\mathrm{Hz}$ AC-cycles. For multiple successive trigger events, a Picoscope® 5000 series, 200 MHz, $250\,\mathrm{MS/s}$, 12-bit and memory size

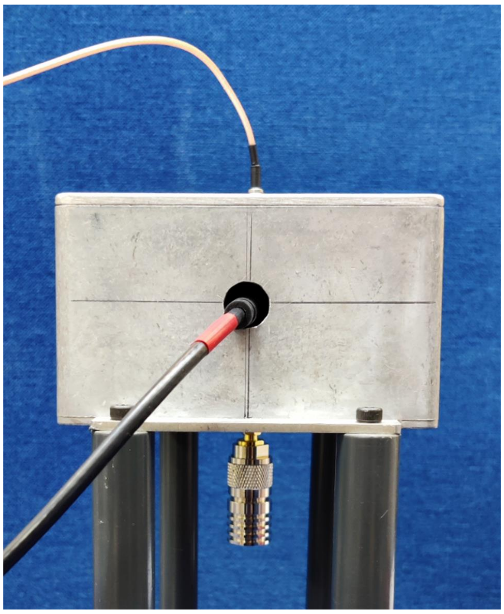

Figure 4.6: 50 Ω load termination connected at the bottom end of the HFCT box configuration.

of 512 MS was used.

Sampling with a rate of 1.25 GS/s with the time duration of the recorded signal being 40 ms effectively means that every 0.8 ns a sample point is obtained. On the other hand, sampling at 250 MS/s with a memory of 512 MS means that a signal of 2 seconds time duration can be recorded. In such a case, a full 50 Hz AC-cycle will have $5.12 \cdot 10^6$ samples which, in turn, means that every 3.9 ns a sample will be generated. The main drawback when sampling at very high rates, above 1 GS/s, is the relatively long processing time. From triggering the device until the recording is saved in a format compatible for post-processing requires at least a few minutes. It is, thus, necessary when dealing with recording of electric impulse signals, such as the partial discharge current pulses, that the experiment includes an approach with high sampling rates. However, the limitations on the buffer size together with the process time required, make the recording of multiple trigger events and multiple signal captures within the same test attempt difficult so a compromise on the sample rate for a gain in speed needs to be done.

4.2.5 Sensitivity of the partial discharge detection circuit

Before proceeding with the main part of the tests, it is necessary that the noise levels of the entire set-up are checked. This is done by using a suitable charge injector/calibrator to inject specific amounts of charge while, at the same time, the generated current pulse is monitored on the recording device(s). Integrating the current pulse signal over time will yield the injected apparent charge, as this was discussed in Section 2.4.2.3 . Figure 4.7 shows the different recordings after injecting pulses of charge magnitudes varying from 10000 pC down to 10 pC.

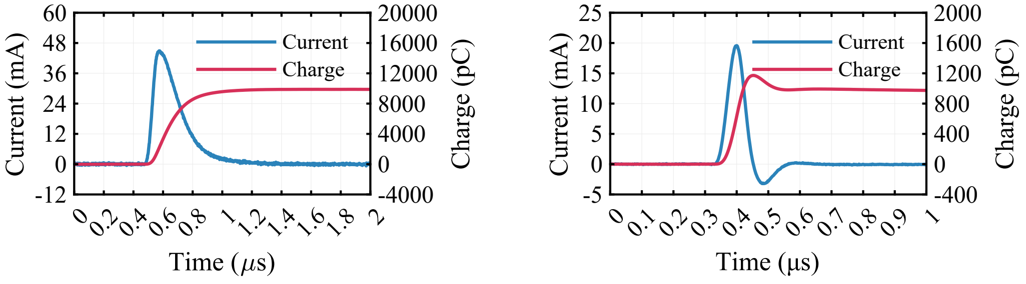

(a) 10000 pC **(b)** 1000 pC

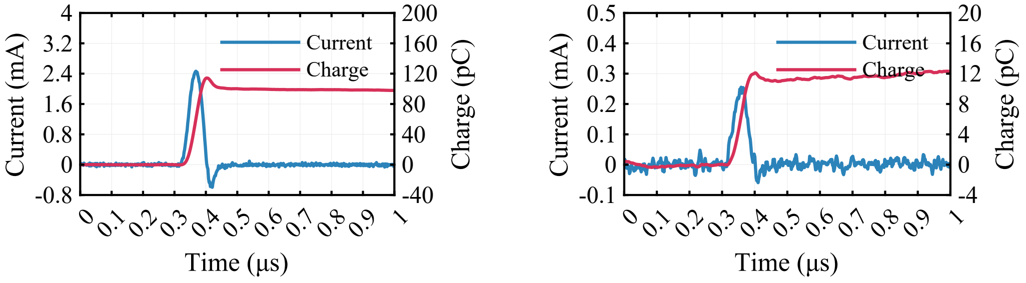

(c) 100 pC **(d)** 10 pC

Figure 4.7: Current measurements using a charge injector/calibrator and the HFCT current sensing technique.

As it can be seen on the figures, the higher the injected charge is, the clearer the current recording will be. Down at 100 pC charge injection, the magnitude of the sensed current pulse is well above the background noise and the current pulse is sufficiently distinguished. For the case of $10\,\mathrm{pC}$, the generated current pulse is relatively close to the background noise levels, something which is expected. However, the corresponding current pulse is still detectable indicating the efficiency of the entire sensing and recording system. The calculation of the apparent charge returns a value higher than $10\,\mathrm{pC}$ which could be attributed to the impact of the background noise and a small DC offset which is a characteristic of ADC converters such as those in digital storage oscilloscopes. The measurements of Figure 4.7 were performed in atmospheric air.

4.3 Investigated gaseous and solid dielectrics

The electrode configuration described in Section 4.2.2 was used. For the disc-shaped insulator sample three different materials of different relative permittivities were investigated, namely PTFE ($\varepsilon_{\mathrm{PTFE}} = 2.1$), silicon rubber ($\varepsilon_{\mathrm{SR}} = 2.9$) and epoxy resin ($\varepsilon_{\mathrm{ER}} = 3.5$) (see Figure 4.8). For each material, two different thicknesses were examined, 4 and $6\,\mathrm{mm}$.

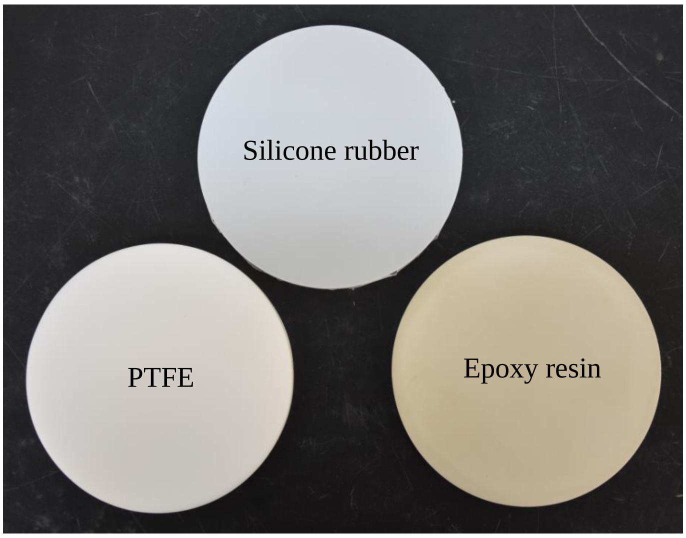

Figure 4.8: Disc-shaped insulator samples of different materials.

Silicone rubber samples were vacuum-cast using WACKER POWERSIL® 600 A/B inside a polished stainless-steel mould followed by at least 24 h curing at 50 °C. The PTFE and epoxy resin samples were polished using sandpaper of 800 grit gradually increasing up to 7000 grit size. For all cases, arithmetic mean height (R_a) is maintained between 0.6 and 0.8 μm, as inspected with a Mahr MarSurf PS10 tester.

The test vessel housing the test electrode configuration is filled, and tests were performed, using three different atmospheric gases: technical air (21/79 % O_2/N_2), oxygen-free nitrogen (N_2) and carbon dioxide (CO_2), and the gas mixture of 30/70 % CF_3I/CO_2.

4.4 Electric field computation

The experimental arrangement has a cylindrically symmetric geometry which implies that the generated electric field is expected to be also symmetrically distributed on the surface of the solid insulator. Practically, this means that, when a surface discharge event appears, it will have equal chances to propagate in any direction on the insulator exposed surface. The implemented electric field computation models are extensively described and presented in the Appendix B. Figure 4.9 shows the electric field distribution over the insulator surface. The presented values are normalised based on the maximum computed value. For readability purposes, the case of insulator sample of 4 mm thickness and $\varepsilon_\mathrm{PTFE} = 2.1$ is shown in this graph, although, the distribution has similar pattern also for the materials of different relative permittivity values.

The curve in Figure 4.9a consists of two mirror parts (from -50 mm to 0 mm and from 0 mm to 50 mm) with maximum percentage deviation between them 0.82 %. Such a low value indicates that the electric field is indeed radially distributed and as expected the generated mesh is well defined. Figure 4.9b shows the potential and electric field lines after the model is solved using COMSOL Multiphysics®. The red dashed line represents the top surface of the insulator sample. This line effectively separates the volumes of the two dielectrics (gaseous and solid) and a small refraction of the potential and electric field lines is visible. Figure 4.10 summarises the maximum electric field

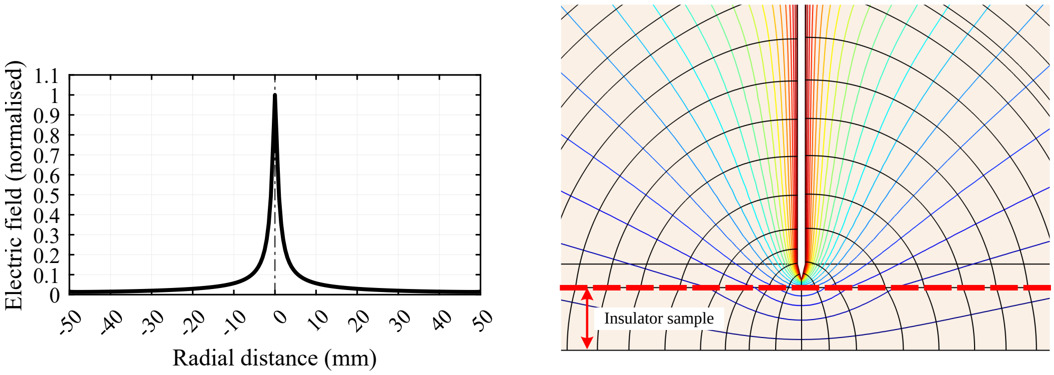

(a) Electric field on the insulator surface

(b) Solved model

Figure 4.9: Electric field computation model implemented using COMSOL Multiphysics®: (a) electric field distribution along the insulator surface and (b) potential (coloured) and electric field (black) lines after the model is solved. As gaseous insulating medium, air at atmospheric conditions was considered. In (a), 0 mm represents the centre of the top surface of the insulator sample while ±50 mm represents its edges.

values that appear on the top surface of the disc insulator sample for different values of relative permittivity and sample thickness.

Despite the small difference, of less than 10 %, it is visible that the higher the relative permittivity is, the higher the generated maximum electric field on the top of the insulator surface. As the relative permittivity of the material increases the potential lines will be refracted more as they cross from the gaseous medium into the solid insulation as a result to the increased difference in the relative permittivities between the two dielectrics and the field line incidence angle. Also, for thinner samples, the same electric field values are higher compared to thicker samples considering that the effective distance to the grounded plane is reduced. Finally, a decrease on the slope of the curve is observed as the thickness of the sample reduces indicating that the impact of the change in the relative permittivity will be more observable for thicker samples. It is worth noticing that the gap distance between the needle tip and the disc insulator top surface was set to at 0.5 mm for all the cases and that the maximum electric field on the top surface of the insulator sample always appears at the point right beneath the needle

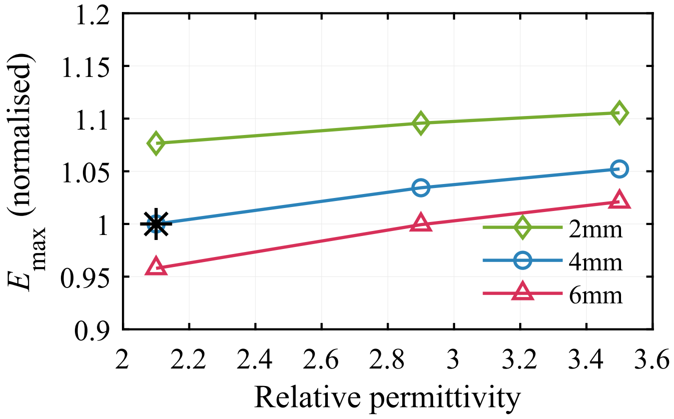

Figure 4.10: Maximum electric field over relative permittivity for samples of different thicknesses. The asterisk indicates the value under which the rest of the values were normalised.

tip (0 mm on Figure 4.9a).

4.5 Disruptive discharge tests for the investigated gaseous and solid dielectrics combinations

A series of flashover tests were performed using all the solid dielectric-insulating gas combinations. The purpose of implementing this test series is to quantify the equivalent threshold voltage level for surface discharges as a percentage of the corresponding mean flashover voltage for each case. Ten flashover events were recorded for each case and the test results are summarised in Figure 4.11. Disruptive discharge voltage and standard deviation were calculated with the use of Equations (3.3) and (3.4). The case of PTFE 6 mm is not included as no flashover event occurred for the maximum allowed AC rms applied voltage (see Table 3.1). The same happened for all the cases where the 30/70 % CF_3I/CO_2 mixture was tested for the maximum allowable applied voltage level of 38 kV rms, as this mixture is known for its superior insulating performance compared to atmospheric gases [121].

For all the different sample types, technical air showed the best insulating performance as compared to the other two atmospheric gaseous media. At the same time, pure carbon dioxide (CO_2) showed a better performance compared to pure nitrogen (N_2) with the difference between them being relatively larger as the relative permittivity of the dielectric insulator material and the sample thickness decrease. Focusing on the calculated standard deviations, nitrogen (N_2) showed a less scattered insulating behaviour for 4 mm samples compared to 6 mm and for all the investigated materials. The standard deviation values for PTFE-6, SR-6 and ER-6 are calculated as 0.96 kV, 1.37 kV and 1.56 kV respectively. It could be said that as the relative permittivity increases, nitrogen (N_2) tends to have a slightly decreased stability in its dielectric performance which is not that visible with the thinner samples. In overall, for all the cases where PTFE was used, it showed a higher flashover voltage compared to the cases where the other two materials were tested. Figure 4.12 shows the dependence of the computed electric field and measured flashover voltages on the different relative permittivity values. The values of each curve are normalised to the, computed or measured, corresponding value of PTFE.

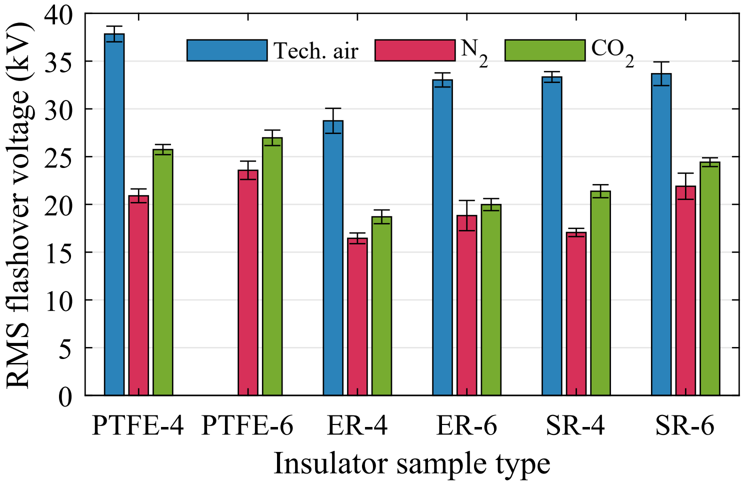

Figure 4.11: Flashover voltage (FOV) test results for six different insulator samples in technical air 21/79 % O_2/N_2, nitrogen (N_2) and carbon dioxide (CO_2), all at 1 bar absolute pressure. ER stands for epoxy resin while SR for silicone rubber. The number next to the material notation indicates the sample thickness in millimetres.

It is obvious that, as the relative permittivity increases, the corresponding flashover levels decrease which is expected as the corresponding maximum electric field magnitudes also increase. Nitrogen, atom or molecule, does not have an affinity for electrons in its ground state [122, 123] while the addition of oxygen will increase the attachment rate and the critical electric field value [124]. Similar patterns were reported in [105, 125] where flashover tests on GIS spacers were performed.

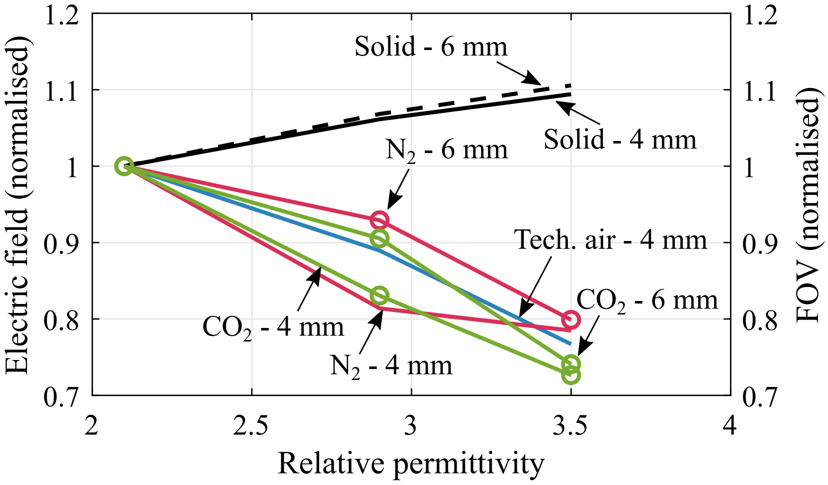

Figure 4.12: Computed electric field (black curves) and measured flashover voltages over relative permittivity. All the curves are normalised to the corresponding values of $\varepsilon_\mathrm{r} = 2.1$ for PTFE.

Figure 4.13 shows the measured PDIV levels for the cases of PTFE and epoxy resin, 4 and 6 mm thick samples in technical air, N_2 and CO_2 at 1 bar absolute pressure. Only these two materials were tested since they show a considerable difference in their relative permittivity values.

It can be seen that, despite differences in absolute values being very small, the measured PDIV levels of the three different gases show a different sequence of performance compared to the FOVs shown in Figure 4.11. Here, $\mathrm{PDIV}_{\mathrm{CO_2}} > \mathrm{PDIV}_{\mathrm{Tech.\ Air}} > \mathrm{PDIV}_{\mathrm{N_2}}$. The same sequence was also observed in the results reported by the authors in [5] where the metal protrusion case was studied at 0.1 MPa pressure. At the same time, again from Figure 4.13, PTFE was again better compared to the higher ε_r epoxy

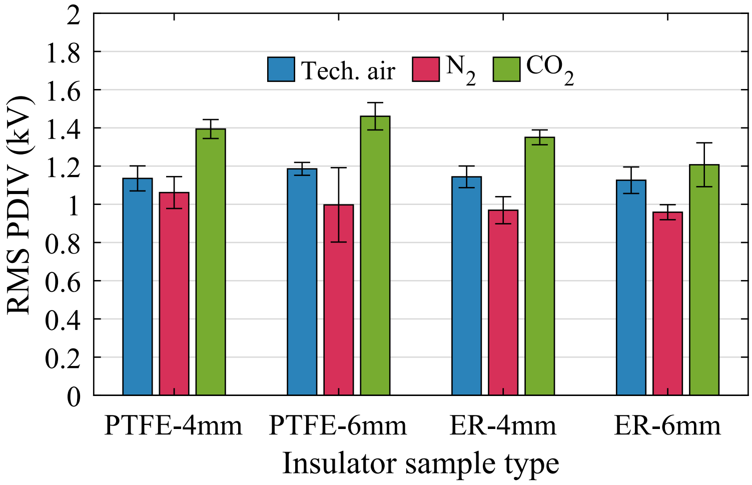

Figure 4.13: Partial discharge inception voltage (PDIV) for PTFE and epoxy resin samples in technical air, N_2 and CO_2, all at 1 bar absolute pressure.

resin, same as happened with the FOVs. This characteristic is more observable for the thicker samples of 6 mm.

4.6 Fast sampling rate recordings and detailed PD observations

4.6.1 Full AC-cycle recordings

High-resolution recordings were obtained through single trigger events of the recording device at dual-channel, sampling at 1.25 GS/s. Two signals, one for the applied voltage and one for the generated current were captured, both of 40 ms duration, the maximum allowed for the available memory of the recording device. The applied voltage levels considered for each case correspond to 85 % of the flashover levels presented in Figure 4.11. As such, it is possible to compare the different cases since the variations in the FOVs do not allow the application of the same test voltage levels. Additionally, maintaining a safety margin of 15 % from the flashover levels helps to avoid unwanted stress of the test configuration and the protection of the recording equipment in case of the appearance of an unexpected flashover. The recording devices are further protected with the use of coaxial overvoltage suppressors rated at 90 V and connected in-line to the coaxial inputs. Figures 4.14 to 4.17 show the high sampling rate measurements obtained using a PTFE insulator sample of 4 mm thickness.

At this stage, it is useful to distinguish the captured discharges in two different types in relevance to the polarity of the current pulse and the polarity of the AC half-cycle. When the polarity of the applied voltage and the polarity of the current pulse are the same, then a forward discharge takes place while, when they are of opposite polarity, a back-discharge occurs [13, 126]. Positive forward discharges appear during the positive AC half-cycle while negative ones occur during the negative half-cycle. In Figures 4.14 to 4.17, each of the different insulating gases presented has a unique pattern on the generated current and for the duration of a full AC-cycle. Also, for all the cases, it is possible to observe discharges of both types, with back-discharges being lower in magnitude for the case of strongly attaching capability gas mixture.

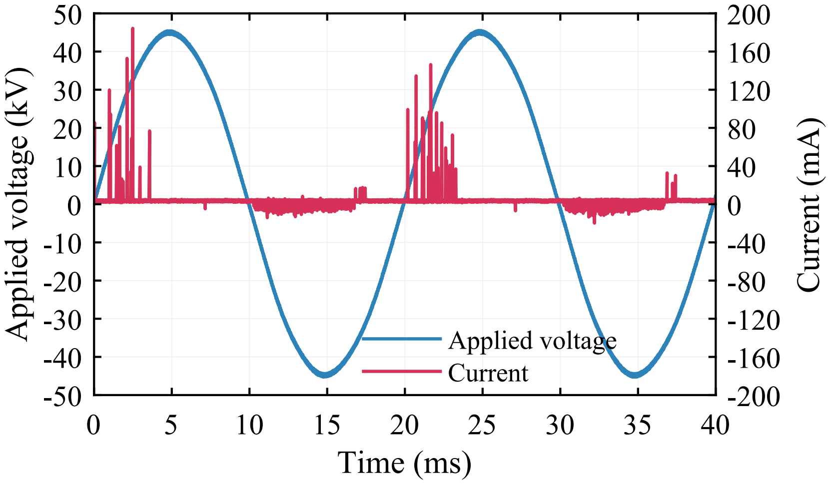

Figure 4.14: Discharge development on the interface of PTFE of 4 mm thickness in technical air (21/79 % O_2/N_2) at 1 bar absolute pressure and 31.74 kV rms applied voltage.

For technical air (21/79 % O_2/N_2) at 1 bar absolute pressure in Figure 4.14, during the rising slope of the positive half-cycle, a large number of relatively high magnitude positive forward discharges are observed. All of them appear before the peak value of the applied voltage is reached. During the falling slope on the same half-cycle a few back-discharge spikes make their appearance. Negative polarity forward discharges during the negative half-cycle begin to appear almost right after the zero crossing of the applied voltage. This type of current pulse seems to be of higher density and of lower magnitude compared to the ones that appeared in the previous half-cycle. The positive polarity back-discharges are again lower in number but they are of relatively higher magnitude compared to the preceding forward discharges. Similar patterns, with regards to the appearance of forward discharges, were also shown in the PRDP plots presented in [104]. During the positive half-cycle, the needle electrode will be positively charged and will attract electrons. As the electrons move towards the needle, their collision with the neutral atoms will create slowly moving positive ions through ionisation while, at the same time, electrons of lower energy will be attached creating negative ions. These ions will be 10^2 to 10^3 times slower compared to the electrons [13, 18]. The positive ions will drift towards the lower electric field regions on the surface of the insulator causing the electric field in the region around the needle to become stronger by their presence. The negative ions will move in the same direction as the electrons at a lower speed. When the electric field magnitudes at the needle tip and the surrounding area become closer, then a positive electric discharge will appear, in the form of a cold plasma channel of considerable propagation length. This positive streamer will attract more electrons around it during its propagation, effectively neutralising the partially positively charged surface. It is not very clear what happens as the applied voltage is around its peak value during the positive half-cycle. One possible explanation is that the charged particles drift movement is the strongest around that point since the alternating electric field will reach its maximum value. However, the electric field formed by the positive ions in the area around the needle tip cannot match that on the needle. When the rms applied voltage is further increased and the conditions are sufficient, most likely this will lead to a flashover along the insulator surface. In Figure 3.16 was shown a flashover event in technical air at 1 bar absolute which appeared very close to the positive half-cycle peak. During the negative polarity half-cycle, the positive ions will be attracted towards the needle electrode. They move slowly while this time electrons move towards the lower electric field regions. While the positive ions are moving towards the needle, much slower than the electrons, they will reduce the electric field in the regions surrounding the needle. So, when a negative polarity discharge initiates, it is most likely that it will not propagate at a long distance.

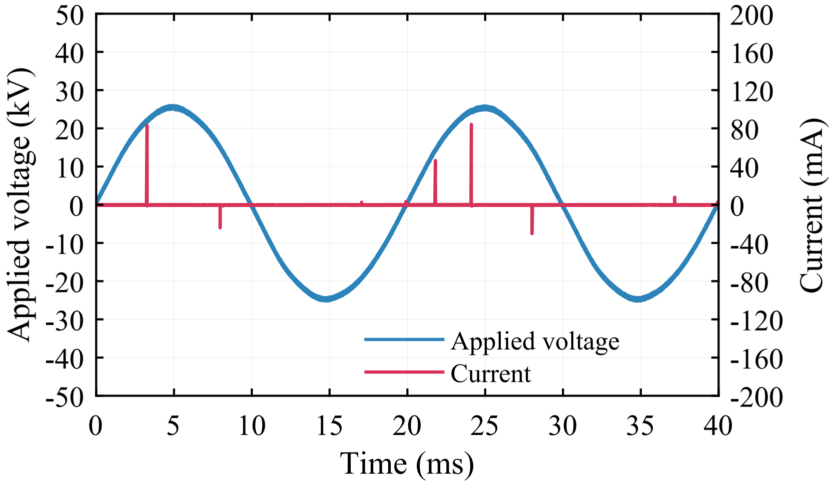

Figure 4.15: PTFE of 4 mm thickness in nitrogen (N_2) at 1 bar absolute pressure and 17.74 kV rms applied voltage.

In Figure 4.15, the recording for nitrogen (N_2) shows a complete absence of negative forward discharges during the negative half-cycle of the applied voltage and for the given vertical resolution (V/div) of the recording device. At the same time, the density of positive forward positive discharges is essentially reduced compared to the case of technical air. It is known that the electron attaching capability of nitrogen is weaker compared to the rest of the gaseous insulating media investigated [122]. This means that the presence of negative ions will be essentially reduced which reflects on the current recordings during the negative half-cycle.

Carbon dioxide (Figure 4.16) is also considered a weakly electron attaching gas, although stronger than nitrogen, which occurs mainly by dissociative attachment [122, 127–129]. The current pulses appearing in the positive half-cycle of the AC applied

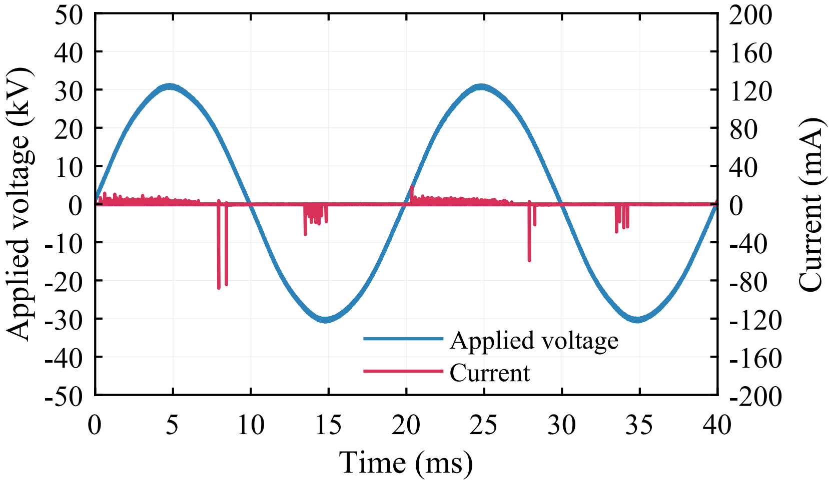

Figure 4.16: PTFE of 4 mm thickness in carbon dioxide (CO_2) at 1 bar absolute pressure and 21.61 kV rms applied voltage.

voltage are very dense but relatively low in magnitude. During the negative half-cycle, the negative forward discharges still appear although compared to the case of technical air, they seem to be of lower density and of higher magnitude. It could be said that the current pulses during that time interval are an indicator of electron attachment capability of the gaseous medium. The addition of the CF_3I compound (Figure 4.17) will improve further the electron attachment capability of the insulating medium in the entire volume filled by the gas mixture. The positive forward discharges will remain very dense after the addition of CF_3I while the negative forward discharges reduce in density.

4.6.2 Individual PD pulses

The patterns of the recorded signals are very similar for all the different insulator sample materials and thicknesses indicating their dependence primarily on the gaseous insulating medium. From the cases presented in Section 4.6.1, individual current pulses are extracted for further investigation. Figures 4.18 to 4.21 show positive forward discharges for each of the gaseous medium cases showed before. Their characteristics, as these were defined in Section 2.4.2.3, are summarised in Table 4.1.

Observing the values of Table 4.1, significant differences in the current pulse char-

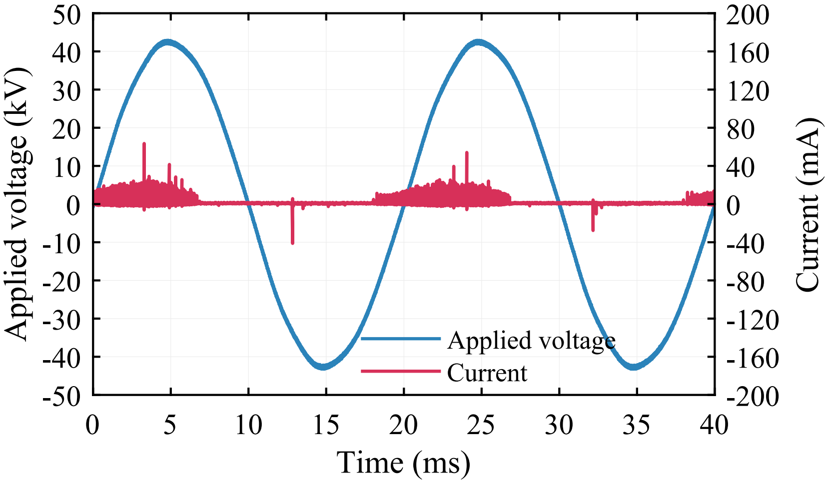

Figure 4.17: PTFE of 4 mm thickness in 30/70 % CF_3I/CO_2 at 1 bar absolute pressure and 30.15 kV rms applied voltage.

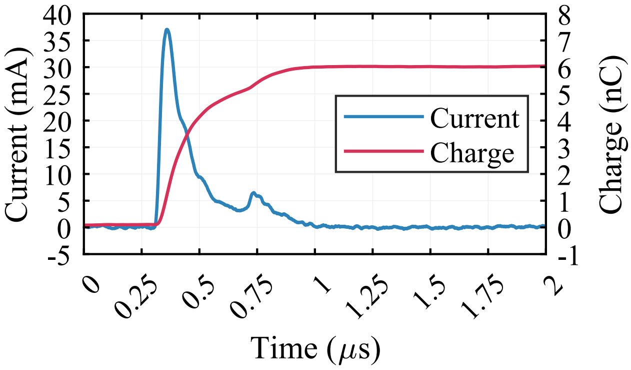

Figure 4.18: Positive forward discharge current pulse for PTFE 4 mm in technical air (21/79 % O_2/N_2) at 1 bar absolute pressure.

acteristics can be noticed. In [122], the authors have correlated the steepness in the rise time with the electron attaching capability and molecular weight of the gaseous insulating compound. From the measurements presented above, no clear observation can be inferred regarding the impact of the compound's molecular weight. However, considering that nitrogen (N_2) has the lowest electron attaching capability and the 30/70 % CF_3I/CO_2 mixture the highest, the reduction in the recorded rise times is easily observable. It is worth to be noted that specifically the pulse of Figure 4.19 potentially comprises more than one discharge events or, possibly, a two-step discharge process. In [130], rise time is correlated to the electron avalanche process during the extension

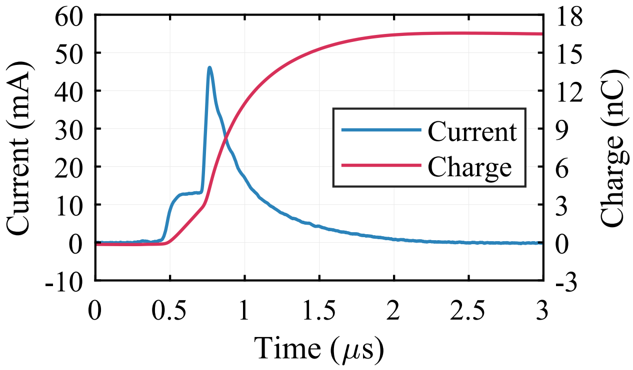

Figure 4.19: Positive forward discharge current pulse for PTFE 4 mm in nitrogen (N_2) at 1 bar absolute pressure.

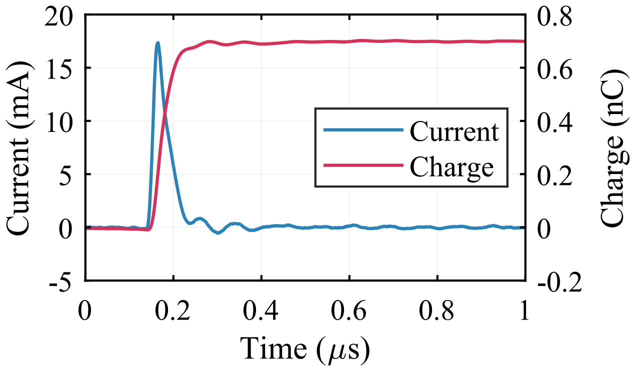

Figure 4.20: Positive forward discharge current pulse for PTFE 4 mm in carbon dioxide (CO_2) at 1 bar absolute pressure.

of the partial discharge while, the fall time with the period of electron drift after the partial discharge extension. Both electron avalanche formation and electron drift processes are related to the electron attachment capability of the gaseous insulating compound. It could be said that the lower the electron attaching capability of the gas is, the longer the rise and fall times will be, with both of these features being observable in the pulses of Figures 4.18 to 4.21.

Figures 4.22 to 4.25 show negative polarity current pulses which were also extracted from the corresponding high-resolution recordings in Figures 4.14 to 4.17 respectively. Table 4.2 summarises the characteristics of these pulses the same way as presented in Table 4.1.

In Table 4.2, the rise time corresponds to the time from 10 % to 90 % of the negative

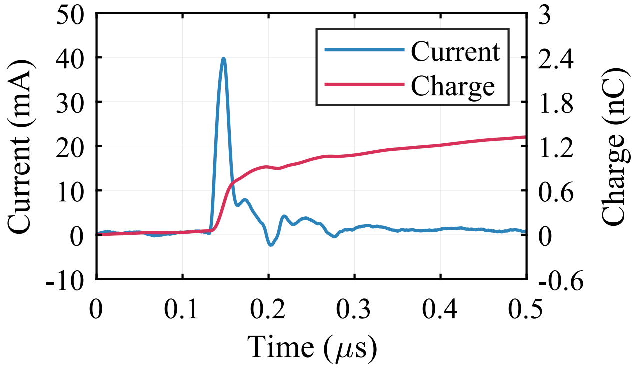

Figure 4.21: Positive forward discharge current pulse for PTFE 4 mm in 30/70 % CF_3I/CO_2 at 1 bar absolute pressure.

Table 4.1: Positive polarity current pulse characteristics (Figures 4.18 to 4.21) at similar test voltage levels relative to the corresponding flashover voltages [9].

Gaseous medium	**Current peak (mA)**	**Rise time (ns)**	**Fall time (ns)**	**Width (ns)**	**Duration (ns)**
21/79 % O_2/N_2	37.07	28.49	263.42	110.26	326.21
N_2	46.14	274.25	662.93	192.94	975.02
CO_2	17.35	13.77	49.06	35.54	73.08
30/70 % CF_3I/CO_2	39.74	9.96	35.95	16.77	52.51

peak value, after the peak has been reached, while the fall time corresponds to the 10 % to 90 % before the same peak has been reached. It is, thus, reasonable to compare the rise time of Table 4.1 with the fall time in Table 4.1 and vice versa. It is important to notice that the negative polarity current pulse for the case of nitrogen (N_2) corresponds to a back-discharge since there is an absence of negative forward discharges during the negative half-cycle and for the given vertical resolution (V/div) of the recording device (see Figure 4.15).

For the case of technical air (21/79 % O_2/N_2) the shorter rise and fall times of negative forward discharges are obvious compared to the positive ones which is also the case for the corresponding pulse durations. The negative polarity back-discharge for nitrogen (N_2) cannot be directly compared with the negative forward discharges of the other

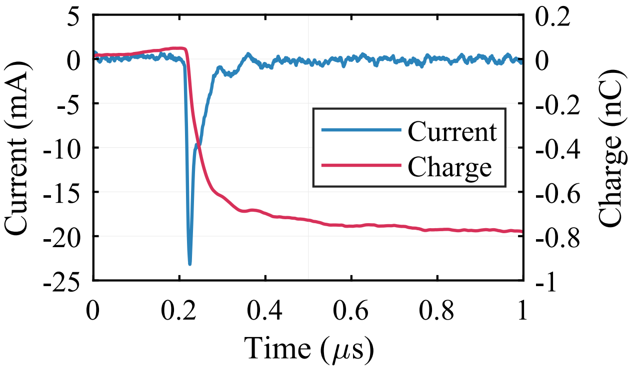

Figure 4.22: Negative forward discharge current pulse for PTFE 4 mm in technical air (21/79 % O_2/N_2) at 1 bar absolute pressure.

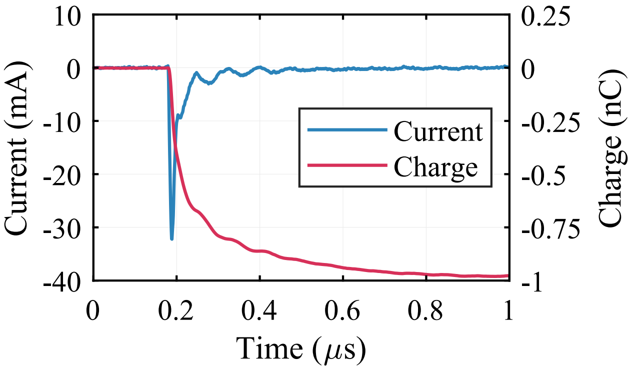

Figure 4.23: Negative polarity back-discharge current pulse for PTFE 4 mm in nitrogen (N_2) at 1 bar absolute pressure.

cases. Back-discharges appear at time points between the voltage peak and the zero-crossing, effectively neutralising the central part of the insulator sample surface [13]. It could be said that the generated current pulses for the strongly attaching gas mixture of 30/70 % CF_3I/CO_2 show very similar characteristics for both polarities and for the two pulses (Figures 4.21 and 4.25) shown in this section. Carbon dioxide (CO_2), for the pulses presented here, shows a different behaviour compared to technical air and nitrogen. Although the front time of the pulse in Figure 4.24 seems to be shorter compared to the pulse in Figure 4.20, the corresponding 90 % to 10 % is essentially larger. It needs to be further investigated the electron attachment behaviour of CO_2.

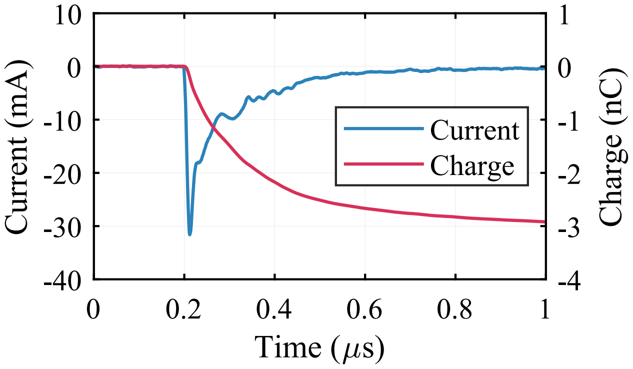

Figure 4.24: Negative forward discharge current pulse for PTFE 4 mm in carbon dioxide (CO_2) at 1 bar absolute pressure.

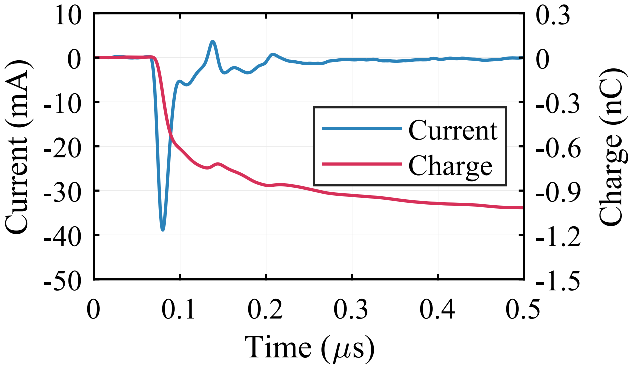

Figure 4.25: Negative forward discharge current pulse for PTFE 4 mm in 30/70 % CF_3I/CO_2 at 1 bar absolute pressure.

4.7 Discussion and conclusions

In the previous sections, the electrical detection of surface/creeping discharges under AC voltage energisation was presented. The complete procedure included the detailed description of the optimised experimental arrangement, the electric field computation for the investigated cases, the implementation of flashover tests and ultimately the study of the surface discharge activity using a high sampling rate recording device.

The experimental arrangement is described extensively in order to demonstrate that the all the necessary qualities are met in a satisfactorily level. Together with the material presented in the previous chapters, it is shown that the current circuit is capable to deliver reliable and accurate measurements which is a very important requirement when

Table 4.2: Negative polarity current pulse characteristics (Figures 4.22 to 4.25) at similar test voltage levels relative to the corresponding flashover voltages [9].

Gaseous medium	Current peak (mA)	Rise time (ns)	Fall time (ns)	Width (ns)	Duration (ns)
21/79 % O_2/N_2	-23.19	51.81	7.95	16.14	65
N_2	-32.23	41.63	5.73	12.94	52.04
CO_2	-31.63	232.38	8.53	38.58	247.65
30/70 % CF_3I/CO_2	-38.89	35.25	7.95	14.73	48.66

such transient current pulses need to be detected. The case study included different gaseous insulating media of different molecules and compositions combined with solid dielectrics of different relative permittivities and thicknesses. All the solid insulator types were simulated to identify the computed electrostatic electric field distribution on the surface where the discharges will supposedly propagate on.

Flashover tests were performed primarily to identify the maximum allowable rms voltage levels that can be applied to the test objects. This is a rather important part of the test process as flashover events may result to the degradation of the test object and expose the recording devices to stresses that may be harmful. The measurements showed that solid insulators of lower permittivity were able to withstand flashover more effectively compared to insulator samples of the same thickness but different material. Thicker samples were better insulators compared to thinner which can be expected as the effective gap distance between the energised and the earthed electrodes was increased and consequently the effective distance that an arc needs to cover to bridge these electrodes is also increased. The capacitance of test object is also altered when the thickness of the insulator sample and the material which affects the energy input into the generated arc. Nitrogen (N_2) showed the weakest insulating capability with technical air being the best, among the atmospheric gases. The mixture of 30/70 % CF_3I/CO_2 was superior of all of them and no flashover was achieved for the given test conditions and allowable test voltage levels. In addition to the FOVs, the partial discharge inception voltage (PDIV) levels of PTFE and epoxy resin in atmospheric gases were shown. In that case, CO_2 seems to perform better than technical air with N_2 being again the least effective.

High resolution and sampling rate of single triggering event recordings were performed. The purpose behind this was to obtain the maximum possible quality of recording in order to depict the evolution of the recorded current signal over the time duration of the full AC-50 Hz cycle and also obtain accurate recordings of individual current transient pulses. The differences between the different gaseous media were clear. It could be said that the surface discharge evolution patterns were unique for each gaseous compound and relatively easily distinguishable. Also, the fastest rising pulses were observed for the strongly attaching 30/70 % CF_3I/CO_2 mixture and the slowest for nitrogen (N_2) which is considered a low electron attaching capability compound. It seems that the pulse characteristics are correlated with the electron attaching capability of the gas, and it has been documented by previously reported works, however, further work will be needed as an extension of the presented outputs to potentially quantify this correlation.

Despite the presence of the dielectric, placed between the two electrodes, the characteristics of the generated PD phenomena are still unique to each gaseous compound. Such sets of data can be a useful so that different gaseous media need to be easily recognisable. The generated PD pulses are also very different between the different gases. This can provide the necessary information of how these pulses will reflect to the corresponding apparent charge which is the detectable quantity in PD detectors. The observations of the next chapter will contribute further into that direction.

Chapter 5

Comparative surface discharge patterns for different gases and solid dielectric materials

5.1 Introduction

High sampling rate recordings, in the GS/s level or higher usually do not allow the capture of multiple trigger events in a reasonable time duration and during the same test attempt. The higher the sampling rate is, the larger the exported file and the time it needs to be saved in the storage drive will be. A possible solution to this is to perform the same test multiple times until sufficient amount of data has been collected or remain in the test voltage level for a relatively longer time period. In both cases, the ratio between the amount of data collected to the number of tests performed and induced stress on the test object may not be considered the most practically well balanced. To overcome this, a lower sampling rate, larger buffer size, fast-triggering device was employed. In this way, the fast recording of multiple full AC-cycle trigger events to demonstrate the repeatability of the generated phenomena was possible for the same applied voltage attempt and without overstressing the test object.

This chapter is a continuation to the work presented previously in Chapter 4. However, because of the different approach in the recording of the generated signals, the relevant tests were repeated under the exact same test conditions. As it was shown in the previous chapter, for each test case the gaseous medium appears to have the largest impact on the overall discharge pattern. The purpose of the larger dataset recordings, presented in this chapter, is to demonstrate potential differences in the PD patterns of different solid dielectric materials and also expand the observations regarding the gaseous media.

5.2 Experimental arrangement

The test object used in this set of experiments was identical to the one presented in Section 4.2.2, i.e., a needle-plane electrode configuration with a solid dielectric placed between them, for replicating highly divergent electric field distribution conditions. The same gaseous insulating media and solid dielectrics were investigated as in Section 4.3.

The employed recording device was a Picoscope® 5000 series, 200 MHz, 250 MS/s, 12-bit with a memory size of 512 MS. With these specifications it is possible the recording of 25 full AC-cycles of 20 ms duration each. In these recordings, two signals are included, one for the applied AC voltage and the other for the signal from the current sensing configuration. The main advantage of such a recording technique is that larger amounts of data can be acquired in a very short duration of time without overstressing the test object. The drawback is the compromise in the lower sampling rate however, it is still comparable to the ones adopted in commercial PD detectors.

All the necessary quality checks were followed and the noise levels of the combined current sensing and signal recording systems were validated in the same way as it was presented in Figure 4.7 of Section 4.2.5. An illustration of the full experimental set-up is shown in Figure 5.1.

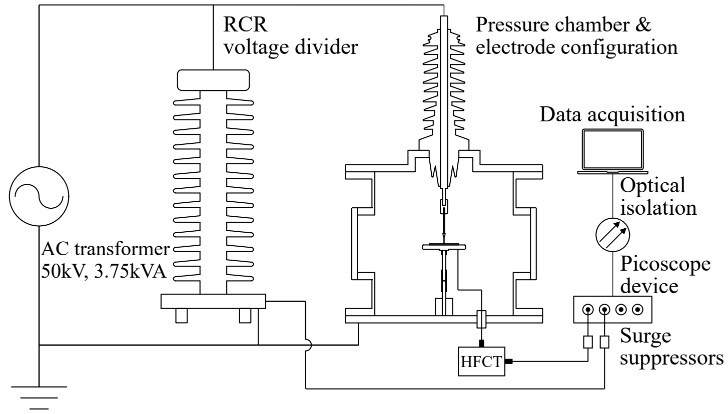

Figure 5.1: Full experimental set-up.

5.3 Current peak density patterns

Post-processing of these recordings involves isolating the peak values of the current pulses within the time domain and incorporate them into a concatenating plot where a colourmap was applied based on the density of these peaks. The colour identification is normalised over the total number of detected peaks. All of the presented measurements were performed with the applied voltage being 85 % of the corresponding flashover levels (Figure 4.11), unless otherwise described in the relevant figure caption. The first batch of the presented recordings represents insulator samples of 4 mm thickness, further insulated by various gaseous insulating media. Each figure incorporates 25 trigger events of 20 ms each, effectively resulting in an acquisition of 500 ms duration.

For the case of technical air (Figures 5.2 to 5.4), the different samples show a fairly similar pattern with the epoxy resin having a higher density of discharge activity during the positive half-cycle. This is attributed to the elevated electric field around the needle tip and the insulator top surface centre since epoxy has the highest relative permittivity value ($\varepsilon_{\mathrm{ER}} = 3.5$) among the investigated dielectric materials.

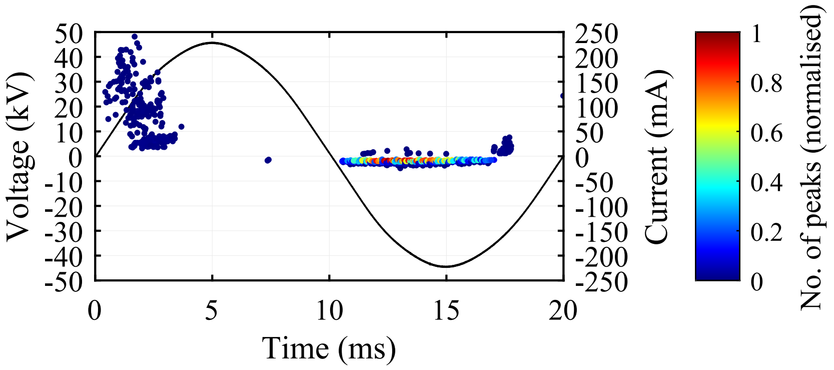

Figure 5.2: Current peaks density for PTFE 4 mm thick insulator sample in technical air (21/79 % O_2/N_2) at 1 bar absolute pressure.

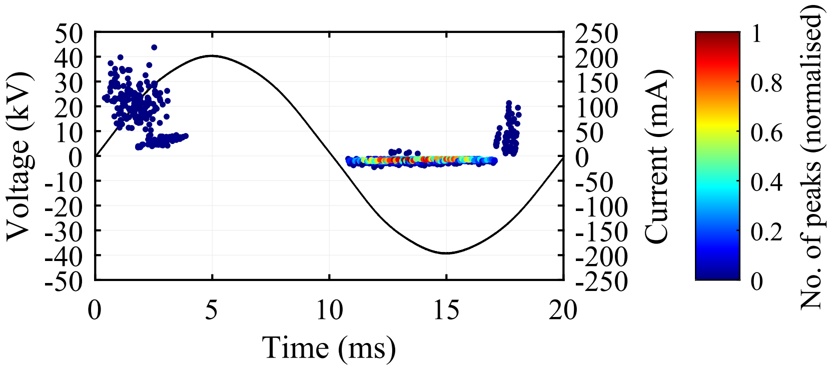

Figure 5.3: Current peaks density for silicone rubber 4 mm thick insulator sample in technical air (21/79 % O_2/N_2) at 1 bar absolute pressure.

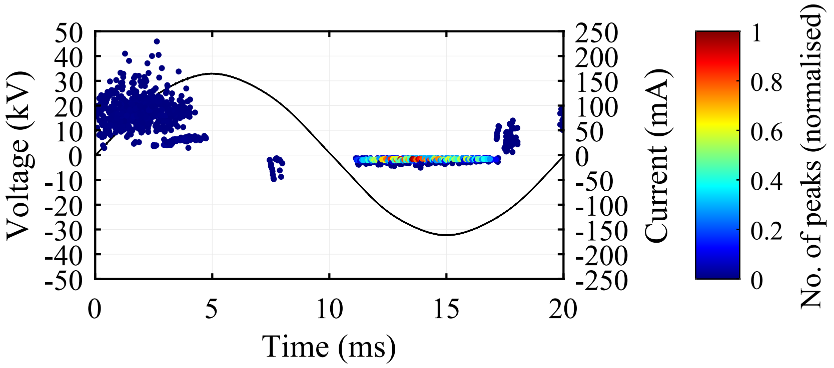

Figure 5.4: Current peaks density for epoxy resin 4 mm thick insulator sample in technical air (21/79 % O_2/N_2) at 1 bar absolute pressure.

All the recordings involving nitrogen (N_2) (Figures 5.5 to 5.7) follow the same pattern in the recorded current signals as the one shown in Figure 4.15.

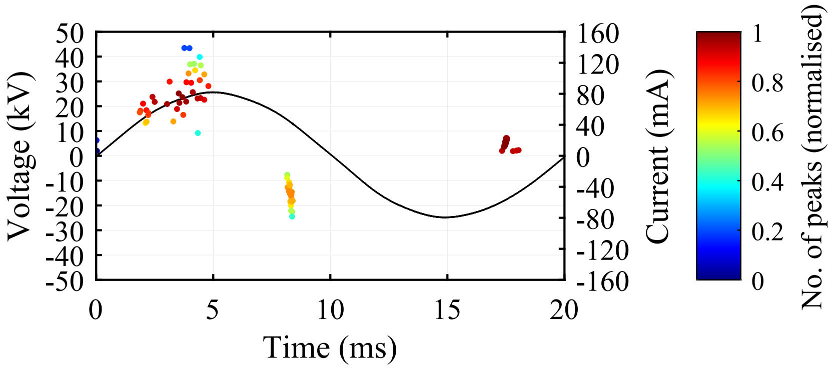

Figure 5.5: Current peaks density for PTFE 4 mm thick insulator sample in nitrogen (N_2) at 1 bar absolute pressure.

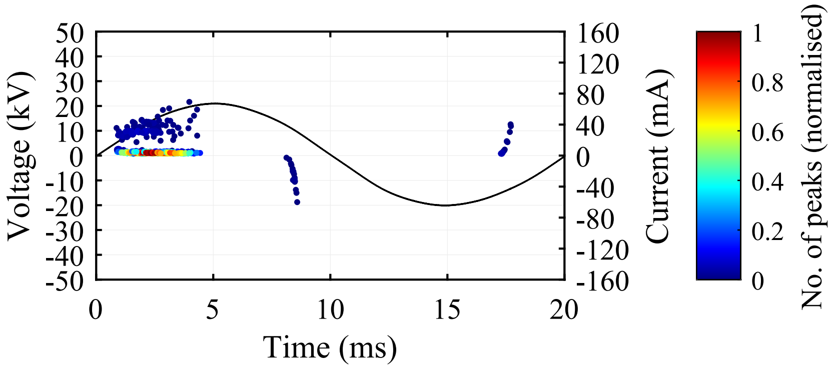

Figure 5.6: Current peaks density for silicone rubber 4 mm thick insulator sample in nitrogen (N_2) at 1 bar absolute pressure.

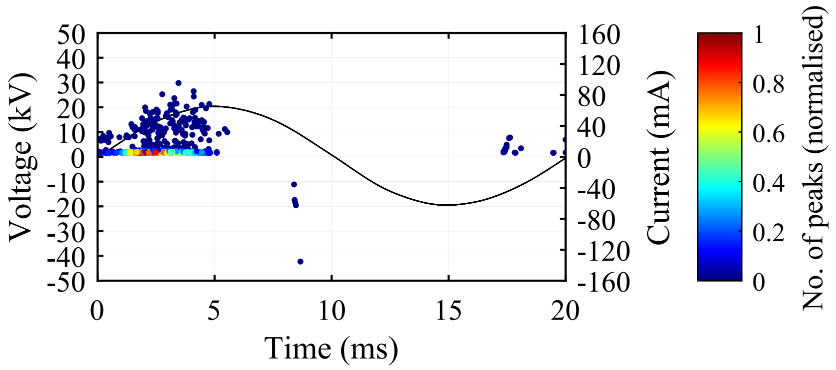

Figure 5.7: Current peaks density for epoxy resin 4 mm thick insulator sample in nitrogen (N_2) at 1 bar absolute pressure.

For epoxy resin again (Figure 5.7), a small number of very high magnitude current peaks were detected possibly indicating that a further increase in the rms applied voltage could possibly result to a flashover. For carbon dioxide (CO_2) (Figures 5.8 to 5.10), the density of the discharge activity during the positive half-cycle is again very dense but relatively low in magnitude for the investigated samples. The back-discharge activity is also detectable, as happens also for technical air and nitrogen however, it seems to be more dense and higher in magnitude. It could be said that there is a correlation between the magnitude of the forward discharge and the back-discharge activities within the same half-cycle, considering the role of back-discharges in neutralising the deposited charge on the insulator sample surface and in the close proximity of the sharp needle electrode.

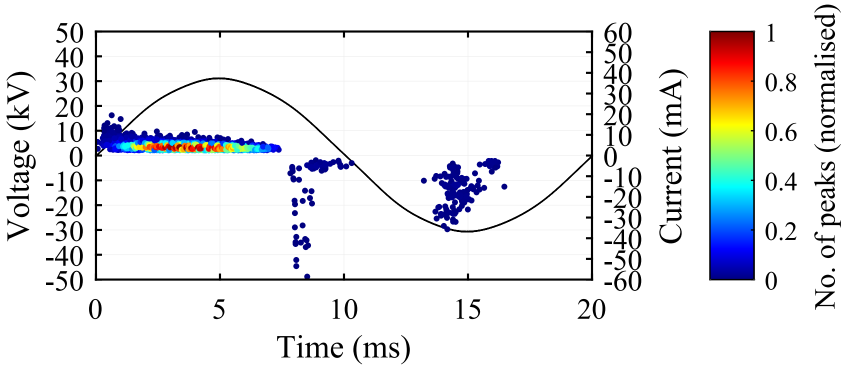

Figure 5.8: Current peaks density for PTFE 4 mm thick insulator sample in carbon dioxide (CO_2) at 1 bar absolute pressure.

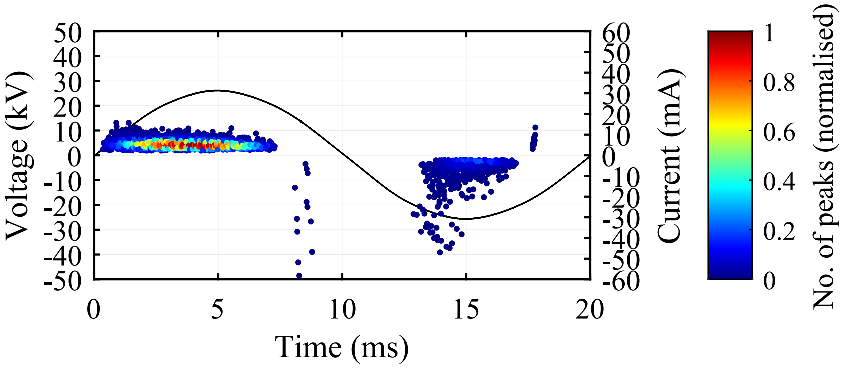

Figure 5.9: Current peaks density for silicone rubber 4 mm thick insulator sample in carbon dioxide (CO_2) at 1 bar absolute pressure.

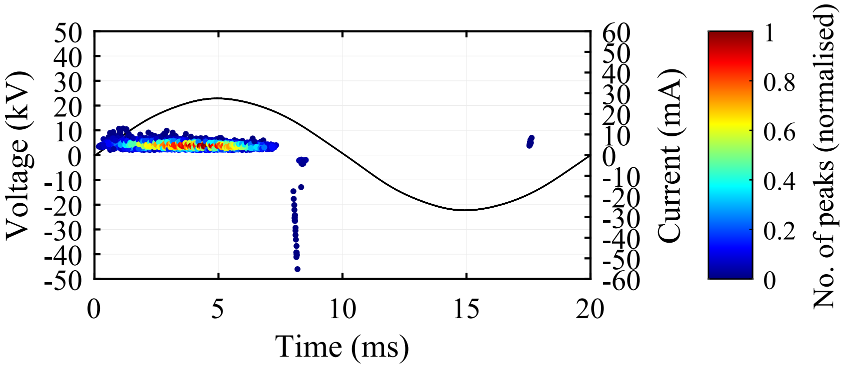

Figure 5.10: Current peaks density for epoxy resin 4 mm thick insulator sample in carbon dioxide (CO_2) at 1 bar absolute pressure.

The rms applied voltage for the 30/70 % CF_3I/CO_2 cases presented is expressed as 80 % of the corresponding flashover levels for the same cases in technical air. Despite the difference in the absolute value of the applied voltage levels ($\sim$ 7 kV), the case of epoxy resin shows again a denser discharge activity. PTFE has the characteristic of having a lower relative permittivity value ($\varepsilon_{\text{PTFE}} = 2.1$), compared to the rest of the dielectric materials and which is closer to the corresponding relative permittivity of the insulating gas. A high divergence between the relative permittivities of the gaseous and solid mediums seem to enhance the appearance of discharge activity especially when strongly non-uniform electric fields occur at low gas densities of the strongly attaching gases.

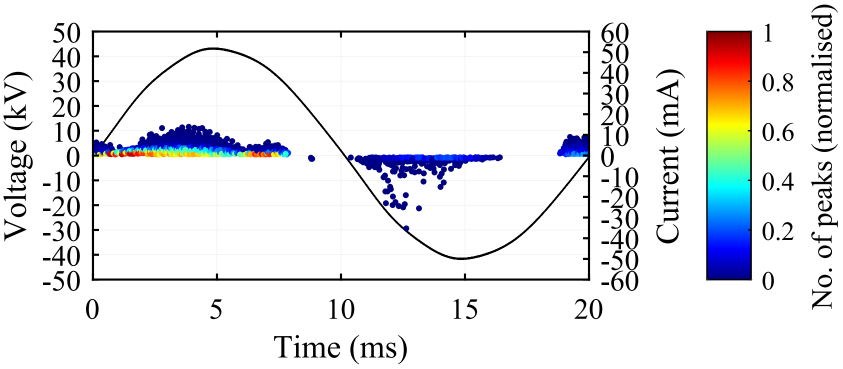

Figure 5.11: Current peaks density for PTFE 4 mm thick insulator sample in 30/70 % CF_3I/CO_2 at 1 bar absolute pressure. Test voltage was 30 kV rms.

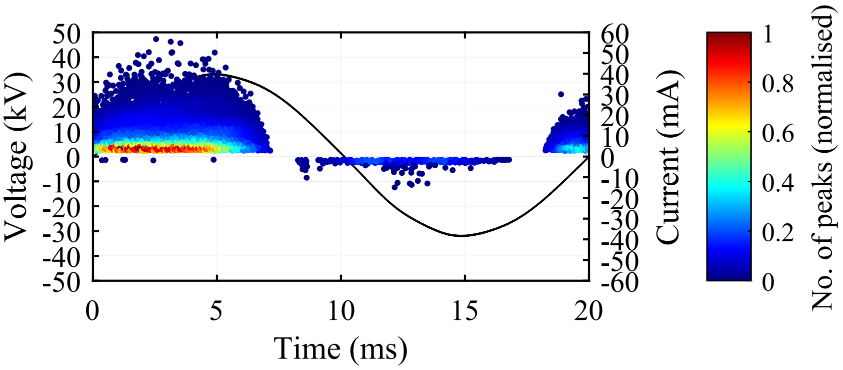

Figure 5.12: Current peaks density for epoxy resin 4 mm thick insulator sample in 30/70 % CF_3I/CO_2 at 1 bar absolute pressure. Test voltage was 22.96 kV rms.

The second batch of measurements includes recordings where insulator samples of 6 mm thickness are investigated. Selected results for atmospheric gases (Figures 5.13 to 5.15) are shown while for the 30/70 % CF_3I/CO_2 mixture all the three different materials are included (Figures 5.16 to 5.18). Once again, the applied test voltages are 85 % of the corresponding FOVs unless otherwise described in the relevant figure caption.

Regarding the atmospheric gases, the most significant difference is observed with epoxy resin in nitrogen (N_2) which for the thicker sample showed considerably decreased current magnitudes sample and smaller variation in the magnitudes of the detected pulses (Figure 5.14). Silicone rubber of 6 mm thickness (Figure 5.15) in tech-

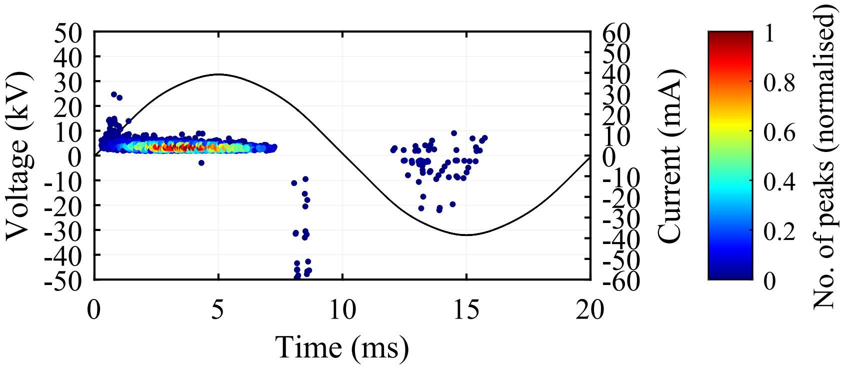

Figure 5.13: Current peaks density for PTFE 6 mm thick insulator sample in carbon dioxide (CO_2) at 1 bar absolute pressure.

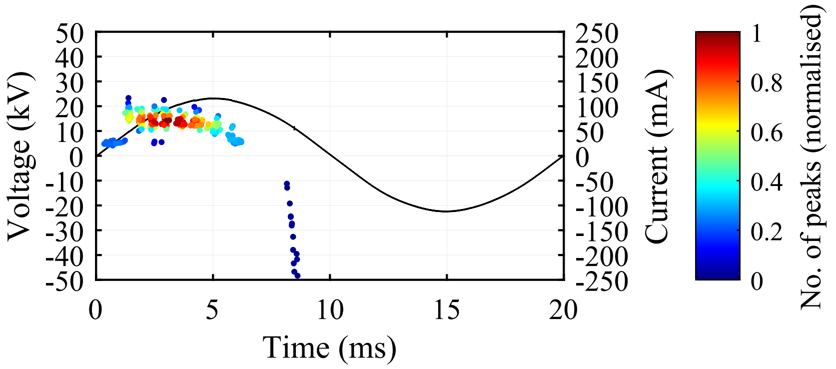

Figure 5.14: Current peaks density for epoxy resin 6 mm thick insulator sample in nitrogen (N_2) at 1 bar absolute pressure.

nical air shows increased resistance to surface discharge activity in comparison to the 4 mm sample of the same material (Figure 5.3), especially when the polarity of the applied voltage is positive. PTFE 4 mm in carbon dioxide (CO_2) and PTFE 6 mm in the same gas do not show significant differences despite the flashover level for the latter case is higher. For the 30/70 % CF_3I/CO_2 cases the recorded results show a slight decrease as the relative permittivity of the insulator sample material increases however, it should noted that for the case of PTFE 6 mm (Figure 5.16) the rms applied voltage is higher compared to the rest two cases (Figures 5.17 and 5.18). It could be said that, overall, the thickness of the insulator sample has an impact on the density and magnitude of the generated discharge events which seem to be more significant for insulating gases of weaker electron attaching capability. When a strongly attaching

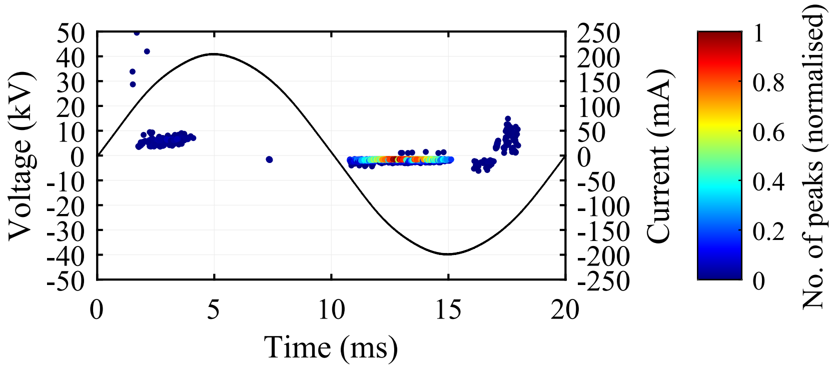

Figure 5.15: Current peaks density for silicone rubber 6 mm thick insulator sample in technical air (21/79 % O_2/N_2) at 1 bar absolute pressure.

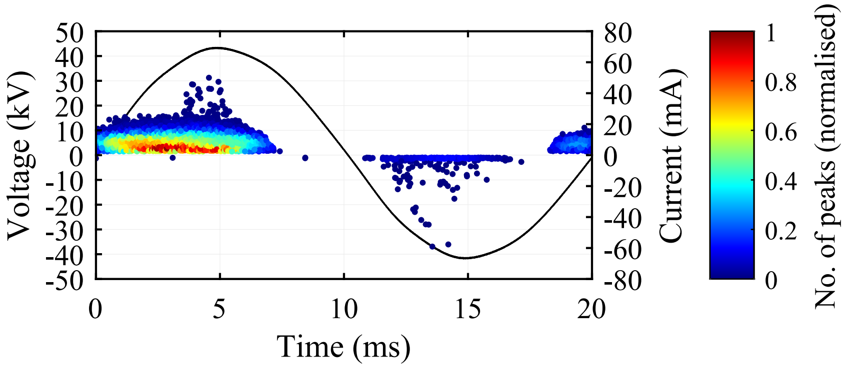

Figure 5.16: Current peaks density for PTFE 6 mm thick insulator sample in 30/70 % CF_3I/CO_2 at 1 bar absolute pressure. Test voltage was 30 kV rms.

insulating medium is used, such as the 30/70 % CF_3I/CO_2 gas mixture, the density of the discharge phenomena increases considerably which can be attributed to the steep increase of the of the ionisation coefficient when the electric field exceeds its critical value. In that case, a strong growth of ionisation occurs [131, 132].

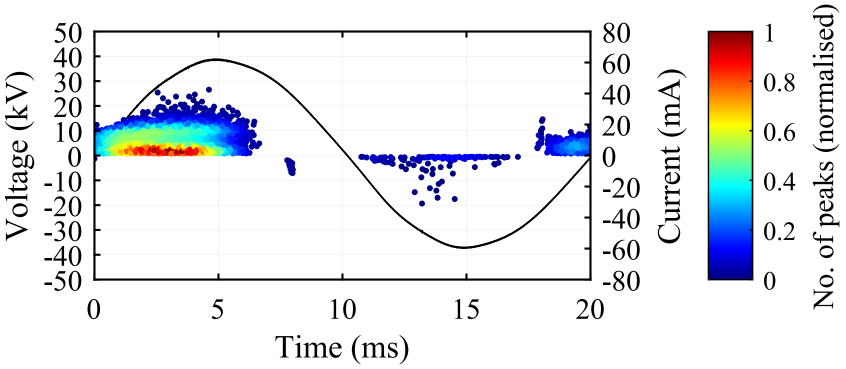

Figure 5.17: Current peaks density for silicone rubber 6 mm thick insulator sample in 30/70 % CF_3I/CO_2 at 1 bar absolute pressure. Test voltage was 26.83 kV rms.

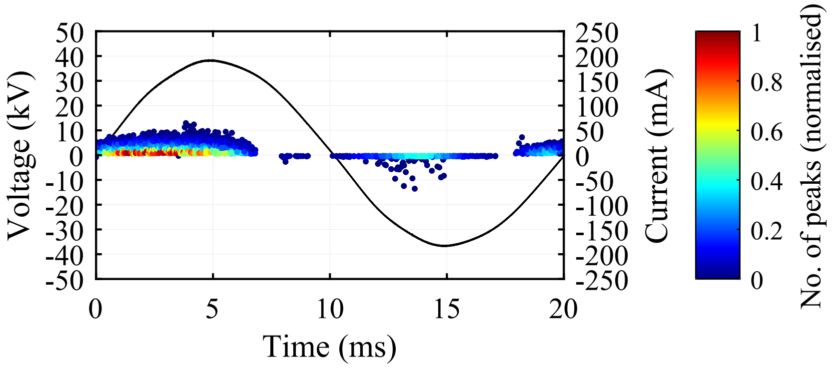

Figure 5.18: Current peaks density for epoxy resin 6 mm thick insulator sample in 30/70 % CF_3I/CO_2 at 1 bar absolute pressure. Test voltage was 26.50 kV rms.

5.4 Charge density patterns

The current density plots described before are very informative regarding the magnitude and density of the discharge activity. They can provide very useful information on the overall appearance pattern of the current pulses which may not be easily observable through recordings of one or two AC cycles. Another very interesting way to illustrate larger data measurements is by plotting the calculated apparent charge that corresponds to each current pulse. As a quantity, the apparent charge can summarise information not only about the current peak but also for the rest of the current pulse characteristics as these were described in Section 2.4.2.3. A similar approach is implemented through partial discharge detection devices to generate the so-called phase-resolved partial discharge (PRPD) graphs. The datasets shown in Figures 5.2 to 5.18 are further processed and the corresponding charge density plots are produced. The first batch of the outputs is shown in Figures 5.19 to 5.29.

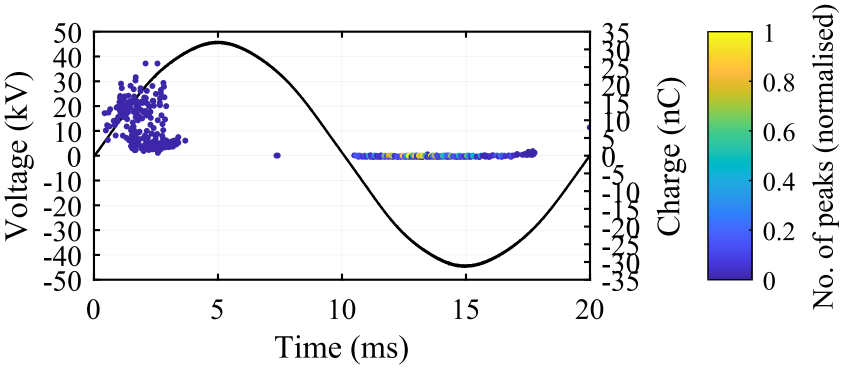

Figure 5.19: Charge density for PTFE 4 mm thick insulator sample in technical air (21/79 % O_2/N_2) at 1 bar absolute pressure.

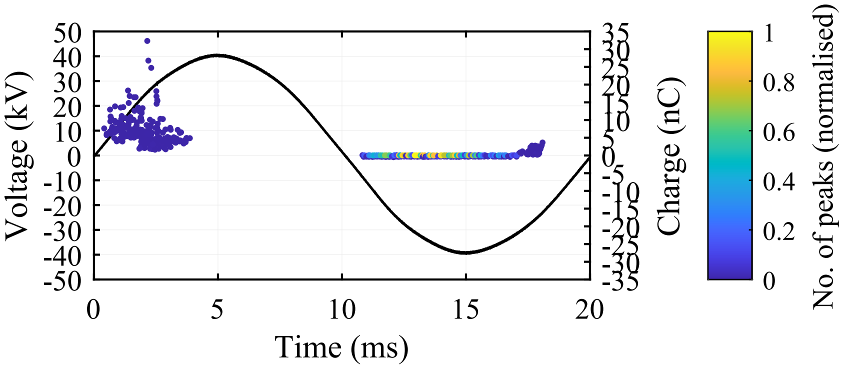

Figure 5.20: Charge density for silicone rubber 4 mm thick insulator sample in technical air (21/79 % O_2/N_2) at 1 bar absolute pressure.

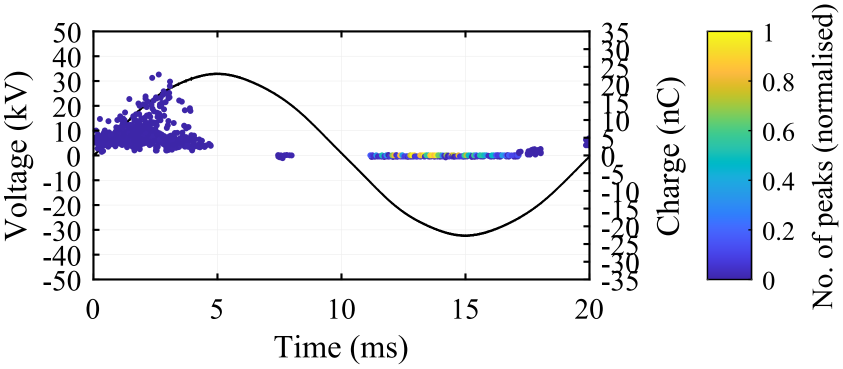

Figure 5.21: Charge density for epoxy resin 4 mm thick insulator sample in technical air (21/79 % O_2/N_2) at 1 bar absolute pressure.

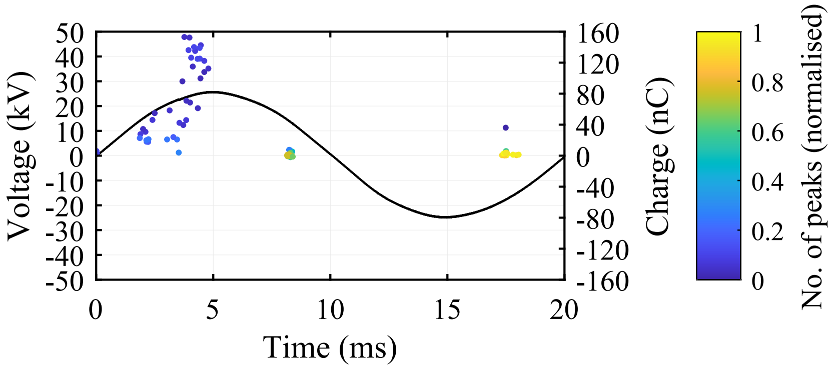

Figure 5.22: Charge density for PTFE 4 mm thick insulator sample in nitrogen (N_2) at 1 bar absolute pressure.

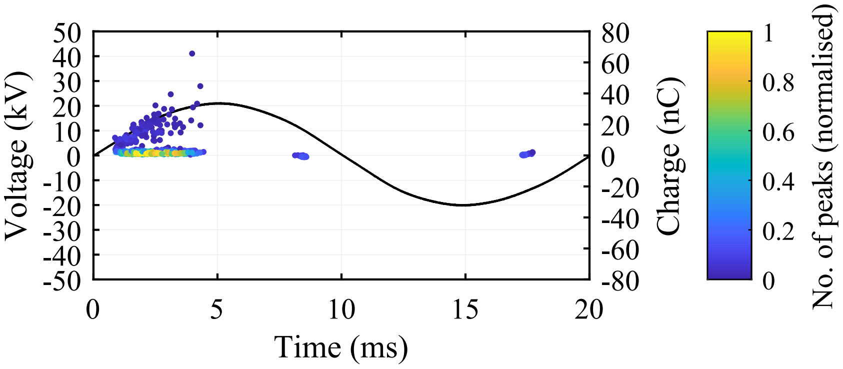

Figure 5.23: Charge density for silicone rubber 4 mm thick insulator sample in nitrogen (N_2) at 1 bar absolute pressure.

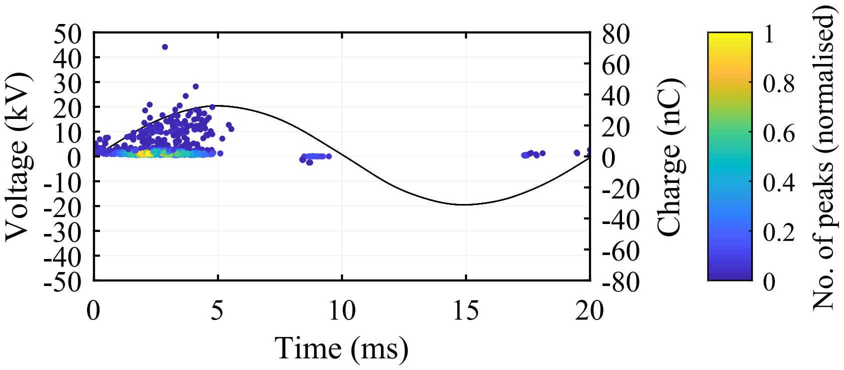

Figure 5.24: Charge density for epoxy resin 4 mm thick insulator sample in nitrogen (N_2) at 1 bar absolute pressure.

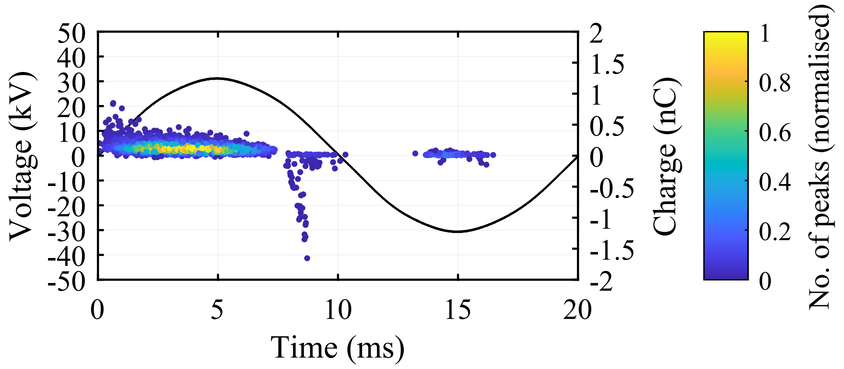

Figure 5.25: Charge density for PTFE 4 mm thick insulator sample in carbon dioxide (CO_2) at 1 bar absolute pressure.

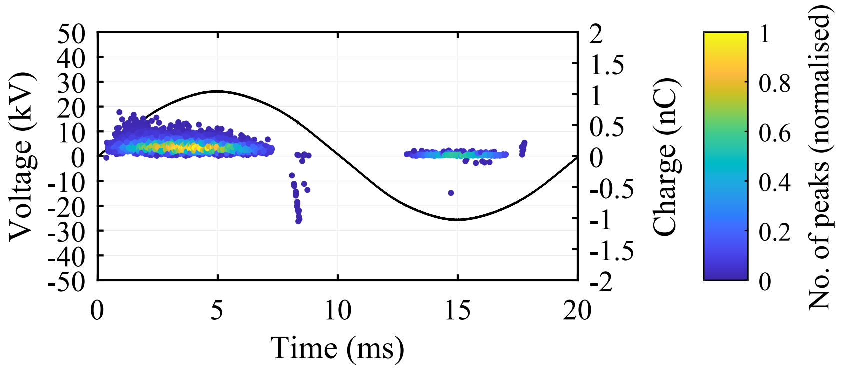

Figure 5.26: Charge density for silicone rubber 4 mm thick insulator sample in carbon dioxide (CO_2) at 1 bar absolute pressure.

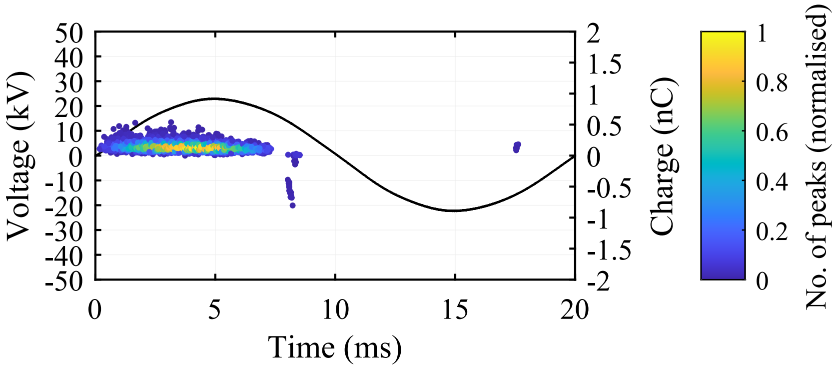

Figure 5.27: Charge density for epoxy resin 4 mm thick insulator sample in carbon dioxide (CO_2) at 1 bar absolute pressure.

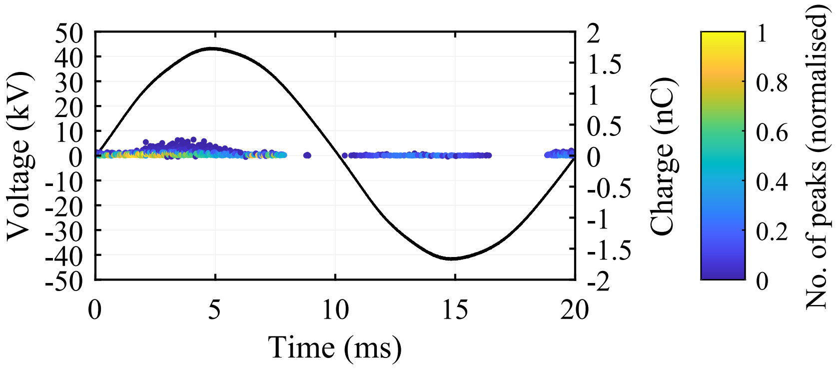

Figure 5.28: Charge density for PTFE 4 mm thick insulator sample in 30/70 % CF_3I/CO_2 at 1 bar absolute pressure. Test voltage was 30 kV rms.

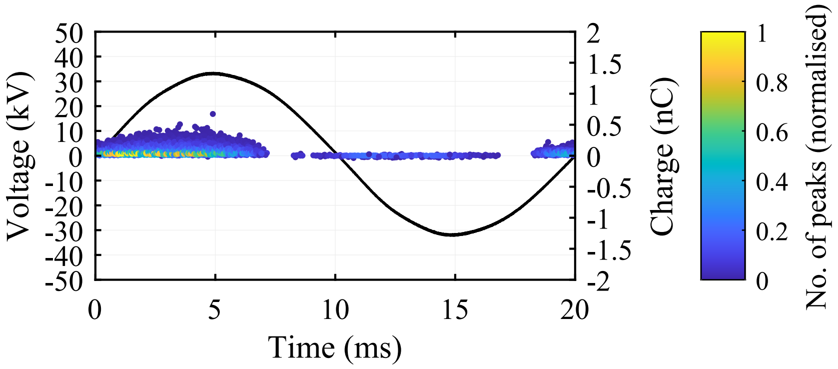

Figure 5.29: Charge density for epoxy resin 4 mm thick insulator sample in 30/70 % CF_3I/CO_2 at 1 bar absolute pressure. Test voltage was 22.96 kV rms.

On initial examination, a clear difference between the cases of different gaseous insulating media is observed. Since the calculated apparent charge values are directly linked to the current pulse characteristics, examples of which were shown in Tables 4.1 and 4.2, it is reasonable that these graphs mostly reflect the influence of the gaseous insulating medium. It is clear that the higher the electron attaching capability of the gaseous medium is, the lower the calculated apparent charge values will be, which is expected considering the very short duration of the generated current pulses. When the low electron attaching capability nitrogen is involved, apparent charge magnitudes increase significantly, but the number of generated pulses is far less compared to the 30/70 % CF_3I/CO_2 mixture with pulse repetition rates 184 pulses/second and 37420 pulses/second respectively.

The second batch of graphs is produced from the data shown in Figures 5.13 to 5.18 with the outputs corresponding to insulator samples of 6 mm thickness.

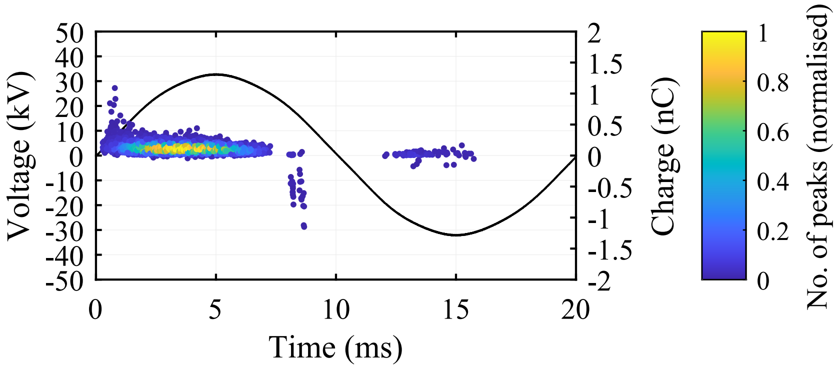

Figure 5.30: Charge density for PTFE 6 mm thick insulator sample in carbon dioxide (CO_2) at 1 bar absolute pressure.

The differences between the various insulating gaseous media are again visible. Gases of higher electronegativity are found to show considerably lower calculated peak apparent charge values compared to the lower electron attaching capability gases. Also, it could be said that thicker samples result in a more intense activity and slightly higher calculated peak apparent charge values (Figures 5.28 and 5.33) especially for insulating gases of higher electronegativity. A possible explanation is that thicker samples may

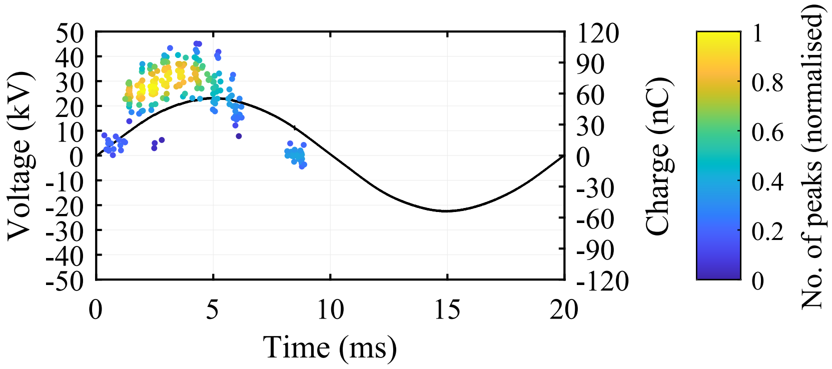

Figure 5.31: Charge density for epoxy resin 6 mm thick insulator sample in nitrogen (N_2) at 1 bar absolute pressure.

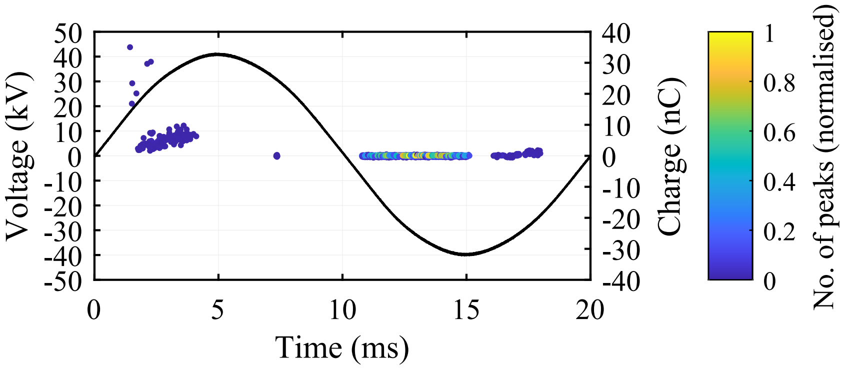

Figure 5.32: Charge density for silicone rubber 6 mm thick insulator sample in technical air (21/79 % O_2/N_2) at 1 bar absolute pressure.

support a more localised discharge activity around the needle tip which must be a result of a more abrupt decrease on the electric field on the surface of the insulator sample when moving away from its centre towards the edges of the sample.

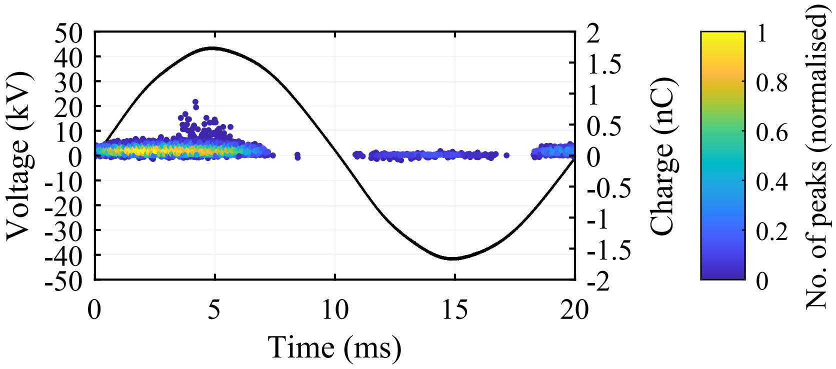

Figure 5.33: Charge density for PTFE 6 mm thick insulator sample in 30/70 % CF_3I/CO_2 at 1 bar absolute pressure. Test voltage was 30 kV.

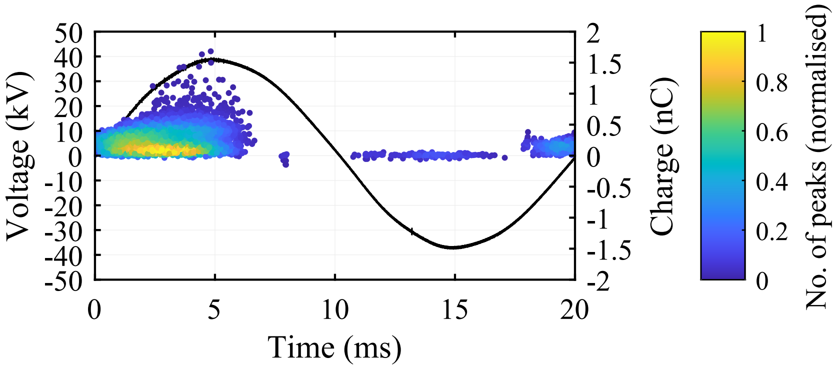

Figure 5.34: Charge density for silicone rubber 6 mm thick insulator sample in 30/70 % CF_3I/CO_2 at 1 bar absolute pressure. Test voltage was 26.83 kV.

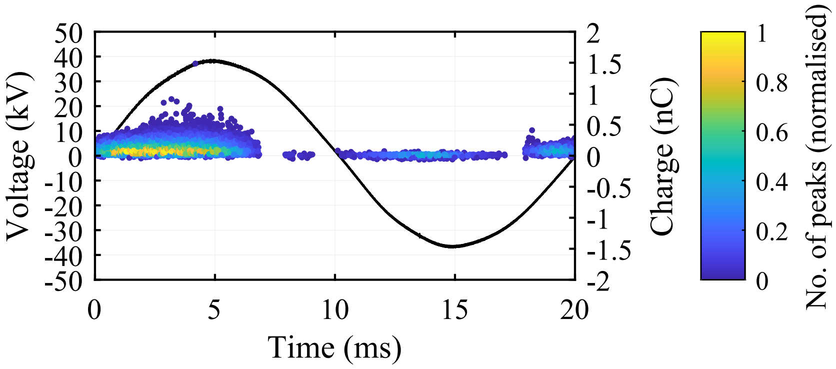

Figure 5.35: Charge density for epoxy resin 6 mm thick insulator sample in 30/70 % CF_3I/CO_2 at 1 bar absolute pressure. Test voltage was 26.50 kV.

In order to quantify part of the presented measurements, three parameters are further calculated from the illustrated data. These are, the pulse repetition rate expressed in pulses per second (pulses/sec), the quadratic rate expressed in C^2/s and the accumulated apparent charge expressed in coulombs (C). The definitions of the first two can be found in the Appendix A.5 while the accumulated apparent charge is defined as the sum of all the charge values recorded within the specified time interval. Reference [133] provides a more descriptive definition of the quadratic rate term indicating that this quantity assigns a greater weight to the larger values which seems reasonable as it expresses the sum of the squares of the individual apparent charge magnitudes divided by the time interval of the recording. In [134], for the same parameter is stated that it helps monitoring insulation state over time which is useful clarification on the interpretation of this quantity when tests conducted in the minute time-scale or longer.

Table 5.1: Comparative analysis of selected charge density plots.

Gaseous medium	**Sample**	**Pulse repetition rate** (pulses/sec)	**Quadratic rate** (C^2/s)	**Accumulated apparent charge** (C)	**Figure**
21/79 % O_2/N_2	PTFE-4	19752	$5.13 \cdot 10^{-14}$	$1.89 \cdot 10^{-6}$	Figure 5.19
N_2	PTFE-4	184	$5.95 \cdot 10^{-13}$	$2.93 \cdot 10^{-6}$	Figure 5.22
CO_2	PTFE-4	7866	$2.05 \cdot 10^{-16}$	$4.61 \cdot 10^{-7}$	Figure 5.25
30/70 % CF_3I/CO_2	PTFE-4	37420	$3.72 \cdot 10^{-17}$	$4.23 \cdot 10^{-8}$	Figure 5.28
21/79 % O_2/N_2	ER-4	15520	$5.50 \cdot 10^{-14}$	$3.63 \cdot 10^{-6}$	Figure 5.21
N_2	ER-4	550	$1.09 \cdot 10^{-12}$	$7.32 \cdot 10^{-6}$	Figure 5.24
CO_2	ER-4	8572	$2.24 \cdot 10^{-16}$	$5.99 \cdot 10^{-7}$	Figure 5.27
30/70 % CF_3I/CO_2	ER-4	36044	$3.09 \cdot 10^{-16}$	$1.26 \cdot 10^{-6}$	Figure 5.29
CO_2	PTFE-6	7934	$1.80 \cdot 10^{-16}$	$4.62 \cdot 10^{-7}$	Figure 5.30
30/70 % CF_3I/CO_2	PTFE-6	29942	$3.19 \cdot 10^{-16}$	$1.31 \cdot 10^{-6}$	Figure 5.33
30/70 % CF_3I/CO_2	ER-6	27700	$7.08 \cdot 10^{-16}$	$1.71 \cdot 10^{-6}$	Figure 5.35

The first four rows of Table 5.1 show the case of PTFE 4 mm thickness in all the experimentally investigated gases. The highest pulse repetition rate is observed for the case of 30/70 % CF_3I/CO_2 although, for the same case, the quadratic rate and accumulated charge are the lowest. Practically that means the discharge activity is quite intense but small in magnitude with pulses that are very short in duration. In comparison, N_2 has a pulse repetition rate of 184 pulses/sec however, the accumulated apparent charge is the highest calculated when PTFE 4 mm is tested. Technical air is more intense than CO_2 likely because of the very intense negative polarity discharge activity during the negative half-cycle of Figure 5.19.

In the next four rows, where epoxy resin of 4 mm thickness is presented, nitrogen shows the same characteristics as happened for PTFE 4 mm. The pulse repetition rates show also the same pattern as before although the comparison of CO_2 and 30/70 % CF_3I/CO_2 show that the difference in the applied voltage level has a considerable impact in the obtained calculations of quadratic rate and accumulated apparent charge. It is worth reminding that the applied voltage levels are specified relevant to the corresponding FOV levels for the cases obtained.

Comparing the cases of PTFE 4 and 6 mm in CO_2, it seems that there is no significant difference in the calculations. It could be assumed that the discharge events at this voltage level are more local in their appearance despite the difference in absolute applied voltage levels. For the same samples this time in 30/70 % CF_3I/CO_2 the discharge activity seems to be less intense for the thicker sample although the accumulated apparent charge is higher and the quadratic rate also higher which is also visible in Figure 5.33. The same happens when epoxy resin of 4 and 6 mm in 30/70 % CF_3I/CO_2 are compared. A possible practical explanation is that when the thicker sample is used and the gap distance is longer then discharges of very small magnitude, very close to the baseline of the time-resolved recording, become very intense. For these pulses it will be more difficult to accurately calculate the apparent charge. At the same time, if the difference between high and small magnitudes is very large then in the calculation of the quadratic rate this difference will be further enhanced. The other explanation is that the thicker sample will result to a higher electric field on the needle tip, as it was shown in Figure 4.12. The discharge that is sensed for 30/70 % CF_3I/CO_2 is localised around the needle tip and they do not propagate, at this applied voltage level, further on the surface of the solid dielectric. In such a case the dielectric thickness seems to have an impact on the discharge activity. In the future, both points made above will be addressed and clarified in additional experimental campaigns.

5.5 Discussion and conclusions

Even if the recordings described in Chapter 4 incorporate a small set of data, still the differences between the different gaseous compounds were quite clear. Larger datasets always contribute to more converging observations and this was attempted to be achieved in this chapter.

The compromise in the presented measurements was that the sampling rate was decreased in an attempt to maximise the capability of capturing larger amounts of data within the same test attempt. The unique patterns of each different gaseous medium are again observable. Overall, it could be said that materials of higher relative permittivity showed denser discharge activity which was observable also during the positive AC half-cycle. As the divergence in the relative permittivities of the tested dielectrics (gaseous and solid) increases, the discharge activity becomes more intense. Back-discharges are also present during each half-cycle, but the correlation between the magnitudes of this kind of discharges and the preceding forward ones need to be assessed following a test process which will be more focused on this type of interaction. The thickness of the insulator sample showed a more considerable impact when atmospheric gases were investigated. It could be assumed that the stronger attaching mixture of 30/70 % CF_3I/CO_2 showed the smallest difference when the sample thickness was increased and for the tested applied voltage levels. For the same gas mixture, the density of the discharge activity was found to be higher compared to atmospheric gases and of considerably high magnitudes. Both observations could be attributed to the fact that such mixtures are proven to be “brittle”, i.e., when the critical electric field is exceeded, the growth of ionisation is very strong [132, 135].

The charge density plots, as these were produced by further processing the data of the corresponding current density plots, is proved to be more informative as practically the calculated apparent charge summarises the discharge current pulse characteristics. With such an illustration, it can be clearly demonstrated the difference between the atmospheric gases of technical air, nitrogen and CO_2 and the 30/70 % CF_3I/CO_2 mixture. During the positive half-cycle of the sinusoidal wave, the density of the discharge activity is much lower in technical air and nitrogen compared to CO_2 and CO_2/CF_3I. However, the apparent charge magnitudes are much higher. It could be said that, CO_2 is more effective in suppressing high induced electric fields compared to the other two atmospheric gases. This is validated by the lower calculated values of quadratic rate and accumulated apparent charge for the case of CO_2 when compared with technical air and N_2 with the solid sample types. Also, visually, the charge patterns for CO_2 are comparable to the ones of the 30/70 % CF_3I/CO_2 mixture despite the applied voltage levels are not the same. The mixture of CF_3I/CO_2 shows a very high pulse repetition rate although that does not reflect to proportionally increased accumulated apparent charge. It could be said that such mixtures are sensitive to PD activity, once the requirements for their appearance are fulfilled, however, the activity as severe in terms of accumulated apparent charge. The comparative analysis will be further improved in future works with even more refined recording and post-processing processes.

Chapter 6

High-speed surface discharge photography

6.1 Introduction

One of the characteristics of partial discharges is light emission, which can result from various processes such as excitation and recombination. Detection systems for light emission can be distinguished in two different general categories [136] considering the more practical application of the method. The first is applicable for discharge phenomena that appear on components and equipment that are partially or entirely insulated by atmospheric air. Considering the solar UV radiation during daytime, UV corona detection camera systems are more suitable. The second refers to enclosed equipment where the ambient light cannot enter the sealed volume. The use of optical fibres for light collection and transmission to a photocathode-based device, such as a photomultiplier, is frequently used [136, 137]. In this way, the emitted and collected light is converted to an electrical signal for recording and further processing.

In this chapter, the capturing of surface discharge activity using a photographic method will be presented. For this purpose, a camera system which combines a high-speed fast-triggering camera combined with a UV image intensifier is proposed and explored. The UV-intensified high-speed camera system is triggered by the current sensing circuit, achieving an event-based recording and PD capturing overall system. Special attention is paid to the technical specifications of the utilised accessories and equipment to maintain the maximum possible accuracy in both frequency response of the recorded signals and the optical requirements of the capturing system. It should to be noted that the high-speed imaging technique, such as the one presented in this chapter, is one of the various methods that have been proposed particularly for the study of surface discharges. Examples of other methods include electro-optical Pockels effect [14–16, 18, 138] and Dust figure technique [15], as these were described previously in Section 2.5.

Two approaches are followed for the capturing of the discharge activity. For the first, captures of longer duration are adopted. The purpose of this is to identify the pattern the surface discharges develop in the duration of the full or half AC-cycle. In that way, it will be possible to observe how such phenomena appear from the zero-crossing of the AC-wave until its peak and from the peak to the zero-crossing again. In the second approach, it is aimed to capture individual discharge events while, at the same time, recording the corresponding the PD current pulse. In that way, it will potentially be possible to observe how the unique pulse characteristics of each gaseous medium reflect on the generated discharge channels and, also, correlate the discharge current magnitude with the overall morphology of the activity.

6.2 Experimental set-up

This section describes in detail the experimental approach and set-up with focus on the technical specifications of the equipment and components used. An illustration of the full experimental set-up is shown in Figure 6.1 [139].

The experimental set-up shown above is practically divided in four sub-systems:

(i). Electrode configuration,
(ii). Current sensing circuit and recording,

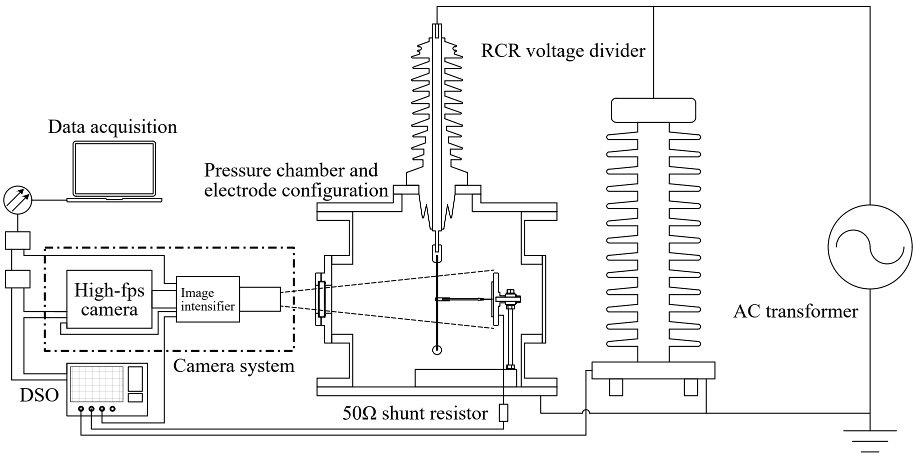

Figure 6.1: Full experimental set-up [139].

(iii). High-speed image capturing camera system, and

(iv). High voltage application

Each of the sub-systems listed above will be described in separate sub-sections as it will be shown next.

6.2.1 Electrode configuration and test object

As it was explained in Section 4.2.2, the main purpose of the needle-plane electrode configuration, among others, is to replicate strongly non-uniform electric field conditions. For this purpose, a very similar needle-plane electrode configuration to the one described in Chapters 4 and 5 was employed. The main difference is that, this time, the orientation of the electrode arrangement is horizontal with the insulator sample surface facing the side viewport of the pressure vessel. The electric field distribution on the top surface of the disc-shaped was again examined from a finite element method (FEM) simulation perspective. It was shown that no considerable differences between the horizontal and the vertical orientation geometries occur and so the conditions of the two different experiments can be considered as similar. The relevant simulation models are extensively described in the Appendix B. This time two different insulator sample materials are investigated namely PTFE with $\varepsilon_{\text{PTFE}} = 2.1$ and epoxy resin with

$\varepsilon_{\mathrm{ER}} = 3.5$. Atmospheric gases, namely technical air (21/79 % O_2/N_2), nitrogen (N_2) and carbon dioxide (CO_2) as gaseous insulating media were investigated. Figure 6.2 shows a picture of the electrode configuration as installed inside the pressure chamber.

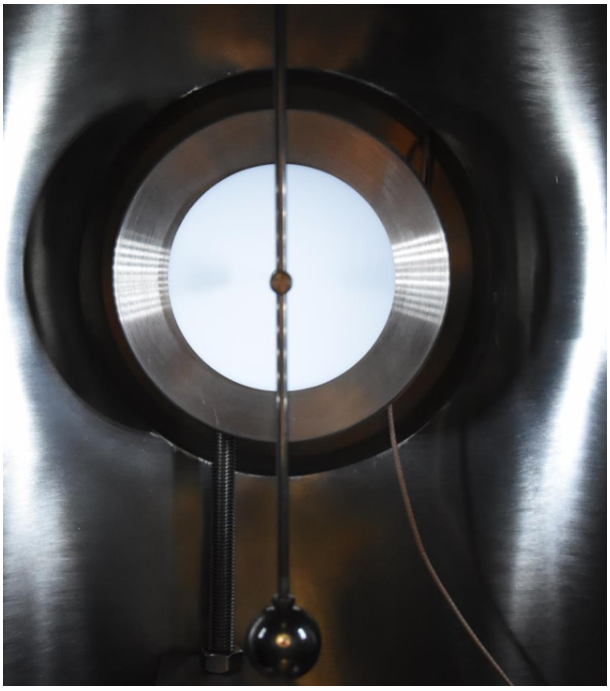

Figure 6.2: Horizontal orientation of the electrode configuration as installed inside the pressure vessel and seen from the side viewport.

6.2.2 Current sensing circuit and recording

The detection of the discharge activity was performed using the shunt resistor technique as this was extensively described in the Section 3.9.3.1.2. A 50 Ω/20 W load termination was installed in series with the grounded plane electrode through a coaxial surface mounted connector (Figure 3.22). An inline coaxial surge suppressor, rated at 90 V, is added for the overvoltage protection of the recording devices in case of unexpected flashover events. Same as was done for the HFCT, the frequency response of the sensing circuit was again validated by measuring the scattering parameters using a 50 Ω two-port calibrated 9 kHz − 6 GHz vector network analyser (VNA), the results of which were shown in Figure 3.23. Figure 6.3 shows the different recordings after injecting pulses of charge magnitudes varying from 10000 pC down to 10 pC, same as it was shown in Figure 4.7 for the case of the HFCT.

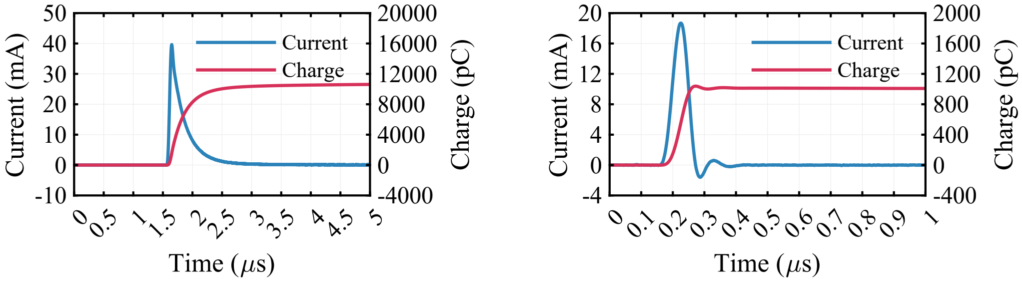

(a) 10000 pC **(b)** 1000 pC

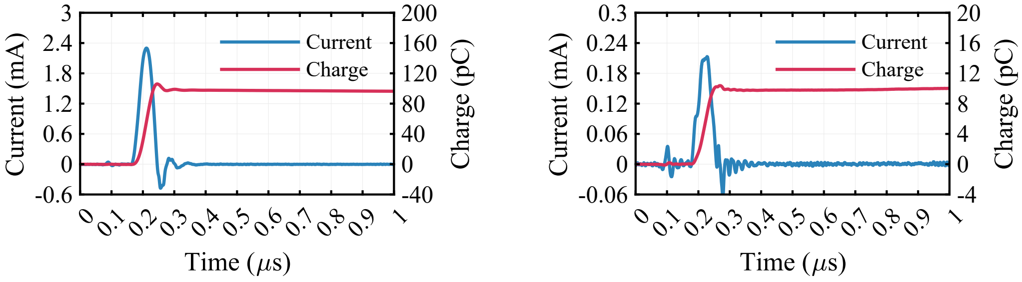

(c) 100 pC **(d)** 10 pC

Figure 6.3: Current measurements using a charge injector/calibrator and the shunt resistor current sensing technique.

It can be clearly seen that the calculated apparent charge matches the charge injected by the calibrator. Even current pulse signals lower than 1 mA in magnitude, can be satisfactorily detected. Compared to the corresponding measurements when the HFCT was calibrated (Figure 4.7), the detected pulse when a charge of 10 pC is injected is clearly reproduced which is helped by the higher amplification of the current signal combined with the lower rated noise on the DSO because of the higher vertical resolution (V/div) used.

For the recording of the waveforms associated with the applied voltage and the generated current signals, a Teledyne LeCroy HDO6104, 1 GHz, 2.5 GS/s, 12-bit oscilloscope was used. The triggering set-ups were adjusted according to the experimental requirements, and this will be extensively described in the corresponding section.

6.2.3 Image intensified high-speed camera system

6.2.3.1 Components and system assembly

The camera system comprises of a UV image intensifier UVi 1850-10-S20, manufactured by Invisible Vision Ltd., incorporating an S20 photocathode mounted on the front of a monochromatic 8-bit Photron SA5 high-speed camera through a Nikon 50 mm f/1.4 lens. A Nikon UV-105, 105 mm f/4.5 lens is installed on the optical input of the intensifier pointing towards the electrode configuration and with the focus adjusted on the surface of the insulator sample. On the side viewport of the stainless-steel pressure vessel, a UV-grade calcium fluoride (CaF_2) glass window is mounted.

The spectral response of the image intensifier ranges from 200 nm to 600 nm while the UV lens is chromatically corrected in the range of $220 - 900$ nm. The UV-grade glass window provides a transmission efficiency greater than 93 % within the range between 200 nm to 7 μm ensuring that the light emitted from the discharge events will not be reflected on its surface. Figure 6.4 summarises the transmittance rate curves for the components of the optical detection system. The UV filter consists of a bandpass filter with centre wavelength at 340 nm and a transmission rate greater than 80 %.

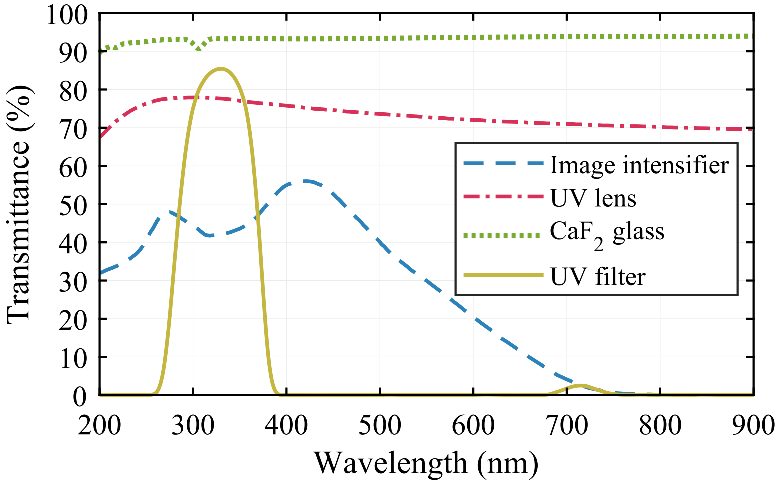

Figure 6.4: Spectral response of the optical system components.

High-speed cameras that employ CMOS sensors show low efficiency in the lower visible wavelength range. For that reason, an image intensifier is employed to enhance the efficiency of the system within the low VIS and the ultraviolet (UV) spectra. The bandpass filter is installed on the front of the UV lens in order to block the visible (VIS) light spectrum and allow only UV to transmit. The whole system is placed at a certain distance from the test object and with accordance to the focal length of the lens. A mat black painted pipe is installed between the UV lens and the side viewport of the pressure vessel to prevent ambient light from reaching the UV lens front. Figure 6.5 shows the set-up of the optical system before starting the test procedure.

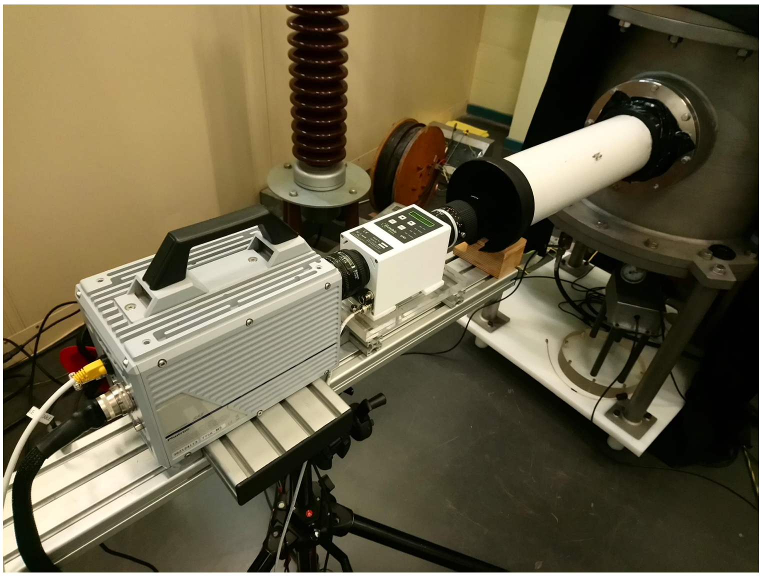

Figure 6.5: Set-up of the UV-intensified high-speed camera system.

6.2.3.2 Operation of the the new camera system and synchronisation with electrical measurements

The challenge for the described camera set-up is related to the synchronisation of all the devices involved: oscilloscope, high-speed camera and UV image intensifier. The high-speed camera and the UV image intensifier incorporate their own shutters which need to operate accordingly during the same time intervals so that the light emitted by the generated discharge activity ultimately reaches the high-speed camera sensor. The operation of the image intensifier photocathode requires to preset an exposure and a delay time which can be implemented in a sequence pattern. These input values are defined based on the recording speed set on the high-speed camera, measured in frames per second (fps), considering also slight delays in the response of the devices. For example, a recording speed of 1000 frames per second will effectively keep the high-speed camera shutter open for 1ms before it closes and opens again in order to record the next frame. This is the time interval during which the UV image intensifier shutter is required to be open. Setting an exposure at 950 μs and a delay time at 20 μs will allow the recording of phenomena that appear during the exposure time maintaining at the same time a sufficient margin of 30 μs to tolerate potential small delays in the response of the devices. Figure 6.6 shows an example of a recording where together with the voltage and generated current signals, the intensifier TTL (transistor-transistor logic) output is included (in green colour).

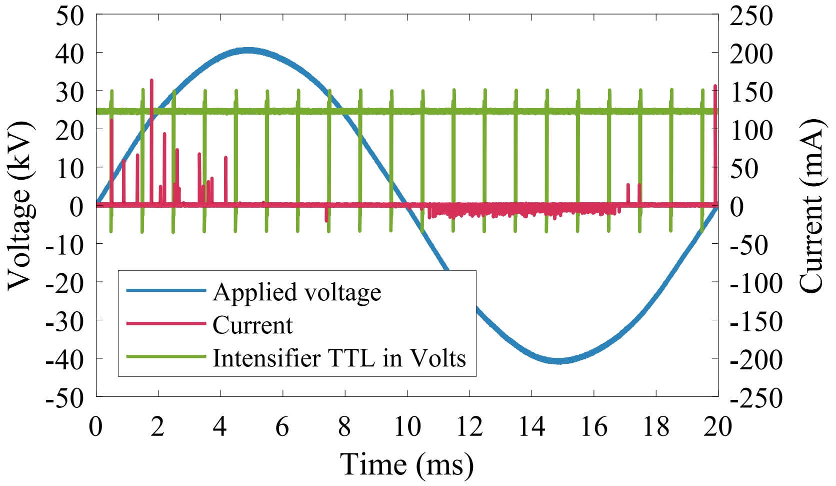

Figure 6.6: Example of recording including the UV-intensified high-speed camera system TTL output.

When the square pulse of the image intensifier TTL output is greater than zero, the shutter is considered open which means that the photocathode is exposed to the input light. The duration of the square pulse equals the pre-set exposure time, which in

Figure 6.6 equals $950\,\mu$s, while the time gap between two consecutive pulses will equal the delay time plus the response delay of the device which is normally a few tens of nanoseconds. If one or more recorded current pulses fall within the exposure duration, they are expected to appear on the corresponding frame of the high-speed camera. For this specific trigger set-up, the high-speed camera is set to generate a TTL square pulse, of around $5\,$V magnitude, at the beginning of each frame. This pulse will be used as an input to the intensifier trigger and, when received, the preset delay time will start counting and right after that the shutter will open for a duration equal to the preset exposure pattern. The high-speed camera will start to record in the preset frame speed once a TTL square pulse is received from the auxiliary output of the oscilloscope.

The trigger set-up described above is very effective when long exposure recordings are required. During this type of recording, more than one discharge events may be captured within the same frame which, in cases where the discharge activity is very intense, it may cause several discharge phenomena to overlap each other. However, the main advantage is that a very good overview of the generated discharge activity pattern can be observed in the duration of a full AC-cycle.

For cases where single discharge events need to be captured, the trigger set-up needs to be adapted to operate based on the occurrence of these events. The implementation of this set-up will be explained with reference to Figure 6.7.

The input signal (blue curve) comes from a signal generator and effectively represents a fast-rising time current pulse that can potentially appear during the actual test process. The red curve is the auxiliary output of the LeCroy HDO6104 oscilloscope which is set to generate a pulse during the arm state of the device meaning that the fall time of this pulse will coincide with the time instant when a trigger is generated (vertical dashed line). The high-speed camera is set to trigger during the rise time of the auxiliary output pulse and to record one single frame for each trigger pulse it receives. The duration of such frame depends on what is considered more efficient for the resolution and recording speed requirements of the particular experiment. The state of the image

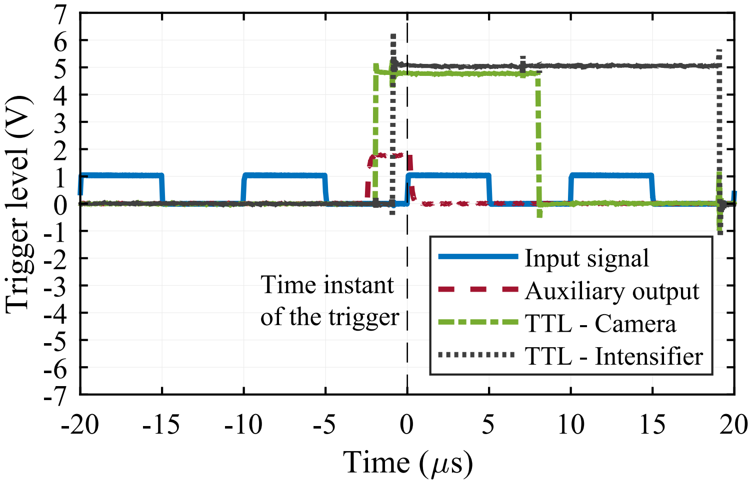

Figure 6.7: Synchronisation of triggers for an event-based recording.

intensifier shutter will become ON once the TTL pulse from the high-speed camera has arrived to its coaxial trigger input. When the shutter opens, the image intensifier will generate another TTL pulse (black curve), the duration of which will equal the preset exposure time, which as illustrated in the example of Figure 6.7 is set to 20 μs. With this set-up, it is possible that each detected current pulse will always fall within one single frame. All this process is implemented in a sequence triggering operation of the digital oscilloscope with the duration of each segment set at 20 μs. The number of segments may vary according to the sample rate and the available memory size. Figure 6.8 shows an oscilloscope screenshot showing the recording after a test attempt implemented with a sequence triggering operation of 100 segments. The signal in yellow is the recorded voltage magnitude, the generated current pulses are in red and, in blue, the 5 V TTL output of the image intensifier.

If the high-speed camera is set to record a frame of full resolution, usually 1024×1024 px, then a recording speed up to 7000 frames/second can be achieved. In this case, the time interval between two consecutive frames is less than 0.15 ms. It should be expected by the user that when the time window is 0.15 ms and the exposure time on the image intensifier is 20 μs, the light emitted from the generated discharge activity will not be captured for the duration which corresponds to the time difference between

Measure	P1:rms(C1)	P2:const	P3:(P1*P2)	P4:max(Z2)	P5:rise(Z2)	P6:fall(Z2)	P7:width(Z2)	P8:- - -
value	10.220 V	3.750000000e+3	38.33 kV	2.42 V	146.065 ns	191.052 ns	66.016 ns	
status	✓	✓	✓	✓	✗	✗	✗	

Figure 6.8: Oscilloscope screenshot after performing a segmented recording.

these two values.

It is recommended that both triggering techniques are implemented. With the first, the user will be able to observe the entire discharge pattern during the full duration of the alternating applied voltage cycle which later will help to set up the second trigger technique to obtain more focused observations.

6.2.3.3 High-voltage application

The test voltage is applied using the same set-up at this was described in Section 3.8 and illustrated in Figure 3.13. Again, an AC waveform at power frequency (50 Hz) generated from a test transformer rated at 50 kV/3.75 kVA was applied. During testing, the applied voltage is gradually increased to the required levels, implementing a voltage ramp increase as described in Section 3.9 [20].

Test voltage levels are specified to 80 % of the corresponding flashover levels (Figure 4.11) for each insulating gas/insulator sample combination [9]. The margin is maintained for the safety of both the recording and image capturing equipment. Unexpected flashover events, even if short in duration, can generate amounts of light that can be harmful for the photocathode of the image intensifier and thus should be avoided. The camera and signal recording systems are powered through a battery system (12 V batteries and a 10 kW inverter) so that all the sensitive equipment is at floating potential. Data acquisition devices are electrically isolated from the experimental set-up through digital to optical converters.

6.3 Test results of synchronised electrical and photography systems

When performing tests that require the synchronisation of multiple devices, it is important to ensure the accuracy in the response of these devices and the repeatability of the outputs. A first round of preliminary tests were performed to ensure that the signal recordings synchronise sufficiently with the camera system. In the second round, everything within the experimental set-up was set to optimal conditions in order to verify the repeatability of the outputs. It is rather challenging and time demanding to keep everything to the maximum possible quality since several technical factors need to be balanced and all the devices need to be adjusted/calibrated before each test round. Synchronisation of the triggers, focus of the lenses, gain set on the image intensifier, minimising ambient light, sampling rates on the recording devices, recording speed on the high-speed camera, proper exposure and delay times for the image intensifier shutter are some of the important factors that were considered in this work, and all have been verified to have an impact on the quality of the outputs and the execution of the test process. After all the control and quality checks were adjusted to acceptable levels, the main round of tests was performed.

The results presented here are classified into two main categories based on the trigger settings described previously in Section 6.2.3.2. The detected surface discharges are classified into two main categories based on the polarity of the recorded current signals and applied voltage AC waveform. When the current pulse and the voltage polarities are the same, a forward discharge takes place while, when they are of opposite polarity, a back-discharge occurs. As an example, Figure 6.9 shows the distinction between the different regions in the duration of a full AC-cycle. This classification was also followed in Chapter 4 and was described again in Section 4.6.

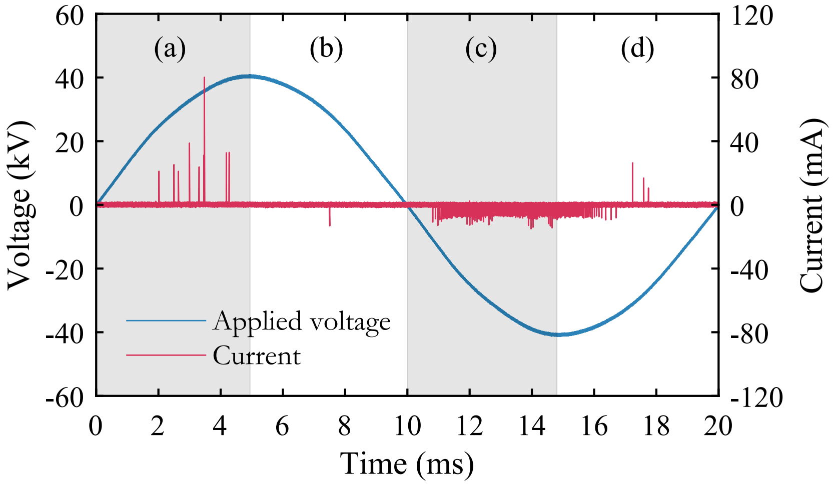

Figure 6.9: Full 50 Hz AC-cycle recording of applied voltage and generated current. Here, the case of PTFE 6 mm thickness in technical air (21/79 % O_2/N_2) at 1 bar absolute pressure is shown. Regions (a), (b), (c) and (d) are distinguished based on the polarity and slope of the applied sinusoidal voltage [139].

In Figure 6.9, region (a), starting from the zero-crossing of the applied voltage and moving towards the peak value, clearly includes positive forward discharges. Region (b) shows back-discharge activity during the positive half-cycle which appears during the falling slope of the positive AC half-cycle. Region (c) includes a big part of the negative forward discharges which appear during the rising slope (absolute) of the voltage magnitude while region (d) describes the falling slope (absolute) of the voltage magnitude and during which back-discharges also appear.

6.3.1 Long exposure time captures

In this section, captured surface discharges are presented as a sequence of frames corresponding to 950 μs image intensifier photocathode exposure time. The time window of each frame roughly sums to 1 ms, considering the preset delay on the image intensifier and the processing time of the capturing and recording devices. Figure 6.10 shows the case of PTFE 4 mm thickness immersed in technical air (21/79 % O_2/N_2) at 1 bar absolute pressure. The white dashed circle in Figures 6.10a to 6.10d represents the edges of the disc-shaped insulator sample. The distance between the vertical gray lines in Figure 6.10e represents approximately each frame's time window. Considering that the duration of each current pulse is in the sub-microsecond time scale, it is reasonable to assume that light emitted from more than one discharge event may be captured within the same frame.

An early observation is that the propagation of discharges is radial and is initiated from the centre of the insulator sample where the charged needle tip is located, and it appears moving in all directions on the insulator sample surface. Following the same presentation approach, Figure 6.11 shows the same insulator sample type this time in nitrogen (N_2) at 1 bar absolute pressure.

Again, it can be clearly seen that, as the voltage magnitude increases from the zero-crossing point towards the peak value of the positive half-cycle, the discharges appear to cover longer distances on the insulator surface. The applied rms voltage in this case is lower compared to the case of Figure 6.10. However, for both cases, it is 80 % of the corresponding rms flashover voltage level.

The capture of positive polarity forward discharges in technical air (21/79 % O_2/N_2) and nitrogen (N_2) was found to be easier compared to the case of carbon dioxide (CO_2) and for voltage levels up to 80 % of the corresponding rms flashover voltage (FOV) levels. A possible explanation is that, in CO_2, long surface discharges over the surface of the insulator samples begin to develop at voltages closer to the flashover. The discharges detected by the current sensing circuit, are of relatively low magnitude and they are likely to propagate over very short distances around the needle tip and within a small region around the electrode. For the test series involving CO_2, the pressure level inside the pressure chamber volume was decreased to 0.5 bar absolute in an attempt to reduce the density of charge carriers. The applied voltage was gradually increased

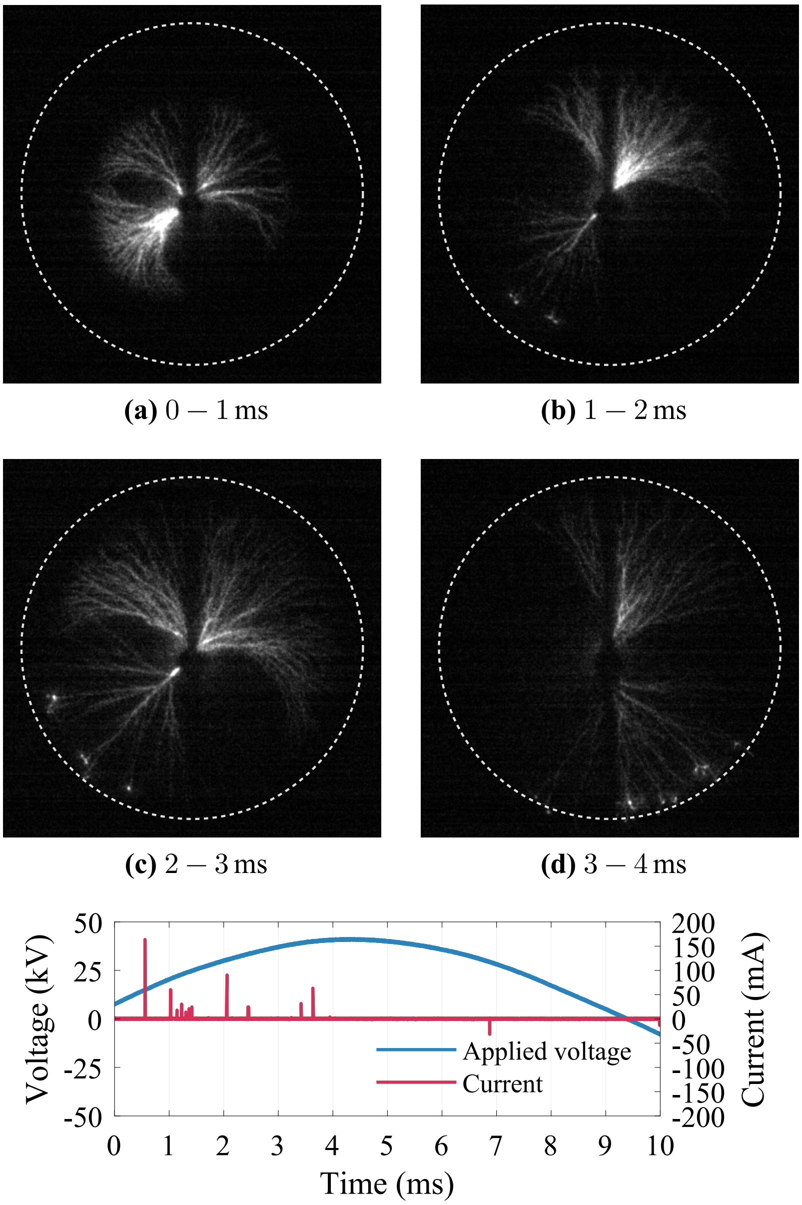

(a) 0 — 1 ms

(b) 1 — 2 ms

(c) 2 — 3 ms

(d) 3 — 4 ms

(e) Voltage and current recordings.

Figure 6.10: Surface discharge development during the rising slope of the positive half-cycle of the applied AC-voltage for the case of PTFE 4 mm thickness in technical air (21/79 % O_2/N_2) at 1 bar absolute pressure and rms applied voltage around 80 % (28.81 kV) of the corresponding FOV [139].

with a rate of 0.5 kV/s up to a level where distinct positive current pulses of high magnitude during the positive half-cycle were detectable. The corresponding captures are

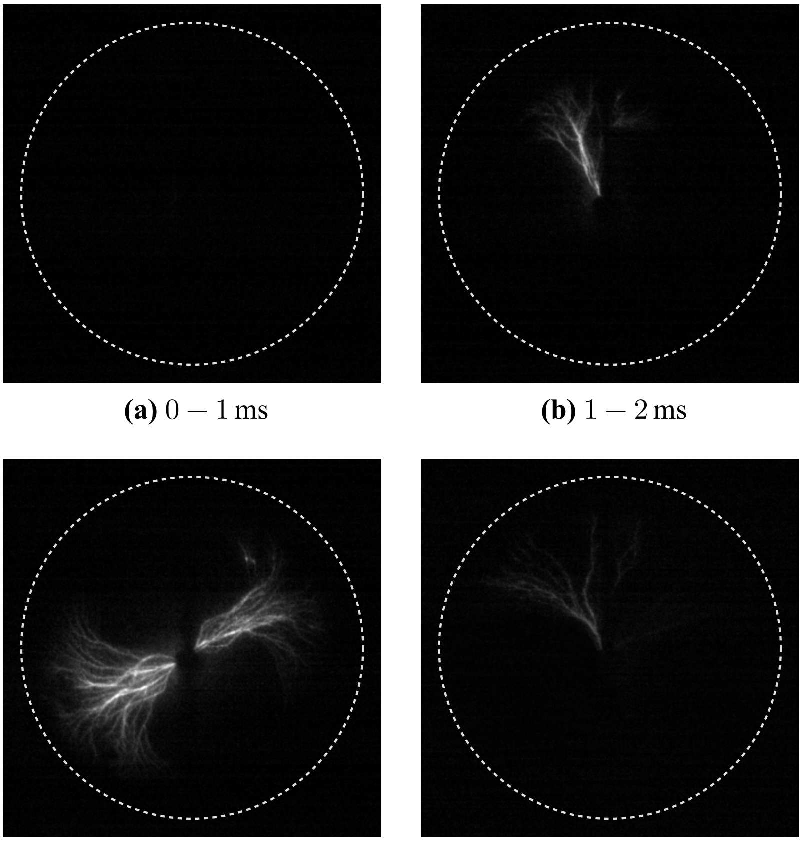

(a) $0 - 1\,\mathrm{ms}$

(b) $1 - 2\,\mathrm{ms}$

(c) $2 - 3\,\mathrm{ms}$

(d) $3 - 4\,\mathrm{ms}$

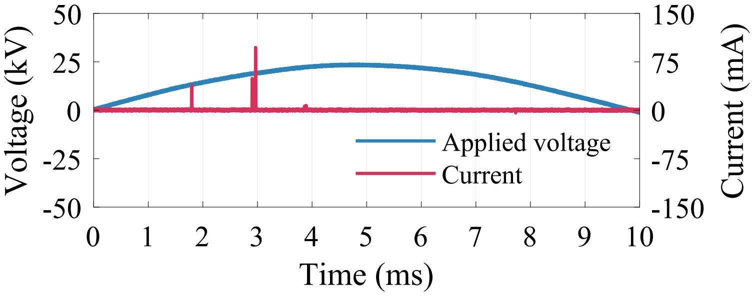

(e) Voltage and current recordings.

Figure 6.11: Surface discharge development during the rising slope of the positive half-cycle of the applied AC-voltage for the case of PTFE 4 mm thickness in nitrogen (N_2) at 1 bar absolute pressure and rms applied voltage around $80\,\%$ $(16.61\,\mathrm{kV})$ of the corresponding FOV [139].

shown in Figure 6.12. It should be noted that the intensifier photocathode gain was approaching values around $70\,\%$, much higher than for the cases of technical air and N_2

$(40 - 45\,\%)$ considering that the gain transfer efficiency in such devices is exponential and not linear.

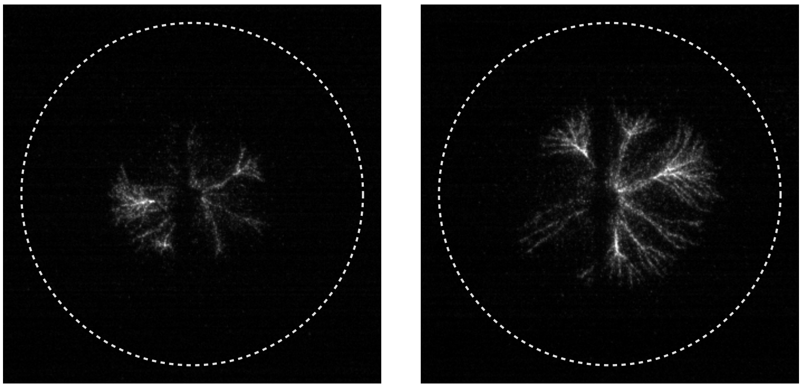

(a) $0 - 1\,\mathrm{ms}$ **(b)** $1 - 2\,\mathrm{ms}$

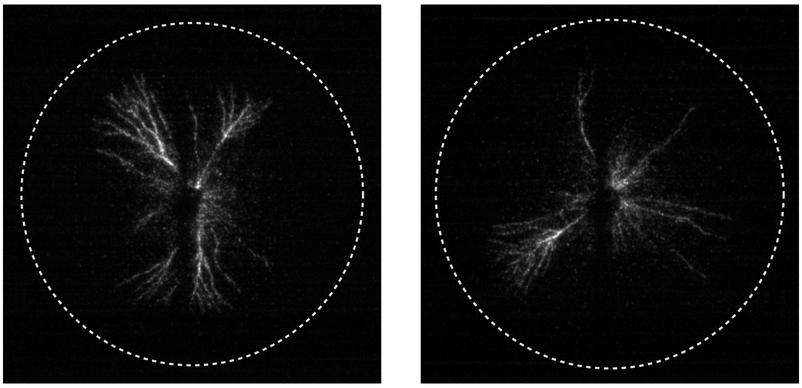

(c) $2 - 3\,\mathrm{ms}$ **(d)** $3 - 4\,\mathrm{ms}$

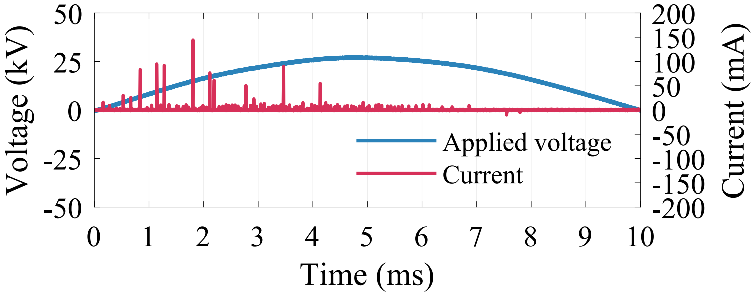

(e) Voltage and current recordings.

Figure 6.12: Surface discharge development during the rising slope of the positive half-cycle of the applied AC-voltage for the case of PTFE $4\,\mathrm{mm}$ thickness in carbon dioxide (CO_2) at $0.5\,\mathrm{bar}$ absolute pressure and $19.31\,\mathrm{kV}$ rms applied voltage [139].

The second sample material investigated was epoxy resin, the relative permittivity of which is $\varepsilon_{\mathrm{ER}} = 3.5$, higher than that of PTFE, $\varepsilon_{\mathrm{PTFE}} = 2.1$. Figure 6.13 shows the relevant recordings where the electrode configuration is further insulated by technical air (21/79 % O_2/N_2) at 1 bar absolute pressure. For this specific test, the test voltage was decreased at 70 % of the corresponding flashover level as it seemed sufficient for the generation of detectable surface discharge activity both electrically and with the camera system.

Epoxy resin of 4 mm thickness in nitrogen at 1 bar absolute pressure showed the lowest flashover withstand level (Figure 4.11) which consequently reflects on the applied voltage level shown in Figure 6.14.

Although the current pulses are relatively low in magnitude, they follow the same pattern as the cases presented previously i.e., as the voltage magnitude increases during the sinusoidal half-cycle, the propagation of the discharge activity extends further on the surface of the insulator sample. The case of PTFE this time of 6 mm thickness in technical air is shown in Figure 6.15. As no flashover occurred up to the maximum allowable level of 38 kV rms, the applied test voltage level is almost the same as for the case of the 4 mm thick sample of Figure 6.10.

It could be said that, the generated current pulses, although being of magnitude comparable to that of the 4 mm thick sample, they appear to exhibit a wider spread on the top surface of the insulator sample. For Figure 6.15c, despite there are five recorded current pulses, shown in Figure 6.15e, not all the generated discharge channels overlap with each other. However, surface discharges appear to propagate in directions where the deposited charge on the surface is not neutralised by a previous discharge event. As four main discharge channels are clearly seen to initiate from the charged needle tip, it can be assumed that within the most luminous or saturated surface region, more than one discharge event may overlap. Such a propagation pattern is more clearly visible in Figure 6.15d where the two recorded pulses, assuming that they represent two separate discharge events, they propagate in opposite directions on the insulator sample surface. The case of nitrogen (N_2) at 1 bar absolute pressure for the same sample type is shown

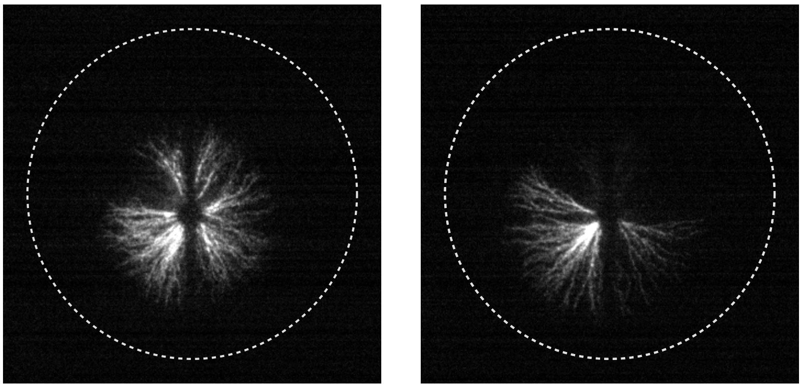

(a) $0 - 1\,\mathrm{ms}$ **(b)** $1 - 2\,\mathrm{ms}$

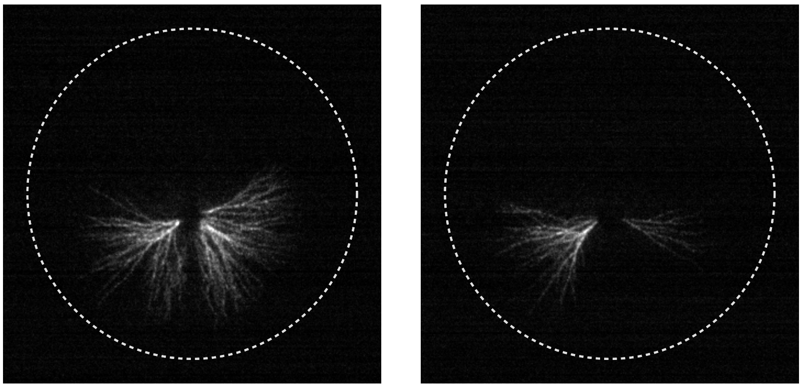

(c) $2 - 3\,\mathrm{ms}$ **(d)** $3 - 4\,\mathrm{ms}$

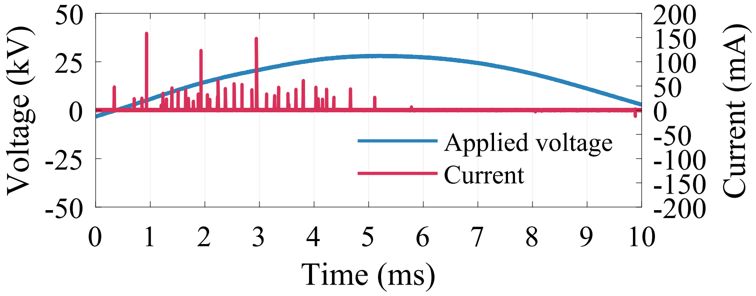

(e) Voltage and current recordings.

Figure 6.13: Surface discharge development during the rising slope of the positive half-cycle of the applied AC-voltage for the case of epoxy resin $4\,\mathrm{mm}$ thickness in technical air ($21/79\,\%$ O_2/N_2) at 1 bar absolute pressure and rms applied voltage around $70\,\%$ $(20.10\,\mathrm{kV})$ of the corresponding FOV.

in Figure 6.16.

A small magnitude pulse recorded during $0 - 1$ ms, very close to the zero-crossing

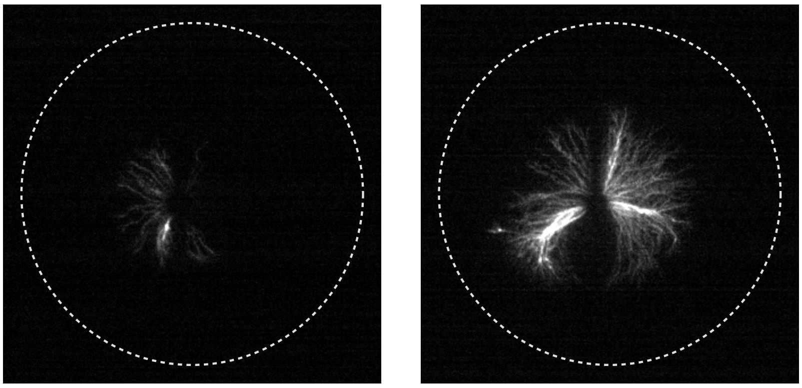

(a) $1 - 2\,\mathrm{ms}$ **(b)** $2 - 3\,\mathrm{ms}$

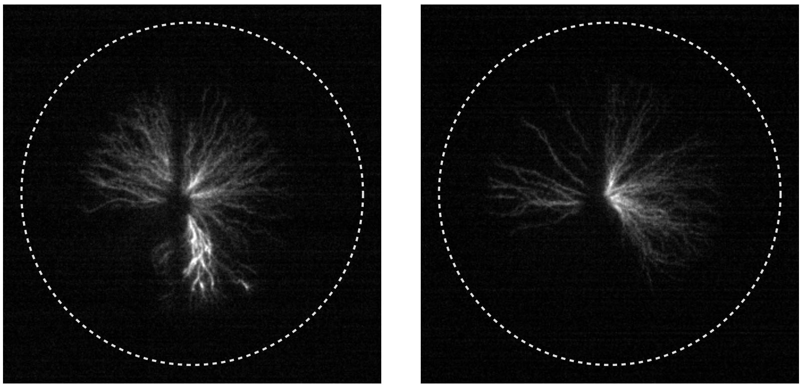

(c) $3 - 4\,\mathrm{ms}$ **(d)** $4 - 5\,\mathrm{ms}$

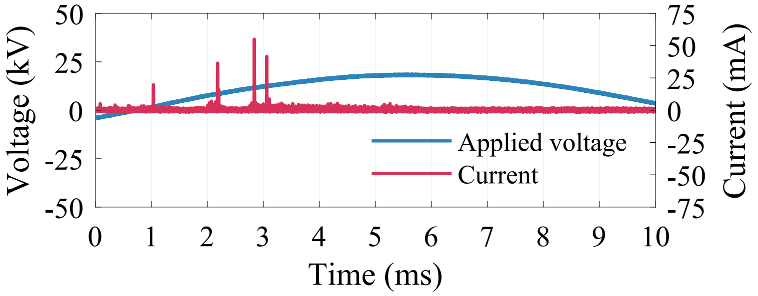

(e) Voltage and current recordings.

Figure 6.14: Surface discharge development during the rising slope of the positive half-cycle of the applied AC-voltage for the case of epoxy resin $4\,\mathrm{mm}$ thickness in nitrogen (N_2) at 1 bar absolute pressure and rms applied voltage around $80\,\%$ $(13.13\,\mathrm{kV})$ of the corresponding FOV [139].

of the applied voltage wave, showed a considerable propagation length. It seems that as the drift of charged particles, mainly positive ions and free electrons, changes di-

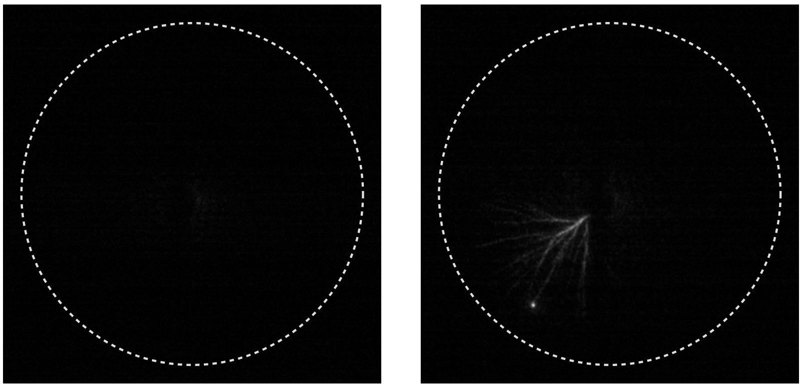

(a) $0 - 1\,\text{ms}$ **(b)** $1 - 2\,\text{ms}$

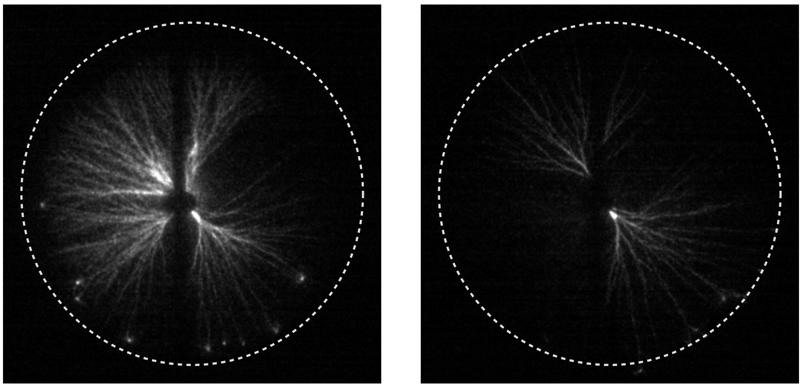

(c) $2 - 3\,\text{ms}$ **(d)** $3 - 4\,\text{ms}$

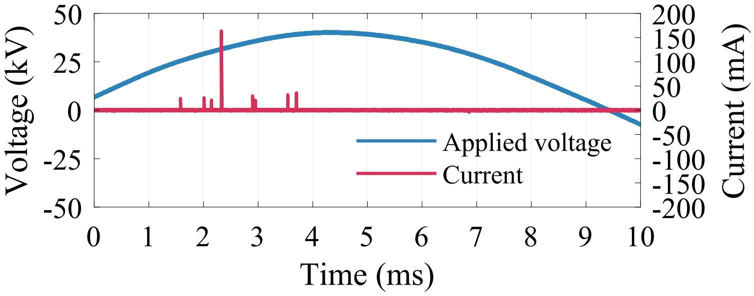

(e) Voltage and current recordings.

Figure 6.15: Surface discharge development during the rising slope of the positive half-cycle of the applied AC-voltage for the case of PTFE 6 mm thickness in technical air (21/79 % O_2/N_2) at 1 bar absolute pressure and 28.58 kV rms applied voltage [139].

rection, the resulted distribution of these charges provides the sufficient conditions for the discharge channel to propagate. In the very next time window, $1 - 2\,\text{ms}$ in Figure 6.16b, the generation of discharges becomes more intense with the appearance of

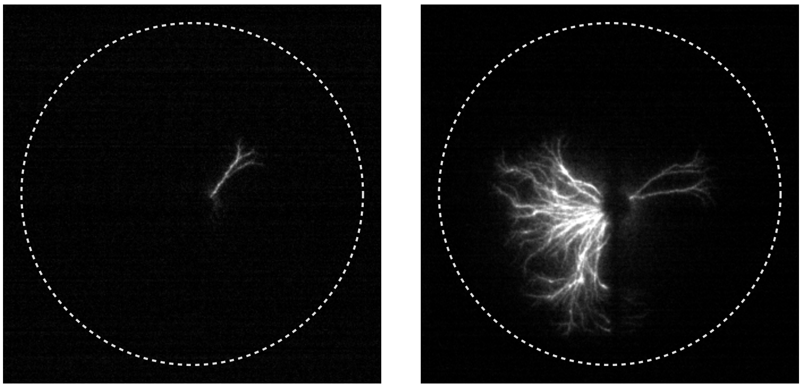

(a) 0 − 1 ms **(b)** 1 − 2 ms

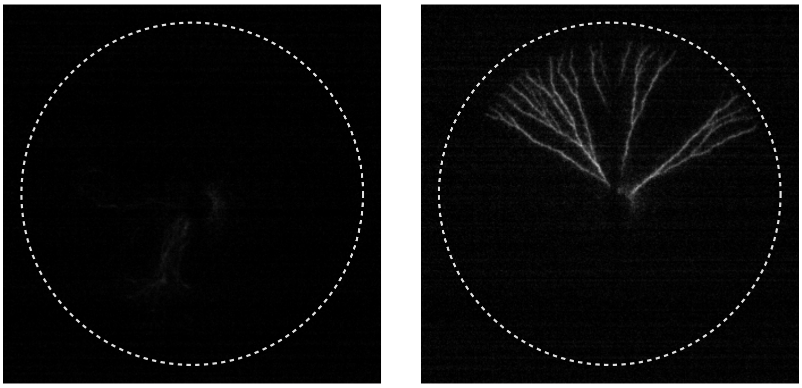

(c) 2 − 3 ms **(d)** 6 − 7 ms

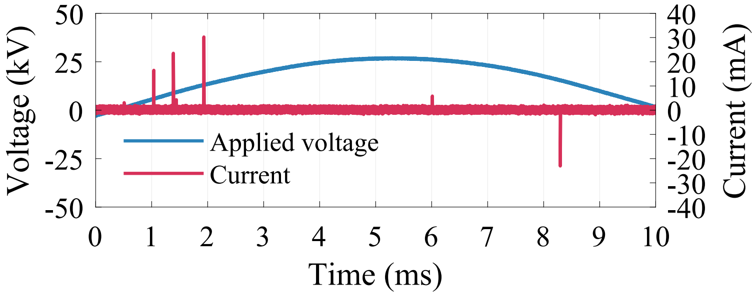

(e) Voltage and current recordings.

Figure 6.16: Surface discharge development during the rising slope of the positive half-cycle of the applied AC-voltage for the case of PTFE 6 mm thickness in nitrogen (N_2) at 1 bar absolute pressure and rms applied voltage around 80 % (18.74 kV) of the corresponding FOV.

higher magnitude current pulses. Within the chromatically saturated region, more than one discharge event are captured while a low luminosity discharge propagates to the opposite direction. Considering the relation between pulse magnitude and discharge morphology from the previous time window i.e., $0 - 1$ ms, it could be said that the small magnitude pulse, third in the sequence of appearance within the $1 - 2$ ms frame, corresponds to the low luminosity discharge of Figure 6.16b. For the same time frame, the time gap between the higher magnitude pulses, roughly 0.5 ms, could be sufficient for the charges to recover their distribution on the surface region according to their expected drift direction. The frame of Figure 6.16d also validates the correlation between the discharge morphology and the current and voltage magnitudes.

The next three sets of captures, in Figures 6.17 to 6.19, present the case of epoxy resin disc insulator of 6 mm thickness in technical air (21/79 % O_2/N_2), nitrogen (N_2) and carbon dioxide (CO_2) respectively.

For all the three atmospheric insulating gases, the generated discharges on the higher relative permittivity sample showed a more radially distributed propagation compared to the case of PTFE. Comparing the captures for samples of the same material of 4 mm thickness (Figure 6.13 and Figure 6.14) with the corresponding cases of the 6 mm thick (Figure 6.18 and Figure 6.19) the radial distribution is maintained even when the applied voltage approaches higher magnitude levels. The differences in the morphology of the generated discharges are clear between gases of different molecules such as nitrogen (N_2) and carbon dioxide (CO_2) and for all the investigated sample types. Also, the differences between nitrogen (N_2) and technical air (21/79 % O_2/N_2), where the content of N_2 is dominant, are more distinct for thicker samples of epoxy resin. The increased distance between the energised needle electrode and the grounded plane.

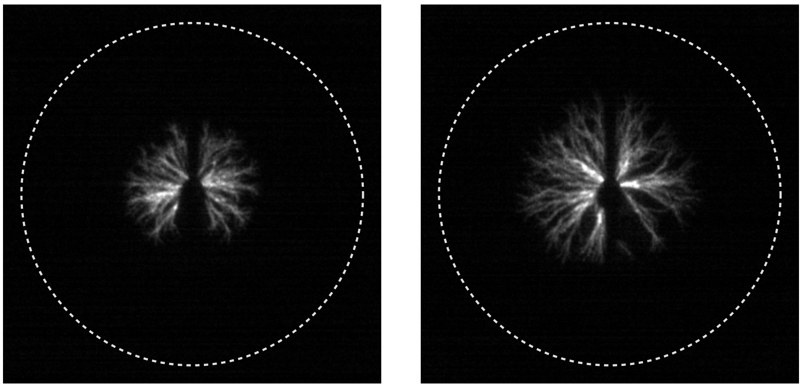

(a) $0-1\,\mathrm{ms}$ **(b)** $1-2\,\mathrm{ms}$

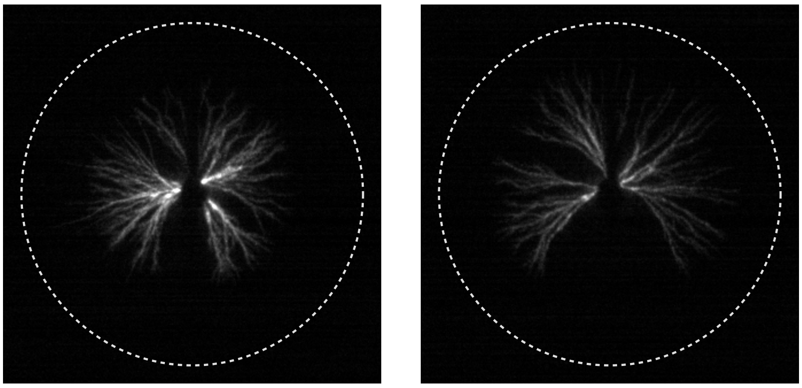

(c) $2-3\,\mathrm{ms}$ **(d)** $3-4\,\mathrm{ms}$

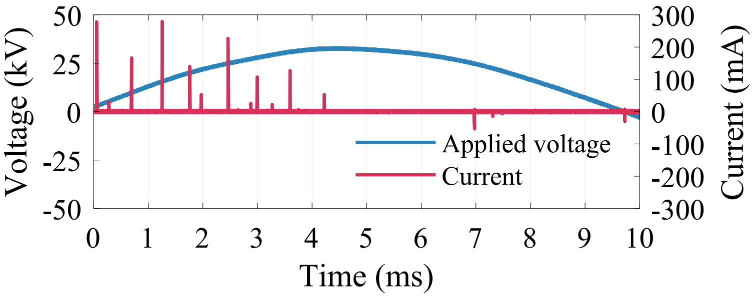

(e) Voltage and current recordings.

Figure 6.17: Surface discharge development during the rising slope of the positive half-cycle of the applied AC-voltage for the case of epoxy resin 6 mm thickness in technical air (21/79 % O_2/N_2) at 1 bar absolute pressure and rms applied voltage around 70 % (23.18 kV) of the corresponding FOV.

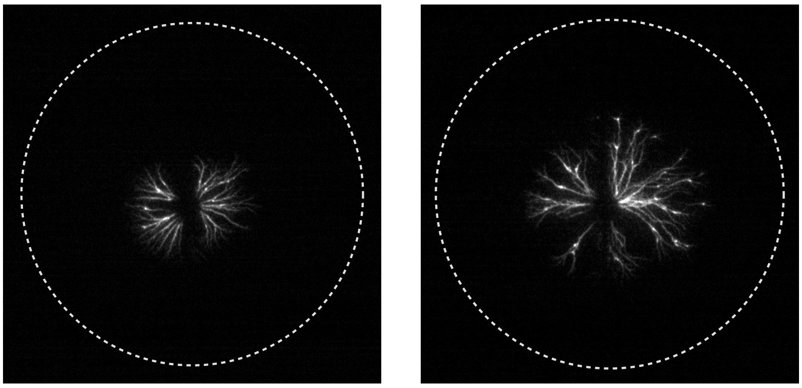

(a) 0 — 1 ms **(b)** 1 — 2 ms

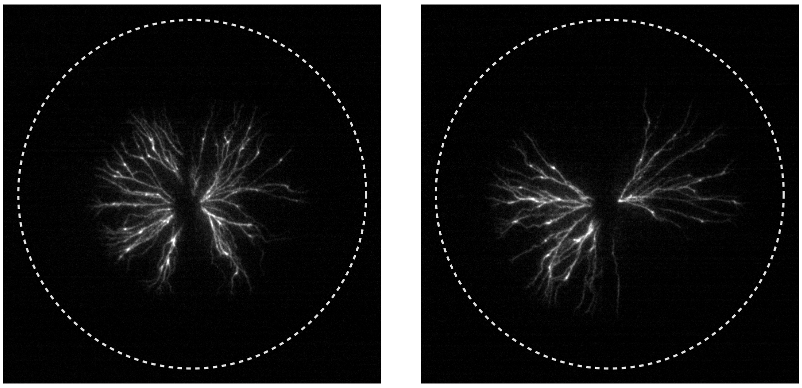

(c) 2 — 3 ms **(d)** 3 — 4 ms

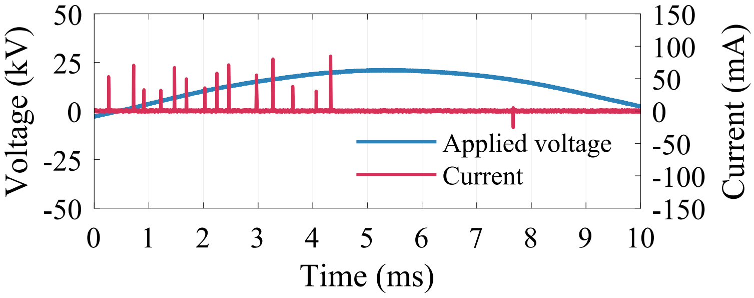

(e) Voltage and current recordings.

Figure 6.18: Surface discharge development during the rising slope of the positive half-cycle of the applied AC-voltage for the case of epoxy resin 6mm thickness in nitrogen (N_2) at 1 bar absolute pressure and rms applied voltage around 80 % (14.86 kV) of the corresponding FOV.

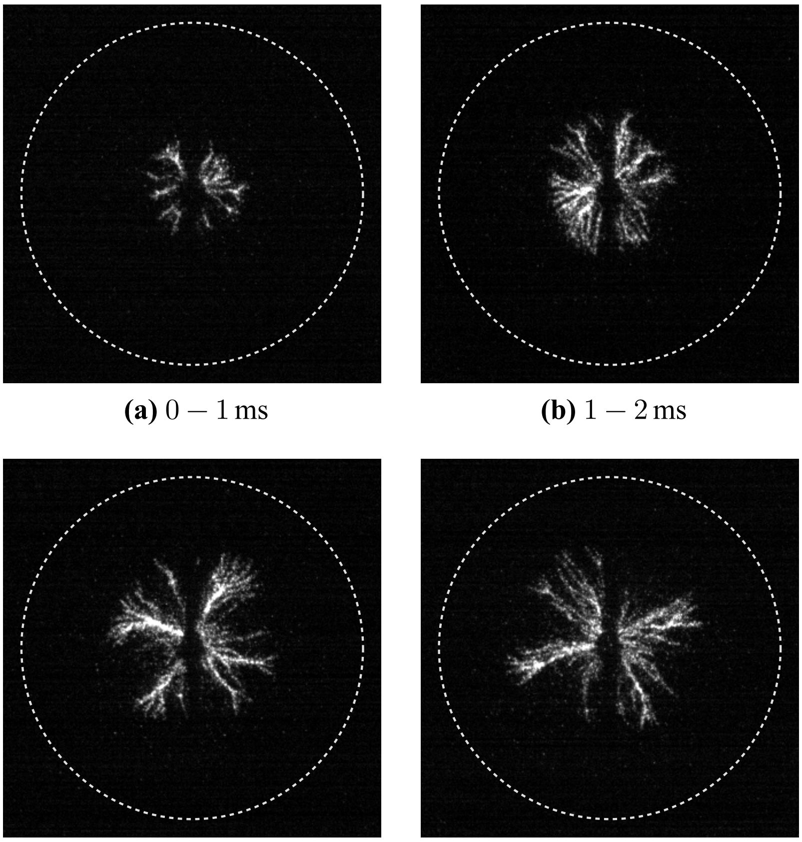

(a) $0 - 1\,\mathrm{ms}$ **(b)** $1 - 2\,\mathrm{ms}$

(c) $2 - 3\,\mathrm{ms}$ **(d)** $3 - 4\,\mathrm{ms}$

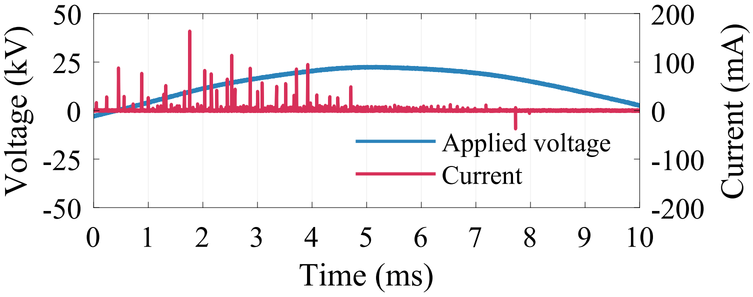

(e) Voltage and current recordings.

Figure 6.19: Surface discharge development during the rising slope of the positive half-cycle of the applied AC-voltage for the case of epoxy resin 6 mm thickness in carbon dioxide (CO_2) at 0.5 bar absolute pressure and 15.93 kV rms applied voltage.

Table 6.1 summarises some of the observations made from the captures presented in Figures 6.10 to 6.19. Part of the listed points were described in the previous paragraphs, while, the same observations, will be further supported by the outputs that will be presented next.

Table 6.1: Summary of findings from the long exposure time synchronised photography (Figures 6.10 to 6.19).

Gas	Solid dielectric	Observation(s)	Figure
21/79 % O_2/N_2 at 1 bar	PTFE 4 mm	• During the positive AC half-cycle, as the voltage magnitude increases, the generated discharges appear to cover longer distances on the solid dielectric surface. • Negative forward discharges and back-discharges of both polarities seem to appear locally around the needle tip and they do not extend their propagation further on the surface. • Multiple electrically detected pulses appeared to overlap each other in the captured frames which is observed from the chromatically saturated regions in the captured frames. • Within the considered spectral range, the generated discharge activity appeared to be brighter compared to CO_2 and less bright compared to N_2.	Figure 6.10

N_2 at 1 bar	PTFE 4 mm	• A relatively small number of pulses are detected however, the captured discharges appear to be very bright with their channels easily distinguishable. • The same observations as the case of the same solid dielectric type in 21/79 % O_2/N_2 apply also here regarding the propagation length of the different types of discharges. • It appears that, once a discharge channel has propagated in one direction then the very next discharge will likely propagate to the opposite. It could be assumed that each discharge neutralises the deposited charge on the part of the surface it propagates on.	Figure 6.11
CO_2 at 0.5 bar	PTFE 4 mm	• The same observations as the cases of 21/79 % O_2/N_2 and N_2 apply also here regarding the propagation length of the different types of discharges. • The pressure is reduced compared to the rest of the cases, effectively decreasing the density of charge carriers. • Most of the captured discharge activity shows a unique morphology: a discharge channel extends up to a certain length and after several smaller discharge branches make their appearance. • The light emitted from the generated discharges was considerably less compared to 21/79 % O_2/N_2 and N_2 which practically required higher preset gain for the intensifier photocathode.	Figure 6.12

21/79 % O_2/N_2 at 1 bar	Epoxy resin 4 mm	• The electrically detected discharge activity is denser compared to the corresponding case with PTFE of the same thickness despite the lower applied voltage level. Pulses of both higher and lower magnitudes appear in short time gaps between them. In PTFE higher magnitude pulses were more distinct. • It can be observed that the generated discharges have a more spread propagation, compared to PTFE, on the central region of the solid dielectric surface. • The same observations as the previously described cases apply also here regarding the propagation length of the different types of discharges.	Figure 6.13
N_2 at 1 bar	Epoxy resin 4 mm	• The same observations as for the case of epoxy resin 4 mm in 21/79 % O_2/N_2 apply also here.	Figure 6.14
21/79 % O_2/N_2 at a bar	PTFE 6 mm	• The same observations as for the case of PTFE 4 mm in 21/79 % O_2/N_2 apply also here.	Figure 6.15
N_2 at 1 bar	PTFE 6 mm	• The same observations as for the case of PTFE 4 mm in N_2 apply also here. • Figure 6.16d shows that an electrically detected discharge of relatively small magnitude can propagate at a significant distance when the electric field conditions are sufficient.	Figure 6.16

21/79 % O_2/N_2 at 1 bar	Epoxy resin 6 mm	• The same observations as for the case of epoxy resin 4 mm in 21/79 % O_2/N_2 apply also here.	Figure 6.17
N_2 at 1 bar	Epoxy resin 6 mm	• The same observations as for the case of epoxy resin 4 mm in N_2, and 21/79 % O_2/N_2, apply also here with regards to the comparison of the outputs with the corresponding ones with PTFE.	Figure 6.18
CO_2 at 0.5 bar	Epoxy resin 6 mm	• As happened for the cases of epoxy resin 6 mm in 21/79 % O_2/N_2 and N_2, again, the spread of the discharge activity is more uniformly distributed in the central region of the solid dielectric surface compared to the cases where PTFE was tested. • The morphology of the captured discharges is very similar to the one described for the case of PTFE 4 mm in CO_2: a discharge channel extends up to point and after that several smaller branches make their appearance.	Figure 6.19

6.3.2 Short exposure time captures

The synchronisation of the recording device(s) with the high-speed camera system for the implementation of an event-based trigger operation was described in detail in Section 6.2.3.2. The exposure time of the UV intensifier was set at 20 μs while the frame rate of the high-speed camera at 1000 frames per second (fps). The exposure time is found to be sufficient for capturing single discharge events with a low risk of additional discharges to appear within the same, short duration, time window. The chosen frame rate on the high-speed camera ensures that the maximum resolution of the CMOS sensor will be employed. It is worth noticing that, in such camera devices, reduction of the resolution indicates cropping the area of observation and not increasing the pixel size while maintaining the area of observation the same. It is, thus, important to maintain the maximum number of pixels in the high-speed camera, considering the relatively large size of the object under observation, and the long distance between the UV lens and the test object which is necessary based on the rated focal length of the lens.

Positive polarity forward discharges, appearing during the positive half-cycle of the AC applied voltage waveform, were again easier to be captured by the high-speed camera system. For the given vertical resolution $(\mathrm{V/div})$ of the fast digital storage oscilloscope, negative polarity discharges were electrically detected only for the cases where either technical air (21/79 $\%$ O_2/N_2) or carbon dioxide (CO_2) was used as gaseous insulating media. However, no discharge channels were captured over the insulator sample surfaces for the applied voltage levels examined during the described test series, indicating that the negative forward discharges may appear locally on the needle tip and within a very small region around it on the insulator surface. Observations regarding the longer propagation length of positive discharges compared to negative were also reported in [13].

Here, a selection of individual surface discharge events is presented. Figure 6.20 presents a set of frames captured following the event-based pattern-generated triggering technique described previously in Section 6.2.3.2. Together with each presented frame capture, the corresponding synchronised current pulse recording is included. On the same plot, the apparent charge is calculated by integrating the current pulse signal over the presented time interval. The last part of this group of figures shows an illustration of the positive AC half-cycle for a $50\,\mathrm{Hz}$ sinusoidal waveform, indicating approximately the time points where the current pulses appear relevant to the applied voltage. For all three cases, the rms applied voltage is $80\,\%$ of the expected FOV and, thus, the illustrated waveform is shown normalised to its peak value.

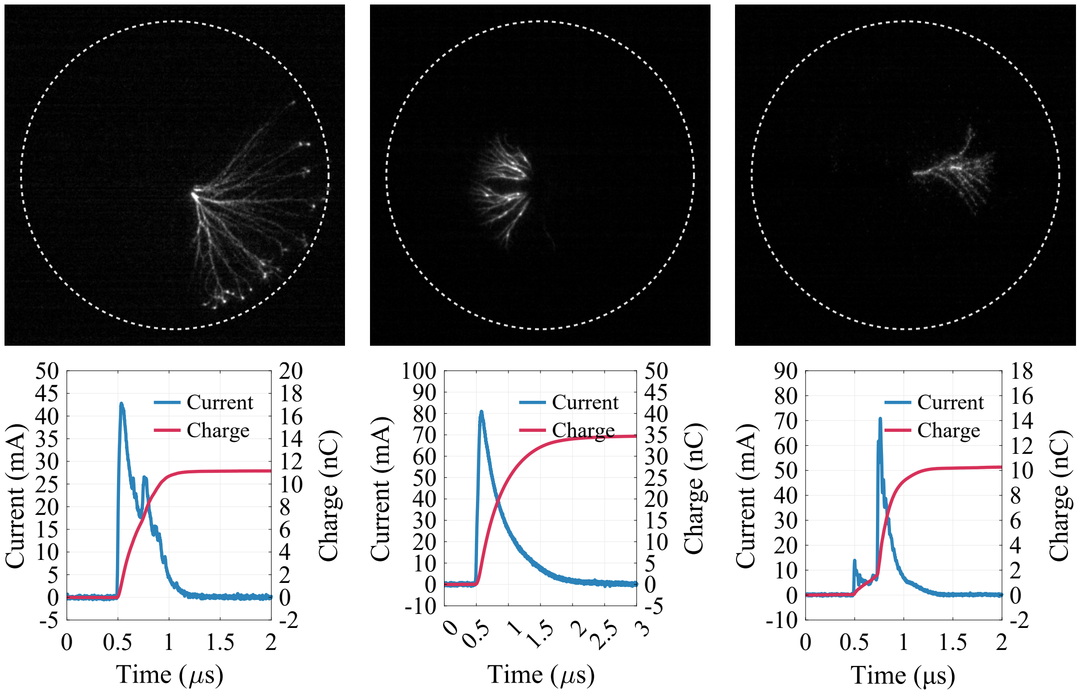

(a) Epoxy resin 6 mm in technical air (21/79 % O_2/N_2) **(b)** Epoxy resin 6 mm in N_2 **(c)** PTFE 4 mm in CO_2

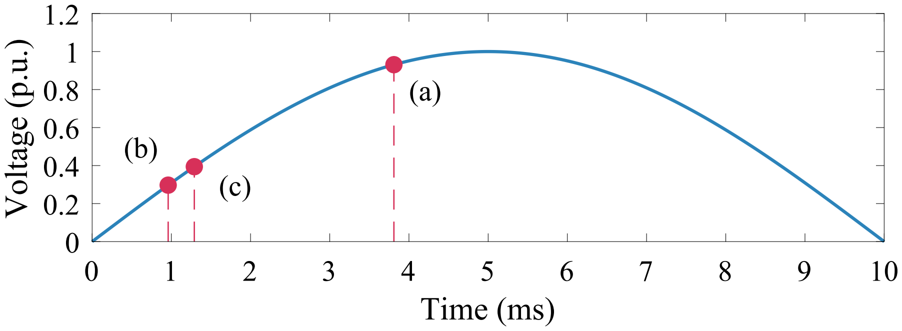

(d) Location of the discharges within the time-resolved AC half-cycle

Figure 6.20: Short exposure 20 μs capturing of surface discharge events: (a) epoxy resin 6 mm in technical air (21/79 % O_2/N_2) at 1 bar absolute (b) epoxy resin 6 mm in nitrogen (N_2) at 1 bar absolute, (c) PTFE 4 mm in carbon dioxide (CO_2) at 0.5 bar absolute and (d) illustration of 50 Hz positive half-cycle showing the approximate location of the discharges within the time domain.

The first case of Figure 6.20a shows a current pulse which is of relatively low magnitude and which appears to extend its propagation up to the edge of the disc-shaped insulator sample and towards the ground potential plane electrode. A similar behaviour was also observed for the cases of Figure 6.10 and Figure 6.15 where technical air was also tested but with different insulator types. Considering both the long and short exposure time cases presented so far, it could be said that, the higher the magnitude of the current pulses is, the wider the spread of the discharge activity on the surface of the solid dielectric will be. As shown in Figure 6.20d, the same pulse appears at a time instant quite close to the peak of the AC-cycle. While approaching the peak value of the applied voltage, it is expected that the positively charged insulator surface will accumulate even more positively charged ions (cations). This will be a result of the positive polarity discharge activity which appeared in the previous time instants and the drift movement of the high mobility electrons towards the positively charged needle, leaving behind the slowly moving positive ions [15, 18]. The electric field on the insulator surface is dependent on both the externally generated electric field and the field generated by the presence of the created space charge. Such behaviour has greater impact especially for relatively slowly varying applied voltages, such as at 50/60 Hz power frequency.

The current pulse of Figure 6.20b takes place at a time point close to the zero-crossing of the sinusoidal applied voltage wave and is of relatively high peak value. As seen from the captured frame, the discharge does not propagate to a great distance, agreeing with the pattern shown in the previous captures. As the instantaneous voltage magnitude increases, within the same AC-cycle, the generated discharges are likely to propagate further on the insulator surface. For CO_2 at 0.5 bar absolute, shown in Figure 6.20c, the morphology of the discharge has similarities with the captures of Figure 6.12, i.e., an initial channel begins to propagate from the needle tip location and as it extends it tends to spread in smaller branches. The current pulse comprises of two superimposed pulses, both developed in the sub-microsecond time scale, indicating a possible two-step process.

Figure 6.21 includes recorded frames and measurements obtained from the same test series as those presented in Figure 6.20. For all the cases, a correlation can be clearly seen between current pulse characteristics and voltage level at these particular short time intervals. The difference is more noticeable by comparing Figure 6.20b and Figure 6.21b. Although occurring at a higher external field, a pulse of less than half the magnitude and apparent charge propagates further on the surface. Figure 6.21a illustrates a discharge event of lower magnitude appearing earlier in the positive AC-cycle compared to Figure 6.20a where both the spread of the branches is narrower and the length of extension is shorter. The test series with CO_2 were performed at a lower pressure level and cannot be easily directly compared with the other cases presented. However, a longer extension of the discharge region of Figure 6.21c compared to Figure 6.20c is noticed.

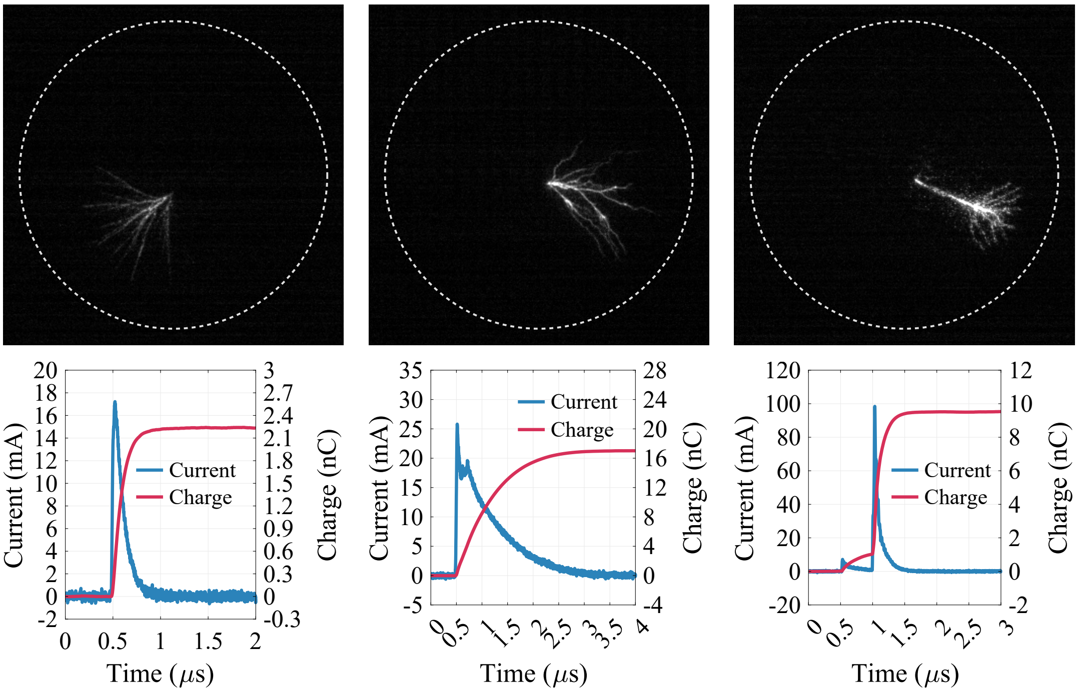

(a) Epoxy resin 6 mm in technical air (21/79 % O_2/N_2)

(b) Epoxy resin 6 mm in N_2

(c) PTFE 4 mm in CO_2

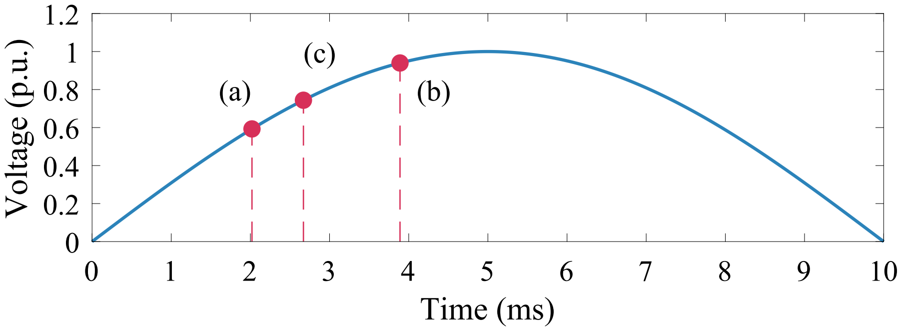

(d) Location of the discharges within the time-resolved AC half-cycle

Figure 6.21: Short exposure 20 μs capturing of surface discharge events: (a) epoxy resin 6 mm in technical air (21/79 % O_2/N_2) at 1 bar absolute (b) epoxy resin 6 mm in nitrogen (N_2) at 1 bar absolute, (c) PTFE 4 mm in carbon dioxide (CO_2) at 0.5 bar absolute and (d) illustration of 50 Hz positive half-cycle showing the approximate location of the discharges within the time domain.

Back-discharges have been reported in previous works where different optical techniques [13, 14, 16, 17] were used. For the presented series of tests, these kinds of discharges appear to be of relatively high magnitude on some occasions. However, they do not propagate over distances far from the needle tip, as happens with positive forward discharges, and thus their capture is difficult. Figure 6.22 shows an example of a positive polarity back-discharge, occurring during the rising slope (from peak to zero-crossing) of the negative half-cycle of the applied voltage (see region (d) in Figure 6.9 for reference) for PTFE of 4 mm thickness in nitrogen (N_2). Regardless of the polarity, back-discharges have been correlated with the charge memory effect [13] and the presence of accumulated surface charge. In [126] a similar observation was made with the application of a positive semi-square voltage and the back-discharge appearing after the voltage had reached zero volts.

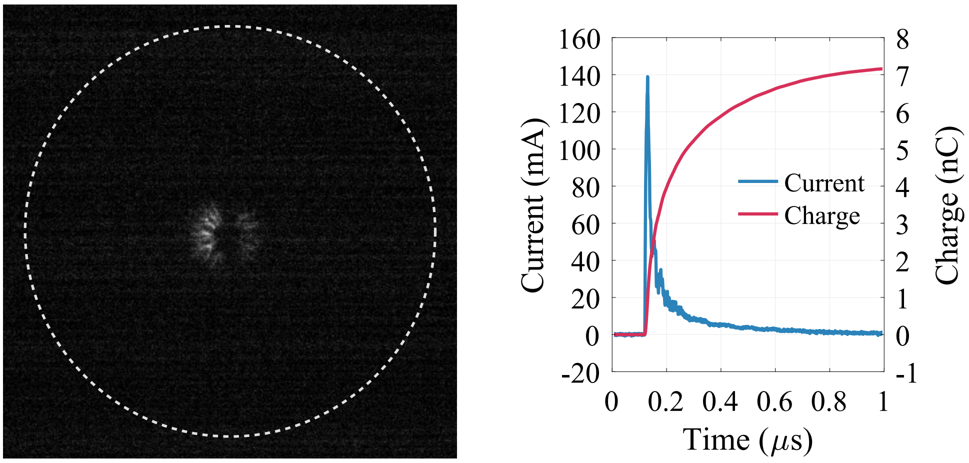

(a) **(b)**

Figure 6.22: Capture of positive polarity back-discharge for PTFE 4 mm thickness in nitrogen (N_2) at 1 bar absolute pressure and rms applied voltage 80 % 16.61 kV of the corresponding rms FOV. The presented discharge event appeared at around −14.10 kV [139].

6.4 Conclusions

In this final chapter the surface discharge imaging technique of high-speed photography was described. The developed camera system comprises an ultra-high-speed camera coupled with a UV image intensifier for enhanced performance in the UV-VIS spectrum of light. The electrode configuration was extensively described also in the previous chapters and is briefly repeated here. The sensitivity of the current measurement circuit is again validated, and the relevant equipment and components are described in detail.

Extensive emphasis is given to the technical specification of the high-speed intensified camera system. In cases where such equipment is used, it is important that all the necessary details are provided so that the capability and potential limitations are well identified. Three main points are specified and justified: (i) the light transmission efficiency of the optical components, (ii) the direct and indirect activation speed for the shutters on the camera and intensifier devices and last (iii) the implemented trigger patterns which are essential for the proper synchronisation of the entire test system.

As part of the cases study, tests were performed using atmospheric insulating gases, namely technical air (21/79 % O_2/N_2), nitrogen (N_2) and carbon dioxide (CO_2). Disc-shaped insulator samples made of polytetrafluoroethylene ($\varepsilon_{\mathrm{PTFE}} = 2.1$) and epoxy resin ($\varepsilon_{\mathrm{ER}} = 3.5$) of 4 mm and 6 mm thicknesses were used, and selected results were presented to demonstrate observed differences in the experimental outputs.

Most of the presented captures were performed entirely within the UV range of light with the use of a bandpass filter installed on the camera system, except for the case of CO_2 because of the lower luminosity of the discharge events. Long and short exposure time trigger set-ups were used for the synchronisation of the waveform recording and image capturing systems. The applied voltage was maintained at 80 % of the expected FOVs for the protection of the used equipment.

Obtained results include capturing and recording of positive polarity discharges during the positive half-cycle of the applied 50 Hz AC voltage, individual current pulses, and back-discharge activity. Through capturing of consecutive long exposure frames, it was shown that the propagation length of discharges increases with the increase of the applied voltage magnitude, from the zero-crossing point towards its peak value. Individual discharge captures helped understanding how applied voltage and generated current reflect to the morphology and propagation of the discharge event. It was demonstrated that the current pulse alone cannot be an indicator of the appeared discharge morphology but when combined with the time or phase angle of occurrence, it can provide a clearer understanding.

The subdivision of AC surface discharges in each half-cycle into forward discharges followed by back-discharges was introduced in the previous section. The present tests allow further understanding on these discharges:

(i). Positive forward discharges are observed to occur as a successive series of separate streamer channels, sometimes traversing the insulator disc radius of 50 mm, with each discharge current rise being established within some nanoseconds depending on the gaseous medium. The current duration is relatively long, in some cases up to the microsecond range, and the charge transported can be tens of nC. It is to be noted that a significant advantage of the needle-insulator-ground plane configuration used in these tests is the achievement of close coupling of the ground plane with the surface space charge of the streamers. As a result, the magnitude of the apparent charge at the planar surface of the insulator samples is much more closely representative of the real surface charge created by the streamers than can be in the case of conventional partial discharge measurement.

(ii). Negative forward discharge streamers were not captured indicating that their propagation does not extend to sufficient distances to be captured by the intensified camera system. When these discharges are detectable, they are of considerably lower magnitude and have different current pulse characteristics.

(iii). The positive back-discharges which are often recorded are streamers initiated by the reversal of surface field by the positive ions of the forward discharges. These are characterized by a distinctive short range and low charge flow.

(iv). Similar surface charge properties to those of positive back discharges are also created by the negative ions deposited on the surface in the negative forward-discharge streamers. Although of too low visibility to be recorded here, the long duration of these discharges is the cause of negative back-discharges.

Successive stages of the development of surface discharge phenomena, ranging from their inception up to the withstand levels of the insulation will potentially provide a complete overview of the surface discharge mechanisms. Larger measurement datasets, either time- or phase-resolved or both, in a test arrangement similar to the one presented in this work, will contribute to more converging observations. Imaging techniques, when combined with accurately performed measurements can provide a very interesting insight on the understanding of such phenomena.

Chapter 7

Conclusion and suggestions for future work

7.1 Conclusion

The research investigation that was reported in this thesis focused on the study of surface discharge activity phenomena and introduced improved and reliable detection methods in laboratory experimental arrangements. In particular, the triple junctions, the points/regions where gaseous and solid dielectrics meet with the metal electrodes, were replicated. As both gaseous and solid dielectrics are involved, the electrical characteristics of these materials, and their interfaces must be understood.

The main contributions of this thesis are:

- An extensive literature review on the different gaseous media highlighted the molecular structure characteristics of the researched compounds and how these affect the physical property of boiling point and their resistance to the dissociative processes in the atmosphere, effectively increasing their overall environmental impact. Furthermore, the review recognised that compounds of high molecular weight show the tendency to exhibit a higher boiling point except for the cases where their geometry is symmetrical with a non-polar overall dipole moment. At the same time, the search revealed that non-polar and symmetrical molecules can survive longer in the atmosphere before they are dissociated, with a very characteristic example being sulphur hexafluoride (SF_6).

- From the review of the published literature again, it was recognised that, under strongly non-uniform electric field conditions, the performance of CF_3I/CO_2 mixtures against breakdown and partial discharge activity is superior to the atmospheric gases. The same happens with the mixture of 30/70 % CF_3I/CO_2 although its performance is not as good as pure SF_6. At atmospheric pressure levels, 0.1 MPa (or 1 bar absolute), in electrode configurations with charged sharp points (needle), it was recognised that $PDIV_{CO_2} > PDIV_{\text{Tech. Air}} > PDIV_{N_2}$. At the same pressure levels, the performance of 30/70 % CF_3I/CO_2 is reported to be reasonably superior to pure CO_2. AC breakdown or flashover tests that involve CF_3I are very few in number as difficulties with the decomposition of the compound have been reported. Regarding flashover in atmospheric gases at pressure levels close to 1 bar, the performance of technical air is very close to that of CO_2 with N_2 being the least effective.
- Regarding the experimental arrangements, the following were implemented which can potentially be found useful when tests with similar requirements need to be produced or replicated:
  - An optimised electrode configuration was implemented which is suitable for electric method performance experiments, as the ones presented in this thesis, but also for image capturing of discharge activity. It is possible to maintain the same test conditions in the different arrangement concepts of the electrodes.
  - Current sensing circuits for accurate electrical detection of PD signals were extensively described. The processes followed of their implementation were presented in detail and can be reproduced.
  - A new high-resolution high-speed camera system with enhanced low light and UV range detection capability was developed. The newly developed camera system was operated in parallel with the electrical detection of surface discharge

  activity. It was possible to investigate (i) the development of surface discharge activity in the duration of the full AC-cycle and (ii) the morphology of individual surface discharge events with the simultaneous recording of the PD electric pulse and capturing of the light emitted.

  - A pressure chamber was designed and manufactured able to incorporate the above.
  - The test methods and protocols for AC voltage testing were sufficiently described.

- Analysis of discharges in various combinations of solid gas insulating media was performed from different standpoints based on the developed detection techniques. Regarding the flashover withstand of the investigated insulating media and solid dielectrics combinations the observations made are:

  - The mixture of 30/70 % CF_3I/CO_2 was found to be superior of all the gaseous media tested as no flashover event was recorded at or below the rated applied voltage level (38 kV rms) of the test vessel.
  - Among the atmospheric gases, technical air (21/79 % O_2/N_2) was found to perform the best in the flashover tests, followed by CO_2, and with N_2 showing the lowest flashover voltage level for all the solid dielectric samples tested.
  - The lower relative permittivity of the solid dielectric is, the higher the resulting average flashover levels are.
  - Test objects with thicker insulator samples have higher flashover level for the examined combinations with atmospheric gases.

  The PDIV levels were measured for the atmospheric gases and the two dielectric materials with the lowest ($\varepsilon_{\mathrm{PTFE}} = 2.1$) and highest ($\varepsilon_{\mathrm{ER}} = 3.5$) relative permittivity values. The observations can be summarised as:

  - $\mathrm{PDIV}_{\mathrm{PTFE}} > \mathrm{PDIV}_{\mathrm{ER}}$: the material with the higher ε_{r} (epoxy resin) exhibits a lower partial discharge inception voltage level compared to the lower permittivity polymer (PTFE).
  - $\mathrm{PDIV}_{\mathrm{CO_2}} > \mathrm{PDIV}_{\mathrm{Tech.\ Air}} > \mathrm{PDIV}_{\mathrm{N_2}}$: This is a different sequence compared to flashover. For the test conditions considered in this work, it seems that CO_2 is more effective in suppressing the inception of PD when compared to technical air however, the flashover withstand is lower. The latter can be a characteristic of considerable significance when it comes to practical designs of equipment that operate with such compounds as insulating media.

- Using the accurate electrical detection combined with recordings of enhanced sampling rate it was found that:

  - The different gaseous compounds show very different discharge activity development patterns in the duration of a full AC-cycle. N_2 does not show negative polarity PD activity in the duration of the negative half-cycle while, at the same time, the positive polarity discharges during the positive half-cycle are not intense although they are high in magnitude. The rest of the gases (technical air, CO_2 and 30/70 % CF_3I/CO_2) tested show activity in both intervals of the applied waveform, of variable intensity and magnitude.
  - 30/70 % CF_3I/CO_2 and pure CO_2 appear to suppress discharges more effectively than technical air and N_2. During the positive half-cycle, the recorded discharges are of considerably lower magnitude and they also make their appearance around the peak of the voltage wave.
  - The high-resolution PD pulses show also well distinguishable differences between the different gases. Faster rising and extinguishing PD pulses are recorded for the strongly attaching mixture of 30/70 % CF_3I/CO_2 followed by CO_2, technical air and, lastly, N_2. The magnitude of the discharge current pulse is one observation parameter, however, the apparent charge q of each pulse will

  be greatly affected by the pulse overall shape. A high current magnitude PD pulse in the mixture of 30/70 % CF_3I/CO_2 will result to a much lower apparent charge compared to a pulse of the same magnitude in technical air and/or N_2 because its faster rise time and shorter overall duration.

  - Negative polarity forward discharges are observed to be much faster compared to the positive polarity ones and much more closer in their characteristics in the different investigated gases. At this point, it is not clear how the movement of positive ions towards a negatively charged tip and the drift of electrons and negative ions away from it reflect to that type of pulses in the different compounds. It is something that needs to be further investigated in the future.
  - Back-discharges in the falling slope (peak to zero-crossing) of the voltage wave make their appearance in all gases. This type of discharges have been linked with the neutralisation of the charged surface when the electric field conditions caused by the charges attracted towards the charged electrode and the ones drifted away from it are sufficient.

- The corresponding current peak and charge pattern plots revealed that:
  - The different gaseous media showed unique patterns in the recorded current signals which make them easily distinguishable. More specifically, technical air showed a considerable dense and relatively high magnitude discharge activity during both positive and negative AC-half cycles. At the same time, N_2 showed low density discharge activity during the positive half-cycle, although, of considerably high magnitude. Both CO_2 and 30/70 % CF_3I/CO_2 displayed much denser discharge activity compared to the previous two insulating media. However, the magnitudes were considerably lower and, as it was later revealed, of much lower apparent charge.
  - In all the examined gaseous medium/solid dielectric combinations, the observed discharge activity comprised forward and back-discharges of both polarities

during both AC half-cycles, with the exception of nitrogen (N_2). Negative polarity forward discharges were not recorded for any tests using N_2 which is attributed to their significantly lower magnitude compared to the corresponding positive forward discharges.

- Pure carbon dioxide (CO_2) showed similarities with the 30/70 % CF_3I/CO_2 mixture, both in the pattern plots and the PD pulse characteristics, which is understandable to an extent since CO_2 holds a big percentage in the composition of the CF_3I/CO_2 mixture (70 %). The recordings that involved technical air were significantly different compared to the rest of the gaseous media. However, the pulse characteristics, although different, can be easier correlated to these of nitrogen (N_2), i.e., longer rise times and pulse durations. From a practical perspective, it is shown that the accurate recording of PD pulses in CO_2 and/or CF_3I/CO_2 requires equipment of wider frequency response compared to technical air and N_2.
- The differences between gaseous media were even more observable in the charge density plots since such illustrations can also incorporate the current pulse characteristics. If the apparent charge magnitudes can be considered as an indicator of insulating performance, again, nitrogen (N_2) was found to be the least effective followed by technical air (21/79 % O_2/N_2) and then carbon dioxide (CO_2) and 30/70 % CF_3I/CO_2. An interesting observation is how the flashover levels and surface discharge patterns do not follow the same sequence in terms of performance of the different gaseous media. It could be said that the charge density plots are more informative compared to the current peak density plots. However, very large datasets of accurate time-resolved PD recordings, as these presented in this thesis, combined with phase-resolved charge recordings may provide an even clearer insight on the discharge mechanisms and further enhance the practical interest of such an approach.
- The quantitative analysis of selected test cases revealed similar observations as

listed above. For the same sample type 30/70 % CF_3I/CO_2 showed the highest pulse repetition rate although a relatively small quadratic rate and accumulated apparent charge. This is an indicator that when the PD inception levels are reached then the activity becomes very intense although the electron attaching capability of the medium suppresses well that activity. Such an observation could rise questions such as what levels of PD activity are acceptable and how these affect the quality of the medium and its performance in the long term. I could be also summarised that the sequence in the performance of the atmospheric gases was the same as the recorded PDIV levels. In the same analysis, the differences between different materials of the same thickness demonstrated an increase in the discharge activity for the higher relative permittivity solids. The quantitative analysis will be further expanded in future studies.

- The newly developed UV-enhanced high-speed camera system, synchronised with the corresponding electrical detection system, provided a further understanding on the development and morphology of the generated discharge activity. The following observations/conclusions, among others, were extracted through these test series:
  - Positive polarity forward discharges were easier to capture compared to negative polarity forward discharges. Such a characteristic can be attributed to the fact that negative polarity forward discharges appear locally around the enhanced electric field region and they do not extend their propagation further than that.
  - Back-discharges of both polarities were again electrically detectable, although very difficult to capture because of their low visibility and short propagation length.
  - Surface discharges in technical air (21/79 % O_2/N_2) and nitrogen (N_2) were easier to capture in the UV range compared to carbon dioxide (CO_2) indicating a possible efficiency of the latter to suppress high electric field magnitudes more

efficiently compared to the other two compounds.

  - Small differences between different solid dielectric sample types were observed indicating a possible dependency of the discharge activity primarily to the gas medium for that concept of test object and for the considered applied voltage levels.
  - The extension length of the generated surface discharges is strongly relevant to the magnitude of the discharge current and the instantaneous voltage magnitude. It is, thus, reasonable that current magnitude and time/phase point within the AC-cycle are necessary parameters to estimate propagation of such discharges.
  - Through the observation of the captured frames, it could be said that higher discharge current magnitudes indicate more spread discharge channels around the triple junction point while higher voltage magnitudes may indicate longer extension.

This work demonstrated the performance of technical air (21/79 % O_2/N_2), nitrogen (N_2), carbon dioxide (CO_2) and the strongly attaching mixture of 30/70 % CF_3I/CO_2 in high electric field stress regions where a charged sharp protrusion meets with gaseous insulation and solid dielectric. Partial discharges and failure of the insulation are the two main insulation defects that appear when the necessary conditions are fulfilled. From an insulation standpoint, the mixture of 30/70 % CF_3I/CO_2 performed the best in all aspects and N_2 was the least efficient. Because of the type of defect (very sharp needle electrode), the measured partial discharge inception voltages were very close to each other, although, CO_2 performed better compared to technical air. The same did not happen with regards to the flashover where technical air showed the best withstand among the atmospheric gases. The insulation performance (FOV, PDIV and PD) of the test objects, was lower when higher permittivity solids were tested, for all the gaseous media considered. Combining the observations made from the pattern recordings and high-speed photography, it could be said that the use of CO_2 in an optimised design, which is able to prevent failure of the gaseous insulation, could provide tolerable performance against elevated stress regions. In a similar case, technical air will likely show a considerable range between initiation of discharge phenomena until failure of the insulation. In this range, surface discharges will extend in considerable distances, when the conditions allow this, which will need to be highly considered in the design processes of equipment. Future works will address in more detail similar experimental concepts with a wider range of gaseous insulating media and solid dielectric types and shapes.

7.2 Suggestions for future work

As happens in research, each work can provide a contribution to a specific topic or research subject. However, at the same time, it may raise new questions and point those interested to new directions and, even, to more detailed approaches and extensive studies. Here, some suggestions for future work are listed relevant to the material presented in this thesis. Some of them can possibly be delivered as experimental works and others may require extensive research of the bibliography and computational modelling, although, all of them may be considered as interesting:

- The presented work listed some practical parameters that need to be validated prior of performing technically demanding current sensing measurements. The vertical resolution of ADC devices is something that does not vary dynamically and can possibly be considered as a limitation. It is something that can possibly be addressed in future works and provide possible solutions.
- The presented current and charge density results can be further analysed in a statistical basis. Works in the past have suggested possible patterns in the distribution of partial discharges of different types. It would be interesting to see whether a similar pattern

can be extracted by such measurements and how similar these can be to ones obtained from real substation assemblies.

- Apart from the practical interest, the AC voltage waveshape is a very informative case of study for the reasons that a voltage polarity reversal occurs within the same period and also the voltage magnitude varies very slowly relevant to the processes associated with gaseous kinetics. As the various researched gaseous compounds have significant differences in their molecular weight and structures, it would be of interest to investigate their partial discharge behaviour in the duration of the full AC-cycle of various frequencies and extract a possible correlation between discharge activity and molecule characteristics, if any.

- Photography of surface discharge activity could potentially be expanded to the capture of discharges during the pre-flashover/pre-breakdown stages. In that way, useful observations may be extracted related to the flashover over withstand of each gaseous medium and the transition from streamer to the self-sustained discharge channels that eventually will bridge the metal electrodes.

- As it was shown, in cases were sharp metallic objects are present under the application of an AC waveform, the voltage level gap between PDIV and failure of the insulation is wide. It would be interesting to assess the condition of solid dielectric materials when they are exposed to partial/surface discharge activity for a long time duration. Most of the synthetic gaseous compounds are known to be vulnerable to decomposition and studies have already been conducted in that topic. Although, it would be interesting to document their interaction with solid dielectrics, such as polymers, and the types of by-products, if any, that are formed.

- The core experimental arrangement/object presented in this thesis showed one case of electric field distribution on the surface of the solid dielectric. It would be useful to perform a comparative study between different surface electric field distribution concepts. It is known that in many of the practical applications these different concepts coexist.

- Surface discharge activity could also be investigated in surface curvature profiles that are in use in transmission systems. The most obvious example is gas insulated line spacers.

References

[1] M. Rabie and C. M. Franck, “Assessment of Eco-friendly Gases for Electrical Insulation to Replace the Most Potent Industrial Greenhouse Gas SF_6,” *Environmental Science & Technology*, vol. 52, no. 2, pp. 369–380, 2018, pMID: 29236468. [Online]. Available: https://doi.org/10.1021/acs.est.7b03465

[2] Z. Li, K. Okamoto, Y. Ohki, and T. Tanaka, “Effects of nano-filler addition on partial discharge resistance and dielectric breakdown strength of Micro-Al_2O_3 Epoxy composite,” *IEEE Transactions on Dielectrics and Electrical Insulation*, vol. 17, no. 3, pp. 653–661, 2010. [Online]. Available: https://doi.org/10.1109/TDEI.2010.5492235

[3] R. E. Jorgenson, L. K. Warne, A. A. Neuber, J. Krile, J. Dickens, and H. Krompholz, “Effect of Dielectric Photoemission on Surface Breakdown: An LDRD Report.” [Online]. Available: https://www.osti.gov/biblio/811483

[4] “Dry air, N_2, CO_2, and N_2/SF_6 mixtures for gas-insulated systems,” WG D1.51, CIGRE, 2018.

[5] A. Pirker and U. Schichler, “Partial discharges of defects in different insulating gases: N_2, CO_2, dry air and SF_6,” in *2018 12th International Conference on the Properties and Applications of Dielectric Materials (ICPADM)*, 2018, pp. 140–143. [Online]. Available: https://doi.org/10.1109/ICPADM.2018.8401150

[6] A. J. Reid, M. D. Judd, R. A. Fouracre, B. G. Stewart, and D. M. Hepburn, “Simultaneous measurement of partial discharges using iec60270

and radio-frequency techniques," *IEEE Transactions on Dielectrics and Electrical Insulation*, vol. 18, no. 2, pp. 444–455, 2011. [Online]. Available: https://doi-org.abc.cardiff.ac.uk/10.1109/TDEI.2011.5739448

[7] A. J. Reid, M. D. Judd, B. G. Stewart, and R. A. Fouracre, "Partial discharge current pulses in sf_6 and the effect of superposition of their radiometric measurement," *Journal of Physics D: Applied Physics*, vol. 39, no. 19, pp. 4167–4177, sep 2006. [Online]. Available: https://doi.org/10.1088/0022-3727/39/19/008

[8] C. Tran Duy, N. Bonifaci, A. Denat, O. Lesaint, L. Caliap, A. Girodet, B. Gelloz, and P. Ponchon, "Partial discharges at a triple junction metal/solid insulator/gas and simulation of inception voltage," *Journal of Electrostatics*, vol. 66, no. 5, pp. 319–327, 2008. [Online]. Available: https://doi.org/10.1016/j.elstat.2008.01.011

[9] M. Michelarakis, P. Widger, A. Beroual, and A. M. Haddad, "Electrical Detection of Creeping Discharges over Insulator Surfaces in Atmospheric Gases under AC Voltage Application," *Energies*, vol. 12, no. 15, 2019. [Online]. Available: https://doi.org/10.3390/en12152970

[10] F. Kreuger, *Discharge Detection in High Voltage Equipment*. American Elsevier Publishing Company, 1965.

[11] F. Kreuger, E. Gulski, and A. Krivda, "Classification of partial discharges," *IEEE Transactions on Electrical Insulation*, vol. 28, no. 6, pp. 917–931, 1993. [Online]. Available: https://doi.org/10.1109/14.249365

[12] R. Bartnikas, "Partial discharges. Their mechanism, detection and measurement," *IEEE Transactions on Dielectrics and Electrical Insulation*, vol. 9, no. 5, pp. 763–808, 2002. [Online]. Available: https://doi.org/10.1109/TDEI.2002.1038663

[13] Y. Zhu, T. Takada, Y. Inoue, and D. Tu, “Dynamic observation of needle-plane surface-discharge using the electro-optical Pockels effect,” *IEEE Transactions on Dielectrics and Electrical Insulation*, vol. 3, no. 3, pp. 460–468, 1996. [Online]. Available: https://doi.org/10.1109/94.506221

[14] Y. Zhu, T. Takada, K. Sakai, and D. Tu, “The dynamic measurement of surface charge distribution deposited from partial discharge in air by Pockels effect technique,” *Journal of Physics D: Applied Physics*, vol. 29, no. 11, pp. 2892–2900, 1996. [Online]. Available: https://doi.org/10.1088/0022-3727/29/11/024

[15] Y. Murooka and S. Koyama, “A nanosecond surface discharge study in low pressures,” *Journal of Applied Physics*, vol. 50, no. 10, pp. 6200–6206, 1979. [Online]. Available: https://doi.org/10.1063/1.325753

[16] ——, “Nanosecond surface discharge study by using Dust figure techniques,” *Journal of Applied Physics*, vol. 44, no. 4, pp. 1576–1580, 1973. [Online]. Available: https://doi.org/10.1063/1.1662414

[17] Y. Murooka, T. Takada, and K. Hiddaka, “Nanosecond surface discharge and charge density evaluation Part I: review and experiments,” *IEEE Electrical Insulation Magazine*, vol. 17, no. 2, pp. 6–16, 2001. [Online]. Available: https://doi.org/10.1109/57.917527

[18] H.-B. Mu, G.-J. Zhang, Y. Komiyama, S. Suzuki, H. Miyake, Y. Tanaka, and T. Takada, “Investigation of surface discharges on different polymeric materials under HVAC in atmospheric air,” *IEEE Transactions on Dielectrics and Electrical Insulation*, vol. 18, no. 2, pp. 485–494, 2011. [Online]. Available: https://doi.org/10.1109/TDEI.2011.5739453

[19] H. M. Ryan, Ed., *High Voltage Engineering Testing*, ser. Energy Engineering. Institution of Engineering and Technology, 2013. [Online]. Available: https://doi.org/10.1049/PBPO066E

[20] "High-voltage test techniques - Part 1: General definitions and test requirements," BS EN 60060-1:2010, 2011-03-31.

[21] *Compressed air - Safety data sheet*, BOC UK, 10 2013.

[22] R. H. Petrucci, F. G. Herring, J. D. Madura, and C. Bissonnette, *General chemistry : principles and modern applications.*, 11th ed. Pearson Education, 2017.

[23] N. H. Malik and A. H. Qureshi, "A Review of Electrical Breakdown in Mixtures of SF_6 and Other Gases," *IEEE Transactions on Electrical Insulation*, vol. EI-14, no. 1, pp. 1–13, 1979. [Online]. Available: https://doi.org/10.1109/TEI.1979.298198

[24] A. Beroual, U. Khaled, and M.-L. Coulibaly, "Experimental Investigation of the Breakdown Voltage of CO_2, N_2, and SF_6 Gases, and CO_2–SF_6 and N_2–SF_6 Mixtures under Different Voltage Waveforms," *Energies*, vol. 11, no. 4, 2018. [Online]. Available: https://doi.org/10.3390/en11040902

[25] A. M. Casanovas and J. Casanovas, "Decomposition of high-pressure (400 kPa) SF_6–CO_2, SF_6–CO, SF_6–N_2–CO_2 and SF_6–N_2–CO mixtures under negative dc coronas," *Journal of Physics D: Applied Physics*, vol. 38, no. 10, p. 010, 2005. [Online]. Available: https://doi.org/10.1088/0022-3727/38/10/010

[26] A. Küchler, "Insulating Materials," in *High Voltage Engineering: Fundamentals - Technology - Applications*, 1st ed. Berlin, Heidelberg: Springer, 2018, pp. 301–354. [Online]. Available: https://doi.org/10.1007/978-3-642-11993-4_5

[27] A. P. Cox, G. Duxbury, J. A. Hardy, and Y. Kawashima, "Microwave spectra of CF_3Br and CF_3I. Structures and dipole moments," *J. Chem. Soc., Faraday Trans. 2*, vol. 76, pp. 339–350, 1980. [Online]. Available: http://dx.doi.org/10.1039/F29807600339

[28] P. Widger and A. M. Haddad, “Analysis of Gaseous By-Products of CF_3I and CF_3I-CO_2 after High Voltage Arcing Using a GCMS,” *Molecules*, vol. 24, no. 8, 2019. [Online]. Available: https://doi.org/10.3390/molecules24081599

[29] P. Widger and A. Haddad, “Solid by-products of a CF_3I-CO_2 insulating gas mixtures on electrodes after lightning impulse breakdown,” *Journal of Physics Communications*, vol. 1, no. 2, p. 025010, sep 2017. [Online]. Available: https://doi.org/10.1088/2399-6528/aa8ab4

[30] P. Widger, “Investigation into CF_3I-CO_2 gas mixtures for insulation,” PhD Thesis, Cardiff University, 2014. [Online]. Available: http://orca.cf.ac.uk/64853

[31] Y.-Y. Duan, M.-S. Zhu, and L.-Z. Han, “Experimental vapor pressure data and a vapor pressure equation for trifluoroiodomethane (CF_3I),” *Fluid Phase Equilibria*, vol. 121, no. 1, pp. 227 – 234, 1996. [Online]. Available: https://doi.org/10.1016/0378-3812(96)03005-1

[32] H. Kasuya, Y. Kawamura, H. Mizoguchi, Y. Nakamura, S. Yanabu, and N. Nagasaki, “Interruption capability and decomposed gas density of CF_3I as a substitute for SF_6 gas,” *IEEE Transactions on Dielectrics and Electrical Insulation*, vol. 17, no. 4, pp. 1196–1203, 2010. [Online]. Available: https://doi.org/10.1109/TDEI.2010.5539690

[33] T. Yamamoto, A. Yasuhara, F. Shiraishi, K. Kaya, and T. Abe, “Thermal decomposition of halon alternatives,” *Chemosphere*, vol. 35, no. 3, pp. 643 – 654, 1997. [Online]. Available: https://doi.org/10.1016/S0045-6535(97)00126-44

[34] *3M^{TM} Novec^{TM} 4710 Insulating Gas*, 3M^{TM} Company, 2017.

[35] A. Beroual and A. M. Haddad, “Recent Advances in the Quest for a New Insulation Gas with a Low Impact on the Environment to Replace

Sulfur Hexafluoride (SF_6) Gas in High-Voltage Power Network Applications," *Energies*, vol. 10, no. 8, 2017. [Online]. Available: https://doi.org/10.3390/en10081216

[36] K. Pohlink, F. Meyer, Y. Kieffel, F. Biquez, P. Ponchon, J. Owens, and R. Van San, "Characteristics of a Fluoronitrile/CO_2 mixture - An alternative to SF_6," paper D1-204, CIGRE, 2014.

[37] M. Hyrenbach and S. Zache, "Alternative insulation gas for medium-voltage switchgear," in *2016 Petroleum and Chemical Industry Conference Europe (PCIC Europe)*, 2016, pp. 1–9. [Online]. Available: https://doi.org/10.1109/PCICEurope.2016.7604648

[38] Y. Kieffel, A. Girodet, F. Biquez, P. Ponchon, J. Owens, M. Costello, M. Bulinski, R. Van San, and K. Werner, "SF_6 alternative development for high voltage switchgears," paper D1-305, CIGRE, 2014.

[39] *3M^{TM} Novec^{TM} 5110 Insulating Gas*, 3M$^{\text{TM}}$ Company, 2017.

[40] *3M^{TM} Novec^{TM} 1230 Fire Protection Fluid*, 3M$^{\text{TM}}$ Company, 2020.

[41] P. E. Tuma, R. M. MINDAY, Z. Zhang, M. G. Costello, R. M. Flynn, J. G. Owens, and M. J. Bulinski, "Fluorinated oxiranes as dielectric fluids," WO2012102915A1, Nov. 2012.

[42] A. Chachereau, "Electron an ion kinetics in fluorinated gases for electrical insulation," Ph.D. dissertation, ETH Zurich, Zurich, 2018. [Online]. Available: https://doi.org/10.3929/ethz-b-000311172

[43] M. Salvi-Narkhede, J. L. Adcock, A. Gakh, and W. Van Hook, "Vapor pressures, liquid molar volumes, vapor non-ideality, and critical properties of $CF_3OCF_2CF_2CF_3$, c-$CF_2CF_2CF_2CF_2O$, $CF_3OCF_2OCF_3$, and $CF_3OCF_2CF_2H$,"

The Journal of Chemical Thermodynamics, vol. 25, no. 5, pp. 643 – 647, 1993. [Online]. Available: https://doi.org/10.1006/jcht.1993.1060

[44] L. Lobo and L. Staveley, “The vapour pressure of tetrafluoromethane,” *Cryogenics*, vol. 19, no. 6, pp. 335 – 338, 1979. [Online]. Available: https://doi.org/10.1016/0011-2275(79)90157-7

[45] C.-P. C. Kao and R. N. Miller, “Vapor Pressures of Hexafluoroethane and Octafluorocyclobutane,” *Journal of Chemical & Engineering Data*, vol. 45, no. 2, pp. 295–297, 2000. [Online]. Available: https://doi.org/10.1021/je9901435

[46] L. A. Forero G. and J. A. Velásquez J., “Wagner liquid–vapour pressure equation constants from a simple methodology,” *The Journal of Chemical Thermodynamics*, vol. 43, no. 8, pp. 1235 – 1251, 2011. [Online]. Available: https://doi.org/10.1016/j.jct.2011.03.011

[47] WMO (World Meteorological Organization), *Scientific Assessment of Ozone Depletion: 2018*, Global Ozone Research and Monitoring Project – Report No. 58, 588 pp., Geneva, Switzerland, 2018. [Online]. Available: https://csl.noaa.gov/assessments/ozone/2018/

[48] M. Koch, “Prediction of Breakdown Voltages in Novel Gases for High Voltage Insulation,” Ph.D. dissertation, ETH Zurich, Zürich, 2015. [Online]. Available: https://doi.org/10.3929/ethz-a-010411940

[49] *Low GWP Hydrofluoroolefins (HFO) - The Environmental Alternative to Traditional Refrigerants*, Honeywell International Inc, 2017.

[50] K. Tanaka and Y. Higashi, “Thermodynamic properties of HFO-1234yf (2,3,3,3-tetrafluoropropene),” *International Journal of Refrigeration*, vol. 33, no. 3, pp. 474 – 479, 2010. [Online]. Available: https://doi.org/10.1016/j.ijrefrig.2009.10.003

[51] K. Tanaka, “Measurements of Vapor Pressure and Saturated Liquid Density for HFO–1234ze(E) and HFO–1234ze(Z),” *Journal of Chemical & Engineering Data*, vol. 61, no. 4, pp. 1645–1648, 2016. [Online]. Available: https://doi.org/10.1021/acs.jced.5b01039

[52] S. Fukuda, C. Kondou, N. Takata, and S. Koyama, “Low GWP refrigerants R1234ze(E) and R1234ze(Z) for high temperature heat pumps,” *International Journal of Refrigeration*, vol. 40, pp. 161 – 173, 2014. [Online]. Available: https://doi.org/10.1016/j.ijrefrig.2013.10.014

[53] M. H. Luly and R. G. Richard, “Gaseous dielectrics with low global warming potentials,” Patent US8080185B2, 2011.

[54] Y. Kieffel, A. Girodet, D. Piccoz, and R. Maladen, “Use of a mixture comprising a hydrofluoroolefin as a high-voltage arc-extinguishing and/or insulating gas and high-voltage electrical device comprising same,” WO/2013/004798, Jan. 2011.

[55] IPCC, 2001: *Climate Change 2001: The Scientific Basis. Contribution of Working Group I to the Third Assessment Report of the Intergovernmental Panel on Climate Change* [Houghton, J.T., Y. Ding, D.J. Griggs, M. Noguer, P.J. van der Linden, X. Dai, K. Maskell, and C.A. Johnson (eds.)]. Cambridge University Press, Cambridge, United Kingdom and New York, NY, USA, 881pp. [Online]. Available: https://www.ipcc.ch/report/ar3/wg1/

[56] M. J. Elrod, “Greenhouse warming potentials from the infrared spectroscopy of atmospheric gases,” *Journal of Chemical Education*, vol. 76, no. 12, p. 1702, 1999. [Online]. Available: https://doi.org/10.1021/ed076p1702

[57] P.J. Linstrom and W.G. Mallard, Eds., NIST Chemistry WebBook, NIST Standard Reference Database Number 69, National Institute of Standards and Technology, Gaithersburg MD, 20899, https://doi.org/10.18434/T4D303, (retrieved August 12, 2020).

[58] Regulation (EU) No 517/2014 of the European Parliament and of the Council of 16 April 2014 on fluorinated greenhouse gases and repealing Regulation (EC) No 842/2006 Text with EEA relevance. [Online]. Available: http://eur-lex.europa.eu/legal-content/EN/TXT/?uri=uriserv:OJ.L_.2014.150.01.0195.01.ENG

[59] E. A. Ray, F. L. Moore, J. W. Elkins, K. H. Rosenlof, J. C. Laube, T. Röckmann, D. R. Marsh, and A. E. Andrews, "Quantification of the SF_6 lifetime based on mesospheric loss measured in the stratospheric polar vortex," *Journal of Geophysical Research: Atmospheres*, vol. 122, no. 8, pp. 4626–4638, 2017. [Online]. Available: https://doi.org/10.1002/2016JD026198

[60] P. Widger, A. Haddad, and H. Griffiths, "Breakdown performance of vacuum circuit breakers using alternative CF_3I-CO_2 insulation gas mixture," *IEEE Transactions on Dielectrics and Electrical Insulation*, vol. 23, no. 1, pp. 14–21, 2016. [Online]. Available: https://doi.org/10.1109/TDEI.2015.005254

[61] L. Pruette, S. Karecki, R. Reif, L. Tousignant, W. Reagan, S. Kesari, and L. Zazzera, "Evaluation of C_4F_8O as an Alternative Plasma-Enhanced Chemical Vapor Deposition Chamber Clean Chemistry," *Journal of The Electrochemical Society*, vol. 147, no. 3, p. 1149, 2000. [Online]. Available: https://doi.org/10.1149%2F1.1393328

[62] Z. Gao, Y. Wang, S. Wang, R. Peng, W. Zhou, P. Yu, and Y. Luo, "Investigation of Synthesis and Dielectric Properties of c-C4F8O With Its CO_2/N_2 Mixtures as SF_6 Alternatives in Gas-Insulated Applications," *IEEE Access*, vol. 8, pp. 3007–3015, 2020. [Online]. Available: https://doi.org/10.1109/ACCESS.2019.2961694

[63] S. Tian, X. Zhang, Y. Cressault, J. Hu, B. Wang, S. Xiao, Y. Li, and N. Kabbaj, "Research status of replacement gases for SF_6 in power industry,"

AIP Advances, vol. 10, no. 5, p. 050702, 2020. [Online]. Available: https://doi.org/10.1063/1.5134727

[64] T. Kawamura, S. Matsumoto, M. Hanai, and Y. Murayama, *SF_6/N_2 Mixtures for HV Equipment and Practical Problems*. Boston, MA: Springer US, 1998, pp. 333–343. [Online]. Available: https://doi.org/10.1007/978-1-4615-4899-7_46

[65] W. C. Martin, R. Zalubas, and A. Musgrove, “Energy Levels of Sulfur, S I Through S XVI,” *Journal of Physical and Chemical Reference Data*, vol. 19, no. 4, pp. 821–880, 1990. [Online]. Available: https://doi.org/10.1063/1.555862

[66] L. Pauling, *The Nature of the Chemical Bond and the Structure of Molecules and Crystals: An Introduction to Modern Structural Chemistry*. Cornell University Press, 1960.

[67] G. Blaise and D. Treheux, “Physics of Dielectrics,” in *Dielectric Materials for Electrical Engineering*. John Wiley & Sons, Ltd, 2013, pp. 1–16. [Online]. Available: https://doi.org/10.1002/9781118557419.ch01

[68] V. H. Dalvi and P. J. Rossky, “Molecular origins of fluorocarbon hydrophobicity,” *Proceedings of the National Academy of Sciences*, vol. 107, no. 31, pp. 13 603–13 607, 2010. [Online]. Available: https://doi.org/10.1073/pnas.0915169107

[69] L. Gao and T. J. McCarthy, “Teflon is Hydrophilic. Comments on Definitions of Hydrophobic, Shear versus Tensile Hydrophobicity, and Wettability Characterization,” *Langmuir*, vol. 24, no. 17, pp. 9183–9188, 2008, pMID: 18672918. [Online]. Available: https://doi.org/10.1021/la8014578

[70] G. Tae, R. Lammertink, J. Kornfield, and J. Hubbell, “Facile Hydrophilic Surface Modification of Poly(tetrafluoroethylene) Using Fluoroalkyl-Terminated Poly(ethylene glycol)s,” *Advanced Materials*, vol. 15, no. 1, pp. 66–69, 2003. [Online]. Available: https://doi.org/10.1002/adma.200390013

[71] K. C. Kao, “Electric Polarization and Relaxation,” in *Dielectric Phenomena in Solids*. San Diego: Academic Press, 2004, pp. 41–114. [Online]. Available: https://doi.org/10.1016/B978-012396561-5/50012-8

[72] E. Kuffel, W. Zaengl, and J. Kuffel, “Chapter 5 - Electrical breakdown in gases,” in *High Voltage Engineering: Fundamentals*, 2nd ed. Oxford: Newnes, 2000, pp. 281–366. [Online]. Available: https://doi.org/10.1016/B978-075063634-6/50006-X

[73] J. Hölzl and F. K. Schulte, “Work function of metals,” in *Solid Surface Physics*, 1st ed. Berlin, Heidelberg: Springer, 1979, pp. 1–150. [Online]. Available: https://doi.org/10.1007/BFb0048919

[74] E. N. Economou, “Surfaces and Interfaces,” in *The Physics of Solids: Essentials and Beyond*, 1st ed. Berlin, Heidelberg: Springer, 2010, pp. 471–498. [Online]. Available: https://doi.org/10.1007/978-3-642-02069-8_17

[75] H. B. Michaelson, “The work function of the elements and its periodicity,” *Journal of Applied Physics*, vol. 48, no. 11, pp. 4729–4733, 1977. [Online]. Available: https://doi.org/10.1063/1.323539

[76] H. Wintle, “Photoelectric effects in insulating polymers and their relation to conduction processes,” in *1976 IEEE International Conference on Electrical Insulation*, 1976, pp. 248–251. [Online]. Available: https://doi.org/10.1109/EIC.1976.7464210

[77] Y. Murata, “Photoelectric Emission and Contact Charging of Some Synthetic High Polymers,” *Japanese Journal of Applied Physics*, vol. 18, no. 1, pp. 1–8, 1979. [Online]. Available: https://doi.org/10.1143/jjap.18.1

[78] E. A. Burke, “Secondary Emission from Polymers,” *IEEE Transactions on Nuclear Science*, vol. 27, no. 6, pp. 1759–1764, 1980. [Online]. Available: https://doi.org/10.1109/TNS.1980.4331102

[79] J. R. Lakowicz, “Introduction to Fluorescence,” in *Principles of Fluorescence Spectroscopy*, 3rd ed. Boston, MA: Springer, 2006, pp. 1–26. [Online]. Available: https://doi.org/10.1007/978-0-387-46312-4_1

[80] J. Tom, H. F. A. Verhaart, A. J. L. Verhage, and C. S. Vos, “Photo-emission of Charged Insulators in Insulating Gases,” in *2nd International Conference on Conduction and Breakdown in Solid Dielectrics*, Erlangen, Germany, 1986, pp. 301–307.

[81] A. A. Guzhov and Y. A. Shuba, “The Photoemission of Some Massive Insulators in the Vacuum Ultraviolet,” *Optical Technology*, vol. 38, pp. 198–199, 1971.

[82] I. Gallimbertti, I. Marchesi, and L. Niemeyer, “Streamer corona at an insulating surface,” in *7th International Symposium on High Voltage Engineering*, vol. 4, Dresden, Germany, 1991, pp. 1–4.

[83] T. Sonoda, S. Ohtsuka, K. Inami, H. Hama, G. Ueta, and S. Okabe, “Breakdown and Partial Discharge Inception Voltages Characteristics in N_2, CO_2, Dry air and SF_6 at Lightning Impulse Voltage,” in *19th International Symposium on High Voltage Engineering*, Pilsen, Czech Republic, 2015.

[84] A. Beroual, U. Khaled, and M.-L. Coulibaly, “Experimental Investigation of the Breakdown Voltage of CO_2, N_2, and SF_6 Gases, and CO_2–SF_6 and N_2–SF_6 Mixtures under Different Voltage Waveforms,” *Energies*, vol. 11, no. 4, 2018. [Online]. Available: https://doi.org/10.3390/en11040902

[85] S. Zhao, D. Xiao, P. Xue, R. Zhong, and Y. Deng, “Analysis of insulation performance and polar effect of CF_3I/CO_2 mixtures,” *IEEE Transactions on Dielectrics and Electrical Insulation*, vol. 25, no. 4, pp. 1364–1370, 2018. [Online]. Available: https://doi.org/10.1109/TDEI.2018.007117

[86] “Electric performance of new non-SF_6 gases and gas mixtures for gas-insulated systems,” WG D1.67, CIGRE, 2021.

[87] X. Zhang, S. Xiao, Y. Han, and Q. Dai, “Analysis of the feasibility of CF_3I/CO_2 used in C-GIS by partial discharge inception voltages in positive half cycle and breakdown voltages,” *IEEE Transactions on Dielectrics and Electrical Insulation*, vol. 22, no. 6, pp. 3234–3243, 2015. [Online]. Available: https://doi.org/10.1109/TDEI.2015.005080

[88] “High-voltage test techniques - Partial discharge measurements,” BSI, BS EN 60270:2001+A1:2016, 2011-03-31.

[89] “Guide for electrical Partial Discharge Measurements in compliance to IEC 60270,” WG D1.33, CIGRE, 2008.

[90] “Measurement System Signal Integrity: Important Factors to Consider,” Technical Brief: 55W-18024-3,Tektronix Inc, 2010.

[91] R. James and B. Phung, “Development of computer-based measurements and their application to PD pattern analysis,” *IEEE Transactions on Dielectrics and Electrical Insulation*, vol. 2, no. 5, pp. 838–856, 1995. [Online]. Available: https://doi.org/10.1109/94.469978

[92] E. Gulski and F. H. Kreuger, “Computer-aided analysis of discharge patterns,” *Journal of Physics D: Applied Physics*, vol. 23, no. 12, pp. 1569–1575, dec 1990. [Online]. Available: https://doi.org/10.1088/0022-3727/23/12/013

[93] A. Abubakar Mas’ud, B. Stewart, and S. McMeekin, “Application of an ensemble neural network for classifying partial discharge patterns,” *Electric Power Systems Research*, vol. 110, pp. 154–162, 2014. [Online]. Available: https://doi.org/10.1016/j.epsr.2014.01.010

[94] B. Karthikeyan, S. Gopal, and S. Venkatesh, “ART 2—an unsupervised neural network for PD pattern recognition and classification,” *Expert Systems with Applications*, vol. 31, no. 2, pp. 345–350, 2006. [Online]. Available: https://doi.org/10.1016/j.eswa.2005.09.029

[95] A. A. Mas'ud, B. G. Stewart, and S. G. McMeekin, "An investigative study into the sensitivity of different partial discharge φ-q-n pattern resolution sizes on statistical neural network pattern classification," *Measurement*, vol. 92, pp. 497–507, 2016. [Online]. Available: https://doi.org/10.1016/j.measurement.2016.06.043

[96] X. Zhang, S. Xiao, J. Zhou, and J. Tang, "Experimental analysis of the feasibility of CF_3I/CO_2 substituting SF_6 as insulation medium using needle-plate electrodes," *IEEE Transactions on Dielectrics and Electrical Insulation*, vol. 21, no. 4, pp. 1895–1900, 2014. [Online]. Available: https://doi.org/10.1109/TDEI.2014.004160

[97] M. Akyuz, L. Gao, V. Cooray, T. Gustavsson, S. Gubanski, and A. Larsson, "Positive streamer discharges along insulating surfaces," *IEEE Transactions on Dielectrics and Electrical Insulation*, vol. 8, no. 6, pp. 902–910, 2001. [Online]. Available: https://doi.org/10.1109/94.971444

[98] N. Allen and P. Mikropoulos, "Streamer propagation along insulating surfaces," *IEEE Transactions on Dielectrics and Electrical Insulation*, vol. 6, no. 3, pp. 357–362, 1999. [Online]. Available: https://doi.org/10.1109/94.775623

[99] N. Allen and D. Faircloth, "Corona propagation and charge deposition on a PTFE surface," *IEEE Transactions on Dielectrics and Electrical Insulation*, vol. 10, no. 2, pp. 295–304, 2003. [Online]. Available: https://doi.org/10.1109/TDEI.2003.1194114

[100] J. Kindersberger and C. Lederle, "Surface charge decay on insulators in air and sulfurhexafluorid - part I: simulation," *IEEE Transactions on Dielectrics and Electrical Insulation*, vol. 15, no. 4, pp. 941–948, 2008. [Online]. Available: https://doi.org/10.1109/TDEI.2008.4591214

[101] ——, “Surface charge decay on insulators in air and sulfurhexafluorid - part II: measurements,” *IEEE Transactions on Dielectrics and Electrical Insulation*, vol. 15, no. 4, pp. 949–957, 2008. [Online]. Available: https://doi.org/10.1109/TDEI.2008.4591215

[102] X. Meng, H. Mei, C. Chen, L. Wang, Z. Guan, and J. Zhou, “Characteristics of streamer propagation along the insulation surface: influence of dielectric material,” *IEEE Transactions on Dielectrics and Electrical Insulation*, vol. 22, no. 2, pp. 1193–1203, 2015. [Online]. Available: https://doi.org/10.1109/TDEI.2015.7076822

[103] D.-Y. Lim and S. Bae, “Study on oxygen/nitrogen gas mixtures for the surface insulation performance in gas insulated switchgear,” *IEEE Transactions on Dielectrics and Electrical Insulation*, vol. 22, no. 3, pp. 1567–1576, 2015. [Online]. Available: https://doi.org/10.1109/TDEI.2015.7116352

[104] S. Z. Dabbak, H. A. Illias, and B. C. Ang, “Effect of surface discharges on different polymer dielectric materials under high field stress,” *IEEE Transactions on Dielectrics and Electrical Insulation*, vol. 24, no. 6, pp. 3758–3765, 2017. [Online]. Available: https://doi-org.abc.cardiff.ac.uk/10.1109/TDEI.2017.006418

[105] D. Denissov, H. Rebholz, W. Köhler, and S. Tenbohlen, “Dielectric Strength of Different Gases in GIS,” in *14th International Symposium on High Voltage Engineering*, Beijing, China, 2005, pp. 1–5.

[106] T. Takeda, S. Matsuoka, A. Kumada, and K. Hidaka, “Sparkover and Surface Flashover Characteristics of CF_3I Gas under Application of Nanosecond Square Pulse Voltage,” in *16th International Symposium on High Voltage Engineering*, Johannesburg, South Africa, 2009.

[107] C. Li, Y. Zhu, Q. Zhi, J. Sun, S. Song, L. Connelly, Z. Li, G. Chen, Z. Lei, Y. Yang, and G. Mazzanti, "Dust Figures as a Way for Mapping Surface Charge Distribution — A Review," *IEEE Transactions on Dielectrics and Electrical Insulation*, vol. 28, no. 3, pp. 853–863, 2021. [Online]. Available: https://doi-org.abc.cardiff.ac.uk/10.1109/TDEI.2021.009432

[108] F. Sadaoui and A. Beroual, "AC creeping discharges propagating over solid–gas interfaces," *IET Science, Measurement & Technology*, vol. 8, no. 6, pp. 595–600, 2014. [Online]. Available: https://doi.org/10.1049/iet-smt.2014.0050

[109] ——, "DC creeping discharges over insulating surfaces in different gases and mixtures," *IEEE Transactions on Dielectrics and Electrical Insulation*, vol. 21, no. 5, pp. 2088–2094, 2014. [Online]. Available: https://doi.org/10.1109/TDEI.2014.004486

[110] "Unfired pressure vessels. Inspection and testing," BS EN 13445-5:2014+A1:2018, 2014-09-30.

[111] "Specification for metric dimensions of toroidal sealing rings ('O'-rings) and their housings," BS 4518:1982+A2:2014, 1982-04-30.

[112] E. Ho, "Elastomeric seals for rapid gas decompression applications in high-pressure services," HSE - Health and Safety Executive, Report, 2006.

[113] J. S. Graham, "High-voltage bushings," in *High Voltage Engineering Testing*, 3rd ed. Institution of Engineering and Technology, 2013, pp. 467–494. [Online]. Available: https://doi.org/10.1049/PBPO066E_ch12

[114] "Insulated bushings for alternating voltages above 1000 V," BS EN 60137:2008, 2009-03-31.

[115] D. C. Harris, “Mechanical Properties,” in *Materials for Infrared Windows and Domes: Properties and Performance*, 3rd ed. SPIE, 1999, pp. 84–125. [Online]. Available: https://doi.org/10.1117/3.349896.ch3

[116] “Thorlabs, Inc.” https://www.thorlabs.com/, Accessed: 04-2022.

[117] “Very Fast Transient Overvoltages (VFTO) in Gas-Insulated UHV Substations,” WG D1.03, CIGRE, 2012.

[118] S. Ziegler, R. C. Woodward, H. H.-C. Iu, and L. J. Borle, “Current Sensing Techniques: A Review,” *IEEE Sensors Journal*, vol. 9, no. 4, pp. 354–376, 2009. [Online]. Available: https://doi.org/10.1109/JSEN.2009.2013914

[119] C. Zachariades, R. Shuttleworth, R. Giussani, and R. MacKinlay, “Optimization of a High-Frequency Current Transformer Sensor for Partial Discharge Detection Using Finite-Element Analysis,” *IEEE Sensors Journal*, vol. 16, no. 20, pp. 7526–7533, 2016. [Online]. Available: https://doi.org/10.1109/JSEN.2016.2600272

[120] X. Hu, W. H. Siew, M. D. Judd, and X. Peng, “Transfer function characterization for HFCTs used in partial discharge detection,” *IEEE Transactions on Dielectrics and Electrical Insulation*, vol. 24, no. 2, pp. 1088–1096, 2017. [Online]. Available: https://doi.org/10.1109/TDEI.2017.006115

[121] L. Chen, P. Widger, M. S. Kamarudin, H. Griffiths, and A. Haddad, “CF_3I Gas Mixtures: Breakdown Characteristics and Potential for Electrical Insulation,” *IEEE Transactions on Power Delivery*, vol. 32, no. 2, pp. 1089–1097, 2017. [Online]. Available: https://doi.org/10.1109/TPWRD.2016.2602259

[122] T. Yamada, T. Takahashi, T. Toda, and H. Okubo, “Generation Mechanism of Partial Discharge in Different Kind of Pure Gases and Gas Mixtures with SF_6,” in *Gaseous Dielectrics VIII*, 1st ed. Boston, MA: Springer, 1998, pp. 125–131. [Online]. Available: https://doi.org/10.1007/978-1-4615-4899-7_18

[123] L. Christophorou and R. Van Brunt, “SF_6/N_2 mixtures: basic and HV insulation properties,” *IEEE Transactions on Dielectrics and Electrical Insulation*, vol. 2, no. 5, pp. 952–1003, 1995. [Online]. Available: https://doi.org/10.1109/94.469988

[124] P. Häfliger and C. Franck, “Critical electric field strength and effective ionization coefficient measurements of nitrogen-oxygen mixtures with variable mixing ratio,” paper D1-306, CIGRE, 2014.

[125] T. Rokunohe, Y. Yagihashi, F. Endo, and T. Oomori, “Fundamental insulation characteristics of air; N_2, CO_2, N_2/O_2, and SF_6/N_2 mixed gases,” *Electrical Engineering in Japan*, vol. 155, no. 3, pp. 9–17, 2006. [Online]. Available: https://doi.org/10.1002/eej.20348

[126] P. Fu, Z. Zhao, X. Li, X. Cui, T. Wen, and S. Mo, “Surface discharge characteristics and initiation mechanism of PEEK in nitrogen under semi-square voltage,” *AIP Advances*, vol. 8, no. 7, p. 075322, 2018. [Online]. Available: https://doi.org/10.1063/1.5034060

[127] R. K. Asundi, J. D. Craggs, and M. V. Kurepa, “Electron Attachment and Ionization in Oxygen, Carbon Monoxide and Carbon Dioxide,” *Proceedings of the Physical Society*, vol. 82, no. 6, pp. 967–978, 1963. [Online]. Available: https://doi.org/10.1088/0370-1328/82/6/316

[128] M. S. Bhalla and J. D. Craggs, “Measurement of Ionization and Attachment Coefficients in Carbon Monoxide in Uniform Fields,” *Proceedings of the Physical Society*, vol. 78, no. 3, pp. 438–447, 1961. [Online]. Available: https://doi.org/10.1088/0370-1328/78/3/313

[129] L. Christophorou and L. Pinnaduwage, “Basic physics of gaseous dielectrics,” *IEEE Transactions on Electrical Insulation*, vol. 25, no. 1, pp. 55–74, 1990. [Online]. Available: https://doi.org/10.1109/14.45234

[130] H. Okubo, N. Hayakawa, and A. Matsushita, “The relationship between partial discharge current pulse waveforms and physical mechanisms,” *IEEE Electrical Insulation Magazine*, vol. 18, no. 3, pp. 38–45, 2002. [Online]. Available: https://doi.org/10.1109/MEI.2002.1014966

[131] L. Chen, P. Widger, M. S. Kamarudin, H. Griffiths, and A. Haddad, “Potential of CF_3I gas mixture as an insulation medium in gas-insulated equipment,” in *2015 IEEE Conference on Electrical Insulation and Dielectric Phenomena (CEIDP)*, 2015, pp. 868–871. [Online]. Available: https://doi.org/10.1109/CEIDP.2015.7352013

[132] O. Farish, M. D. Judd, B. F. Hampton, and J. S. Pearson, “SF_6 insulation systems and their monitoring,” in *Advances in High Voltage Engineering*. Institution of Engineering and Technology, 2004, pp. 37–76. [Online]. Available: https://doi.org/10.1049/PBPO040E_ch2

[133] “Ieee guide for the measurement of partial discharges in ac electric machinery,” *IEEE Std 1434-2014 (Revision of IEEE Std 1434-2000)*, pp. 1–89, 2014. [Online]. Available: https://doi.org/10.1109/IEEESTD.2014.6973042

[134] A. Audoli and J.-L. Drommi, “Generator and motor stator monitoring based on partial discharge quadratic rate measurement,” in *Conference Record of the 1992 IEEE International Symposium on Electrical Insulation*, 1992, pp. 359–362. [Online]. Available: https://doi.org/10.1109/ELINSL.1992.246976

[135] P. Widger, M. Hills, and D. Mitchard, “Schlieren Images of Negative Streamer and Leader Formations in CO_2 and a CF_3I-CO_2 Electronegative Gas Mixture,” *Applied Sciences*, vol. 10, no. 22, 2020. [Online]. Available: https://doi.org/10.3390/app10228006

[136] R. Schwarz and M. Muhr, “Modern technologies in optical partial discharge detection,” in *2007 Annual Report - Conference on Electrical Insulation*

and Dielectric Phenomena, 2007, pp. 163–166. [Online]. Available: https://doi.org/10.1109/CEIDP.2007.4451557

[137] M. Ren, J. Zhou, B. Song, C. Zhang, M. Dong, and R. Albarracín, “Towards Optical Partial Discharge Detection with Micro Silicon Photomultipliers,” *Sensors*, vol. 17, no. 11, 2017. [Online]. Available: https://doi.org/10.3390/s17112595

[138] T. Kawasaki, T. Terashima, S. Suzuki, and T. Takada, “ac surface discharge on dielectric materials observed by advanced Pockels effect technique,” *Journal of Applied Physics*, vol. 76, no. 6, pp. 3724–3729, 1994. [Online]. Available: https://doi.org/10.1063/1.357443

[139] M. Michelarakis, D. Clark, P. Widger, A. Beroual, R. T. Waters, and M. A. Haddad, “Triple Point Surface Discharge Photography in Atmospheric Gases Using Intensified High-Speed Camera System,” *IEEE Transactions on Dielectrics and Electrical Insulation*, vol. 29, no. 1, pp. 153–161, 2022. [Online]. Available: https://doi.org/10.1109/TDEI.2022.3148481

[140] M. P. Edejer and G. Thodos, “Vapor pressures of liquid nitrogen between the triple and critical points,” *Journal of Chemical & Engineering Data*, vol. 12, no. 2, pp. 206–209, 1967. [Online]. Available: https://doi.org/10.1021/je60033a014

[141] M. Moussa, R. Muijlwijk, and H. Van Dijk, “The vapour pressure of liquid nitrogen,” *Physica*, vol. 32, no. 5, pp. 900–912, 1966. [Online]. Available: https://doi.org/10.1016/0031-8914(66)90021-8

[142] *Dortmund Data Bank*, 2022. [Online]. Available: www.ddbst.com

[143] C. Guder and W. Wagner, “A Reference Equation of State for the Thermodynamic Properties of Sulfur Hexafluoride (SF_6) for Temperatures from the

Melting Line to 625K and Pressures up to 150MPa," *Journal of Physical and Chemical Reference Data*, vol. 38, no. 1, pp. 33–94, 2009. [Online]. Available: https://doi.org/10.1063/1.3037344

[144] E. A. Mason and E. W. McDaniel, "Introduction," in *Transport Properties of Ions in Gases*. John Wiley & Sons, Ltd, 1988, pp. 1–29. [Online]. Available: https://doi.org/10.1002/3527602852.ch1

[145] G. J. M. Hagelaar and L. C. Pitchford, "Solving the Boltzmann equation to obtain electron transport coefficients and rate coefficients for fluid models," *Plasma Sources Science and Technology*, vol. 14, no. 4, pp. 722–733, oct 2005. [Online]. Available: https://doi.org/10.1088/0963-0252/14/4/011

[146] L. G. Christophorou and J. K. Olthoff, "Electron Interactions With CF_3I," *Journal of Physical and Chemical Reference Data*, vol. 29, no. 4, pp. 553–569, 2000. [Online]. Available: https://doi.org/10.1063/1.1318910

[147] S. Marienfeld, I. I. Fabrikant, M. Braun, M.-W. Ruf, and H. Hotop, "High resolution low-energy electron attachment to CF_3I," *Journal of Physics B: Atomic, Molecular and Optical Physics*, vol. 39, no. 1, pp. 105–126, 2005. [Online]. Available: https://doi.org/10.1088/0953-4075/39/1/010

[148] A. V. Phelps and R. J. Van Brunt, "Electron-transport, ionization, attachment, and dissociation coefficients in SF_6 and its mixtures," *Journal of Applied Physics*, vol. 64, no. 9, pp. 4269–4277, 1988. [Online]. Available: https://doi.org/10.1063/1.341300

[149] E. Kuffel, W. Zaengl, and J. Kuffel, "Chapter 4 - Electrostatic fields and field stress controln," in *High Voltage Engineering: Fundamentals*. Oxford: Newnes, 2000, pp. 201–280. [Online]. Available: https://doi.org/10.1016/B978-075063634-6/50005-8

[150] A. Hopf, M. Rossner, F. Berger, and U. Prucker, “Dielectric strength of alternative insulation gases at high pressure in the homogeneous electric field,” in *2015 IEEE Electrical Insulation Conference (EIC)*, 2015, pp. 131–136. [Online]. Available: https://doi.org/10.1109/ICACACT.2014.7223575

[151] J. Townsend, *Electricity in Gases*. Clarendon Press, 1915.

[152] E. Husain and R. S. Nema, “Analysis of Paschen Curves for air, N_2 and SF_6 Using the Townsend Breakdown Equation,” *IEEE Transactions on Electrical Insulation*, vol. EI-17, no. 4, pp. 350–353, 1982. [Online]. Available: https://doi.org/10.1109/TEI.1982.298506

[153] A. Pedersen, “Criteria for Spark Breakdown in Sulfur Hexafluoride,” *IEEE Transactions on Power Apparatus and Systems*, vol. PAS-89, no. 8, pp. 2043–2048, 1970. [Online]. Available: https://doi.org/10.1109/TPAS.1970.292789

[154] H. M. Ryan, W. L. Watson, S. J. Dale, D. J. Tedford, A. Kurimoto, H. N. Banford, and B. F. Hampton, “Factors affecting the insulation strength of SF_6 filled systems,” paper 15-02, CIGRE, 1976.

[155] D. Xiao, “Fundamentals of Gas Discharge,” in *Gas Discharge and Gas Insulation*, 1st ed. Berlin, Heidelberg: Springer, 2016, pp. 19–45. [Online]. Available: https://doi.org/10.1007/978-3-662-48041-0_2

[156] B.-T. Wu, D.-M. Xiao, Z.-S. Liu, L.-C. Zhang, and X.-L. Liu, “Analysis of insulation characteristics of c-C_4F_8 and N_2 gas mixtures by the Monte Carlo method,” *Journal of Physics D: Applied Physics*, vol. 39, no. 19, pp. 4204–4207, 2006. [Online]. Available: https://doi.org/10.1088/0022-3727/39/19/012

[157] E. Krylov and E. Nazarov, “Electric field dependence of the ion mobility,” *International Journal of Mass Spectrometry*, vol. 285, no. 3, pp. 149–156, 2009. [Online]. Available: https://doi.org/10.1016/j.ijms.2009.05.009

[158] B. M. Smirnov, “Elementary Plasma Processes,” in *Physics of Ionized Gases*. John Wiley & Sons, Ltd, 2001, pp. 45–62. [Online]. Available: https://doi.org/10.1002/9783527617708.ch4

[159] “COMSOL Multiphysics® Reference Manual v.5.5,” COMSOL AB, Stockholm, Sweden, 2019.

[160] D. J. Griffiths, “Electric Fields in Matter,” in *Introduction to Electrodynamics*, 4th ed. Cambridge: Cambridge University Press, 2017, pp. 167–209. [Online]. Available: https://doi.org/10.1017/9781108333511

Appendix A

Supplementary content

A.1 Saturation vapour pressure curves

In Figure A.1 are summarised the saturation vapour pressure curves of the gaseous insulating media which were presented in Section 2.2. The purpose of that illustration is to provide a direct comparison between the different compounds.

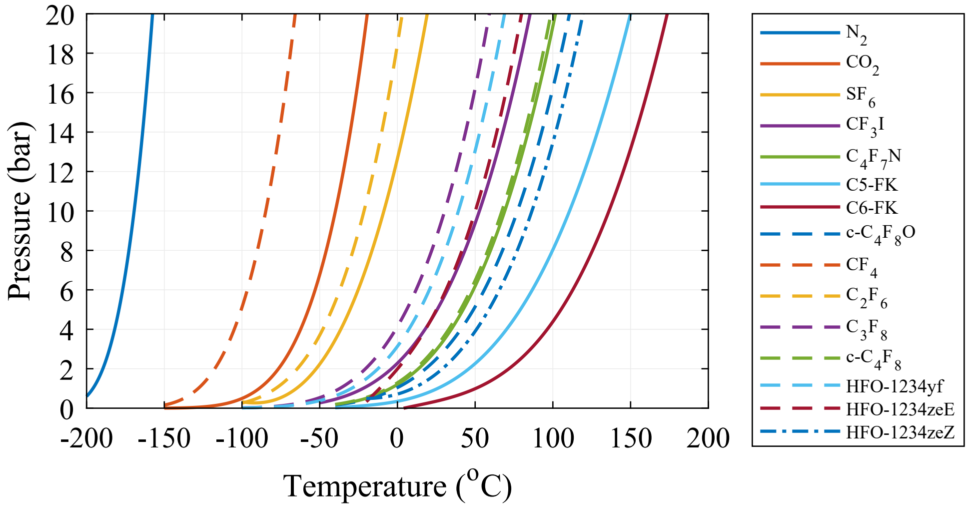

Figure A.1: Saturation vapour pressure curves of the presented gaseous insulating media.

The data for the curves of Figure A.1 were collected as follows:

(i). *Nitrogen (N_2)*

$$\log_{10}(P) = A - \left(\frac{B}{T+C}\right) \tag{A.1}$$

where the vapour pressure P in bar and the temperature T in Kelvin. The fitting parameters for Equation (A.1) are shown in Table A.1.

Table A.1: Fitting parameters for Equation (A.1).

Temperature (K)	A	B	C
$63.14 - 126$	3.7362	264.651	-6.788
$63.14 - 78$	3.63792	257.877	-6.344

The data was taken from [57] which, in turn, was retrieved from [140, 141]

(ii). *Carbon dioxide (CO_2)*

$$P = 10^{A-\frac{B}{C+T}} \tag{A.2}$$

where the vapour pressure P in mmHg and the temperature T in $^{\circ}C$. The fitting parameters for Equation (A.2) are shown in Table A.2.

Table A.2: Fitting parameters for Equation (A.2).

Temperature ($^{\circ}C$)	A	B	C
$-62 - 31$	7.5322	835.06	268.223
$-57 - 31$	7.8101	987.44	290.9

The data was taken from [142].

(iii). *Sulphur hexafluoride (SF_6)*

$$p = p_{\mathrm{c}}\left(\frac{T}{T_{\mathrm{c}}}\left(A_1\tau + A_2\tau^{1.5} + A_3\tau^{2.5} + A_4\tau^4 + A_5\tau^{4.5}\right)\right) \tag{A.3}$$

where $\tau = 1 - T/T_{\mathrm{c}}$, $T_{\mathrm{c}} = 318.7232\,\mathrm{K}$, $p_{\mathrm{c}} = 3754.983\,\mathrm{kPa}$. The fitting parameters for Equation (A.3) are shown in Table A.3.

The data was taken from [42] which, in turn, was retrieved from [143].

Table A.3: Fitting parameters for Equation (A.3).

A_1	A_2	A_3	A_4	A_5
-7.0963642	1.676662	-2.3921599	5.86078302	-9.02978735

(iv). *Trifluoroiodomethane (CF_3I)*

$$\ln\left(\frac{P}{P_\mathrm{c}}\right) = \left(A_1\tau + A_2\tau^{1.25} + A_3\tau^3 + A_4\tau^7\right)\frac{T_\mathrm{c}}{T} \tag{A.4}$$

where $\tau = 1 - T/T_\mathrm{c}$, $T_\mathrm{c} = 395.05\,\mathrm{K}$, $P_\mathrm{c} = 3.8617\,\mathrm{MPa}$. The fitting parameters for Equation (A.4) are shown in Table A.4.

Table A.4: Fitting parameters for Equation (A.4).

A_1	A_2	A_3	A_4
-7.19045	1.34829	-1.58035	-5.46680

The data was taken from [31].

(v). *C_4F_7N Fluoronitrile*

The data was extracted directly from the curve provided in [34].

(vi). *C5-FK Fluoroketone*

The data was extracted directly from the curve provided in [39].

(vii). *C6-FK Fluoroketone*

The data was extracted directly from the curve provided in [40].

(viii). *c-C_4F_8O Fluorooxirane*

$$p = \exp\left(A_0 + \frac{A_1}{T} + A_2T + A_3\log(T)\right) \tag{A.5}$$

where p is the pressure in Pa and T the temperature in Kelvin. The fitting parameters for Equation (A.5) are shown in Table A.5.

The data was taken from [42] which, in turn, was retrieved from [43].

(ix). *Tetrafluoromethane (CF_4)*

Table A.5: Fitting parameters for Equation (A.5).

A_0	A_1	A_2	A_3
133.633	-6016.20	0.028363	-19.2157

$$\ln(p) = \ln(p_\mathrm{c}) + \left(A_1\tau + A_2\tau^{1.5} + A_3\tau^3 + A_4\tau^6\right)\frac{1}{T_\mathrm{R}} \tag{A.6}$$

where $\tau = (1 - T_\mathrm{R})$ and p_c and T_R are the critical pressure and the reduced temperature respectively. The fitting parameters for Equation (A.6) are shown in Table A.6.

Table A.6: Fitting parameters for Equation (A.6).

A_1	A_2	A_3	A_4
-6.7651056	1.0777437	-1.7490971	-2.5845119

The data was taken from [44].

(x). *Hexafluoroethane (C_2F_6)*

$$\ln(P) = A + \frac{B}{T} + CT + DT^2 \tag{A.7}$$

where P the pressure in kPa and T the temperature in Kelvin. The fitting parameters for Equation (A.7) are shown in Table A.7.

Table A.7: Fitting parameters for Equation (A.7).

A	B	C	D
23.855755	-2714.8507	-0.036895822	4.934326×10^{-5}

The data was taken from [45].

(xi). *Octafluorocyclobutane (c-C_4F_8)*

$$\ln(P) = A + \frac{B}{T} + CT + D\ln(T) + ET^2 \tag{A.8}$$

where P the pressure in kPa and T the temperature in Kelvin. The fitting parameters for Equation (A.8) are shown in Table A.8.

Table A.8: Fitting parameters for Equation (A.8).

A	B	C	D	E
-98.499002	-18054910	-0.11720375	24.247841	7.9735652×10^{-5}

The data was taken from [45].

(xii). *2,3,3,3-tetrafluoropropene (HFO-1234yf)*

$$T_{\text{r}}\ln\left(\frac{P_{\text{s}}}{P_{\text{c}}}\right) = A\tau + B\tau^{1.5} + C\tau^{2.5} + D\tau^{5} \tag{A.9}$$

where $\tau = 1 - T_{\text{r}}$, $T_{\text{r}} = T/T_{\text{c}}$, P in kPa and T in Kelvin. The fitting parameters for Equation (A.9) are shown in Table A.9.

Table A.9: Fitting parameters for Equation (A.9).

A	B	C	D
-7.42628	1.98692	-3.60052	6.45367

The data was taken from [50].

(xiii). *Trans-1,3,3,3-tetrafluoropropene (HFO-1234zeE)*

$$\log_{10}(P) = \frac{A_0}{T + 273.15 + A_1} + A_2 \tag{A.10}$$

where P in bar and T in $^{\circ}C$. The fitting parameters for Equation (A.10) are shown in Table A.10.

Table A.10: Fitting parameters for Equation (A.10).

A_0	A_1	A_2
1115.58	-6.78	4.52

The data was taken from [49].

(xiv). *Cis-1,3,3,3-tetrafluoropropene (HFO-1234zeZ)*

The data was extracted directly from the curve provided in [51].

A.2 Fundamental discharge mechanisms in gaseous dielectrics

A.2.1 Electronic avalanche and ionisation coefficients

For high electric fields, ionisation by electron impact is the most important factor that can lead to the breakdown of the gas insulation. The energy an electron can gain moving in the direction of the electric field and for a distance equal to the effective mean free path needs to be equal or higher than the energy required to ionise the molecules of the gaseous medium. If an electron has not gained enough energy, then upon its collision with a neutral gas molecule, the struck particle will most likely become excited at this specific stage, depending on the cross-section that describes the process. Townsend's first ionisation coefficient α describes the number of electrons produced during inelastic collisions of one electron with neutral gas particles per unit length in the direction of the applied electric field. The total number of electrons produced by one electron starting its movement from the cathode and until it reaches the anode is defined as the electron avalanche. The general expression of a neutral particle ionisation when it collides with electrons of sufficient energy, frequently referred to as the α-process, is described by Equation (A.11) [72]

$$\frac{\alpha}{p} = f\left(\frac{E}{p}\right) \tag{A.11}$$

where E is the applied electric field, and p the gas pressure, showing that the first ionisation coefficient is dependent upon these values. The electron attachment coefficient η is another important parameter especially in cases where gases with high electron attaching capability are considered or cases of high applied electric fields are examined where the impact ionisation by electron collision is significant. In such cases the difference between α and η is defined as the effective ionization coefficient:

$$\bar{\alpha} = \alpha - \eta \tag{A.12}$$

As mentioned before, positive ions will move towards the cathode. When these ions hit the cathode surface, secondary electrons will be released, the average number of which is defined as the secondary ionisation coefficient γ. The values of γ are greatly affected by the cathode surface condition and material: materials of low work function i.e., the energy required to remove one electron from a point immediately outside its surface, will produce higher electron emissions.

A.2.2 Critical reduced electric field

Through the effective ionisation coefficient of Equation (A.12), it is possible to calculate the critical reduced field strength. At the point where $\alpha{-}\eta = 0$ i.e., when ionisation equals attachment, the critical reduced electric field $(E/N)_{\mathrm{lim}}$ will be specified [60]. The ratio of the electric field E over the gas number density N determines the average ionic energy gained from the field in steady state above the energy associated with thermal motion [144]. For values $(E/N) < (E/N)_{\mathrm{lim}}$, the electron attachment rate will be higher than the ionisation rate meaning that electrical discharges will be suppressed. For the calculation of Townsend coefficients, electron Boltzmann equation in two-term approximation is employed where the collision cross-sections are used as inputs. The Boltzmann equation in an ionised gas, as described in [145], is:

$$\frac{\theta f}{\theta t} + \vec{u} \cdot \nabla - \frac{e}{m} \vec{E} \cdot \nabla_{\mathrm{v}} f = C\left[f\right] \tag{A.13}$$

where f is the electron distribution in the six-dimensional phase space which corresponds to the velocity coordinates, e the elementary charge, m the electron mass, $\vec{E}$

the electric field, ∇_{v} the velocity gradient operator and C is the rate of change in f due to collisions. Solving Equation (A.13) can be performed using BOLSIG+ application developed by Gerjan Hagelaar of the Laboratoire Plasma et Conversion d'Energie (LAPLACE) [145]. As an example, effective ionisation coefficients of SF_6 and CF_3I are compared in Figure A.2. The cross-section sets were retrieved from the LXcat database project.

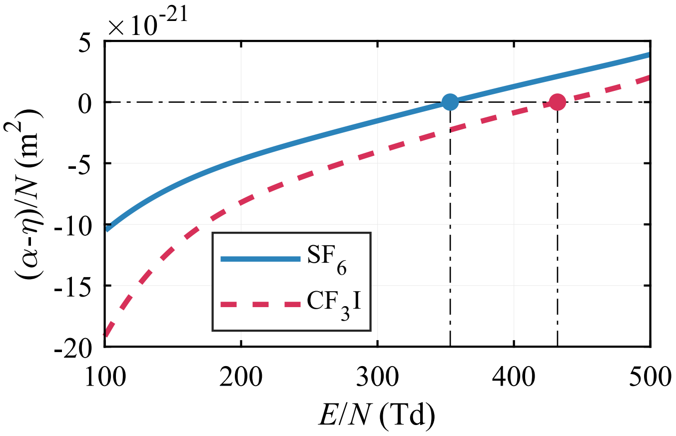

Figure A.2: Effective ionisation coefficient for SF_6 and CF_3I [146–148].

The ratio of the reduced electric field values at the intersection points of the curves of Figure A.2 with the horizontal line $(\alpha - \eta)/N = 0$ is specified at 1.22 which is in very good agreement with similar reported calculations [121].

A.2.3 Electric field distribution concepts

It is true that the need for compact and robust devices in medium- and high-voltage applications has increased the complexity of the commercial assemblies. During service, the gaseous insulation of enclosed compressed equipment may be subjected to electric field stresses of various uniformity levels. For that reason, relevant international standards require the assessment of such devices at elevated voltage magnitudes, far above the rated operational ones, for relatively short time durations and under different applied waveshapes. In many cases, not only the fully assembled device shall undergo the dielectric performance assessment process, but even different compartments should be tested separately in order to ensure that they comply with the relevant withstand regulations.

In fully controlled laboratory experiments, it is possible to achieve different levels of uniformity and investigate the withstand levels of the gaseous insulation. The simplest form of a test consists of a two-electrode arrangement, with one of the electrodes being at ground potential while a voltage waveform is applied at the other, with both of them installed in a container (vessel) filled with the insulating gas under study. Different voltage waveshapes at variable magnitudes and frequencies may be applied in an attempt to replicate different stress conditions or initiate different types of discharge phenomena which need to be observed.

The most known electrode configurations are: (1) the plane-plane, (2) sphere-plane, (3) sphere-sphere (4) rod-plane and (5) needle-plane, each one able to achieve a different electric field distribution pattern. Figure A.3 summarises the electric field distribution concepts for four of the listed electrode configurations. The case of rod-plane can produce an electric field distribution pattern similar to that of either the sphere- or needle-plane depending on the dimensions (rod diameter and gap distance) of the configuration. Calculations were performed through simplified electrostatic field modelling using COMSOL Multiphysics® in order to demonstrate the basic characteristics for the different cases. The same gap distances were considered for all the cases for comparison purposes. The electric field magnitude was expressed normalised to its maximum value which always appears at the point with the shortest distance to the zero potential electrode. For better readability of the graphs, gap distances were also normalised, with 0 representing no gap distance and 1 the maximum possible for each computed case. For the model of Figure A.3d, no special edge profile was considered, and the electric field shown represents the gap distance between the centre points of the two planes.

The needle-plane case shows the most abrupt decrease in the electric field along the

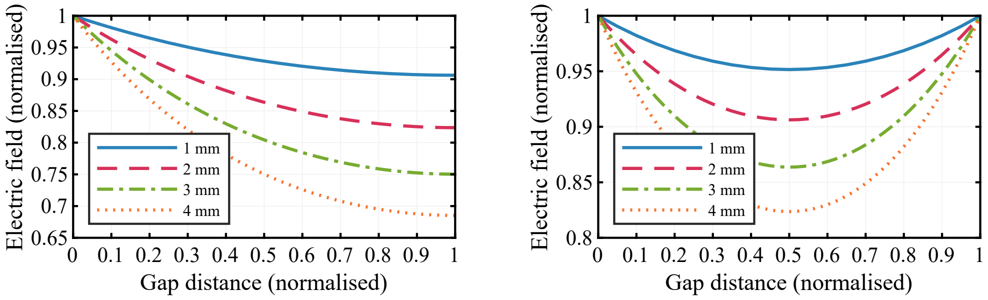

(a) Sphere-plane **(b)** Sphere-sphere

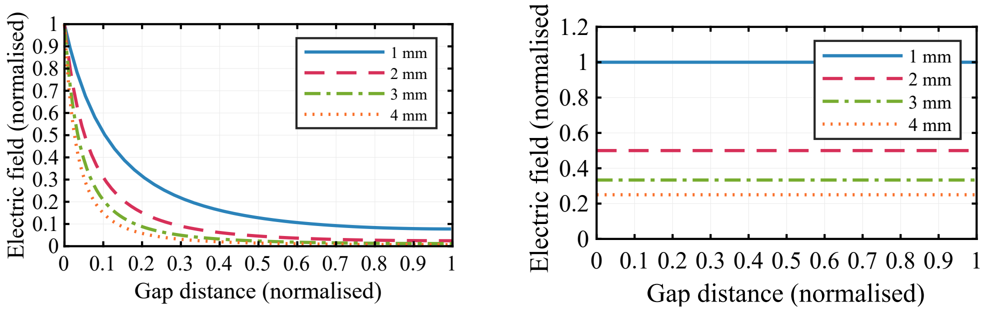

(c) Needle-plane **(d)** Plane-plane

Figure A.3: Electric field distribution for different electrode configuration types.

gap distance, followed by the sphere-plane. The plane-plane shows a uniform distribution, however, it is obvious the decrease in magnitude as a function of the gap distance. Only for this case, normalisation was performed using as basis the average of the computation for the 1 mm case. The lowest field values for sphere-sphere configuration are shown around the middle of the gap distance.

A parameter that is frequently used to describe the homogeneity of the electric field within an electrode gap distance is the field utilisation, or efficiency, factor. It is defined as the ratio between the mean electric field along the gap distance over its maximum value [149].

$$\eta_{\text{E.F.}} = \frac{E_{\text{mean}}}{E_{\text{max}}} \tag{A.14}$$

Since E_{max} is always greater than E_{mean} then $\eta_{\text{E.F.}}$ will always be less than 1, except for the case where a perfectly homogenous electric field distribution is achieved for which $\eta = 1$. Quasi-homogeneous electric field distribution is characterised by $\eta < 1$ while, for the very low values, at 0.2 or lower, the electric field distribution is considered to be strongly divergent [150].

A.2.4 Townsend discharge mechanism

When describing electrical discharge phenomena in gaseous insulation, it is inevitable not to refer to the fundamental theory of Townsend discharge. In 1915, Sir John Sealy Townsend described the principle of electron avalanche, among other fundamental principles regarding gas discharges [151]. He provided the example of gas current measurement between two parallel plate electrodes as a function of the applied voltage. He found that the current increases almost proportionally with the increase of the applied voltage up to a value where saturation occurs (point U_2, I_2 in Figure A.4).

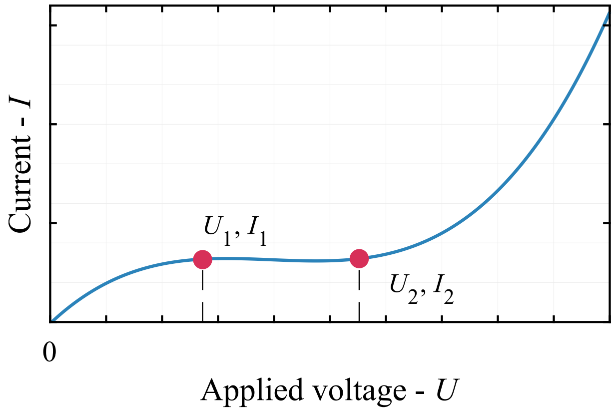

Figure A.4: Evolution of current over voltage for a parallel plate electrode arrangement, as described in [151].

When the voltage further increases ($U > U_2$), and thus the induced electric field, the electrons that leave the anode will accelerate until they obtain enough energy to ionise the gas molecules. At a distance dx, from the anode the number of electrons will have increased to

$$\mathrm{d}n_{\mathrm{e}} = \alpha n_{\mathrm{e}} \mathrm{d}x \tag{A.15}$$

where α is Townsend's first ionisation coefficient and n the number of electrons at a distance $\mathrm{d}x$ from the anode. Integrating Equation (A.15) over the entire electrode gap distance $\mathrm{d}x = d$ will return,

$$n_{\mathrm{e}} = n_{\mathrm{e},0} e^{\alpha d} \tag{A.16}$$

where $n_{\mathrm{e},0}$ is the number of primary electrons generated at the anode. The current leaving the anode will be:

$$I = I_0 e^{\alpha d} \tag{A.17}$$

The term $e^{\alpha d}$ describes the number of electrons produced by one electron travelling along the gap distance. In the same study, Townsend observed that Equation (A.17) was not applicable for higher applied voltage magnitudes, and thus higher induced electric fields. A second mechanism was proposed which associates the liberation of electrons from the gas molecules and the cathode due to collisions of positive ions and photons. In terms of current, the mechanism is expressed as:

$$I = I_0 \frac{e^{\alpha d}}{1 - \gamma \left(e^{\alpha d} - 1\right)} \tag{A.18}$$

where γ is known as Townsend's second ionisation coefficient and represents the secondary electron emission number per positive ion colliding with the surface of the cathode. The values of γ are less than 1 which is practically justified by the low kinetic energy the positive ions will have by the time they reach the cathode because of the collisions with gas molecules preceding that time instant. Thus, is significant the contribution of secondary electron emission from the cathode surface by photon impact. The coefficient γ strongly depends on the condition and material of the electrodes and the impurities of the gaseous medium.

The Townsend breakdown mechanism is described based on Equation (A.18). Considering also the electron attachment, then $\bar{\alpha} = \alpha - \eta$. The denominator will become zero when

$$\gamma \left(e^{\bar{\alpha} d} - 1 \right) = 1 \tag{A.19}$$

Three options are possible [149]:

- $\gamma \left(e^{\bar{\alpha} d} - 1 \right) = 1$: Emission of secondary electrons is sustainable and causes the repetition of the electron avalanche.
- $\gamma \left(e^{\bar{\alpha} d} - 1 \right) > 1$: The ionisation becomes cumulative and intensifies the larger the $\gamma \left(e^{\bar{\alpha} d} - 1 \right)$ becomes.
- $\gamma \left(e^{\bar{\alpha} d} - 1 \right) < 1$: The discharge is not self-sustained.

The transition from self-sustained to non-self-sustained discharge is commonly referred to as the breakdown of the gas. Based on the Townsend breakdown criterion, the breakdown voltage is given as [152]:

$$V_{\mathrm{b}} = \frac{Bpd}{\ln \left[Apd / \ln \left(1 + 1/\gamma \right) \right]} \tag{A.20}$$

where p is the pressure, d the gap distance, A the saturation ionisation in the gas at a particular reduced electric field E/p level and B is related to the excitation and ionisation energies. From Equation (A.20), and considering the case of low space charge distortions (low gap current), the breakdown voltage can be expressed as a function of the pd product. Such a variation is expressed by Paschen's law.

A.2.5 The streamer mechanism

The description of Townsend mechanism assumes that, within the uniform electric field gap distance, the impact of space charges of electrons and ions, and thus the distortion in the electric field they can cause, are negligible. In such a case, the resulting growth of the electron avalanche will be stable, and an almost constant applied voltage is required. In many practical applications, the applied voltage varies with time, in some cases slowly, such as AC $50/60\,\mathrm{Hz}$ or it is characterised by very fast front-times such as impulse voltages or fast transients.

The streamer mechanism describes the growth and instability of a single electron avalanche which results in the generation of ionisation channels that lead to the development of breakdown. As described in [153], three general conditions are necessary for the streamer propagation:

1. Photons of high energy should be produced in the head of the initial avalanche
2. This energy is sufficiently high to ionise molecules within the vicinity of the avalanche head
3. The electric field induced by the space charge at the head of the avalanche must be sufficient to produce secondary avalanches

Meek formulated a criterion for streamer breakdown in non-attaching gases which is mathematically represented by Equation (8)

$$\left(\alpha_{\mathrm{x}}-\eta_{\mathrm{x}}\right) e^{\int_0^x (\alpha-\eta)\mathrm{d}x} = G\left(x,\rho\right) \tag{A.21}$$

where x is the length of the avalanche at the time of its formation, α_{x} the first Townsend ionisation coefficient, η_{x} the electron attachment coefficient at the avalanche head, ρ the gas density and $G\left(x,\rho\right)$ an empirical function derived from experimental breakdown experiments in uniform electric fields. In [153], Pedersen proposed another version of Equation (A.21) applicable in strongly attaching gases

$$\frac{1}{2}\ln\left(\alpha_{\mathrm{x}}\right) + \int_0^x \left(\alpha-\eta\right)\mathrm{d}x = f\left(x,\rho\right) \tag{A.22}$$

Assuming that the variation of $f\left(x,\rho\right)$ with x and ρ in Equation (A.22) is small, even in non-uniform electric fields, and that the contribution of the logarithmic part is almost constant, then the criterion is reduced to:

$$\int_0^x (\alpha - \eta)\,\mathrm{d}x = K \tag{A.23}$$

In the same work [153], the value for K for the case of SF_6 was estimated at approximately 18.

A.2.6 Breakdown in gases

Space charge has a direct impact also in the breakdown mechanism. Its generation is linked to the time variation of the applied voltage. As described in [132], there are two distinct types of breakdown: (a) when the voltage is applied relatively slowly and (b) when the applied voltage has a short rise time. The first category includes alternating polarity waveshapes at power frequency $(50\,\mathrm{Hz})$, where the space charge has a direct impact on the distribution of the electric field by the corona stabilisation process. The second category includes cases such as standard lightning impulse and/or transients, where breakdown of the gas insulation is driven by a stepped leader mechanism.

In strongly non-uniform electric fields, for instance a needle-plane or rod-plane electrode configurations, over a pressure range, there is a region where the breakdown level is much higher than the onset voltage for corona discharge, and a point after which the appearance of the first streamer will lead to the breakdown of the gap. The described behaviour is depicted in Figure A.5.

When an electric field of high magnitude appears at a sharp point of positive polarity applied voltage, the electrons will move quickly towards the charged point while positive ions will move slower to the lower electric field region. The positive space charge created will shield the region around the high field point and stabilise it to a level close to the onset value. As the applied voltage increases, the shielding space charge will also increase, and a much higher voltage level will be required to cause a breakdown. As the pressure increases, the region of corona discharge will become smaller and its stabilisation will be less effective. The streamer which will form at the

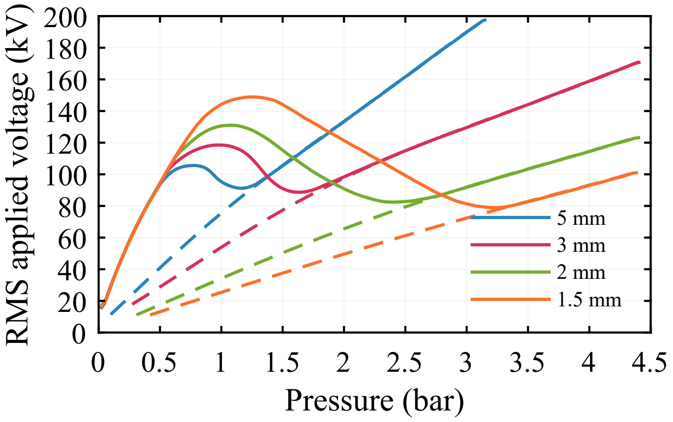

Figure A.5: AC corona and breakdown characteristics for a 40 mm rod-plane gap in SF_6. The continuous lines represent the breakdown voltage while the dashed ones show the onset corona. Each colour represents a different rod radius. Figure was replotted from [132].

onset voltage will be capable of initiating a breakdown across the gap.

For applied voltages of fast rising times, such as standard lightning impulses $(1.2/50\,\mu\text{s})$ and voltage transients, the time for the formation of space charge might not be enough as in the case of a slowly varying AC. When the applied voltage exceeds the corresponding onset level, very intense streamer activity may initiate which, in turn, may lead to the formation of an ionised highly conductive channel. Around the tip of that channel, new streamers will appear which may lead to the further extension of the ionised channel. At some point, the streamers will become weak and they will force the conductive channel to propagate further. If the electric field is large enough, then the formatted ionised leader channel will bridge the two electrodes and lead to breakdown of the gap [132].

In [154], positive polarity switching impulse $(130/2000\,\mu\text{s})$ breakdown test results on SF_6 for a range of pressures $0 - 2$ bar were performed using a rod-plane electrode configuration. The rod diameter was 19 mm and the gap distance was 30 cm. The corona stabilisation trend on the exported voltage/pressure characteristic curve was again present. The corresponding results are replotted in Figure A.6. As discussed by the authors, the corresponding curve for negative polarity was similar to the $U_{50\%}$, with the critical pressure being higher.

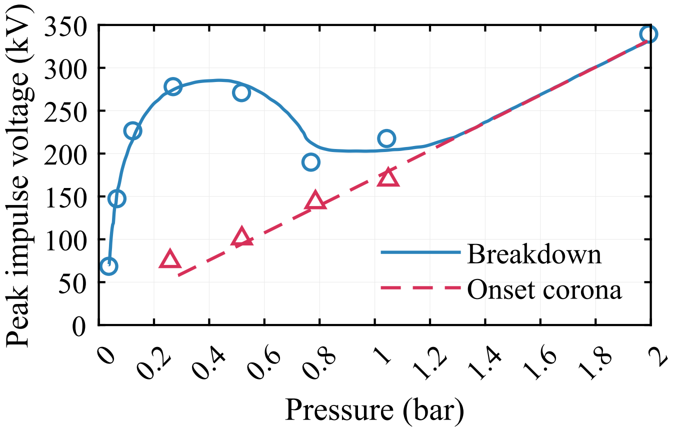

Figure A.6: Voltage-pressure characteristic of SF_6 for a rod-plane electrode arrangement (19 mm rod diameter/30 mm gap distance) and switching impulse waveform of $130/2000\,\mu$s [154].

This particular set of results was used also in [23]. An interesting comment was that, at pressures below the critical (the minimum value of pressure attained after the peak of voltage-pressure characteristic), the ratio of impulse breakdown over power frequency breakdown was less than unity while, for higher pressures than the critical pressure, the same ratio was higher than 1.

A.3 Movement and collision of particles

Two basic categories of particles are considered when describing gas discharge electronics, charged particles which include electrons and ions (cations and anions), and neutral particles which include atoms and molecules. Electron rest mass $(m_\mathrm{e} = 9.109 \cdot 10^{-31}\,\mathrm{kg})$ and size are essentially smaller compared to molecules. Size of ions is similar to molecules since they are formed by molecules which lost or gained at least one electron. Without any applied external electric field, all the particles are under thermal motion with elastic collisions taking place between different particles and between particles and the walls of the gas container. Weakly ionised gases will follow the classical kinetic gas theory. The distance that the particles cover between collisions is defined as the free path (λ) and its mean value $\bar{\lambda}$ is described by Equation (A.24)

$$\bar{\lambda} = \frac{1}{N\pi\left(r_1 + r_2\right)^2} = \frac{1}{N\sigma} \tag{A.24}$$

where N is the gas density, r_2 is the radius of stationary molecules, r_2 the radius of moving particles $(r_1 \gg r_2)$ and σ the collision cross-section [72,155]. Thermal motion is also a key parameter of gas molecules diffusion especially when two different gases are mixed or two volumes at different pressures are linked. Diffusion also applies for charged particles especially in cases of their non-uniform distribution, for instance after an electrical discharge. It describes the tendency of charged particles to move from regions of high to low concentration, and its magnitude depends on the pressure and temperature of the gas [72, 156].

With the presence of an externally electric field, usually appearing between two electrodes, charged particles will be accelerated proportionally to the electric field and that motion will be superimposed to the thermal movement resulting to the drift motion of charged particles. Positive ions will move towards the cathode while negatively charged particles toward the anode. Charged particles will not accelerate infinitely but during their movement in the direction of the electric field, collisions with surrounding molecules will slow down their motion i.e., they will lose amount of their kinetic energy previously obtained through the electric field acceleration. The state of motion of the gas is described by the mobility μ and is expressed as

$$\mu = \frac{u_\mathrm{d}}{E} \qquad \left[\mathrm{m^2/V \cdot m}\right] \tag{A.25}$$

where u_d the drift velocity in $\mathrm{m/s}$ and E the electric field in $\mathrm{V/m}$. For low magnitude electric fields, the ion mobility is independent of the electric field as most of their kinetic energy is a result of their thermal motion. In that case, where the mobility in Equation (A.25) depends on the gas pressure and ion mass, the higher these values are, the lower the μ will be. However, for high electric fields, ion mobility becomes field dependent [157]. Mobility of electrons has different dependencies, and is much higher, compared to that of ions. As electrons have considerably smaller mass compared to ions, they can acquire kinetic energy from the electric field much faster, losing a small part of it in inelastic collisions with molecules, or store it until inelastic collisions become important. Even at low electric fields the electron kinetic energy may be much higher compared to the kinetic energy of ions [144]. In other words, the electron drift velocity will be much larger than that of ions.

Collisions between particles may result in processes like excitation and ionisation. When the electron of an atom or molecule absorbs energy and moves to a higher energy state, maintaining its orbital rotating movement around the nucleus, then the atom becomes excited. For the case where the income energy exceeds the ionisation levels of the atom or molecule, then the electron detaches and ionisation takes place.

The energy transfer through a collision is expressed by the conservation laws of energy and momentum. Following the basic representation of Figure A.7 [72] and assuming that the particle with larger mass was not moving prior to the collision, these laws are described by the Equations (A.26) and (A.27) respectively.

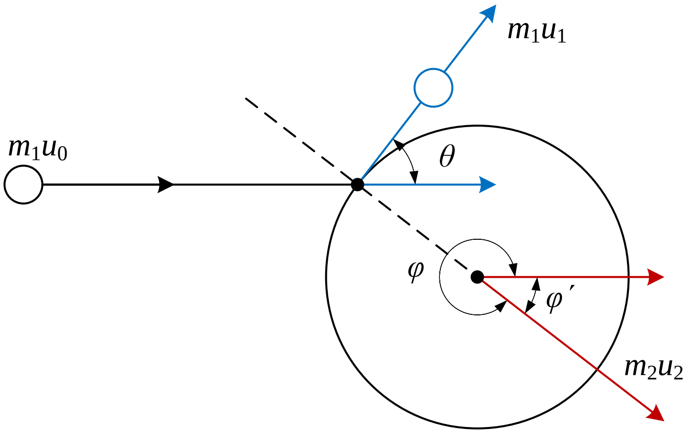

Figure A.7: Collision of two particles when $m_1 \ll m_2$ [72].

$$\frac{1}{2}m_1 v_0^2 = \frac{1}{2}m_1 v_1^2 + \frac{1}{2}m_1 v_2^2 + Q \tag{A.26}$$

$$m_1 v_1 = m_1 v_1 \cos\theta + m_1 v_1 \cos\phi' \tag{A.27}$$

The masses of the two particles are m_1 and m_2 with their corresponding speeds being v_1 and v_2. The variable Q represents the increase in the potential energy of the particles after the collision. Two types of collisions may occur between particles: elastic or inelastic. For the case of elastic, $Q = 0$ after the collision, means that there is no change in the potential energy of the particles after the event, while for inelastic collisions, $Q \neq 0$, part of the kinetic energy is converted into potential energy. The average energy loss per collision fraction and the maximum integral energy gained during the event are used to express the energy transfer between the particles during the two types of collisions [72, 155].

$$\overline{\delta\left(\phi'\right)} = \frac{2m_1 m_2}{\left(m_1 + m_2\right)^2} \qquad \text{(Elastic)} \tag{A.28}$$

$$Q_{\text{max}} = \frac{m_1 m_2}{2\left(m_1 + m_2\right)} v_1^2 \qquad \text{(Inelastic)} \tag{A.29}$$

When $m_1 \ll m_2$ i.e., in the case where an electron collides with an atom / molecule / ion, for elastic collisions the electron will give a small part of its energy while, for inelastic collisions, it will be able to transfer all of its kinetic energy as potential energy to the much heavier particle. When $m_1 \approx m_2$, for example, when ions collide with other ions or atoms/molecules, for the elastic collisions the energy loss rate will be high while, in inelastic collisions, half of their kinetic energy can transform to maximum potential energy to ionise or excite the collided particle [72, 155]. The elementary collision processes that involve charged particles (electrons and/or ions) and neutral particles (atoms/molecules), in weakly ionised gases, are listed in Table A.11 below:

Table A.11: Collision processes in weakly ionised gases [42, 72, 155, 158].

Process	**Expression**	
Collisions between electrons and atoms/molecules		
Elastic collision between electron and molecule	$e^- + AB \rightarrow e^- + AB$	
Inelastic collision between electron and molecule	$e^- + AB \rightarrow e^- + AB^*$	Excitation
Inelastic collision between electron and molecule	$e^- + AB \rightarrow AB^+ + 2e^-$	Ionisation - Non-dissociative
Inelastic collision between electron and molecule	$e^- + AB \rightarrow A^+ + B + 2e^-$	Ionisation - Dissociative
Superelastic collision between electrons and excited molecules	$e^- + A^* \rightarrow e^- + A$	De-excitation
Dissociative electron attachment to a molecule	$e^- + AB \rightarrow (AB^-)^* \rightarrow A + B^-$	
Electron attachment in three-body collisions	$e^- + A + B \rightarrow A^- + B$	
Dissociation of molecule by electron impact	$e^- + AB \rightarrow e^- + A + B$	
Electron-ion recombination in three-body collisions	$e^- + A^+ + B \rightarrow A^* + B$	
Collisions between ions and atoms/molecules		
Electron detachment	$A + B^- \rightarrow AB + e^-$ $A + B^- \rightarrow A + B + e^-$	Decay of negative ions
Charge exchange	$A^+ + A \rightarrow A + A^+$ $A^+ + B \rightarrow A + B^+$	
Ion conversion	$A^- + B \rightarrow AB^-$	

Neutralisation of ions	$A^+ + B^- \rightarrow A + B$	
Conversion of atomic to molecular ions	$A^+ + B + C \rightarrow AB^+ + C$	
Collisions between atoms and molecules		
Elastic collision	$A + B \rightarrow A + B$	
Elastic collision	$A + B \rightarrow A^* + B$	Excitation
Inelastic collision	$A + B \rightarrow A^+ + B + e^-$	Ionisation
Associative ionisation	$A^* + B \rightarrow AB^+ + e^-$	
Penning ionisation	$A^* + B \rightarrow A + B^+ + e^-$	
Transfer of excitation	$A^* + B \rightarrow A + B^*$	
Formation of molecules	$A + B + C \rightarrow AB + C$	
Chemical reactions	$A + BC \rightarrow AB + C$	

A.4 Relative permittivity and polarisation

Polarisation induced in a medium is expressed dependent to the electric field, as shown in Equation (A.30)

$$\boldsymbol{P} = \chi_{\mathrm{e}} \varepsilon_0 \boldsymbol{E} \tag{A.30}$$

where χ_{e} is the dimensionless quantity of electric susceptibility and $\varepsilon_0\,(8.85 \times 10^{-12}\mathrm{C}^2/\mathrm{N} \cdot \mathrm{m}^2)$ the permittivity of free space. The permittivity of the material is related to χ_{e} as shown in Equation (A.31)

$$\varepsilon = \varepsilon_0 \left(1 + \chi_{\mathrm{e}}\right) \tag{A.31}$$

Multiplying ε with the electric field vector defines the electric displacement field, expressed in C/m^2, within the dielectric material,

$$\boldsymbol{D} = \varepsilon \boldsymbol{E} = \varepsilon_0 \left(1 + \chi_{\mathrm{e}}\right) \boldsymbol{E} = \varepsilon_0 \boldsymbol{E} + \chi_{\mathrm{e}} \varepsilon_0 \boldsymbol{E} = \varepsilon_0 \boldsymbol{E} + \boldsymbol{P} \tag{A.32}$$

One of the electrical parameters always listed in data sheets of dielectric materials is the relative permittivity, or dielectric constant, ε_{r} which is a dimensionless quantity. When multiplied with the permittivity of free space ε_0 $(8.85 \times 10^{-12} \mathrm{C}^2/\mathrm{N} \cdot \mathrm{m}^2)$, it results into the permittivity of the material,

$$\varepsilon = \varepsilon_{\mathrm{r}} \cdot \varepsilon_0 \Rightarrow \varepsilon_{\mathrm{r}} = 1 + \chi_{\mathrm{e}} \tag{A.33}$$

A.5 Definitions of PD quantities

Some quantities related to partial discharges, which help to quantify their impact on the insulation system under study, are those listed below, the definitions of which are retrieved by the relevant standards [88] and which are widely accepted [89, 91]:

i. Apparent charge, q

   The apparent charge represents the amount of charge that if injected between the terminals of the test object it will produce the same current pulse on the recording instrument as would be produced by an actual detected partial discharge. It is usually expressed in picocoulombs (pC). Suitable charge calibrators which can inject apparent charge pulses can be used for that purpose.

ii. Pulse phase, ϕ_{i}, and time of occurrence, t_{i}

   In case an AC voltage waveform of specific frequency f_{AC} and period T_{AC} is applied to a test object, the time of appearance t_{i} refers to the time instant the partial discharge appears with reference to the zero-crossing of the voltage signal at the beginning of the positive half-cycle. The phase angle is defined as:

$$\phi_{\mathrm{i}} = 360 \cdot (t_{\mathrm{i}}/T_{\mathrm{AC}}) \tag{A.34}$$

iii. Pulse repetition rate, n_{pd}

It expresses the ratio between the number of partial discharge pulses detected/recorded within a specified time interval, over this time interval.

iv. Pulse repetition frequency, N_{pd}

The number of partial discharges per second in case of equidistant pulses.

v. Average discharge current, I_{avg}

It is expressed as the sum of the absolute values of individual apparent charge magnitudes, q_{i}, during a specified time interval, T_{ref}, over that time interval:

$$I_{\mathrm{avg}} = \frac{1}{T_{\mathrm{ref}}} \sum_{i=1}^{k} |q_{\mathrm{i}}| \tag{A.35}$$

vi. Discharge power, P_{pd}

The average pulse power fed into the terminals of the test object due to apparent charge for a chosen time interval:

$$P_{\mathrm{pd}} = \frac{1}{T_{\mathrm{ref}}} \sum_{i=1}^{k} (q_{\mathrm{i}} u_{\mathrm{i}}) \tag{A.36}$$

vii. Quadratic rate, D_{pd}

The sum of squares of the individual apparent charge magnitudes, q_{i}, during a chosen time interval over that time interval:

$$D_{\mathrm{pd}} = \frac{1}{T_{\mathrm{ref}}} \sum_{i=1}^{k} (q_{\mathrm{i}}^{2}) \tag{A.37}$$

Parameters associated with partial discharges are not limited to the ones listed above. An extensive list can be found in the relevant standards [88]. The parameters listed above are mostly associated with the apparent charge derived from partial discharge pulses, and the statistical patterns of long duration tests.

Appendix B

Numerical computation of electric field distribution in experimental electrode systems

B.1 Simulation workflow

The process of implementing a simulation model in COMSOL Multiphysics® requires specific steps before the user is able to initiate the computation and ultimately solve the model. However, the model's complexity, requirements in hardware resources and the overall flexibility of the user vary when the dimension level of the geometry increases. A standard workflow procedure is shown in the graph chart of Figure B.1 below.

Every step is required to be implemented before solving the model. However, the order these steps are executed can vary from the way they are illustrated in the flowchart above. Prior to the process shown in Figure B.1, the user needs to become familiar with the graphical interface of the software package and more importantly with the mathematical and physics related principles that run in the background of each module.

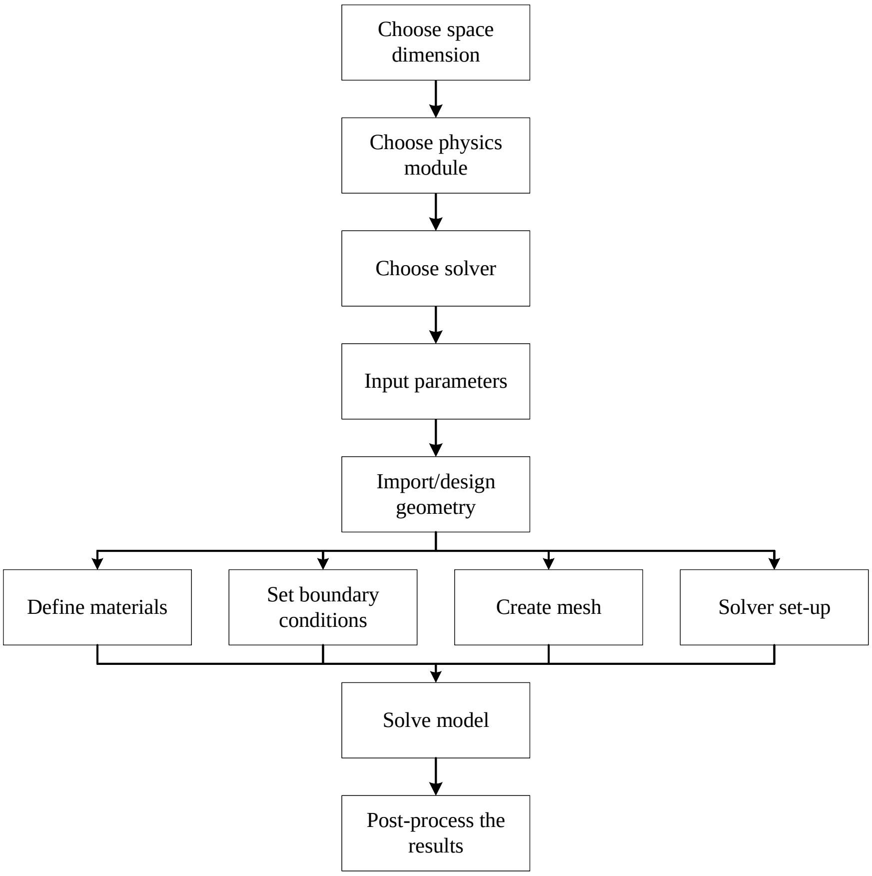

Figure B.1: Workflow for the implementation of a model in COMSOL Multiphysics®.

B.2 Physics modules

For the computation of electric field in a specific geometry, the most convenient physics modules to be used are the Electrostatics (ES) and the Electric Currents (EC). The sets of equations executed in the background of the computation do not differ in a great extent in the two modules. However, in case complex geometries are studied, these small differences might have a significant impact in the computation time.

B.2.1 Electrostatics

In static conditions the electric field vector is proportional to the electric potential scalar, and is expressed by Equation (B.1)

$$\boldsymbol{E} = -\nabla V_{\mathrm{e}} \tag{B.1}$$

In dielectric materials the electric field displacement vector $\boldsymbol{D}$ is correlated to the electric field vector through Equation (A.32) which is reproduced below [159, 160]

$$\boldsymbol{D} = \varepsilon_0 \boldsymbol{E} + \boldsymbol{P} \tag{B.2}$$

where ε_0 is the relative permittivity of vacuum and $\boldsymbol{P}$ the electric polarisation vector. In terms of $\boldsymbol{D}$, Gauss's law is expressed as

$$\nabla \boldsymbol{D} = \rho_{\mathrm{c}} \tag{B.3}$$

where ρ_{c} is the free charge or space charge as described in [159]. Combining Equations (B.1) to (B.3), then Gauss's law can be represented as

$$-\nabla\left(\varepsilon_0 \nabla V_{\mathrm{e}} - \boldsymbol{P}\right) = \rho \tag{B.4}$$

which is the fundamental equation behind the Electrostatics module.

B.2.2 Electric Currents

The Electric Currents (EC) module deals with a current conservation problem for a scalar electric potential V_{e}. As Gauss's law was the basis for the Electrostatics module, here Ohm's law has a major role and is expressed as

$$\boldsymbol{J}_{\mathrm{c}} = \sigma \boldsymbol{E} + \boldsymbol{J}_{\mathrm{e}} \tag{B.5}$$

where $\boldsymbol{J}_{\mathrm{c}}$ is the conduction current density, σ is the electrical conductivity, $\boldsymbol{E}$ the electric field vector and $\boldsymbol{J}_{\mathrm{e}}$ the external current density. In stationary conditions, the vector $\boldsymbol{J}_{\mathrm{c}}$ will be divergence-less

$$\nabla \cdot \boldsymbol{J}_{\mathrm{c}} = 0 \tag{B.6}$$

which leads to

$$-\nabla \left(\sigma \nabla V_{\mathrm{e}} - \boldsymbol{J}_{\mathrm{e}}\right) = 0 \tag{B.7}$$

When current sources are considered, then Equation (B.7) is generalised to

$$-\nabla \left(\sigma \nabla V_{\mathrm{e}} - \boldsymbol{J}_{\mathrm{e}}\right) = Q_{\mathrm{j}} \tag{B.8}$$

where Q_{j} represents the distributed current source defined in $\mathrm{A/m^3}$, $\mathrm{A/m^2}$, $\mathrm{A/m}$ or A, depending on the dimension level of the assigned source [159].

B.3 Study of different dimension levels

As an example case, a needle-plane electrode configuration will be considered with a disc-shaped insulator between the two electrodes. The same model will be examined in two different geometry settings, the two- and the three-dimensional for two main reasons: the first is to compare the two different approaches and conclude which one is more convenient with regards to computational efficiency while the second is related to the stability of the calculation when varying different mesh parameters. Such an evaluation process is easier to be performed in a model with theoretically lower requirements in hardware resources and then transferred to the higher dimension model version, if this is found to be necessary.

B.3.1 Two-dimensional (2D) geometry

The first approach involves a simplified 2D-axisymmetric model version of the needle-plane electrode configuration, as shown in Figure B.2.

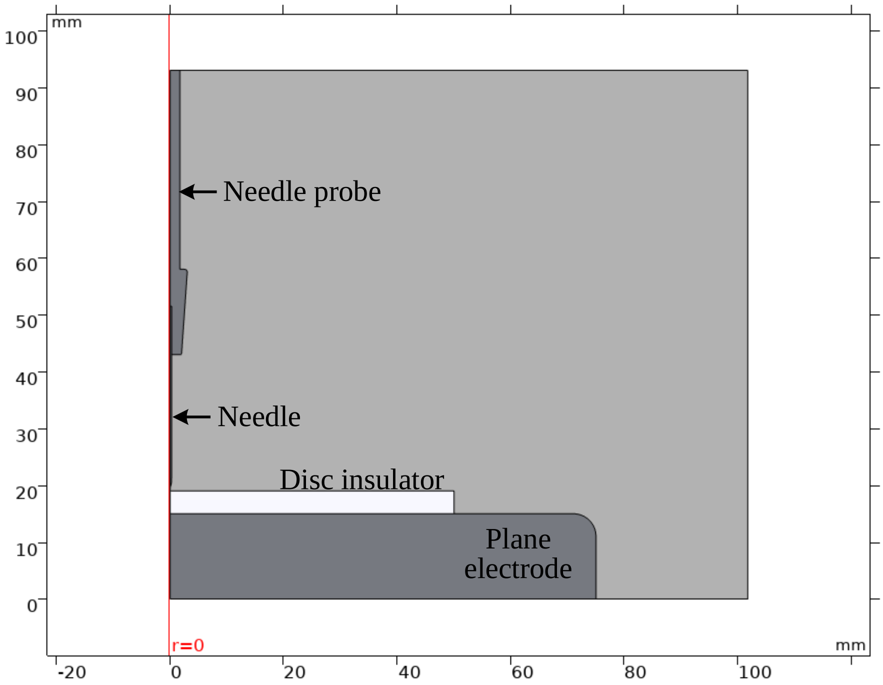

Figure B.2: 2D-axisymmetric model of a needle-plane electrode configuration with a disc-shaped insulator placed between the two electrodes.

The disc-shaped insulator is of 100 mm diameter and 4mm thickness while the plane electrode has a diameter of 150 mm and is of 15 mm thick. The needle has a tip diameter of 20 μm. The distance between the needle tip and the insulator sample is set to $\leq$ 0.5 mm. The current model is studied under electrostatic conditions which means that the electric field inside the charged and grounded domains is expected to be zero, so they can be disregarded from the computation process. For the mesh evaluation process, the applied voltage is set to be 1 V.

As a starting point, the values listed in Table B.1 were considered which corresponds to a “Fine” mesh as it is commonly referred in the COMSOL Multiphysics® interface, with one major adjustment. The minimum element size needs to be relevant to the smallest object within the domain that needs to be meshed. For the current case, the needle has a tip of 10 μm radius so it would be insufficient to assume a minimum element size larger or equal to this value. The starting point is not the maximum possible automatic resolution, as this would go against the main purpose of this process. The chosen mesh elements are of triangular shape since they generate the lowest number of nodes per mesh element compared to the rest of the available mesh shapes in the two-dimensional geometry environment.

Table B.1: Initial mesh parameters in COMSOL Multiphysics®.

Maximum element size	$2\,\mathrm{mm}$
Minimum element size	$(0.01/1000)$ mm
Maximum element growth rate	1.35
Curvature factor	0.3
Resolution of narrow regions	1

The first parameter that will be adjusted is the maximum element size. This will be done by setting a parametric sweep during which the entire model will be solved for different values of the maximum element size, and the variations in the computed electric field values will be observed. By setting the maximum element size of a domain to a specific value, it practically means that within that domain no mesh element will have a size bigger than this specified value. In case the domain is not sufficiently large, it is possible that the resulting maximum element size will be smaller than the preset values since the mesh will not have enough space to stretch considering also the preset minimum element size and element growth rate. Figure B.3 shows the results of this first simulation attempt. The electric field values are normalised to the electric field value that corresponds to the lowest maximum element size value as this is assumed to have the potential to provide the closest to an accurate computation.

It can be inferred from this figure that the solution tends to stabilise as the maximum element size gets very small, close to $0.1\,\mathrm{mm}$. It is also stable at higher values which possibly means that the preset values of minimum element size and maximum element growth rate have a stronger impact in the computation. The considerable increase in the number of degrees of freedom is also visible as the maximum element size gets smaller. The user needs to define what level of compromise is acceptable, if any. The

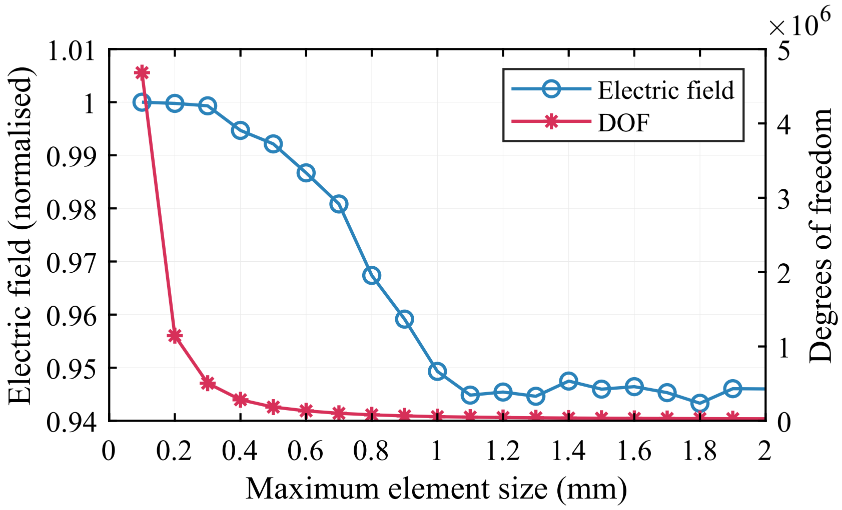

Figure B.3: Normalised electric field and degrees of freedom (DOF) over the maximum element size.

theoretically worst quality solution, at 2 mm maximum element size, is $\sim 6\,\%$ lower than the theoretically best quality solution. However, the degrees of freedom are ~ 170 times higher for the latter case. A good choice could be the maximum element size to be set at 1 mm, and this is what will be kept at this stage.

The next parameter that will be examined is the maximum element growth rate. This value expresses approximately the maximum size ratio between consecutively generated mesh elements. Once again, a parametric sweep is performed for a specific range of values of that parameter. The electric field values and degrees of freedoms (DOF) are illustrated in Figure B.4.

The variation of the electric field seems to be not affected significantly from the variation in the maximum element growth rate. The main reason may be that examined domain is of small size relevant to the pre-set values of the mesh parameters and the mesh itself does not have enough space to stretch. This is reasonable considering that the maximum dimensions of the geometry are approximately 93×100 mm $(h \times w)$ and the mesh is currently set to start from a size of $(0.01/100)$ mm and stop at a size of 1 mm with a relatively small growth rate. For small values of the maximum element growth, the number of degrees of freedom does not increase significantly as happens

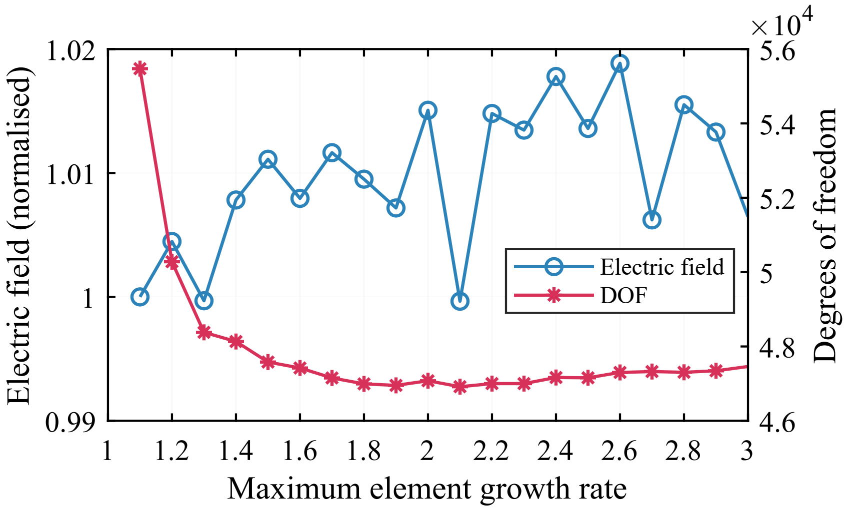

Figure B.4: Normalised electric field and degrees of freedom (DOF) over the maximum element growth rate.

in the case of Figure B.3. A value of 1.3 seems to be a reasonable choice.

Curvature factor is always a positive scalar which expresses the ratio between maximum allowed element size along a curved boundary within the domain that needs to be meshed, over the radius of that curvature. The purpose is to allow the mesh to generate several elements along even the smallest curvature. For this reason, the values considered for that parameter need to be less or equal to 1. Figure B.5 shows the relevant results.

It seems that the curvature factor does not have a big impact on the computed electric field since the difference between 0.1 and 0.2 is less than $1\,\%$. The increase in the number of degrees of freedom between the same points is $\sim 5\,\%$ which can be avoided in case a value of 0.2 is chosen.

Finally, the resolution of narrow regions parameter helps to define the layers of elements that are created in small size regions. This value shall not be lower than 1. Figure B.6 shows the variation in the same parameters as the previous figures this time over the resolution of narrow regions parameter values

The variation in both the electric field computation and the number of degrees of freedom can be considered negligible. This can be justified by the fact that parameters

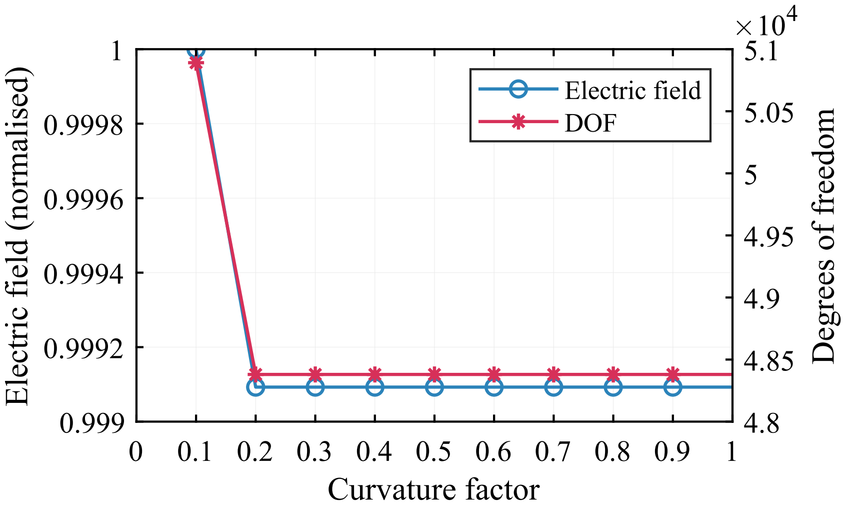

Figure B.5: Normalised electric field and degrees of freedom (DOF) over the curvature factor.

such as the minimum element size and the maximum element growth rate are properly defined in the previous steps. The minimum element quality is 0.2054 while the average element quality is 0.9338, with minimum and maximum possible values for both parameters 0 and 1 respectively. The mesh area is computed at $8235\,\text{mm}^2$. The ratio between the areas covered by the largest and the smallest mesh elements is $2.428 \cdot 10^{-6}$, the total number of triangular elements is 23911 and the total number degrees of freedom is 48380. From an electrical simulation perspective, the electric field at the needle tip appears to be, as was theoretically expected, with a value of $39.23\,\text{V}/\text{mm}$, as this is shown in Figure B.7.

The evaluation process described before was implemented based on the geometry of Figure B.2. The domain surrounding the electrode configuration, and which represents the gaseous insulating medium, is designed as a continuous domain which needs to be treated as such when it comes to the generation of the mesh. Another technique could be to divide the larger domain to smaller segments around the areas of high interest. In this way, the mesh within the smaller domains can be resolved to enhanced resolution levels, maintaining at the same time a reasonable resolution for the rest of the domains and sub-domains which are not expected to affect the computation. An example of the

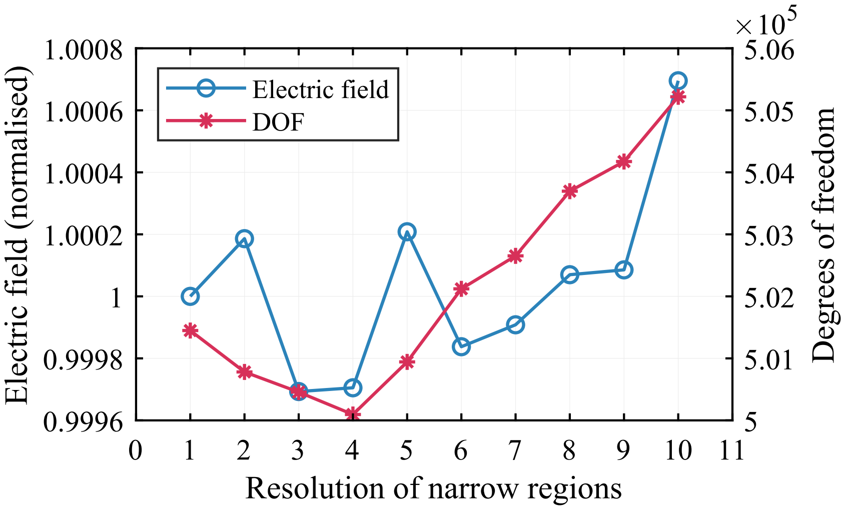

Figure B.6: Normalised electric field and degrees of freedom (DOF) over the resolution of narrow regions.

described implementation is shown in Figure B.8. The comparison between the two cases can be done by comparing the skewness mesh quality histograms as illustrated in Figure B.9.

For Version 2, the minimum element quality is 0.5304 while the average element quality is 0.9233. The average quality seems to be slightly smaller compared to Version 1 for the reason that the enhanced resolution is applied locally to the regions shown in Figure B.8a. However, the minimum quality value is improved for the second case. The total number of mesh triangular elements is 107283, approximately 4.5 times bigger than the first version while the element area ratio is calculated close to $5.11 \cdot 10^{-7}$, almost 4.8 times smaller. The same maximum electric field value, as the one in Figure B.7, is computed, at $39.04\,\mathrm{V/mm}$, $0.48\,\%$ smaller than Version 1 of the geometry, which indicates an acceptable difference between the two versions. Finally, the number of degrees of freedom is identified at 215298, ~ 4.45 times larger than the first version. It could be said that the second approach is a more convenient way to implement a COMSOL Multiphysics® model when there is no time available to go through all the evaluation processes, as it was done for the first version.

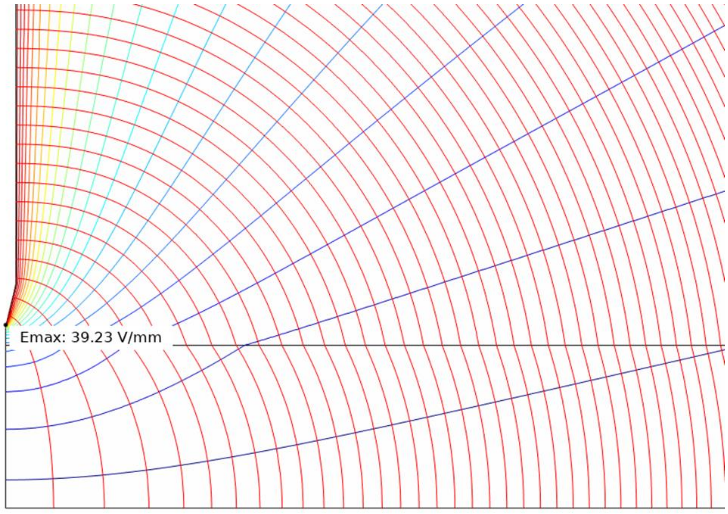

Figure B.7: COMSOL Multiphysics® model solved. With the colourmap are represented the potential lines and in red are represented the electric field streamlines.

B.3.2 Comparison of Electrostatics and Electric Currents modules

All the simulation models presented up to this point were implemented using the Electrostatics – Stationary interface. Another module for electric field computations is the Electric Currents which can also be used combined with different available solvers, such as Stationary and Frequency Domain. As described in [159], the right choice of the physics/solver interface shall be done based on the charge relaxation time which is given by Equation (B.9) for a homogeneous medium

$$\tau = \frac{\varepsilon}{\sigma} \tag{B.9}$$

where ε the material permittivity and σ the electrical conductivity. Conductive materials have a very small charge relaxation time, which is assumed to be zero for perfect conductors. For insulators, Equation (B.9) returns very high values and, for perfect insulators, it becomes infinite. From a physics perspective, the charge relaxation time

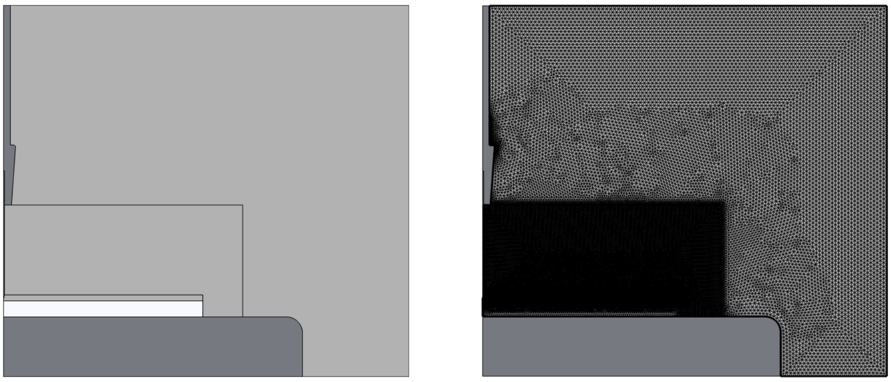

(a) Designed geometry **(b)** Generated mesh

Figure B.8: Alternative version of the geometry of Figure B.2.

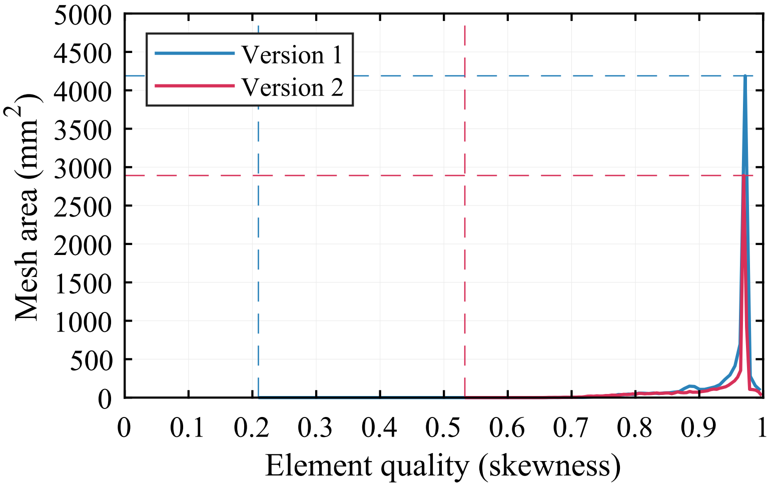

Figure B.9: Comparison of skewness histograms between the two different versions of the same geometry (Figures B.2 and B.8).

expresses the exponential decay of charge within a domain of uniform permittivity and conductivity, with a rate of decay equal to the relaxation time. In a configuration with domains assigned to different types of materials, including conductors and insulators and with an applied voltage which exhibits a frequency component in its waveshape such as the AC, the charge relaxation time can be considered comparable to the observation time. For this reason, the preferred interface is the Electric Currents – Frequency Domain.

The model of Figure B.8 was adapted to the requirements of the new physics/solver interface and it was solved in COMSOL Multiphysics®. The computed electric field was specified to $39.04\,\mathrm{V/mm}$, the same as the Electrostatics – Stationary version of the model. The number of degrees of freedom was identified to 376248, larger than the Electrostatics mainly because the conductive and grounded electrode metal domains needed to be included in the simulation. Figure B.10 shows the computed maximum electric field which appears at the tip of the needle electrode.

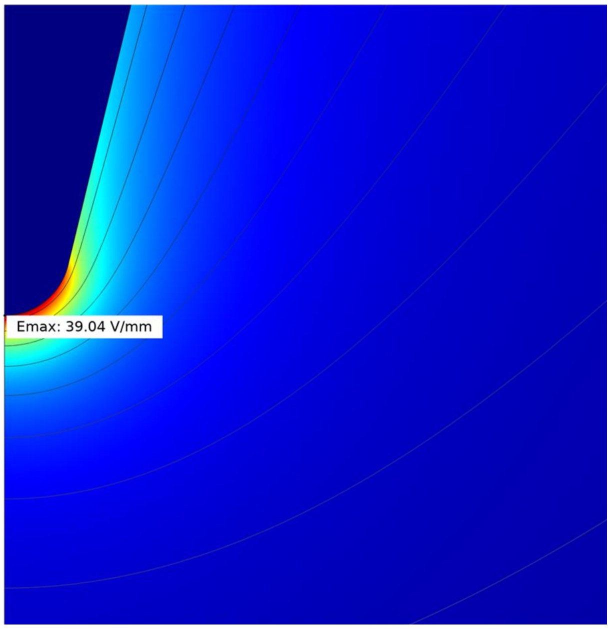

Figure B.10: Maximum electric field using the Electric Currents module.

B.3.3 Three-dimensional (3D) geometry

The mesh evaluation process described before for the two-dimensional (2D) geometry will be now applied to a the three-dimensional (3D) model. Three-dimensional (3D) geometries are considerably more complex and demanding in hardware resources which makes the mesh evaluation process very time consuming and computationally executable only in high-end computer machines or clusters.

The 3D model that will be shown next will combine the values for the mesh parameters that were defined for the first version of the 2D geometry together with the technique that was described in the second version. After solving the 3D model, the value of the computed maximum electric field will be compared with the values obtained from the cases examined previously. The model geometry that was imported into COMSOL Multiphysics® was directly exported from SOLIDWORKS® in a .step file format and is shown in Figure B.11.

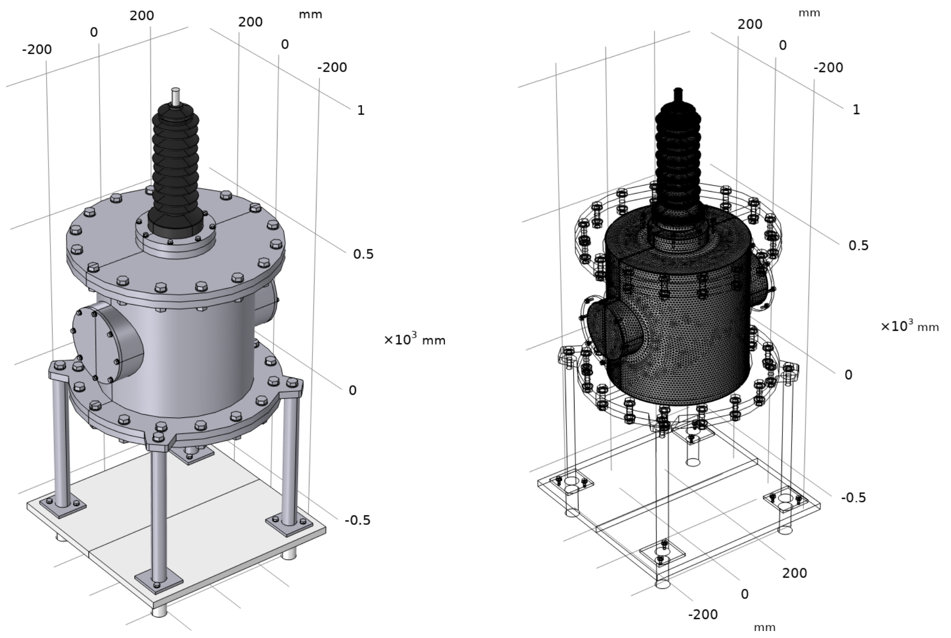

(a) Imported geometry **(b)** Generated mesh

Figure B.11: Full 3D model in COMSOL Multiphysics®.

The final generated mesh is the one shown in Figure B.11b and consists of 29414694 mesh elements which on its own is an indicator of how much demanding the computation is expected to be. The number of degrees of freedom are specified to be 40922582, which is approximately 190 times higher than the 2D version. The overall quality of the mesh is summarised in the corresponding histogram shown in Figure B.12, which follows the same approach as in Figure B.9, with the difference that this time the generated mesh consists of volume elements with considerably higher number of nodes.

The quality of the elements is more distributed compared to the cases in Figure B.9 where the majority were concentrated around the maximum element quality value. It

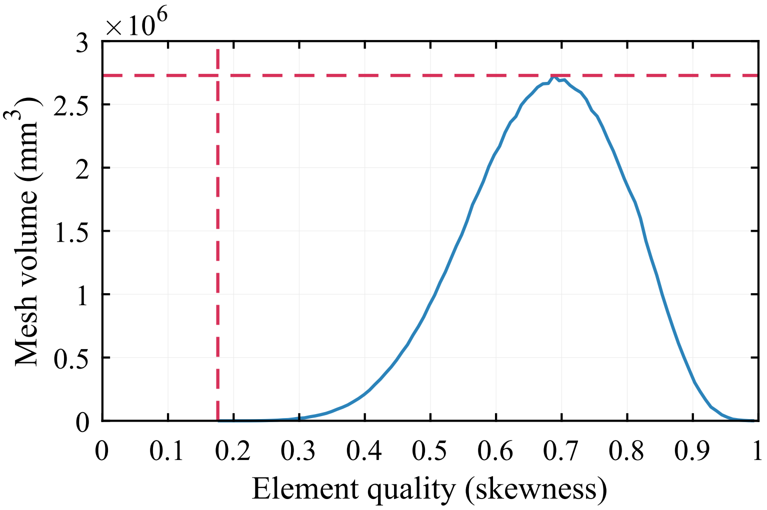

Figure B.12: Skewness histogram for the generated mesh of the three-dimensional (3D) model (Figure B.11).

is worth recalling that, for the 3D case the mesh refinement was performed within the specific volumes of high computational interest. If the same resolution was adopted for the entire 3D geometry, the number of degrees of freedom would have exceeded manageable levels. An illustration of the solved model is shown in Figure B.13.

The computed maximum electric field appears again at the needle tip with a value of $38.82\,\mathrm{V/mm}$. The difference between the 3D version and the corresponding 2D is $0.56\,\%$. This observation makes the use of complex 3D geometries not advantageous in this case considering the requirements in hardware and time to prepare and solve such a computationally demanding model. It is important for the user to take advantage of any available symmetries in the model geometries and reduce the requirements of the model down to a level where the quality of the computation is not distorted. There are cases where the use of 3D geometries is unavoidable although it is advised that the mesh refinement focuses on the areas of high interest which of course requires a good knowledge of the geometry characteristics and possibly a good estimation of the computation output.

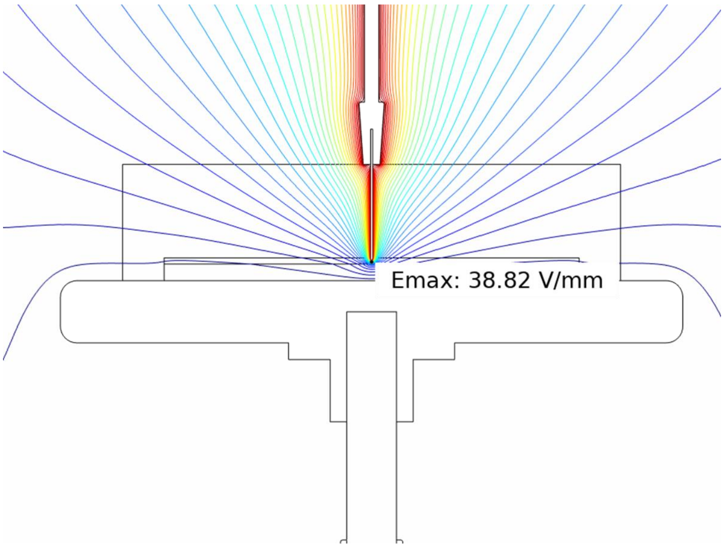

Figure B.13: Cut-plane of the three-dimensional (3D) model (Figure B.11) after it is solved.

B.4 Horizontal orientation of the electrodes

In this section, another version of the needle-plane configuration will be presented. The electrode configuration together with the disc-shaped insulator are placed horizontally, instead of vertically. The presented model does not add anything to the already discussed topics. However, this electrode arrangement was used for part of the experiments that were presented in Chapter 6 and, thus, it is necessary to demonstrate that there are no differences between the arrangements of different orientation.

The mesh was generated following the approach which was shown in Figure B.8 and in a three-dimensional geometry similar to the approach of Figure B.11. The simulated geometry is depicted in Figure B.14.

The purpose of this arrangement is to achieve that the top surface of the disc-shaped insulator will face the side viewport with the needle electrode perpendicularly placed and aligned to the centre of the insulator. The radius of the supporting metal rods attached to the high-voltage bushing was kept small, so they visually cover the smallest possible portion of the insulator top surface. Figure B.15 shows the potential lines and

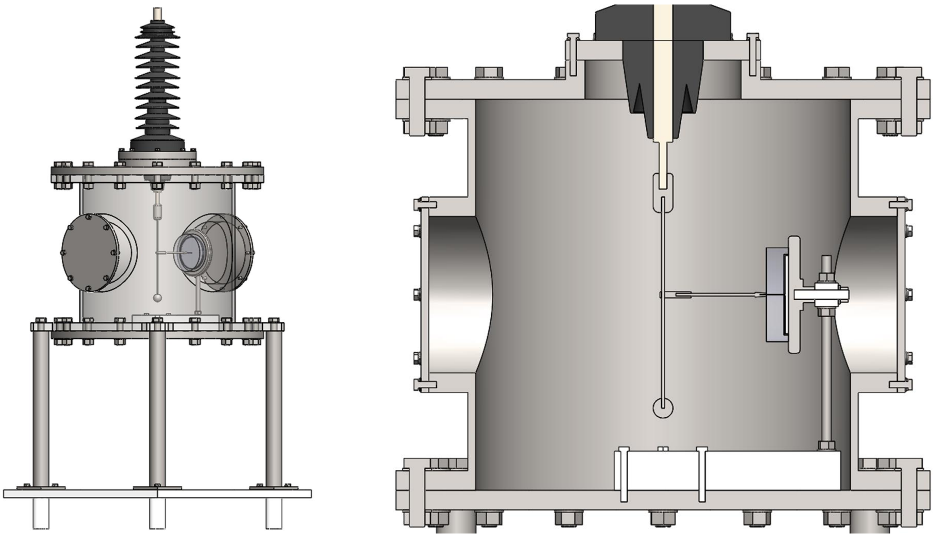

(a) Full geometry **(b)** Side view of the electrode arrangement

Figure B.14: Horizontal arrangement of the electrode configuration inside the pressure vessel.

the place where the maximum electric field appears.

Again, the maximum electric field appears on the needle tip, as it was initially expected. Its magnitude is computed as $39.20\,\mathrm{V/mm}$ which is $0.97\,\%$ higher than the vertical orientation three-dimensional model. Compared to the two-dimensional model of Figure B.8, the same computed value is $0.41\,\%$ higher.

B.5 Summary of the presented model versions

The models presented in the previous section describe different versions of practically the same implementation of an electrode configuration. A brief comparison between them, with regards to the computed value of highest interest, i.e., the maximum electric field E_{max}, is shown in Table B.2.

It is obvious that no remarkable differences in the computed values of the different implemented versions were found. Variations between $0-3\,\%$ are usually reasonable.

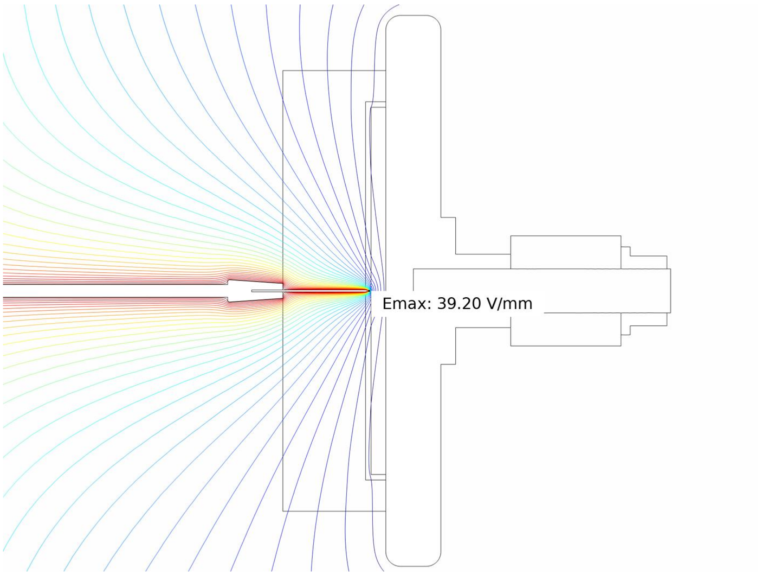

Figure B.15: Maximum electric field for the horizontal orientation case (Figure B.14).

Table B.2: Comparison of the different FEM model versions.

Version	**Model type**	$E_{\max}$	**Absolute difference**	**Figure no.**
Version 1	2D - ES - no.1	39.23 V/mm	0.47 %	Figure B.7 and Figure B.8
Version 2	2D - ES - no.2	39.04 V/mm	0 % (Reference)	Figure B.8
Version 3	2D - EC	39.04 V/mm	0 %	Figure B.10
Version 4	3D - vertical	38.82 V/mm	0.56 %	Figure B.13
Version 5	3D - horizontal	39.20 V/mm	0.41 %	Figure B.15

As expected, adopting a sufficiently refined mesh can be time demanding. A more focused mesh refinement can be performed to ensure that the regions of high interest will return an acceptable computation.